NEW AVENUES FOR THE CHEMICAL MODIFICATION OF 1D AND 2D NANOMATERIALS

Memoria presentada por
Sofía Leret García
Para optar al título de doctora en Química Orgánica
Departamento de Química Orgánica
Universidad Autónoma de Madrid
Madrid, 2017

Memoria Presentada para optar al título de doctora en Química Orgánica

Director tesis:

Dr. Emilio M. Pérez Álvarez

Tutor académico:

Drª. Gema De la Torre Ponce

A mi madre

Agradecimientos

El presente trabajo ha sido realizado en el IMDEA Nanociencia bajo la supervisión de Emilio M. Pérez, por lo que en primer lugar me gustaría agradecer a Emilio la oportunidad de realizar esta Tesis, con el he aprendido de ciencia pero sobre todo a pensar.

El comienzo de esta andadura no hubiera sido posible sin María Jose Mancheño, quien me enseñó a trabajar en un laboratorio, es un placer terminar esta etapa también con ella. A Stephane Rigaut por darme la oportunidad de hacer la estancia en su grupo.

Un agradecimiento muy especial a todas las personas con las que he trabajado, entre ellas resaltar, Andrés Black por enseñarme casi todo lo que sé sobre el grafeno, hemos aprendido mucho juntos y lo más importante siempre ha sido con una gran sonrisa. Es una pena que esos trabajos no hayan salido a la luz con todo el esfuerzo que hubo detrás de ellos. En esta última etapa también he tenido el placer de poder trabajar con Fernando, gracias por tu paciencia al explicarme esas cosas de físicos que a veces los químicos no vemos de una forma tan fácil. Dentro de las colaboraciones realizadas agradezco también a Ramón, Juan Jesús, Fabián, Aday, Andrés Castellanos, Amadeo, Dani, Santi y Cristina.

A mis compañeros durante la estancia: Klaus, Rachid, Eleonora, Huseim, Pramila y Lucie.

Por supuesto agradecer a todo mi grupo de laboratorio, de todos he aprendido cosas, porque de las cosas malas también se aprende. Pero especialmente agradezco a Leyre con la que he compartido la mayor parte del tiempo en el laboratorio, es importante tener una persona al lado en la que apoyarte, gracias por ser una gran compañera. A los de la planta de arriba, Tere y Fran por su sonrisa y vitalidad y Sofi por ser siempre tan cariñosa. A mi compañero de vitrina Emerson por ayudarme tantas veces. A las nuevas incorporaciones Belén, Zulay, Mariano, Matias, Enrique y Julia, y por supuesto a todos los que han pasado en estos cuatro años, Dario, Mar, Lidia, Prabash, Javi y María.

A Diego, Leo y Rebe, por ser mis compañeros de comida, té, cervezas, pero sobretodo compañeros de risas y frustraciones. Agradecer también a Gorka, Alfonso, Adriana, Alberto y tanta gente del IMDEA con la que da gusto encontrarse.

No se me puede olvidar agradecer a Juancar por alegrarme cada mañana al entrar por la puerta y por supuesto a Antonio de manteniemiento por estar siempre dispuesto a ayudarnos con una sonrisa.

Y un especial agradecimiento a aquellos con los que he tenido la suerte de hacer una amistad más allá del IMDEA, a mi franchute, Pierre, por todas las cervezas artesanas y conversaciones compartidas, gracias maestro cervecero. A Helena y Juanpa porque con ellos volvería a irme de estancia con los ojos cerrados, puedo decir que ha sido una de las etapas más bonitas del doctorado. A María, para ella no tengo palabras, compañera de universidad y trabajo pero sobretodo amiga, de verdad que he estado un rato intentando poner todo lo que significas para mí pero es imposible, además no te molan mucho las ñoñerías luego simplemente GRACIAS.

A mi gente, Nerea, Irene, Sara, Garci, Vallekano, Jorge, Toni, Paredes, Silvia, Martita, José, Arturo, Nacho, Alejandra, Isato, Mila...porque hay vida más allá del trabajo y es la más importante.

Y por supuesto el agradecimiento mas grande a mi familia y compañero de viaje Raúl. A mis hermanos, a mi padre, para él hubiera sido un orgullo verme terminar la carrera y la tesis, sin toda la paciencia que invertiste en enseñarme nunca sería lo que soy, esta tesis es tuya. Por su puesto a mi fan más incondicional, mi madre, porque no entiende lo que hago pero lleva mis papers allá donde va, para ella necesitaría otra tesis, no hay amor más incondicional. Y por supuesto a Raúl, unas gracias inmensas por todo lo que me aportas cada día, difícil de expresar con palabras.

ABSTRACT

In this work we presented three main results:

i) The use of naphthalene bisimides as recognition motifs for the synthesis of mechanically-interlocked derivatives of SWNTs. The mechanically interlocked nature and polymer wrapping of NDI was probed by analytical and spectroscopic techniques (TGA, NMR, UV-vis-NIR and Raman) and adequate control experiments. Furthermore, individual macrocycles were be seen around the nanotubes under TEM scrutiny.

ii) The development of a simple method for the covalent modification of graphene with strict spatial periodicity at the nanometer scale, based on selective adsorption of cyanomethyl radicals ($CH_2CN^{\bullet}$) produced by homolytic breaking of acetonitrile (CH_3CN), which present a nearly complete selectivity to bind covalently to graphene grown on Ru(0001) on specific atomic sites. The results obtained experimentally were validated through Density Functional Theory (DFT) calculations.

iii) The development of a high performance photodetector through reversible, and reproducible noncovalent functionalization of MoS_2-devices with molecular dyes. We found an enhancement of the photoresponse of four orders of magnitude and responsivities up to 100 AW^{-1}.

RESUMEN

En este trabajo se presentan tres resultados principales:

i) El uso de naftaleno bisimidas como motivo de reconocimeinto para la síntesis de derivados mecánicamente enlazados de SWNTs. La naturaleza de los enlaces mecánicos y y la formación de polímeros de NDI ha sido probada a través de técnicas analíticas, espectroscópicas (TGA, NMR, UV-vis-NIR y Raman) y los correspondientes experimentos control. Además ha sido posible observar la presencia de macrociclos individules alrededor de los nanotubos gracias al microscopio de transmisión electrónica.

ii) El desarrolo de un metodo simple para la modificación covalente de grafeno con una cierta periodicidad, este método se basa en la adsorción selectiva de radicales de cianometilo ($CH_2CN^{\bullet}$) producidos mediante ruptura homolítica de acetonitrilo (CH_3CN), El cual presenta una gran selectividad para enlazar covalentemente sobre sitios atómicos específicos del grafeno crecido sobre Ru(0001). Los resultados expermientales obtenidos fueron confirmados a través de cálculos DFT.

iii) El desarrollo de fotodetectores de alto rendimiento a través de funcionalziación no covalente reversible y reproducible de dispositivos de MoS_2 mediante el uso de distintas moléculas. A través de este trabajo hemos obtenido un incremento de la fotorespuesta de cuatro órdenes de magnitud y responsividades de hasta $100AW^{-1}$.

TABLE OF CONTENTS

CHAPTER 1

CHAPTER 2

CHAPTER 3

REFERENCES, ABBREVIATIONS AND ACRONYMS

In this thesis we have chosen to focus on published work only. Many projects and results have been left out.

Bibliographic citations have been placed as footnotes in the pages where they were first cited in the section and at the end of each section or chapter; they were added independently at every section or chapter, so they are duplicated in different chapters when necessary.

Throughout this manuscript, abbreviations and acronyms recommended by the American Chemical Society in the Organic Chemistry area (revised in the Journal of organic chemistry on January 2016; http://pubs.acs.org/paragonplus/submission/joceah_authguide.pdf) have been employed.

0D	Zero dimensional
1D	Unidimensional
2D	Bidimensional
3D	Tridimensional
ADMP	Acyclic Diene *Metathesis* Polymerization
AFM	Atomic Force Microscopy
BV	Benzyl viologen
C_{60}	Fullerene
C_h	Chiral vector
CH_2Cl_2	Dichloromethane
CNTs	Carbon nanotubes
CPs	Coordination polymers
CP-Ms	Metal coordination polymers
CVD	Chemical vapor deposition
D_2O	*Deuterium* Oxide
DFT	*Density functional theory*
DMF	Dimethylformamide
EG	Epitaxial graphene
exTTF	π-extended tetrathiafulvalene
FETs	Field-effect transistors
GOx	Glucose oxidase enzyme
LDOS	*Local density of states*
LED	Light-emitting diode
LT-STM	Low-temperature scanning tunneling microscopy
MINT	Mechanically *Interlocked Nanotubes*
MOSFET	Metal-oxide-semiconductor Field-effect transistor
MWNTs	*Multi*-Walled *Nanotubes*
NDA	4-nitrophenyl diazonium tetrafluoroborate
NDIs	Naphthalene Diimides
P3HT	Poly (3-hexylthiophene-2, 5-diyl)

PAHs	*Polycyclic aromatic hydrocarbons*
PDIs	Perylenediimides
PDMS	Polydimethylsiloxane
PLE	*Photoluminescence Excitation*
PMMA	poly (methyl methacrylate)
PVA	Polyvinylalcohol
QMS	Quadrupole mass spectrometer
RBM	Radial breathing modes
RCM	Ring-Closing Metathesis
SiC	Silicon carbide
SDS	*Sodium* dodecyl sulfate
STM	Scanning tunneling microscopy
STS	Scanning tunneling spectroscopy
SWNTs	Single-Walled *Nanotubes*
TCE	Tetrachloroethane
TCNQ	Tetracyanoquinodimethane
TEM	Transmission Electron Microscopy
TGA	Thermogravimetric Analysis
TMDCs	Transition metal dichalcogenides
TPP	Tetraphenyl porphyrin
UHV	Ultra-high vacuum
UPS	*Ultraviolet Photoelectron Spectroscopy*
V_T	Threshold voltage
VT-STM	Variable-temperature scanning tunneling microscopy
ω_{RBM}	Radial breathing modes frequencies
XRD	x-ray diffraction
XPS	*X-ray Photoelectron Spectroscopy*

CHAPTER 1

1. Introduction

In 1985 Kroto, Smalley, and Curl discovered fullerenes,[1] and received the 1996 Nobel Prize in Chemistry for this discovery. A few years later, carbon nanotubes (CNTs) were discovered serendipitously during the synthesis of fullerene C_{60}. More recently graphene was isolated and characterized by A. K. Geim and K. S. Novoselov in 2004[2] as we will explain in the chapter 2. All of them sparked the interest of the scientific community, becoming very active areas of research.

The structure of single-walled carbon nanotubes (SWNTs) consists of a graphene sheet rolled up into a seamless cylinder with diameter of the order of a nanometer. Carbon atoms are linked into hexagon, and the hexagonal pattern makes up the walls of a cylinder. It was in 1952 when Radushkevich and Lukyanovich[3] published the first evidence about the formation of multiwalled carbon nanotubes (MWNTs), but it was in 1991 when Iijima[4] systematically described this nanostructure (see Figure 1.1).

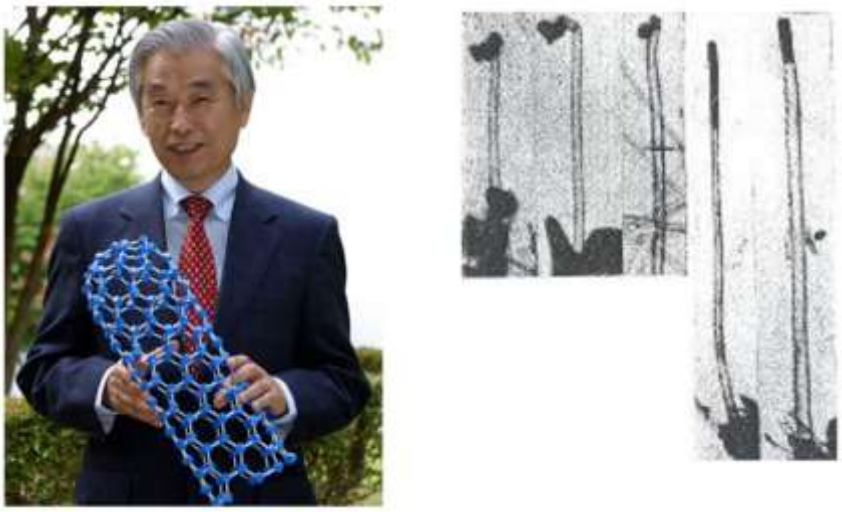

Figure 1.1. Sumio Iijima, he is recognized as the dicoverer of CNTs (left) and TEM images of nanometrics MWNTs obtained by Radushkevich and Lukyanovich in 1952 (right).

[1] H. W. Kroto, J. R. Heath, S. C. O'Brien, R. F. Curl and R. E. Smalley, *Nature*, **1985**, *318*, 162.
[2] (a) K. S. Novoselov, A. K. Geim, S. V. Morozov, D. Jiang, Y. Zhang, S. V. Dubonos, I. V. Grigorievam and A. A. Firsov, *Science,* **2004**, *306*, 666-669. (b) A. K. Geim and K. S. Novoselov, *Nat. Mater.* **2007,** *6*, 183-191.
[3] L. V. Radushkevich and V. M. Lukyanovich, *Zurn. Fisic. Chim.,* **1952**, *26*, 88-95.
[4] S. Iijima, *Nature,* **1991**, *356*, 56-58.

Ijima discovered them as a by-product of C_{60} fullerenes synthesis while studying the carbon materials formed on the negative end of the cathode electrode of an arc-discharge evaporator. It was observed this by-product by transmission electron microscopy when he found the MWNTs. These tubes contained at least two layers and ranged in outer diameter from about 3 to 30 nm. But it wasn't until 1993 when a scanning of some MWNTS showed a new class of CNTs with just a single layer with diameter typically in the range of 1-2 nm.[5] It was later found that the presence of certain transition metal in the arc catalyzed the production of carbon nanotube with one layer. Ever since the discovery of carbon nanotubes several ways of preparing them have been explored. MWNTs and SWNTs have been synthesized using methods which include arc evaporation of graphite,[6] laser ablation[7] and chemical vapor deposition[8,9] (CVD). Specific methods have been developed to the synthesis of SWNTs, the chirality and diameter-dependent properties make the development of new techniques to obtain SWNTs with a specific diameter necessary.[10] Chemical vapor deposition is currently the best way to scale up production to industrial levels.

1.1 Structure and spectroscopy properties of SWNTs

Conceptually, SWNTs may be formed by cutting a strip of graphene sheet and rolling it into a tube.[11] The lattice vector that connects the two points that will roll into each other is called chiral vector (see Figure 1.2). The electronic properties of carbon nanotubes are defined by its structure, which in turn is defined by a chiral angle and this chiral vector given by:

$$C_h = na_1 + ma_2$$

Electron diffraction was the first technique employed to identify the structure of carbon nanotubes.[12] The (n, m) index determine the atomic structure and electronic properties of SWNTs. Armchair nanotubes with n = m are metals and the zigzag nanotubes correspond to the case of m=0, and are generally semiconducting and only metal when n-m is an integer multiple of three; all other (n,m) chiral vectors correspond to chiral semiconducting nanotubes where n> m> 0. Calculations[13] predict that armchair (n = m) tubes have bands crossing the Fermi level and are therefore metallic. For all other tubes (chiral and zigzag) there are two possibilities: when n - m = 3q (where q is an integer), the nanotubes are metals, while in the case of n - m ≠ 3q, tubes are predicted to be semiconducting with an energy gap that depends on the diameter according to $E_{gap}= 2\gamma_0 a_{c\text{-}c}/d_t$, where γ_0 is the interaction energy between neighboring C atoms, $a_{C–C}$ the nearest-neighbour C–C distance (0.142 nm) and d_t the diameter.

---

[5] a) S. Iijima, T. Ichihashi, *Nature* **1993**, *363*, 603-605; b) D. S. Bethune, C. H. Kiang, M. S. De Vries, G. Gorman, R. Savoy and J. Vázquez, *Nature,* **1993**, *363*, 605-607.
[6] Y. Ando, X. Zhao, T. Sugai and M. Kumar, *Mater. Today*, **2004**, *7*, 22-29.
[7] T. Guo, P.Nikolaev, A. Thess, D. T. Colbert and R. E. Smalley; *Chem. Phys. Lett*., **1995**, *243*, 49-54.
[8] M. José-Yacamán, M. Miki-Yoshida, L. Rendón and J. G. Santiesteban, *Appl. Phys. Lett*., **1993,** *62*, 657-659.
[9] M. Kumar and Y. Ando, *J. Nanosci. Nanotechnol*., **2010**, *10*, 3739.
[10] H. W. Zhu, C. L. Xu, D. H. Wu, B. Q. Wei, R. Vajtai and P. M. Ajayan, *Science*, **2003**, *296*, 884-886.
[11] R. Saito, M. Fujita, G. Dresselhaus and M. S Dresselhaus *Appl. Phys. Lett*. **1992**, *60*, 2204-2206.
[12] a) L. C. Qin, *Rep. Prog. Phys*., **2006**, *69*, 2761-2816. b) L. C. Qin, *Phys. Chem. Chem. Phys.*, **2007**, *9*, 31-48.
[13] M. S. Dresselhaus, G. Dresselhaus, and P. C. Eklund, *Science of Fullerenes and Carbon Nanotubes* (Academic, San Diego, 1996).

The quasi-one-dimensionality of nanotubes has an important electronic consequence for all (n,m) species: it introduces sharp spikes, called van Hove singularities, into the densities of states.

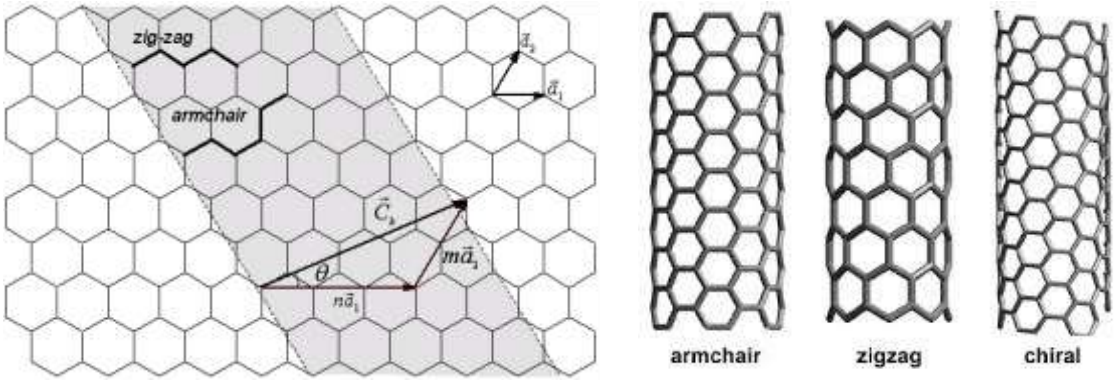

Figure 1.2. Graphene sheet map illustrating possible single-walled nanotube structures that can be formed by wrapping the sheet to form a cylindrical tube (left) and the schematic model for single-wall carbon nanotube that can be formed (right).

The interest in the separation of the different nanotubes types (metallic or semiconductor) in a non-aggregated state has developed many methods for the enrichment or selective synthesis of these SWNTs. These methods include electrophoresis, ultracentrifugation, and selective destruction of one type of nanotubes by irradiation or by chemical interaction with molecules and covalent or non-covalent functionalization.[14,15]

This variety of structures makes it necessary to develop techniques to characterize the SWNTs after fabrication and purification process, a wide range of techniques have been applied to characterize functionalized SWNTs: IR, Raman, UV/vis, thermogravimetric analysis (TGA), Atomic force microscopy (AFM), Transmission electron microscopy (TEM), X-ray photoelectron spectroscopy (XPS). TEM images allows characterize the morphology and structure of carbon nanotubes whereas analytical techniques as Raman spectroscopy[16,17] and optical absorption spectroscopy[18,19] are used to elucidate the atomic structure and to obtain the chiral indices of carbon nanotubes. The combination of both techniques, Raman and electronic spectra, enables an excellent means for specifying the purity and chirality aspects of the nanotube.

[14] M. S. Arnold, S. I. Stupp and M. C. Hersam, *Nano Lett*., **2005**, *5*, 713-718.
[15] R. Krupke, F. Hennrich, M. M. Kappes and H. V. Lohneysen, *Nano Lett*., **2004**, *4*, 1395-1399.
[16] A. M. Rao, E. Richter, S. Bandow, B. Chase, P. C. Eklund, K. A. Willams, S. Fang, K. R. Subbaswamy, M. Menon, A. Thess, R. E. Smalley, G. Dresselhaus and M. S. Dresselhaus, *Science*, **1997**, *275*, 187-191.
[17] A. Jorio, M. A. Pimenta, A. G. Souza, R. Saito, G. Dresselhaus and M. S. Dresselhaus, *New J. Phys*., **2003**, *5*, 139.
[18] S. M. Bachilo, M. S. Strano, C. Kittrell, R. H. Huage, R. E. Smalley and R. B. Weisman, *Science*, **2002**, *298*, 2361-2366.
[19] M. S. Strano, S. K. Doorn, E. H. Haroz, C. Kittrell, R. H. Huage and R. E. Smalley, *Nano Lett*., **2003**, *3*, 1091-1096.

1.1.1 Raman Spectroscopy

Raman spectroscopy has played an important role in the study and characterization of graphitic materials.[20] For sp^2 nanocarbons, Raman spectroscopy can give information about crystallite size, the presence of sp^3 hybridization and chemical impurities, optical energy gap, doping, defects, number of layers, nanotube diameter, chirality and metallic versus semiconductor behavior.

The resonance results from the 1D quantum confinement of the electrons in the nanotubes. Kasuya et al.[21] provided the first evidence for a diameter-dependent dispersions arising from the cylindrical symmetry of the nanotubes and the characteristic Raman features of SWNTs (see Table 1.1).

Notation	*Frecuency (cm^{-1})*	*Symmetry*	*Type of mode*
RBM	$248/d_t$	A	In phase radial displacements
D-band	~ 1350	–	Defect-induced dispersive
G-band	1550-1605	A, E_1, E_2	Graphite-related optical mode
G'-band	~2700	–	Overtone of D-band, highly dispersive

Table 1.1 Raman peaks observed in the CNTs spectra at room temperature and the corresponding symmetry.

The Raman spectrum of nanotubes has three characteristic bands:

- The ***G-band*** (1500-1600 cm^{-1}) corresponds with the stretching of the C-C bond which is common to all sp^2 carbon systems , this band is highly sensitive to strain effects in sp^2 nanocarbons and can be used to probe any modification to the graphitic structure.[22,23]
- The ***D band*** around 1350 cm^{-1} results from a second order two-phonon process and indicates the presence of disorder in sp^2-hybridized carbon systems .The *2D band* which results from a second-order two-phonon process and exhibits a strong frequency dependence on the excitation laser energy.
- The ***radial breathing modes*** **(RBM)** in the 100-200 cm^{-1} region, it is the unique phonon mode appearing only in carbon nanotubes and it is especially important in two ways: (1) for the determination of the diameter of the nanotubes through the dependence of ω_{RBM} and d_t, and (2) for relating the ω_{RBM} and the resonant optical transition energies E_{ii} for a given tube.

[20] M. S. Dresselhaus, A. Jorio, M. Hofmann, G. Dresselhaus and R. Saito, *Nano Lett.*, **2010**, *10*, 751-758.
[21] A. Kasuya, Y. Sasaki, Y. Saito, K. Tohji and Y. Nishina, *Phys. Rev. Lett.*, **1997**, *78*, 4434-4437.
[22] L. M. Malard, M. A. Pimenta, G. Dresselhaus and M. S. Dresselhaus, *Phys. Rep.*, **2009**, *473*, 51-87.
[23] Z. H. Ni, T. Yu, Y. H. Lu, Y. Y. Wang, Y. P. Feng and Z. X. Shen, *ACS Nano,* **2008**, *2*, 2301-2305.

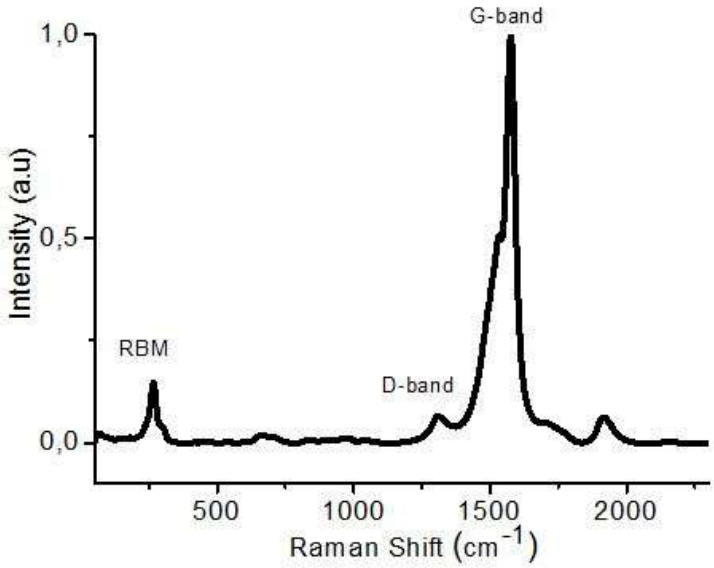

Figure 1.3. Raman spectra of **(6,5)** SWNTs.

1.1.2 Optical Spectroscopy

Optical absortion and fluorescence spectroscopy have also been used to study the SWNTs. To be able to use these techiques it was first necessary obtain a SWNTs suspension. In this way the use of non-covalent common surfactans in water breaks the bundle of nanotubes allowing a suspension that can be analyzed by both tecniques. The signals observed in semiconducting and metallic SWNTs are assigned to transition between Van Hove singularities. In the case of optical absortion the SWNTs presents characterisitcs bands in the visible and near IR regions. The semiconducting SWNTs exhibit near-infrared transition (S_{11} and S_{22}) that arise from the inter-Van Hove energy levels while metallic SWNTs show a absortion band (M_{11}) in the visible region due to the curvature of the graphene sheet (see Figure 1.4).[24,25]

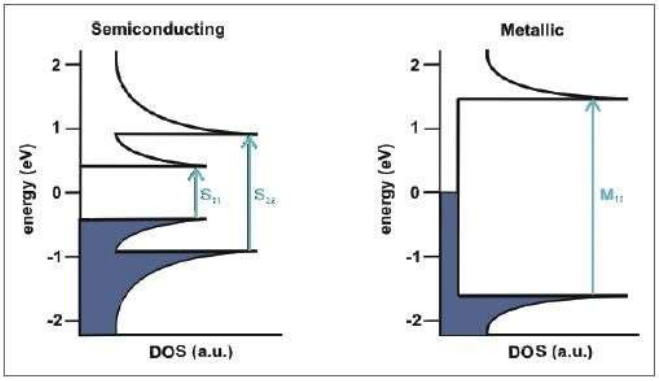

Figure 1.4. Schematic density of states for a semiconducting and metallic SWNTs in a simple band theory model. Allowed optical transition are illustrated as vertical arrows.

[24] M. J. O'Connell, S. M. Bachilo, C. B. Huffman, V. C. Moore, M. S. Strano, E. H. Haroz, K. L. Rialon, P. J. Boul, W. H. Noon, C. Kittrell, J. P. Ma, R. H. Hauge, R. B. Weisman and R. E. Smalley, *Science*, **2002**, *297*, 593-596.
[25] T. Hertel, A. Hagen, V. Talalaev, K. Arnold, F. Hennrich, M. Kappes, S. Rosenthal, J. McBride, H. Ulbricht and E. Flahaut, *Nano Lett.*, **2005**, *5*, 511-514.

In addition, the fluorescence emission enabled the detection of many optical transition and their assignment to specific (n,m) chiral indices of semiconducting SWNTs. The photoluminescence process occurs in three step (see Figure 1.5): a) absorption of light at phonon energy E_{22} (S_{22}) due to the second Van Hove transition b) rapid electronic relaxation from E_{11} (S_{11}). The values of E_{11} and E_{22} changes depending of the SWNTs structures, so fluorescence provides an experimental basis for checking and refining models of nanotube electronic structure.

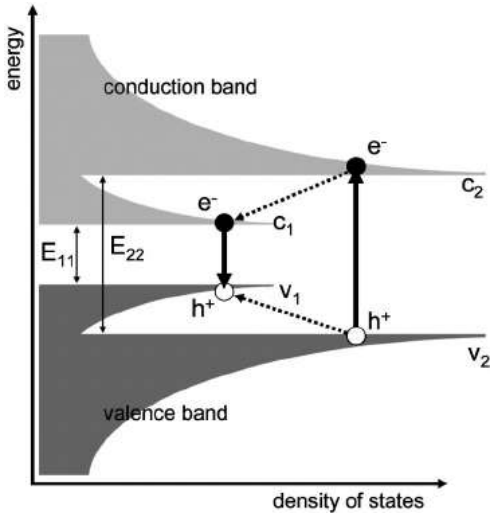

Figure 1.5. Schematic of the density of electronic states for a single nanotube.

1.2 Properties and chemical modification of SWNTs

Their unique mechanical, electrical and thermal properties make SWNTs suitable for a variety of different applications where these 1D nanostructures could be exploited. Due to their unique tubular structure and large length/diameter ratio SWNTs can be used for efficient transport of electrons[26] and optical excitation[27] making them promising materials for applications in nanotechnologies. But the main disadvantage of this material is the insolubility and the strong tendency to "rope up" in solution that hamper molecular level studies, characterization and device applications, chemical functionalization is the major route to overcome such difficulties. Another benefit from functionalization is that the SWNTs can be multifunctional after attachment of the chemical functional groups on the surface, making them ideal candidate for applications. There are two types of methodologies for functionalization and solubilization of the SWNTs: covalent and noncovalent functionalization. Covalent functionalization needs covalent linkage of functional groups onto the surface of SWNTs, especially the sidewall of SWNTs. Noncovalent functionalization is mainly achieved by polymer-wrapping and π-π stacking of aromatic compound.[28]

[26] P. L. McEuen and J. Y. Park, *MRS Bulletin*, **2004**, *72*.
[27] M. Y. Sfeir, T. Beetz, F. Wang, L. Huang, X. M. Huang, M. Huang, J. Hone, S. O'Brien, J. A. Misewich, T. F. Heinz, L. Wu, Y. Zhu and L. E. Brus, *Science*, **2006**, *312*, 554-556.
[28] A. Hirsch, *Angew. Chem. Int. Ed*., **2002**, *41*, 1853.

1.2.1 Covalent chemistry of SWNTs

SWNTs present two regions of different reactivity where we can carry out a covalent chemical modification, the end of the nanotube are more reactive than their sidewalls. The addition reaction to the C-C double bond cause the transformation of sp^2 into sp^3 hybridized carbon atoms losing the structure and electronic properties of the tubes,[29] whereby new functions can be implemented that cannot otherwise be acquired by pristine nanotubes.

Smalley and co-workers developed the first covalent functionalization cutting the nanotubes by thermal oxidation process using a mixture of concentrated nitric and sulfuric acid.[30] The final products are nanotube fragments with lengths in the range of 100-300 nm, whose ends and sidewall are decorated with a high density of various oxygen containing groups (mainly carboxyl groups). This carboxyl groups represent useful sites for further modifications with amides or esters (see Figure 1.6).

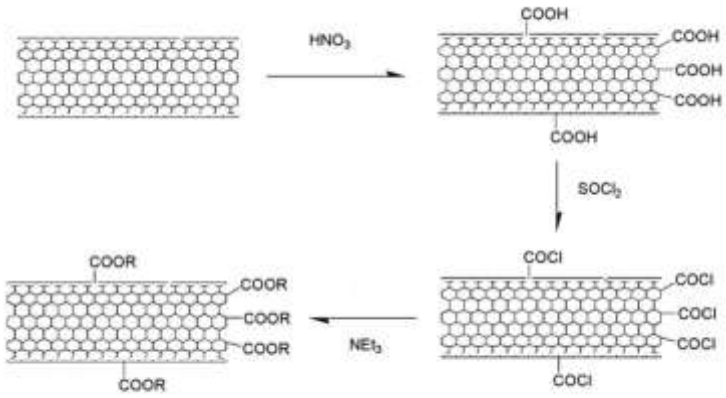

Figure 1.6. Covalent functionalization of SWNTs following esterification reaction of carboxylic acid groups.

This chemical modification has a relatively weak influence on the electrical and mechanical properties compared to addition reactions on the sidewall onto de π-conjugated carbon framework. Most of the covalent modifications for SWNTs are based on addition reactions, many reactions of modification of fullerenes have been adapted to the chemistry of nanotubes as for example the Bingel reaction, Tour reaction, free radical addition, azomethyne ylide addition, alkyl diazonium addition, 1, 3 dipolar cycloaddition and fluorination (see Figure 1.7).[31]

[29] P. Avouris, *Acc. Chem. Res.*, **2002,** *35*, 1026-1034.
[30] J. Liu, A. G. Rinzler, H. Dai, J. H. Hafner, R. K. Bradley, P. J. Boul, A. Lu, T. Iverson, K. Shelimov, C. B. Huffman, F. Rodriguez-Macias, Y. S. Shon, T. R. Lee, D. T. Colbert and R. E. Smalley, *Science*, **1998**, *280*, 1253-1256.
[31] W. Jia, Y. Wu, J. Huang, Q. An, D. Xu, Y. Wu, F. Li and G. Li, *J. Mater. Chem*., **2010**, *20*, 8617-8623

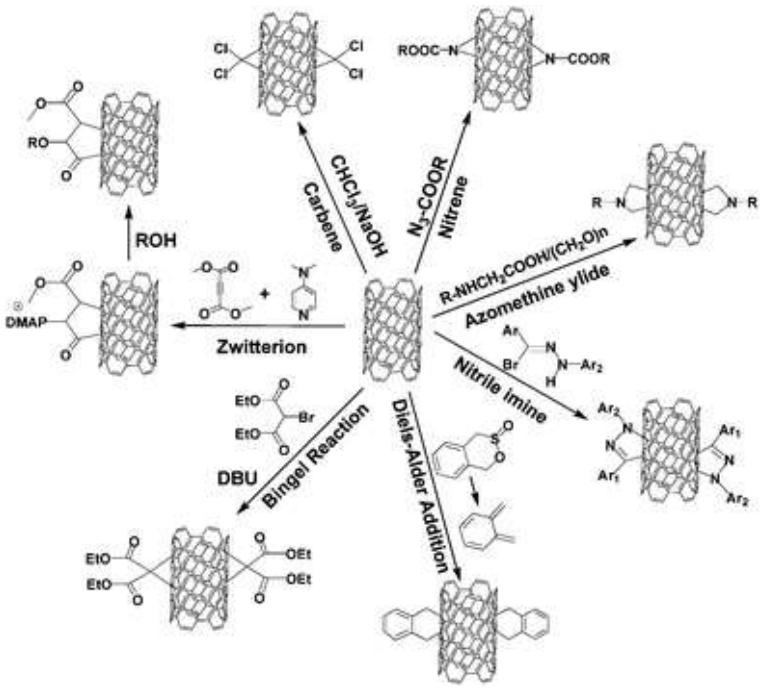

Figure 1.7. Schematic of some sidewalls functionalization methods for SWNTs. Reproduced with permission from reference 29 (Copyright © 2010 Royal society of chemistry).

In addition the fluorinated nanotubes can be further substituted with other organic functionalities using a substitution reactions, this approach was first reported by Margrave and co-workers.[32] The fluorine atoms can be replaced relative easy, thus opening a flexible approach to provide the sidewalls with different types of functional groups. Many types of nucleophilic reagents, including alcohols, amines, Grignard reagents and alkyl lithium[33,34] compounds have been employed obtaining up to 15% of the carbon atoms of the sidewall with a functional group.

1.2.2 Non-covalent chemistry of SWNTs

In this section I will focus the attention on the supramolecular functionalization of nanotubes with non-covalent chemistry. This functionalization leaves virtually intact the inherent properties of SWCNTs, and ensure a good CNTs dispersion, breaking up the SWCNT bundles of the raw material (see Figure 1.8).

[32] E. T. Mickelson, C. B. Huffman, A. G. Rinzler, R. E. Smalley, R. H. Hauge and J. L. Margrave, *Chem. Phys. Lett.*, **1998**, *296*, 188-194.

[33] P. J. Boul, J Liu, E. T. Mickelson, C. B. Huffman, L. M. Ericson, I. W. Chiang, K. A. Smith, D. T. Colbert, R. H. Hauge, J. L. Margrave and R. E. Smalley, *Chem. Phys. Lett.,* **1999**, *310*, 367.

[34] Y. M. Ying, R. K. Saini, F. K. Liang, A. Sadana and W. E. Billups, *Org. Lett*., **2003**, *5*, 1471-1473.

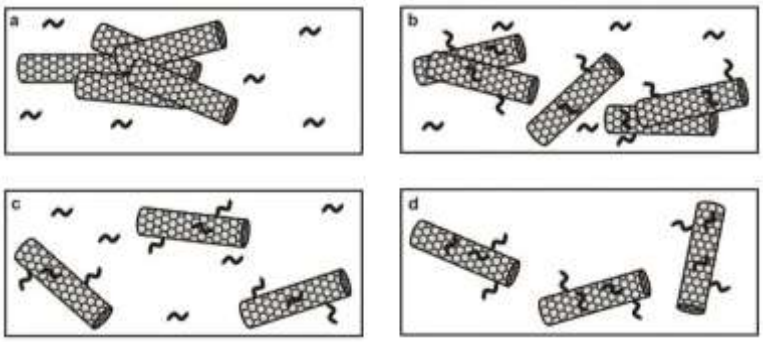

Figure 1.8. Dispersion-scheme using non-covalent interaction.

In this way polycyclic aromatic hydrocarbons (PAHs) such as pyrene, anthracene, tetracene and phenanthrene have a strong affinity for graphitic surfaces via π–π stacking, this molecular absorption is one of the important topics in the science and technology of carbon nanotubes and it has been extensively explored by different groups. In 2003 Nakashima's group demonstrated how porphyrins molecules dissolve both individual and bundled SWCNTs in organic solvents and that the solid SWCNTs–Zn-protoporphyrin nanocomposite is readily separable from the solution and can be easily re-dissolved in DMF.[35] Another important step in the understanding about this type of interactions was carried out by Wang's group which demonstrated that adsorption of phenanthrene and naphthalene to CNTs can be correlated with the hydrophobicity of the corresponding PAH.[36] Another typical non-covalent interaction are polymers formed by repetitive units of alkyl chains and aromatic moieties which exploit both π-stacking to the CNTs surface and van der Waals interactions between the hydrophobic nanotube surface and alkyl tails. Two main strategies have been reported in the literature, the first using direct ultrasonic mixing of the nanotubes and the polymer in organic solvent and the second one based on the polymerization of the monomer in the presence of the nanotube. Poly (*meta*-phenylenevinylene) (PmPV) was the first π-conjugated polymer found to wrap around the nanotubes.[37,38] These nanotubes /polymer hybrids opened interesting perspectives for the realization of optoelectronics devices thanks to the combination of the electronic properties of the nanotubes with the optical properties of the polymers. In 2005, Chichak et al. reported the functionalization of SWNTs with supramolecular porphyrin polymers[39] (see Figure 1.9), the electronic effect of the supramolecular structure was probed within a nanotube field-effect transistor devices demonstrating that SWNTs/porphyrin-FET could act as a light detector.[40]

[35] H. Murakami, T. Nomura and N. Nakashima, *Chem. Phys. Lett.,* **2003,** *378,* 481-485.
[36] X. Wang, S. Tao and B. Xing, *Environ. Sci. Technol.,* **2009,** *43,* 6214-6219.
[37] J. N. Coleman, A. B. Dalton, S. Curran, A. Rubio, A. P. Davey, A. Drury, B. McCarthy, B. Lahr, P. M. Ajayan, S. Roth, R. C. Barklie and W. J. Blau, *Adv. Mater.*, **2000**, *1*, 213.
[38] A. Star, J. F Stoddart, D. Steuerman, M. Diehl, A. Boukai, E. W. Wong, X. Yang, S. W. Chung, H. Choi and J. R. Heath, *Angew. Chem. Int. Ed*., **2001**, *40*, 1721-1725.
[39] K. S. Chichak, A. Star, M. V. P. Altoe and J. F. Stoddart, *Small*, **2005**, *4*, 452-461.
[40] D. S. Hecht, R. J. A. Ramirez, M. Briman, E. Artukovic, K. S. Chichak, J. F. Stoddart and G. Gruner, *Nano Lett*., **2006**, *6*, 2031-2036.

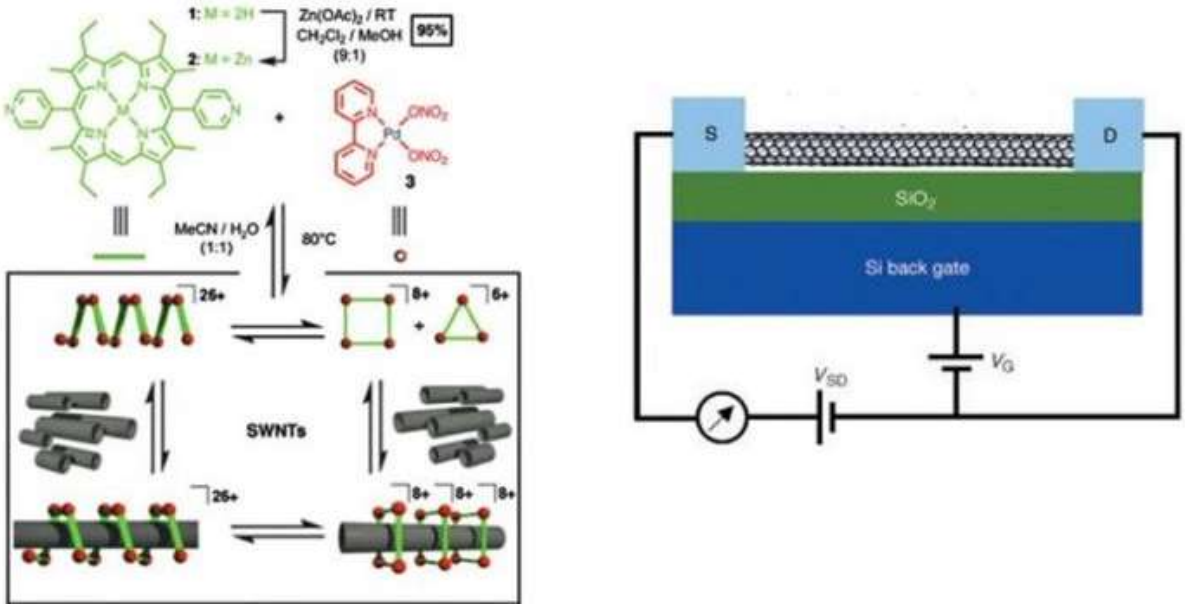

Figure 1.9. Example of supramolecular structures formation around SWNTs. Reproduced with permission from reference 39 (Copyright © 2005 American Chemical Society).

Following the previous investigation Nichola and co-workers showed that the P3HT polymer could be used to individualize SWNTs, they found that this combination improve the crystallinity of the polythiophene ,decrease the optical band gap and an increases the carrier mobility in the polymer.[41] The use of supramolecular chemistry become essential to obtain highly pure semiconducting single-walled carbon nanotubes (SWNTs) due to the properties and potential applications of SWNTs depend strongly on tube chirality and diameter. In 2008 Komatsu's group take advantage of π-stacking interactions between the porphyrins and the nanotube sidewalls[42] to separate the SWNTs by chirality and diameter (see Figure 1.10).

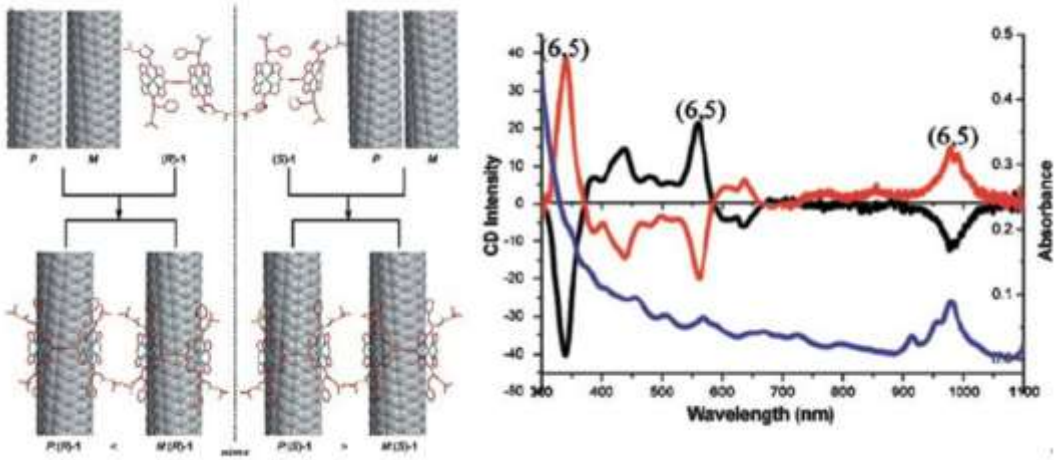

Figure 1.10. Example of selection of chiral (6,5)-SWNTs through supramolecular chemistry with R and S porphyrin. Reproduced with permission from reference 42 (Copyright © 2008 American Chemical Society).

[41] T. Schuettfort, H. J. Snaith, A. Nish and R. J. Nicholas, *Nanotechnology*, **2010**, *21*, 025201.
[42] X. Peng, N. Komatsu, T. Kimura and A. Osuka, *ACS Nano*, **2008**, *2*, 2045-2050.

More recently Nakashima's group developed a strategy for the extraction of highly pure semiconducting-SWNTs based on supramolecular coordination using metal coordination polymers (CP-Ms)[43] composed of a fluorene-bridged bis-phenanthroline ligand and metal ions. They synthesized one-dimensional coordination polymers (CPs) with well-regulated geometries around metal ions by a simple bottom-up self-assembly method, the design molecule recognize/solubilize sem-SWNTs based on the difference in the 'solubility product' between the sem- and met-SWNTs, this methodology also allows the detachment of the solubilizes from the SWNTs surfaces making possible reuse it in the next sorting as show Figure 1.11.

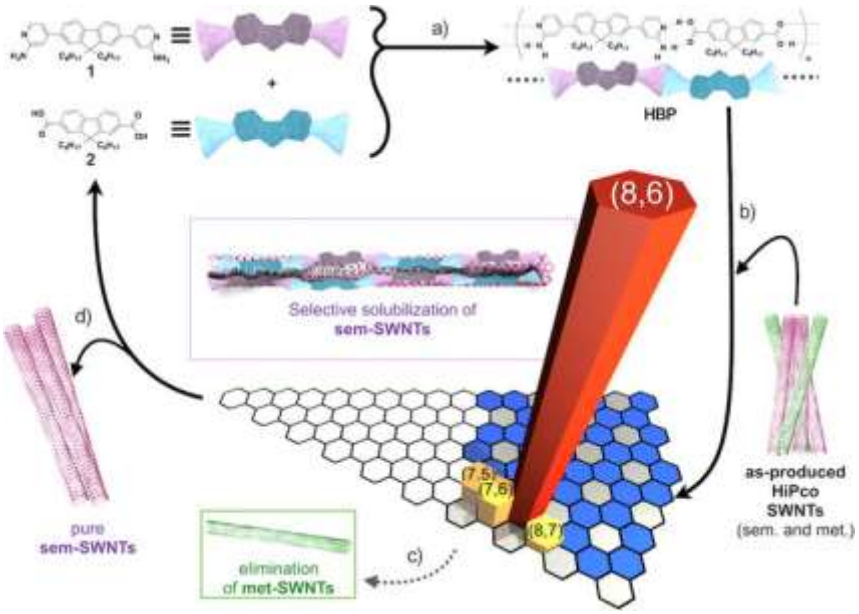

Figure 1.11. a) Chemical structure of HBP formed by 1 and 2, **b)** Solubilization/sorting of the sem-SWNTs **c)** elimination of met-SWNTs in toluene-acetone mixed solvent. **d)** Molecule regeneration after the separation of chemically-pure sem-SWNTs. Reproduced with permission from reference 43 (Copyright © 2014 Nature Publishing group).

SWNTs are not only important for their possible applications in the electronics and optics materials, but also in biological applications like: biosensing,[44] drug delivery,[45] and cancer targeting treatment,[46] but it present the difficulty to be dispersed or dissolved in water because of their hydrophobic nature. However, over the last few years several methods have been developed to functionalize SWNTs bundles with water solubilizing substituents or using surfactants and sonication,[47] this water-dispersible SWNTs can be used in biological applications. Nakashima's group opened new avenues for water-dispersible SWNTs showing that aromatic compound with a polar head were able to give stable suspension of SWNTs in

[43] F. Toshimitsu and N. Nakashima**,** *Nat. Commun*., **2014**, *5*, 5041.
[44] M. T. Martínez, Y. C. Tseng, J. P. Salvador, M. P. Marco, N. Ormategui, I. Loinaz and J. Bokor*, ACS Nano*., **2010**, *41*, 473-480.
[45] B. S. Wong, S. L. Yoong, A. Jagusiak, T. Panczyk, H. K. Ho, W. H. Ang and G. Pastorin, Adv. *Drug Del. Rev*., **2013**, *65*, 1964-2015.
[46] A. A. Bhirde, V. Patel, J. Gavard, G. Zhang , A. A. Sousa, A. Masedunskas, R. D. Leapman, R. Weigert, J. S. Gutkind and J. F. Rusling, *ACS Nano*, **2009**, *3*, 307-316.
[47] J. Liu, A.G. Rinzler, H. Dai, J.H. Hafner, R. K. Bradley, P. J. Boul, A. Lu, T. Iverson, K. Shelimov, C. B. Huffman, F. Rodriguez-Macias, Y. S. Shon, T. R. Lee, D. T. Colbert and R. E. Smalley, *Science*, **1998**, *280*, 1253-1256.

water.[48,49] One of the last investigation in bio-related applications has been the simple dispersion of intact multi-walled carbon nanotubes (MWNTs) by adding them directly into an aqueous solution of glucose oxidase enzyme (GOx),[50] which present a amphiphilic nature, where hydrophobic moieties enable interaction with the hydrophobic CNTs surface while hydrophilic moieties interact with the aqueous solution, thereby preventing CNTs aggregation and leading to effective CNTs dispersion (see Figure 1.12).

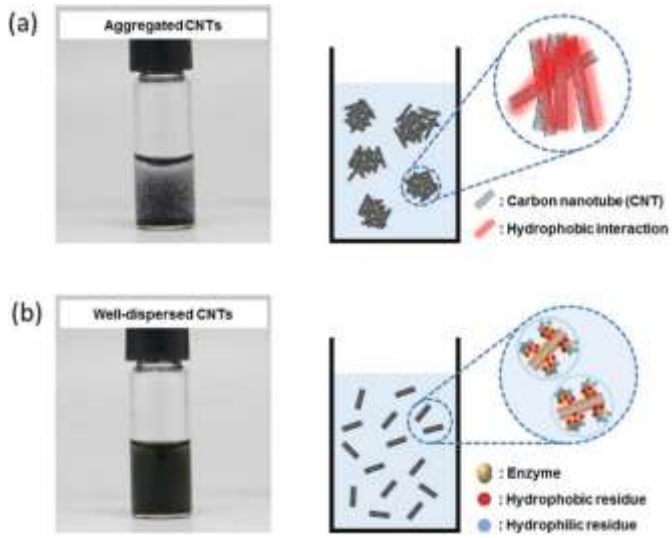

Figure 1.12. a) Aggregated CNTs in aqueous solution and **b)** well-dispersed CNTs in GOx enzyme solution, together with hypothetical schematics for both CNTs aggregation in aqueous solution and dispersed CNTs in enzyme solution.

[48] N. Nakashima, Y. Tomonari and H. Murakami, *Chem. Lett*., **2002**, *31*, 638.
[49] Y. Tomonari, H. Murakami and N. Nakashima, *Chem. Eur. J.*, **2006**, *12*, 4027-4034.
[50] B. C. Kim, I. Lee, S. J. Kwon, Y. Wee, K. Y. Kwon, C. Jeon, H. J. An, H. T. Jung, S. Ha, J. S. Dordick and J. Kim, *Scientific Reports*, **2017**, *7*, 40202.

1.3 Mechanically Interlocked Molecules

One of the most influential chemistry book ever to be written is Linus Pauling´s 1939 monograph on *The Nature of the chemical bond.*[51] In this book Pauling classifies chemical bonding into three categories- electrostatic, covalent, and metallic bonds representing extremes between which many intermediate types of bonds may exist. According to Pauli:

…there is a chemical bond between two atoms or groups of atoms in case that the forces acting between them are such as to lead to the formation of an aggregate with sufficient stability to make it convenient for the chemist to consider it as an independent molecular species.

More than two decades later a new type of bond in chemistry, the mechanical bond, emerged in the scene when Wasserman described in the literature what is commonly known as the first wholly synthetic catenane.[52]

Mechanically interlocked molecules possess two or more separate covalent components, and are defined as an entanglement in space between two or more molecular entities (components parts) such that they cannot be separated without breaking or distorting chemical bonds between atoms.

The mechanical bond presents chemist with the best of both the covalent and the supramolecular worlds, since they come with the robustness provided by covalent bonding and the subtleties associated with coordinative and noncovalent bonding, rendering the molecules ideal for the control of function at the single molecules, the nanoscopic, the microscopic and the macroscopic levels. Figure 1.13 shows some examples of mechanically interlocked molecular architectures include catenanes, rotaxanes, molecular knots and molecular Borromean rings.[53,54]

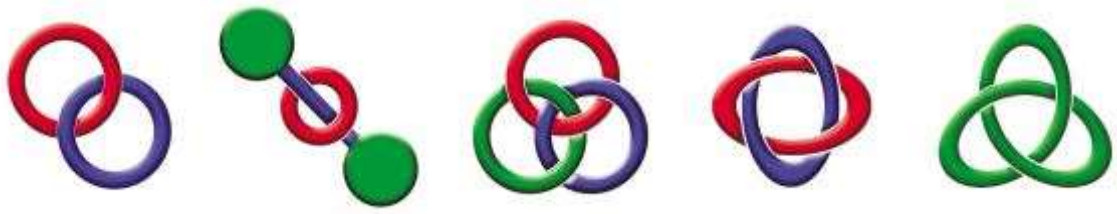

Figure 1.13. Five types of interlocked molecules which have been synthesized by chemist (from left to right) [2] catenane, [2] rotaxane, Borromean rings, Solomon link and a trefoil knot.

[51] L. C. Pauling*, the Nature of the Chemical Bond*, **1939**, Cornell University Press, Ithaca, New York.
[52] E. Wasserman, *J. Am. Chem. Soc.*, **1960**, *82*, 4433-4434.
[53] J. P. Sauvage and C. Dietrich-Buchecker, *Wiley-VCH, Weinheim*, **1999**, *72*, 2265-2274.
[54] D. B. Amabilino and J. F. Stoddart, *Chem. Rev.*, **1995**, *95*, 2725-2828.

The name is derived from the Latin word for a wheel (rota) and an axle (axis). Rotaxanes are molecules comprised of a dumbbell-shaped fragments with sufficiently large “stoppers” to trap the macrocycle(s) mechanically. It was in 1967 when Harrison and Harrison synthetized the first wholly synthetic rotaxanes.[55] This work was soon followed by a covalent-directed synthesis by Schill and coworkers.[56] Both examples were extremely low yielding, so the field lay dormant for several decades, due to the lack of robust synthetic strategies.

In recent years, chemists have developed several ways to avoid the poor yields of traditional synthetic methods by using template-directed synthetic strategies. At least three different strategies for the construction of rotaxanes can be identified,[57] these three methods involve threading followed by stoppering, slipping or clipping (see Figure 1.14). In the threading method, a preformed macrocycle is first coordinated onto a thread via attractive interactions, and after that stopper groups are attached to the end of the thread, which prevent dissociation of the newly formed rotaxane.[58] In the slipping strategy, a pre-synthesized macrocycle is slipped over an already stoppered thread.[59] The third approach is the clipping method, where a macrocycle is formed in the presence of a thread.[60] In 2007, Leigh and co-workers developed a new strategy for the synthesis of rotaxanes called the active metal template method, where a metal is used both to promote the formation of the thread and the coordination of the preformed macrocycle.[61]

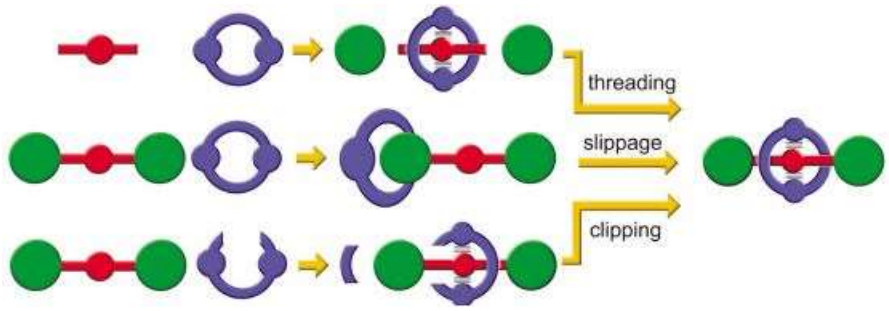

Figure 1.14. Graphical representation of three methods of rotaxane formation-threading-followed by stoppering slippage of the macrocycle over the stoppers at elevated temperatures, and clipping of the macrocycle around the thread.

[55] I. T. Harrison and S. Harrison, *J. Am. Chem. Soc.*, **1967**, *89*, 5723-5724.
[56] G. Schill and H. Zollenkopf, *Liebigs. Ann. Chem.,* **1969**, *721*, 53-74.
[57] a) G. Wenz, *Angew. Chem. Int. Ed. Engl.,* **1994**, *33*, 803-822. b) D. B. Amabilino and J. F. Stoddart, *Chem. Rev*. **1995**, *95*, 2725-2828. c) M. C. T. Fyfe and J. F. Stoddart, *Acc. Chem. Res.*, **1997**, *30*, 393-401.
[58] J. Cao, M. C. T. Fyfe, J. F. Stoddart, G. R. L. Cousins and P. T. J. Glink, *Org. Chem.,* **2000**, *65*, 1937-1946.
[59] M. Händel, M. Plevoest, S. Gestermann and F. Vögtle, *Angew. Chem. Int. Ed*., **1997**, *36*, 1199.
[60] J. M. Lehn, Angew. *Chem. Int. Ed.,* **1988**, *27*, 89-112.
[61] D. J. Crowley, S. M. Goldup, A. L. Lee, D. A. Leigh and R. T. McBurney, *Chem. Soc. Rev.*, **2009**, *38*, 1530-1541.

2. Previous work: Supramolecular chemistry of SWNTs

We have explored the combination of both covalent and noncovalent chemistries through the mechanical link with carbon nanotubes. The 1D structure of SWNTs allow for utilizing them as threads in the synthesis of rotaxane type mechanically interlocked nanotubes. In the following, we explain the use of π extended derivatives of tetrathiafulvalene (exTTF) and pyrene as recognition fragments to encapsulate SWNTs.

2.1 exTTF and Pyrene as molecular recognition motifs for the synthesis of MINTs.

The SWNTs elongated structures open up the possibility of using these as axis in the synthesis of rotaxanes-type mechanically interlocked nanotubes (MINTs). Previous work by Martín's group[62,63] confirmed the excellent behavior of the exTTF moiety as recognition motif for fullerenes. Given the structural similarities between fullerenes and SWNTs, we performed the synthesis of new macrocyclic receptors based on exTTF[64] to encapsulate the SWNTs obtaining the corresponding rotaxanes. Similarly, we also exploited the very well-known interactions between pyrene and SWNTs to the same end.[65] The synthesis of macrocycles was carried linked the recognitions units through 1, 4 xylene and alkenyl spacers with different lengths. We use the nanotube as a template for the linear receptor, which would be formed around it following a clipping strategy, as shown in Figure 1.15.

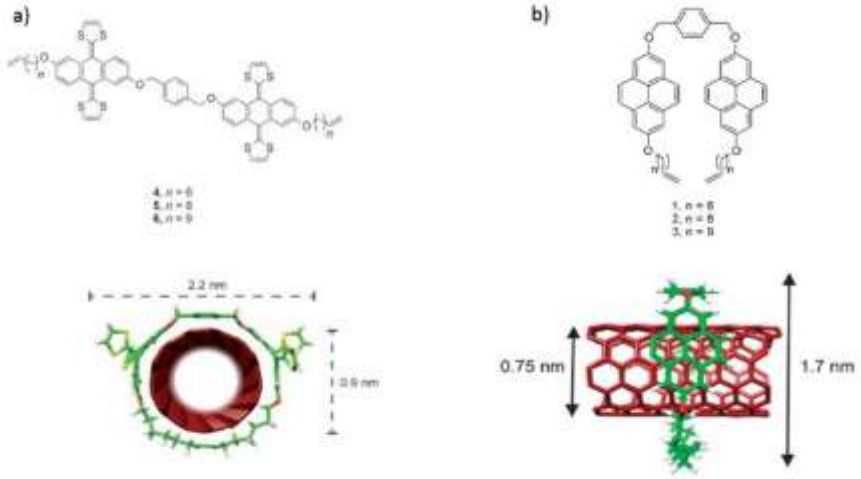

Figure 1.15. **a)** Chemical structure exTTF linear precursors (on top) and the energy-minimized (MMFF94) molecular model of MINTs-**(7,6)**-**1** (down). **b)** Chemical structure pyrene linear precursors (on top) and the energy-minimized (MM^+) model of MINT-**(6,5)-4.**

[62] E. M. Pérez, L. Sánchez, G. Fernández and N. Martín, *J. Am. Chem. Soc.,* **2006,** *128*, 7172-7173.
[63] H. Isla, M. Gallego, E. M. Pérez, R. Viruela, E. Ortí and N. Martín*, J. Am. Chem. Soc*., **2010**, *132*, 1772-1773.
[64] A. de Juan, Y. Pouillon, L. Ruiz-González, A. Torres-Pardo, S. Casado, N. Martín, A. Rubio, and E. M. Pérez, *Angew. Chem. Int. Ed*., **2014**, *53*, 5394-5400.
[65] A. López-Moreno and E. M. Pérez, *Chem. Commun.,* **2015**, *51*, 5421-5424.

Thermogravimetric analysis (TGA) of MINT with exTTF and pyrene macrocycles showed a weight loss of 37% and 25% at around 360ºC corresponding to the macrocycle. The samples were also characterize by UV/vis/NIR spectroscopy, photoluminescence excitation intensity mapping (PLE) and Raman spectroscopy all of which were in agreement with the formation of MINTs. Finally the high-resolution transmission electron microscopy (TEM) confirms the presence of organic molecules around the carbon nanotubes (see Figure 1.16). In conclusion, we introduced the mechanical bonds as a new tool for the chemical manipulation of SWNTs, the synthetic approach is based on a clipping strategy in which the macrocycles are formed around the SWNTs by ring-closing metathesis (RCM).

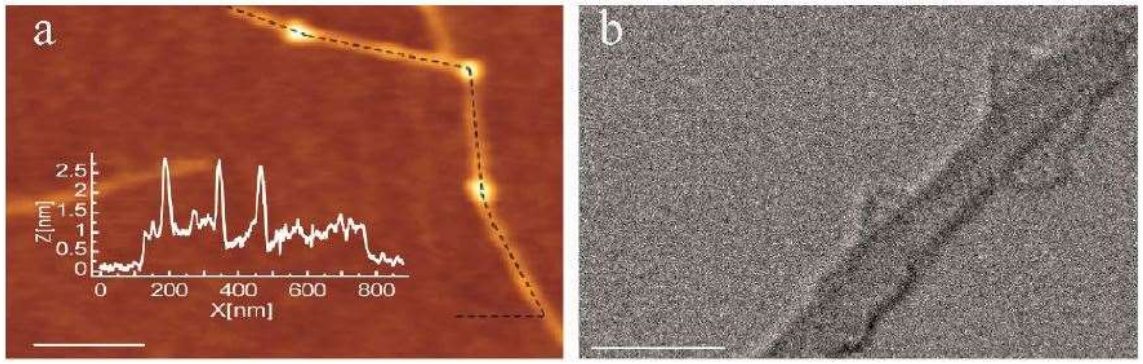

Figure 1.16. **a)** AFM topography. Inset shows the profile along the dashed black line. **b)** HR-STEM bright-field image of a single SWNTs surrounded by two macrocycles. Scale bars are 100 nm for a) and 2nm for b).

3. Objectives

The present chapter addresses one main objective: the design and synthesis of new NDIs based receptors to build new MINTs. This main objective can be divideds in different steps:

i) Synthesis of NDIs based U-shaped molecules with different length of alkyl chain.

ii) Formation of MINTs using different SWNTs.

iii) Study the MINTs reaction with different solvents.

As part of the study of the MINTs structure we will investigate:

iv) Electronic properties of the SWNTs with the MINTs and supramolecular functionalization, through spectroscopy measurement.

v) The relationship of functionalization with SWNTs diameter and macrocyclic cavity.

4. Bimodal Supramolecular Functionalization of Carbon Nanotubes Triggered by Covalent Bond Formation.

4.1 Introduction

Single wall carbon nanotubes (SWNTs)[66,67] show a unique collection of physical properties that make them one of the most promising nanomaterials.[68] Their mechanical properties are already exploited in a variety of commercial applications,[69] and examples of advanced SWNT-based electronic devices are being developed.[70,71,72,73,74,75] The chemical modification of SWNTs can tune their properties and/or improve their processibility. To this end, both covalent and supramolecular approaches have been extensively explored.[76,77,78,79,80] Each approach shows advantages and disadvantages that make it suitable for certain applications. The formation of covalent bonds implies higher stability and is typically used if permanent changes to the surface of the SWNTs are required.[81,82,83] On the other hand, noncovalent chemistry occurs under equilibrium, and offers the possibility of switching the interactions on and off in response to stimuli.[84,85,86]

[66] S. Iijima and T. Ichihashi., *Nature,* **1993**, *363*, 603-605.
[67] D. S. Bethune, C. H. Kiang, M. S. de Vries, G. Gorman, R. Savoy, J. Vazquez and R Beyers, *Nature* **1993**, *363*, 605-607.
[68] J. M. Schnorr and T. M. Swager, *Chem. Mater.,* **2011**, *23*, 646-657.
[69] M. F. L. De Volder, S. H. Tawfick, R. H. Baughman and A. J. Hart, *Science,* **2013**, *339*, 535-539.
[70] Y. Cao, Y. Che, J. W. T Seo, H. Gui, M. C. Hersam and C. Zhou, *Appl. Phys. Lett.,* **2016**, *108*, 233105.
[71] J. G. Weis, J. B. Ravnsbaek, K. A .Mirica and T. M. Swager, *ACS Sensors,* **2016**, *1*, 115-119.
[72] S. Ishihara, J. M. Azzarelli, M. Krikorian and T. M. Swager, *J. Am. Chem. Soc.,* **2016**, *138*, 8221-8227.
[73] Q. Cao, S.-J. Han, J. Tersoff, A. D. Franklin, Y. Zhu, Z. Zhang, G. S. Tulevski, J. Tang and W. Haensch, Science, **2015**, *350*, 68-72.
[74] W. Qin, M. Gong, X. Chen, T. A. Shastry, R. Sakidja, G. Yuan, M. C. Hersam, M. Wuttig and S. Ren, *Adv. Mater*., **2015**, *27*, 734-739.
[75] S. F. Liu, A. R. Petty, G. T. Sazama and T. M. Swager, Angew. *Chem., Int. Ed*., **2015**, *54*, 6554-6557.
[76] P. Singh, S. Campidelli, S. Giordani, D. Bonifazi, A. Bianco and M. Prato, *Chem. Soc. Rev*., **2009**, *38*, 2214-2230.
[77] E. Bekyarova, S. Sarkar, F. Wang, M. E. Itkis, I. Kalinina, X. Tian and R. C. Haddon, *Acc. Chem. Res*., **2013**, *46*, 65-76.
[78] Y. L. Zhao and J. F. Stoddart, *Acc. Chem. Res*., **2009**, *42*, 1161-1171.
[79] K. Dirian, M. A. Herranz, G. Katsukis, J. Malig, L. RodríguezPérez, C. Romero-Nieto, V. Strauss, N. Martín and D. M. Guldi, *Chem. Sci.*, **2013**, *4*, 4335-4353.
[80] S. Marchesan, M. Melchionna and M. Prato, *ACS Nano*, **2015**, *9*, 9441-9450.
[81] H. Kwon, A. o. Furmanchuk, M. Kim, B. Meany, Y. Guo, G. C. Schatz and Y. H. Wang, *J. Am. Chem. Soc*., **2016**, *138*, 6878-6885.
[82] M. Barrejon, H. B. Gobeze, M. J. Gomez-Escalonilla, J. L. G. Fierro, M. Zhang, M. Yudasaka, S. Iijima, F. D'Souza and F. Langa, *Nanoscale*, **2016**, *8*, 14716-14724.
[83] J. Chen, J. H. Walther and P. Koumoutsakos, *Adv. Funct. Mater*., **2015**, *25*, 7539-7545.
[84] I. Pochorovski, H. Wang, J. I. Feldblyum, X. Zhang, A. L. Antaris and Z. Bao, *J. Am. Chem. Soc*., **2015**, *137*, 4328-4331.
[85] A. Feng, L. Peng, B. Liu, S. Liu, S. Wang and J. Yuan, *ACS Appl. Mater. Interfaces*, **2016**, *8*, 11024-11030.
[86] M. Mollahosseini, E. Karunaratne, G. N. Gibson, J. A. Gascon and F. Papadimitrakopoulos, *J. Am. Chem. Soc*., **2016**, *138*, 5904-5915.

A much less explored alternative is the combination of both covalent and noncovalent chemistries for nanotube functionalization, where the formation of covalent bonds triggers a particularly stable noncovalent interaction. Campidelli and co-workers have described the supramolecular encapsulation of SWNTs within porphyrin networks linked in situ co-workers have exploited the through either S-S[87] or C-C[88] covalent bonds. More recently, Bao and co-workers have exploited the reversibility of imine bonds for the formation and removal of a conjugated polymer that wraps around large diameter SWNTs with extreme selectivity, allowing for their facile purification.[89]

4.2 Results and Discussion

We have introduced the mechanical bond as a new tool for the modification of SWNTs that exploits and combines the advantages of the covalent and noncovalent chemistries.[90,91,92,93] Briefly, we utilized linear precursors equipped with terminal alkenes and two recognition units for SWNTs that help template the macrocyclization around the nanotubes through ring-closing metathesis (RCM). The products obtained are pseudorotaxane-like mechanically interlocked derivatives of SWNTs (MINTs).[94] Due to the use of alkene metathesis in the final clipping synthetic step, a possible competing reaction is the formation in situ of oligomers/polymers of the linear precursor through acyclic diene metathesis polimeryzation (ADMP). The oligomers could then wrap around the SWNTs forming particularly stable supramolecular associates (see Figure 1.17). A series of control experiments showed that in the case of both exTTF and pyrene-based macrocycles, the fraction of SWNTs functionalized by oligomers was insignificant compared to MINTs.[90-92] However, as illustrated by the examples described above,[85-87] the formation of oligomer-wrapped SWNTs is often advantageous.

[87] G. Clavé, G. Delport, C. Roquelet, J.-S. Lauret, E. Deleporte, F. Vialla, B. Langlois, R. Parret, C. Voisin, P. Roussignol, B. Jousselme, A. Gloter, O. Stephan, A. Filoramo, V. Derycke and S. Campidelli, *Chem. Mater.*, **2013**, *25*, 2700-2707.
[88] I. Hijazi, T. Bourgeteau, R. Cornut, A. Morozan, A. Filoramo, J. Leroy, V. Derycke, B. Jousselme and S. Campidelli, *J. Am. Chem. Soc.*, **2014**, *136*, 6348-6354.
[89] T. Lei, X. Chen, G. Pitner, H. S. P. Wong and Z. Bao, *J. Am. Chem. Soc.*, **2016**, *138*, 802-805.
[90] A. de Juan, Y. Pouillon, L. Ruiz-González, A. Torres-Pardo, S. Casado, N. Martín, A. Rubio and E. M. Pérez, *Angew. Chem. Int. Ed.*, **2014**, *53*, 5394-5400.
[91] A. López-Moreno and E. M. Pérez, *Chem. Commun.*, **2015**, *51*, 5421-5424.
[92] A. de Juan, M. Mar Bernal and E. M. Pérez, *ChemPlusChem,* **2015**, *80*, 1153-1157.
[93] E. Martínez-Periñán, A. de Juan, Y. Pouillon, C. Schierl, V. Strauss, N. Martín, A. Rubio, D. M. Guldi, E. Lorenzo and E. M. Pérez, *Nanoscale*, **2016**, *8*, 9254-9264.
[94] Rotaxanes and pseudorotaxanes are both topologically trivial and, mathematically speaking, neither is mechanically interlocked, since they can be converted into the macrocycle-dumbell or macrocycle-thread pairs by shrinking the stoppers and/or stretching out the macrocycle to allow dissociation. From a chemical perspective, this would require that the species withstand the shrinking or stretching without breaking a covalent bond. This, we believe, is a more adequate criterion than the presence or absence of stoppers to decide if the species are mechanically interlocked or not (see: A. de Juan and E. M. Pérez, *Nanoscale*, **2013**, *5*, 7141). Since MINTs require breaking of covalent bonds to dissociate, we consider them mechanically interlocked.

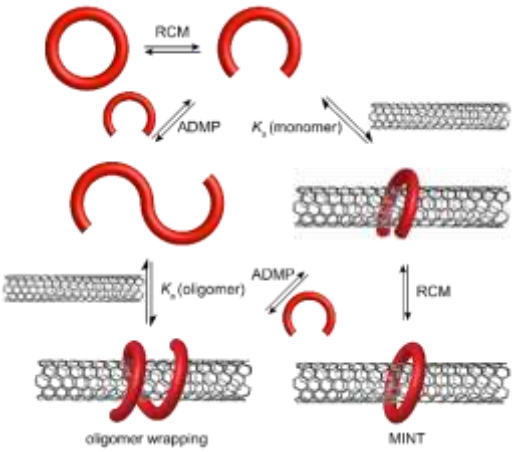

Figure 1.17. Reaction pathways for the bimodal noncovalent functionalization of SWNTs to afford either oligomer-wrapped SWNTs or MINTs. Grubb's catalyst has been omitted for clarity.

Naphthalene diimides (NDIs)[95] are part of the rylene tetracarboxylic diimides family,[96] they show remarkable photophysical properties, and are well known air-stable electron acceptor building blocks in organic electronics.[97,98,99,100,101] Their π-basicity has been extensively utilized in supramolecular chemistry, most notably in the emerging field of anion-π interactions,[102,103,104,105] but also in the molecular recognition of fullerenes.[106,107] Of more relevance to the present work, NDI derivatives are known to interact with SWNTs to form supramolecular hybrids.[108] With all these appealing properties in mind, we decided to explore the use of NDIs as recognition fragments in the synthesis of MINTs.

Here, we show that alkene-terminated NDI derivatives can be utilized to synthesize MINTs and oligomer-wrapped SWNTs through RCM and/or ADMP. The balance between MINTs and oligomer-wrapped nanotubes can be tuned by varying the solvent system.

---

[95] S. V. Bhosale, C. H. Jani and S. J. Langford, *Chem. Soc. Rev*., **2008**, *37*, 331-342.
[96] X. Zhan, A. Facchetti, S. Barlow, T. J. Marks, M. A. Ratner, M. R. Wasielewski and S. R. Marder, *Adv. Mater*., **2011**, *23*, 268-284.
[97] H. E. Katz, A. J. Lovinger, J. Johnson, C. Kloc, T. Siegrist, W. Li, Y. Y. Lin and A. Dodabalapur, *Nature*, **2000**, *404*, 478-481.
[98] M. Sommer, *J. Mater. Chem. C*, **2014**, *2*, 3088-3098.
[99] R. Kim, P. S. K. Amegadze, I. Kang, H. J. Yun, Y. Y. Noh, S.-K. Kwon and Y. H. Kim, *Adv. Funct. Mater*., **2013**, *23*, 5719-5727.
[100] V. Senkovskyy, R. Tkachov, H. Komber, M. Sommer, M. Heuken, B. Voit, W. T. S. Huck, V. Kataev, A. Petr and A. Kiriy, *J. Am. Chem. Soc.,* **2011**, *133*, 19966-19970.
[101] S. L. Suraru and F. Wurthner, *Angew. Chem. Int. Ed*., **2014**, *53*, 7428-7448.
[102] P. Ballester, *Acc. Chem. Res*., **2012**, *46*, 874-884.
[103] S. Guha, F. S. Goodson, L. J. Corson and S. Saha, *J. Am. Chem. Soc.*, **2012**, *134*, 13679-13691.
[104] S. Guha and S. Saha, *J. Am. Chem. Soc*., **2010**, *132*, 17674-17677.
[105] V. Gorteau, G. Bollot, J. Mareda, A. Pérez-Velasco and S. Matile, *J. Am. Chem. Soc*., **2006**, *128*, 14788-14789.
[106] N. Ponnuswamy, G. D. Pantos, M. M. J. Smulders and J. K. M. Sanders, *J. Am. Chem. Soc*., **2012**, *134*, 566-573.
[107] A. R. Stefankiewicz, E. Tamanini, G. D. Pantos and J. K. M. Sanders, *Angew. Chem., Int. Ed*., **2011**, *50*, 5725-5728.
[108] Z. Hu, G. D. Pantos, N. Kuganathan, R. L. Arrowsmith, R. M. J. Jacobs, G. Kociok-Koehn, J. O'Byrne, K. Jurkschat, P. Burgos, R. M. Tyrrell, S. W. Botchway, J. K. M. Sanders and S. I. Pascu, *Adv. Funct. Mater*., **2012**, *22*, 503-518.

Design and synthesis of NDI macrocycle/oligomer precursors: The design of the NDI-based bisalkene linear precursors **1-3** is directly based on the exTTF and pyrene precedents.[90-92] The molecules feature two NDI units as recognition motifs for SWNTs, a p-xylylene aromatic spacer, and alkene-terminated alkyl spacers of different lengths. Solubilizing branched alkyl chains had to be added to the aromatic spacer, as the products obtained otherwise are intractable due to their insolubility. Linear precursors **(1-3)** and macrocycles **(4-6)** were synthesized as shown in Scheme 1.1.

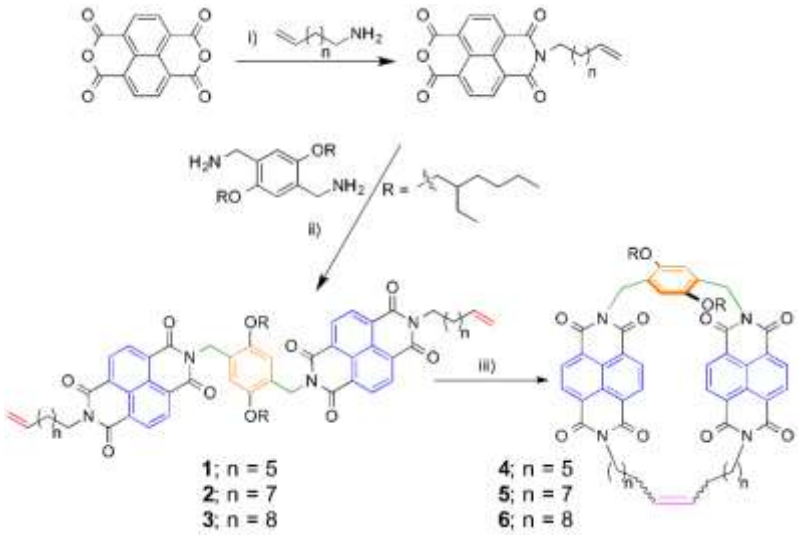

Scheme 1.1. Synthesis of linear precursors 1-3 and macrocycles 4-6. Reaction conditions: i)H_2O, 110^{0}C, 12h and acetic anhydride, 110^{0}C, 12h, y = 96%; ii) DMF, 130^{0}C, 5h, y= 78%; iii) DCM, 4h, room temperature, y= 83%. The color code in linear precursors and macorcycle matches that of Figure 1.20.

We modeled the interaction of the macrocycles with SWNTs in MINT topology (see Figure 1.18a), at the Molecular Mechanics (MM) level using the MMFF94 force field, in order to accelerate the preparation of the experiments. The use of MM allows for a fast screening of candidate macrocycles, while providing a qualitatively correct description of their compatibility with the SWNTs. If the diameter of the SWNT is smaller than the cavity of the macrocycle, their mutual interaction remains very weak and can become slightly attractive when the macrocycle closes around the nanotube, thanks to a template effect. However, when the SWNT diameter increases, internal tensions within the structure of the NDI macrocycle become relevant and make the interaction become increasingly repulsive, which would favor the formation of oligomers. As in previous examples,[90,91] we remain attentive to the quantitative limitations of this approach. In the present case, we have even increased the error bar to 20 kcal/mol, to account for the higher deviation of the force field with respect to ab initio calculations regarding the description of the diimide group. This larger uncertainty brings the favourable formation area below 20 kcal/mol and the validity limit of our model to 60 kcal/mol, still within range of half the intensity of a covalent C-H bond (40 kcal/mol). In addition, the flexibility of the alkyl chain −which was the key factor of compatibility for the molecules we studied previously− is partly compensated for by the rigidity of the diimides. Figure 1.18b illustrates

this effect when the diameter of the SWNT increases: while the interaction between the macrocycle and the nanotube smoothly increases within the validity limits of our model for small diameters, it abruptly goes away to strongly repulsive interactions above 0.88 nm. From a geometrical perspective, this corresponds to a mechanical deformation of the diimides, which is highly unfavourable to the stability of 6. In experiments, its formation around wider nanotubes, such as (7,6) and (9,5), will thus not occur. Still, most of the chiralities present in the samples are found in the favorable diameter and energy ranges for the formation of MINTs.

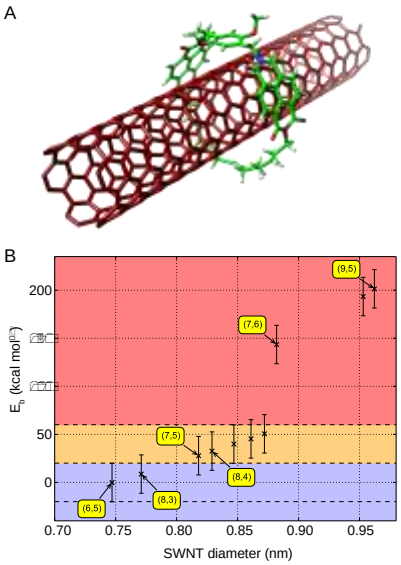

Figure 1.18. a) Energy-minimized molecular model of a MINT architecture featuring macrocycle 8 and a (6,5) SWNT. **b)** Interaction energies of a series of SWNTs with macrocycle **6** (negative = attractive). Error bars of 20 kcal/mol have been represented for each combination. Blue: most favorable formation energy range. Orange: unfavourable formation energy range. Red: limit of the model. The SWNT chiralities observed experimentally have been labelled, as well as the largest diameter in the favourable area. The complete dataset is available in the supplementary material.

Relationship of NDI loading with SWNT diameter and macrocyclic cavity: With the MM data in mind, we explored the RCM of 1-3 in the presence of (7,6)-enriched SWNTs (0.7-1.1 nm diameter, 95% purity after purification), and (6,5)-enriched SWNTs (0.7-0.9 nm diameter, 95% purity after purification), purchased from Sigma Aldrich Co. The nanotubes (5 mg) were suspended in 5 mL of either tetrachloroethane (TCE) or dimethylformamide (DMF), and mixed with the corresponding linear precursor 1-3 (0.83 mM) and Grubb's 2nd generation catalyst at room temperature for 72 hours. After this time, the suspension was filtered through a PTFE membrane of 0.2 µm pore size, and the solid washed profusely with CH_2Cl_2 to remove non-threaded macrocycles, catalyst, and any remaining linear precursor. The solid products thus obtained were analyzed through thermogravimetric analysis (TGA), affording the results summarized in Table 1.2.

	1	2	3
(6,5) in TCE	19%	19%	21%
(6,5) in DMF	56%	51%	54%
(7,6) in TCE	20%	21%	23%
(7,6) in DMF	49%	48%	52%

Table 1.2. Degree of functionalization from TGA data (10ºC min^{-1}, air) for products of the reaction between linear precursors **1-3** and SWNTs in TCE and DMF.

Control experiments with preformed macrocycles 4-6 or linear precursors 1-3 without Grubbs' catalyst lead to much lower functionalization. In contrast, if Grubbs' catalyst is added the reaction leads to the same products using either the macrocyclic or linear precursors, proving that the metathesis reaction is reversible under our experimental conditions.

The first observation is that the degree of functionalization in TCE is significantly lower for the NDI macrocycles than for the previously reported exTTF or pyrene macrocycles. For instance, for the product of the reaction between **1** and (6,5) SWNTs in TCE, a functionalization of 19% was observed, compared to 35% for an exTTF macrocycle with the same alkyl spacer under identical experimental conditions.[90] These results suggest a significant decrease in affinity of the NDI macrocycles for the SWNTs when compared to their exTTF counterparts, which can be accounted for by the smaller van der Waals surface of NDI and its lack of curvature, compared to exTTF.[109] Considering that it is known that the NDI-SWNT interaction is enhanced in polar solvents,[108] we attempted the MINT formation reaction in DMF, a polar solvent compatible with RCM conditions in which the nanotubes are satisfactorily dispersed. First, we measured the association constants of the monomer towards the nanotubes in both TCE and DMF at room temperature, using our previously reported method.[110] As expected, we observed a significant increase of one order of magnitude of the binding constant in the more polar DMF with respect to TCE. In particular, we measured log K_a = 2.6 ± 0.1 M^{-1} for **3**·(6,5) SWNTs in TCE and log K_a = 3.5 ± 0.2 M^{-1} for the same system in DMF. This explains the larger degree of functionalization that we consistently observe in DMF, as it would favor both the formation of MINTs and of oligomer-wrapped SWNTs. A second fact is that the degree of functionalization bears no clear dependence on the match between the diameter of the nanotubes and the size of the cavity of the macrocycles, particularly for the reactions run in DMF. For example, for the reaction of linear precursors **1**, **2**, and **3** with (7,6) SWNTs in TCE, the TGA shows 20, 21 and 23% functionalization, respectively. That is, the degree of functionalization increases with cavity size, even if only slightly.[91] However, for the same reactions in DMF, TGA analysis yields 49, 48, and 56% functionalization.

[109] E. M. Pérez and N. Martín, *Chem. Soc. Rev*., **2008**, *37*, 1512-1519.

[110] Our method is based on the direct measurement of the concentration of bound and free host molecule in the equilibrium, so that the "concentration" of SWNTs does not need to be known. See: A. de Juan, A. López-Moreno, J. Calbo, E. Ortí and E. M. Pérez, *Chem. Sci*., **2015**, *6*, 7008-7014.

Stability of the noncovalent functionalization: We have previously reported that MINTs are sufficiently stable to withstand a strong thermal treatment, namely reflux in TCE (b.p. = 147°C) for 30 min, followed by a thorough rinse with CH_2Cl_2. Under these high-temperature conditions, even particularly stable supramolecular complexes should dissociate, due to the weakening of noncovalent interactions. Indeed, when we subjected our samples to this demanding test of stability, a decrease in the degree of NDI material was observed in all cases, in agreement with the presence of oligomer-SWNT supramolecular hybrids. Moreover, a difference between the solvents is also apparent. For the reactions run in the nonpolar TCE, the loss of NDI loading upon thermal treatment is small. For instance, for linear precursor **3**, the functionalization decreases from 23 to 19% for (7,6) SWNTs. However, for the reactions run in DMF, the loss of functionalization is much larger. Taking the same linear precursor and nanotubes for comparison, the loading goes from 52% to 38%. This is in sharp contrast with our previous findings for the exTTF-based or pyrene-based MINTs, where no significant loss of functionalization was observed.[90,91]

The large initial loading of NDI material, the lack of a clear relationship between macrocycle cavity and SWNT diameter and functionalization, and the significant loss of loading upon refluxing in TCE observed for the MINT-forming reactions run in DMF can all be understood if the participation of oligomers is significantly larger in the more polar solvent. In that case, the oligomers, which are attached to the SWNTs through noncovalent forces only, would be removed after the thermal treatment, leaving the mechanically interlocked macrocycles behind.

Persuasive experimental evidence for this hypothesis was provided by analysis of the filtrate resulting from the TCE boiling experiment. Figure 1.19 displays the MALDI-TOF spectrum of the filtrate of the thermal treatment of **3**-(7,6)-DMF. Complex peaks at m/z = 2360-2479, 3529-3632, 4695-4770, and 5864-5924, corresponding to the dimeric (calcd. m/z = 2361), trimeric (calcd. m/z = 3528), tetrameric (calcd. m/z = 4695), and pentameric (calcd. m/z = 5861) linear metathesis products of **3**. No signs of cyclic species were observed, proving that the MINTs do not dissociate even under these harsh conditions. Moreover, analysis of the filtrate originated from the reaction run in TCE showed no signs of oligomers.

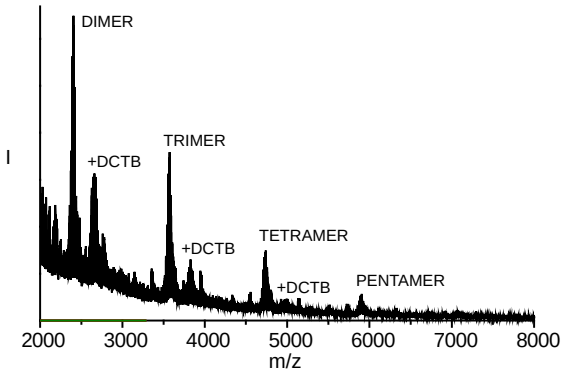

Figure 1.19. MALDI-TOF spectrum (DCTB matrix) of the filtrate of the thermal treatment of the product of the reaction of 3 with (7,6) SWNTs in DMF.

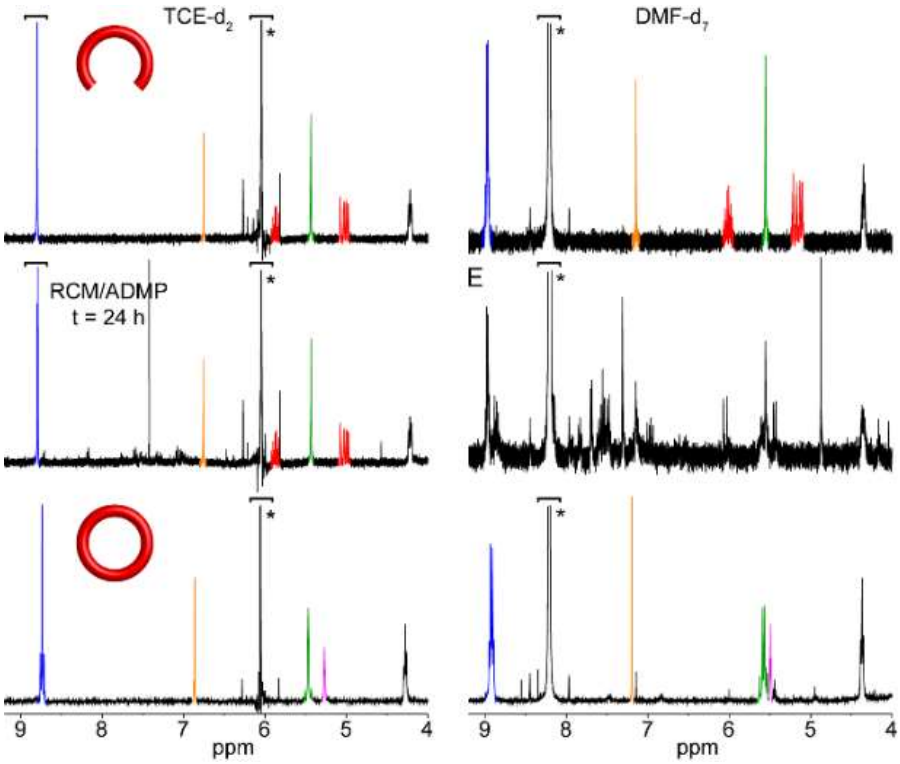

Figure 1.20. Partial ^{1}H NMR (400 MHz, room temperature) of the untemplated metathesis reaction in TCE-d_2 (left panel) and DMF-d_7 (right panel). The NMRs of the linear precursor **3** and macrocycle **6** are shown as reference. Color code corresponds to the assignment as depicted in Scheme 1.1. Residual solvent peaks are marked with an asterirk.

Investigation of the metathesis reaction of **3** in the absence of template through ^{1}H NMR provided complementary information (see Figure 1.20). In TCE, the reaction is very slow, and only a very small concentration of oligomers, with no significant amount of macrocycle **6** can be found after 24 h of reaction. In contrast, in DMF, all the starting material was consumed to produce a com complex mixture composed mainly of oligomers with only a small fraction of **6**. The faster reaction rate for the formation of oligomers in DMF favors the non-templated pathway depicted in Figure 1.17 which can only lead to oligomer-wrapped SWNTs.

TEM and AFM imaging: Investigation of the reaction products under transmission electron microscopy (TEM) and atomic force microscopy (AFM) is also consistent with the coexistence of MINT-like products and oligomer-wrapped SWNTs. For example, exploration under TEM of the product of the reaction of **3** with (6,5)-enriched SWNTs in DMF shows SWNTs with quite heavily functionalized walls (Figure 1.21a). Although the material is much more sensitive to the electron beam than our previous MINT samples, which hampered correct focusing, we could observe individual circular objects of adequate size to be macrocycle **6** (ca. 2 nm), which are highlighted with red arrows in Figures 1.21b and c. Besides that, areas of the nanotubes which are continuously modified by what appear as helical elongated molecules are also apparent, for instance that marked between two white arrows in Figure 1.21b.

AFM reveals individualized SWNTs (height ca. 0.6 nm, odd profiles in Figures 1.21d and e), which in several areas are fully covered with a dense layer of NDI material of height around 2

nm (even profiles in Figures 1.21d and e), which could be either oligomer-wrapped SWNTs, or densely packed macrocycles in MINTs. Some individual macrocycles can also be seen, such as those shown in Figure 1.21f.

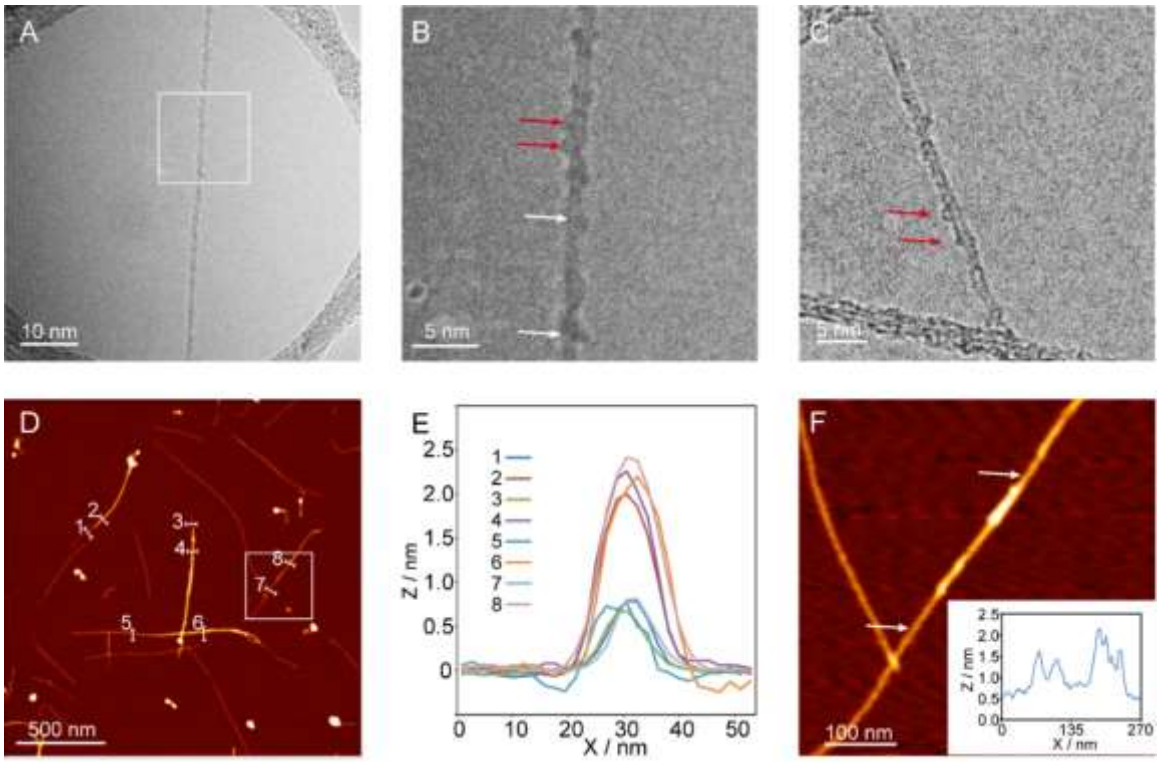

Figure 1.21. a-c) TEM micrographs of the product of the reaction of (6,5)-SWNTs with **3** in DMF. **d)** large-area AFM micrograph of the product of the reaction of (6,5)-SWNTs with **3** in DMF; **e)** height profiles along the lines marked in (d). **f)** Zoom-in on the area marked with a white square in (d), showing two individual macrocycles, and a region that could be oligomer-wrapped. The inset shows the height profile between the points marked with white arrows from left to right.

Effects of the supramolecular functionalization on the electronic properties of the SWNTs: As we have shown, the use of TCE results in mostly MINT-type products, while the reactions run in DMF show a mixture of MINTs and oligomer-wrapped SWNTs. Do these structural differences reflect in altered spectroscopic features? Indeed, we found significant differences in the Raman spectra of the products obtained from the metathesis reaction in TCE and DMF. The results of an average of at least three spectra for each product for linear precursor **3** under 532, 633, and 785 nm excitation are summarized in Table 1.3.

The lack of a consistent increase in the I_D/I_G ratio, together with the clearly visible RBMs (see Figure 1.22), indicates that the products are not functionalized covalently in any case,[111] as expected for the metathesis reaction conditions. Compared to the pristine nanotubes, the samples run in TCE show larger differences in their G band Raman shift than those from reactions carried out in DMF, even though their degree of functionalization is significantly

[111] C. Fantini, M. L. Usrey and M. S. Strano, *J. Phys. Chem. C*, **2007**, *111*, 17941-17946.

smaller. For instance, under 532 nm excitation, all products show a small downshift of the G band, indicative of the absence of significant charge-transfer from the nanotubes to the acceptor NDI unit under these conditions. Quantitatively, the shifts for the products from reactions run in TCE and DMF are on average −3 cm^{-1} and −1 cm^{-1}, respectively.

The difference between the products obtained in each solvent becomes clearer under red and near-infrared irradiation, where there is a marked upshift of the G band (9-12 cm^{-1}) for the products of the TCE reaction, consistent with significant charge transfer from the SWNTs to the NDI units. In contrast, the products of the reactions run in DMF show much smaller shifts (2-8 cm^{-1}). For instance, in the case of **3**-(7,6) under 633nm excitation the G^+ band appears at 1580 cm^{-1} for the pristine SWNTs, at 1590 cm^{-1} for **3**-(7,6)-TCE and at 1583 cm^{-1} for **3**-(7,6)-DMF (see Figure 1.22b). These results confirm a less efficient SWNT-NDI interaction in the case of the DMF compared to the TCE products, despite the larger degree of functionalization.

Sample	λ_{exc} = 532 nm		λ_{exc} = 633 nm		λ_{exc} = 785 nm	
	I_D/I_G	G^+shift (cm^{-1})	I_D/I_G	G^+shift (cm^{-1})	I_D/I_G	G^+shift (cm^{-1})
(6,5) SWNTs	0.06	1576	0.07	1580	0.07	1576
3-(6,5) TCE	0.06	1573	0.07	1589	0.07	1585
3-(6,5) DMF	0.01	1574	0.13	1588	0.23	1579
(7,6) SWNTs	0.07	1570	0.05	1580	0.02	1576
3-(7,6) TCE	0.05	1567	0.07	1590	0.09	1588
3-(7,6)DMF	0.07	1570	0.07	1583	0.09	1584

Table 1.3. Summary of most relevant Raman data for samples of the reaction between linear precursor **3** and both types of SWNTs in TCE and DMF.

Remarkably, after the thermal treatment, the TCE samples show basically no change in their Raman spectra, whereas those from reactions carried out in DMF suffer larger shifts with respect to the pristine SWNTs, approximating those of the TCE samples. For example, for **3**-(7,6)-DMF, the G^+ band shifts from 1583 cm^{-1} to 1587 cm^{-1}, compared to 1590 cm^{-1} for **3**-(7,6)-TCE (see Figure 1.22c and d). The absorption and photoemission spectroscopy of the samples also reflects the type of functionalization. Figure 1.23a depicts the UV-vis-NIR absorption spectra of pristine (7,6)-enriched SWNTs (black), and the products of their reactions with **3** in TCE (red) and DMF (green).

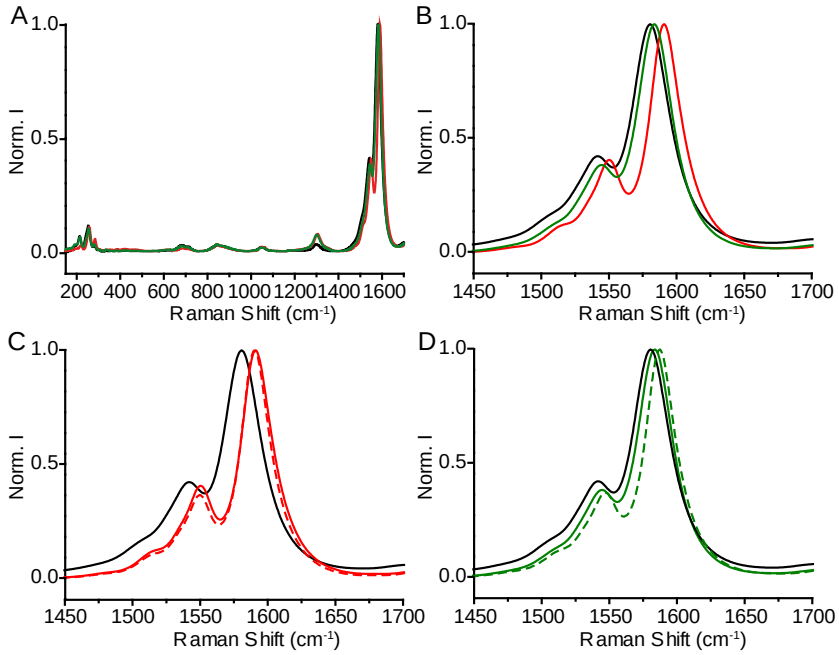

Figure 1.22. Raman spectra (λ_{exc} = 633 nm) of **a)** (7,6) SWNTs (black line), reaction product of **3** with (7,6) SWNTs in TCE (red line) and in DMF (green line). **b)** Zoom in of the G band of the spectra shown in a). **c)** Partial Raman spectra (λ_{exc} = 633 nm) of (7,6) SWNTs (black line) and the reaction product of **3** with (7,6) SWNTs in TCE before (solid red line) and after (dashed red line) reflux in TCE. **d)** Partial Raman spectra (λ_{exc} = 633 nm) of (7,6) SWNTs (black line) and the reaction product of **3** with (7,6) SWNTs in DMF before (solid green line) and after (dashed green line) reflux in TCE.

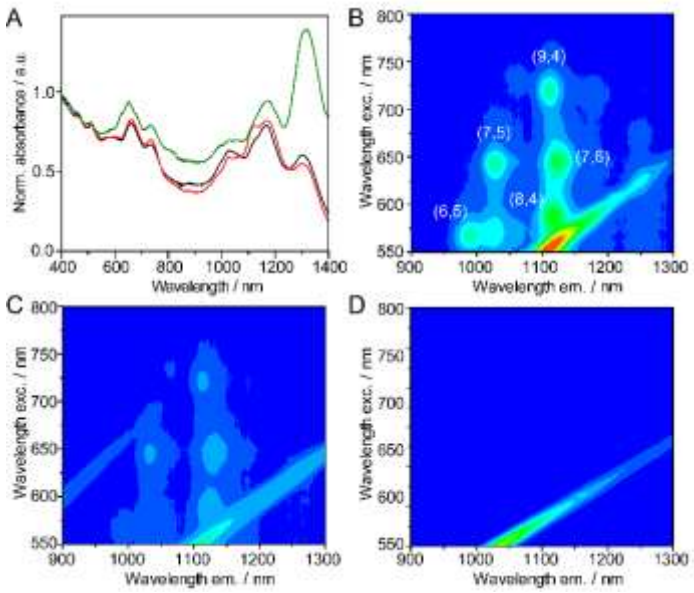

Figure 1.23. a) UV-vis-NIR absorption spectra of pristine (7,6)-enriched SWNTs (black), and the products of their reactions with **3** in TCE (red) and DMF (green). **b)** PLE spectrum of pristine (7,6)-enriched SWNTs and the products of their reactions with **3** in TCE **(c)** and DMF **(d)**. All spectra in D_2O with 1% sodium dodecylsulfate as surfactant and acquired at room temperature. Scattering has not been filtered.

The SWNTs show absorption features in the S_{22} and S_{11} regions of the spectra corresponding to various chiralities, with the (7,6) features at approximately 660 nm and 1120 nm being particularly prominent.[112] Upon functionalization in TCE, we observe small red shifts of all bands in analogy with our previous results for MINTs.[90,91,92] The absorption features of the sample treated in DMF are remarkably different. The relative intensity of the absorption at 1310 nm, which we tentatively assign to either (13,2) or (9,7) SWNTs[112] increases significantly, most likely due to improved solubility due to functionalization. Since such SWNTs have diameters of around 1.1 nm, and are way too large to undergo MINT formation (see Figure 1.18b), we assume they must be oligomer-wrapped.

The 3D photoluminescence excitation (PLE) maps shown in Figure 1.23b-d provide more information. The pristine SWNTs show emissions corresponding to (6,5), (7,5), (8,4), (9,4) and (7,6) SWNTs. Upon functionalization in TCE, the luminescence of the smaller (6,5) SWNTs is nearly completely quenched, the (7,5) SWNTs also suffer strong quenching, but are still visible, and the larger nanotubes are quenched to lesser extent. In contrast, the nanotubes functionalized in DMF show no photoluminescence irrespective of their chirality, and despite being well dispersed according to their absorption spectra. Although luminescence quenching is a complex phenomenon and quantitative conclusions cannot be extracted, our observations point to a chirality-dependent functionalization in TCE and to a nonselective functionalization in DMF, in line with the MM calculations and TGA data.

[112] S. M. Bachilo, M. S. Strano, C. Kittrell, R. H. Hauge, R. E. Smalley and R. B. Weisman, *Science*, **2002**, *298*, 2361-2366.

Figure 1.24a shows the changes to the C 1s region of the X-ray Photoelectron Spectra (XPS) upon functionalization of the (7,6) SWNTs with **3**. The pristine sample is intrinsically asymmetric and its main component, related to primary graphitic peak of carbon or sp^2, is represented by a Doniach-Sunjic function with an asymmetry parameter $\alpha = 0.18$ and centered in a binding energy of 284.4 eV. The asymmetry of this component is associated with the many-electron response to the sudden creation of a photohole.[113] The rest of the peaks can be perfectly reproduced by Gaussians, as the typical plasmon loss centered at 290.8 eV and the sp^3 or amorphous carbon at 285.3 eV, visible even in the pristine sample as a result of the hybridization of the sp^2 component.

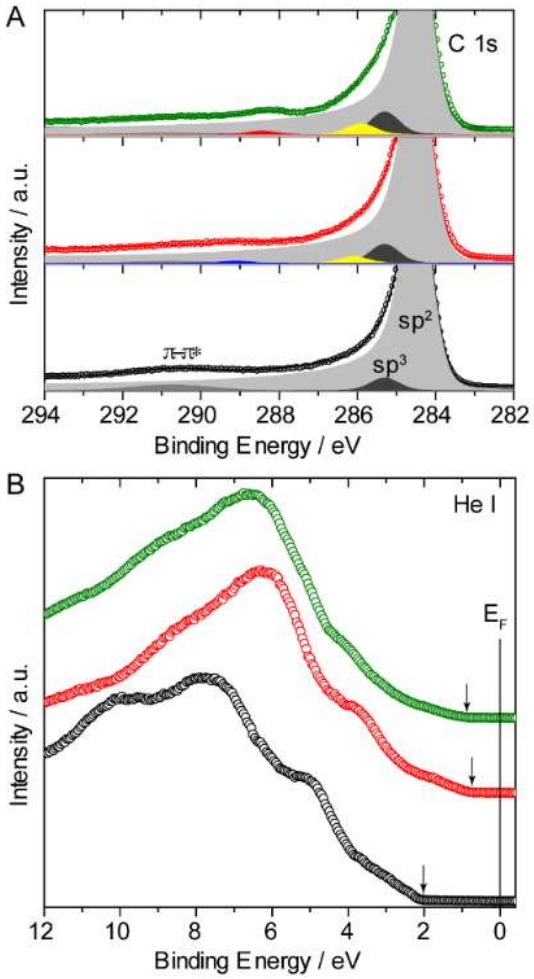

Figure 1.24. a) XPS spectra of C 1s core level for the pristine SWNTs (lower panel, black circles and line), functionalized with **3** in TCE (middle pannel, red circles and line) and in DMF (upper panel, green circles and line). Circles are experimental data and the lines represent the fits. **b)** UPS spectra measured with He I line of the pristine SWNTs (black circles), functionalized with **3** in TCE (red circles) and in DMF (green circles).

[113] S. Hüfner, Photoelectron Spectroscopy. Principles and Applications, Springer, Berlin Heidelberg, 3 edn., **2003**.

After treatment with **3**, new features appear in the spectra. Centered at 286.1 eV and at 285.9 eV there is a component that can be assigned either to C-N bonds and/or C-O bonds. In agreement with the small degree of functionalization, N is hardly detected for the TCE sample so the peak at 286.1 eV can be safely assigned to C-O species, which are more abundant in **3**. In the DMF case, this peak is centered at a slightly smaller energy (285.9 eV), and we assume both C-O and C-N functional groups are contributing. To complete the fit it was necessary to add another component at 289.1 eV for the TCE and 288.4 eV to DMF, related to O-C=C and C=O respectively. Interestingly, all features related with the NDI functionalization show noticeable shifts depending on the solvent used for the reaction.

To study the changes in the valence band with the different functionalization protocols, UPS spectra were also acquired. Figure 1.24b shows the valence band of the pristine (7,6) sample (black circles), where most of its features are typical of semiconducting SWNTs, which are in turn directly related to those of graphite: the 2p-σ states around 5 and 8 eV below the Fermi level and the mixed σ-π hybridized states around 10 eV, that come from the curvature of the SWNTs.[114,115]

However, in the pristine sample, the 2p-π band located at 3 eV expected for graphite, is not evident here due to the proximity of the border of the valence band at 2 eV, far away from the Fermi level, which gives the semiconductor character to the SWNTs. After reaction with **3** in TCE (red circles) and DMF (green circles) the valence bands show in both cases the typical oxygen band around 6 eV and a significant approach of the border of the valence bands towards the Fermi level (see vertical arrows in Figure 1.24b). In line with the Raman results, this effect is more marked for the samples functionalized in TCE, despite the smaller degree of functionalization.

[114] P. Chen, X. Wu, X. Sun, J. Lin, W. Ji and K. L. Tan, *Phys. Rev. Lett.*, **1999**, *82*, 2548-2551.
[115] M. Scardamaglia, C. Struzzi, F. J. Aparicio Rebollo, P. De Marco, P. R. Mudimela, J. F. Colomer, M. Amati, L. Gregoratti, L. Petaccia, R. Snyders and C. Bittencourt, *Carbon*, **2015**, *83*, 118-127.

4.3 Conclusions

In summary, we have described a novel method for the noncovalent functionalization of SWNTs. We used NDI-based bisalkene precursors that can either ring-close around the SWNTs to form rotaxane-like MINTs or oligomerize through ADMP and then wrap the SWNTs. Varying the solvent system can control the final outcome of the reaction. In TCE, the NDI precursors show lower affinity for the SWNTs, and the non-templated metathesis reaction is very slow. The combination of these two factors favors the formation of the more stable MINTs. In contrast, in DMF, the non-templated reaction is significantly faster, and the NDI precursors show much larger binding constants towards SWNTs, which results in the formation of a substantial amount of oligomer-wrapped SWNTs.

The formation of MINTs in TCE depends on the match between the cavity of the macrocycle(s) and the diameter of the SWNTs. Meanwhile, the degree of functionalization in the reactions run in DMF is fundamentally diameter-independent and consistently leads to larger NDI loading. Each type of functionalization affects the electronic properties of the SWNTs differently, which is reflected in changes in their Raman, UV-vis-NIR, PLE, XPS and UPS spectra. Our results illustrate how the combination of covalent and noncovalent chemistries opens the door to novel types of functionalization of SWNTs, in which the topology, the degree of functionalization, and the electronic interaction between the nanotubes and their supramolecular partners, and, most remarkably, their topology[116] can be varied.

[116] A. López-Moreno, B. Nieto-Ortega, M. Moffa, A. de Juan, M. M. Bernal, J. P. Fernández-Blázquez, J. J. Vilatela, D. Pisignano and E. M. Pérez, *ACS Nano*, **2016**, *10*, 8012-8018.

4.4 Experimental Section

All solvents were dried according to standard procedures. Reagents used as purchased. Flash chromatography was performed using silica gel (Scharlau 60, 230-240 mesh). Analytical thin layer chromatography (TLC) were performed using aluminiun-coated Merck Kieselgel 60 F254 plates. NMR spectra were recorded on a Bruker Avance 300 (^{1}H: 300MHz, ^{13}C: 75MHz) spectrometers at 298K, unless otherwise stated using partially deuterated solvents as internal standards. Coupling constants (J) are denoted in Hz and chemical shifts (δ) in ppm. Multiplicities are denoted as follows: s = singlet, d = doublet, t = triplet, m = multiplet. Electrospray ionization mass spectrometry (ESI-HR-MS) and Matrix-assisted Laser desorption ionization (coupled to a Time-Of-Flight analyzer) experiments (MALDI-TOF HR-MS) were recorded on an HP1100MSD spectrometer and a Bruker REFLEX spectrometer, respectively. Thermogravimetric analyses (TGA) were performed using a TA Instruments TGAQ500 with a ramp of 10 °C/min under air from 100 to 1000 °C.

UV-vis-NIR spectrums were performed using a Shimadzu UV-VIS-NIR Spectrophotometer UV-3600.Photoluminescence excitation intensity maps (PLE) were obtained with NanoLog 4 HORIBA. Raman spectra were acquired with a Bruker Senterra confocal Raman microscopy instrument, equipped with 532, 633 and 785 nm lasers. Transmission electron microscopy (TEM) images were obtained with JEOL-JEM 2100F (2.5 Å resolution) instrument.

XPS (X ray Photoelectron Spectroscopy) measurements were performed under Ultra High Vacuum conditions (UHV, with a base pressure of 7×10^{-10} mbar), using a monochromatic Al Kα line as exciting photon source for core level analysis ($h\nu$ = 1486.7 eV) and He I line for the Ultraviolet Photoelectron Spectroscopy valence band measurements (UPS, $h\nu$ = 21.2 eV). The emitted photoelectrons were collected in a hemispherical energy analyzer (SPHERA-U7, pass energy set to 20 eV for the XPS measurements to have a resolution of 0.6 eV and 5 eV to have a resolution of 0.1 eV for UPS) and to compensate the built up charge on the sample surface it was necessary (for the XPS measurements) the use of a Flood Gun (FG-500, Specs), with low energy electrons of 3 eV and 40 μA.

General procedure synthesis lineal amines.

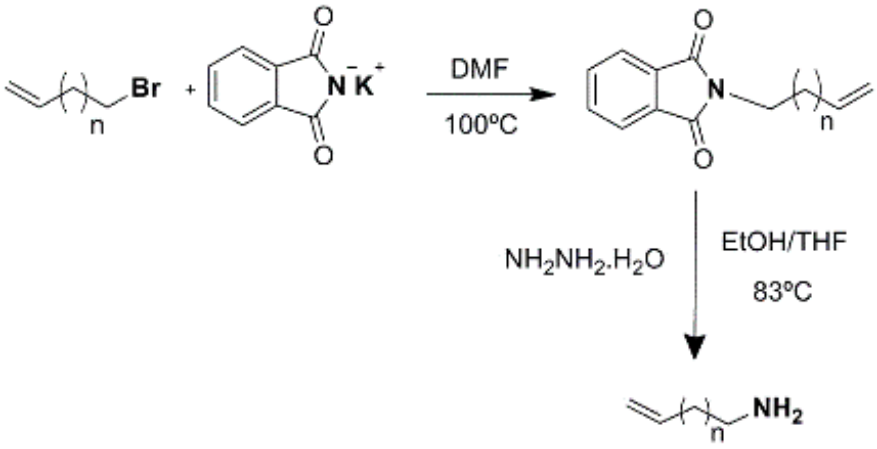

Compound 7 a-c: the alkene was charged in a flask, N, N-dimethylformamide was added and the reaction was heated at 100^0C during 2h. The solution was then allowed to come back to room temperature and filtered over celite and the filtrate concentrate in vacuo to give a pale yellow solid in 90-92% yield.

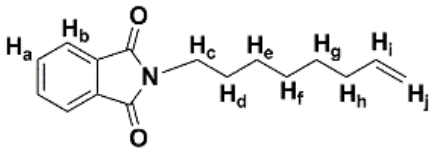

Compound 7a: ^{1}H NMR (300 MHz, $CDCl_3$) δ 7.99 (m, $2H_b$), 7.76 (m, $2H_a$), 5.78 (m, $1H_i$), 5.10 (m, $2H_j$), 3.78 (m, $2H_c$), 2.01 (m, $2H_h$), 1.53 (m, $2H_d$), 1.49 (m, $6H_{e,f,g}$),^{13}C NMR (75 MHz, $CDCl_3$) δ 168.42, 138.89 , 133.97, 132.09, 123.21, 114.20, 28.65, 28.58, 28.48, 26.64. MS m/z calculated for $C_{16}H_{19}NO_2$ [M-H$^+$] 257.1416 found HR-MS 257.1432.

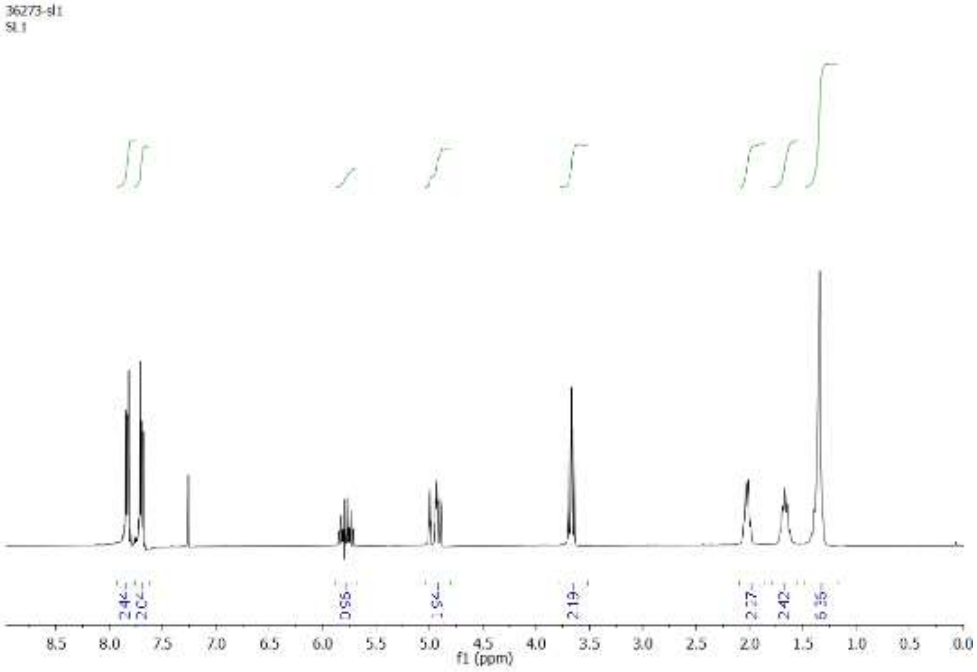

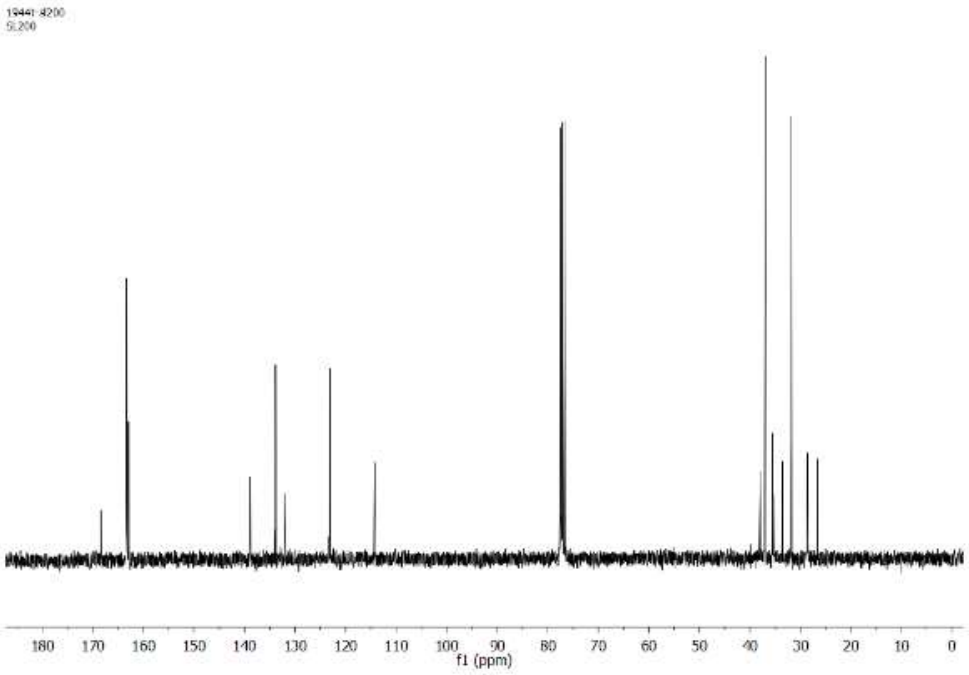
f1 (ppm)

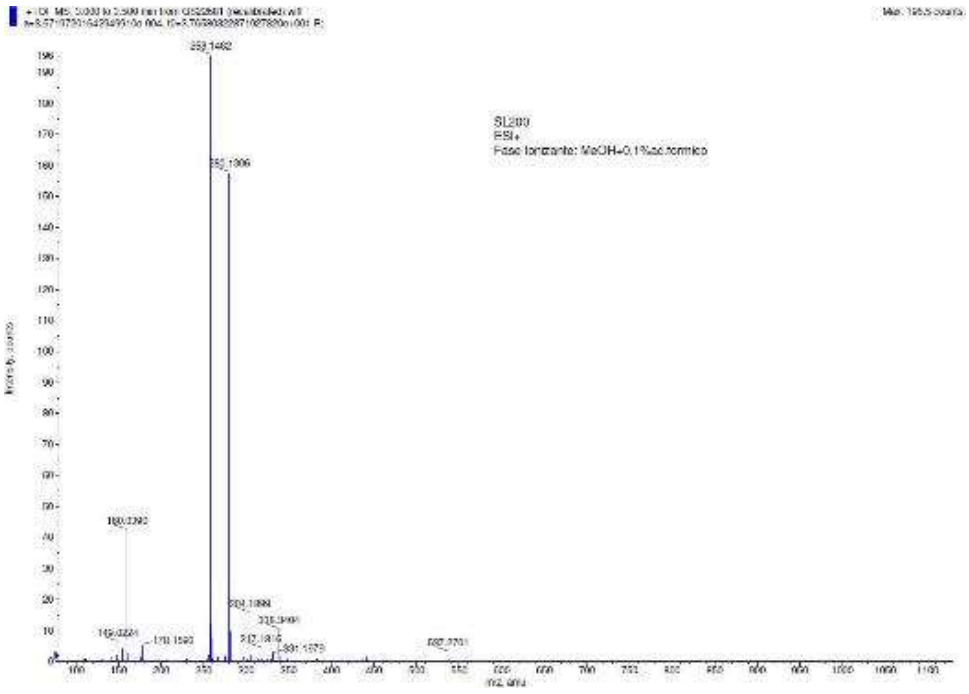
SL200
ESI+
Fase fortemente: MeOH+0,1%ac.formico

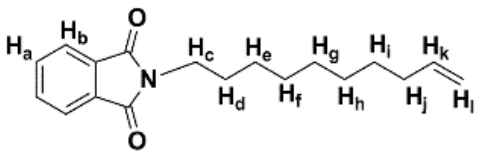
Ha
Hb
O
N
O
Hc
Hd
He
Hf
Hg
Hh
Hi
Hj
Hk
Hl

Compound 7b: ^{1}H NMR (300 MHz, $CDCl_3$) δ 7.89 (m, $2H_b$), 7.70 (m, $2H_a$), 5.72 (m, $1H_k$), 5.04 (m, $2H_l$), 3.70 (m, $2H_c$), 2.03 (m, $2H_j$), 1,53 (m, $2H_d$), 1.45 (m, $10H_{e,f,g,h,i}$), ^{13}C NMR (75 MHz, $CDCl_3$) δ 168.43, 139.14, 133.81, 132.18, 123.12, 114.12, 38.04, 33.74, 29.28, 29.10, 29.00, 28.84, 28.57, 26.82. MS m/z calculated for $C_{18}H_{23}NO_2$ 285.17 found MALDI TOF 285.17.

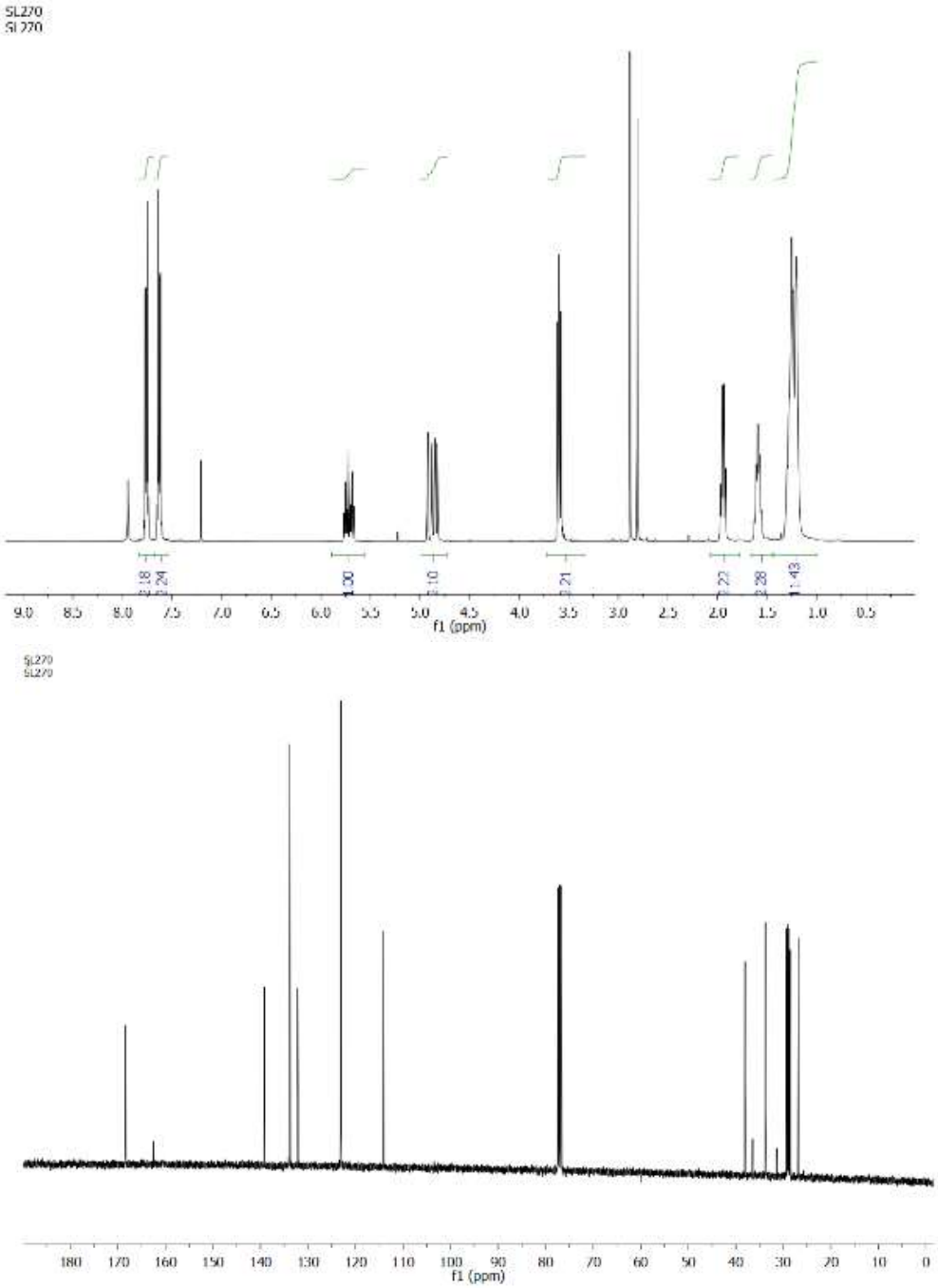

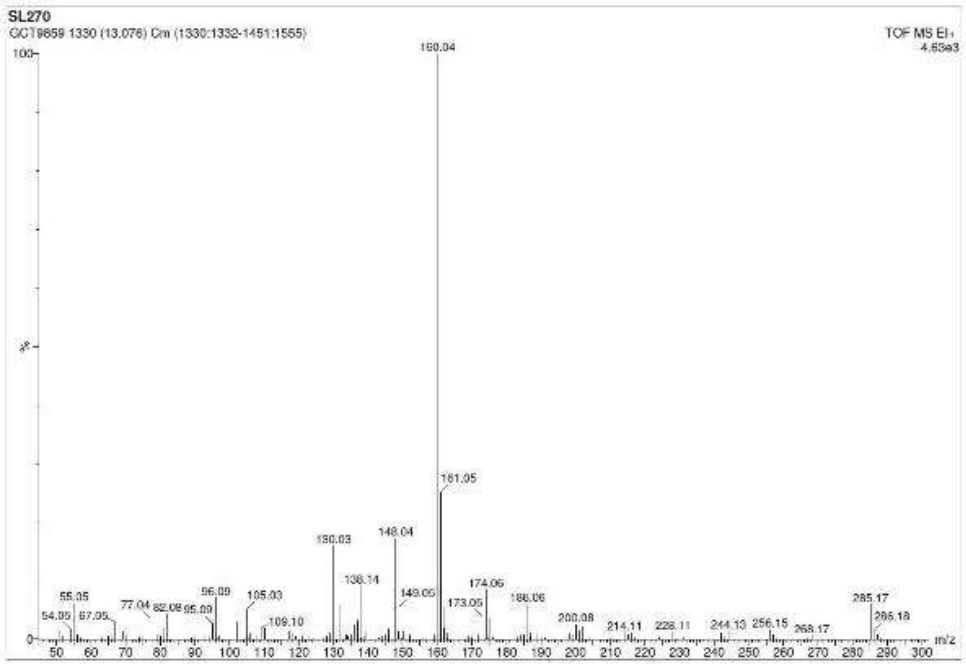

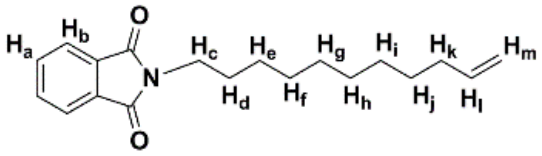

Compound 7c: ^{1}H NMR (300 MHz, $CDCl_3$) δ 7.89 (m, $2H_b$), 7.69 (m, $2H_a$), 5.93 (m, $1H_l$), 5.06 (m, $2H_m$), 3.75 (m, $2H_c$), 2.10 (m, $2H_k$),1.53 (m, $2H_d$), 1.46 (m, $12H_{e,f,g,h,i,j}$), ^{13}C NMR (75 MHz, $CDCl_3$) δ 168.34, 139.08, 133.86, 132.10, 123.14, 114.03, 37.97, 33.70, 29.37, 29.03, 28.81, 28.51, 26.77. MS m/z calculated for $C_{19}H_{25}NO_2$ 299.1885 found HR-MS 299.1968.

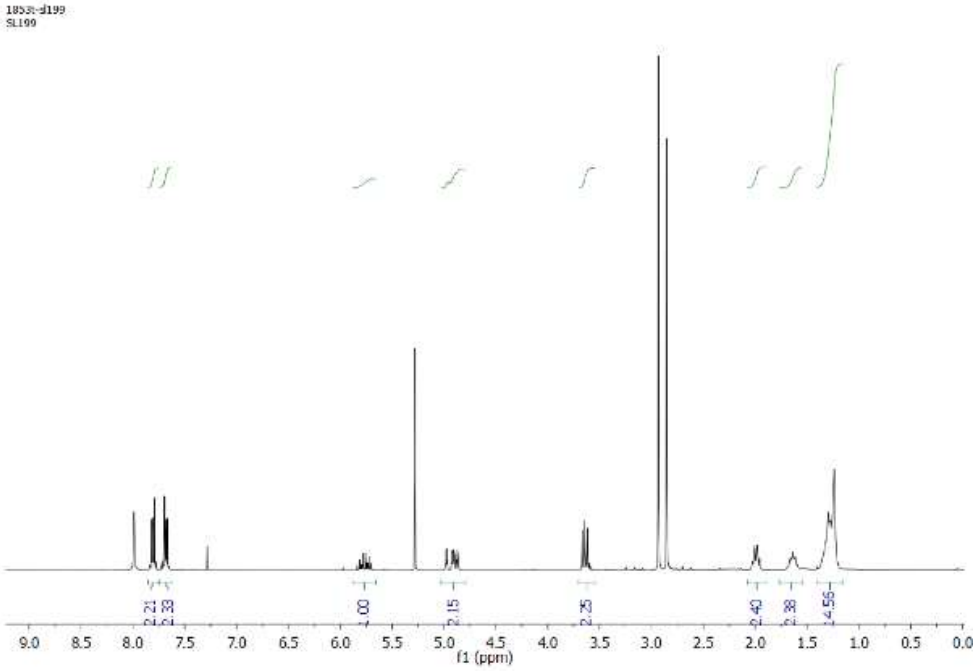

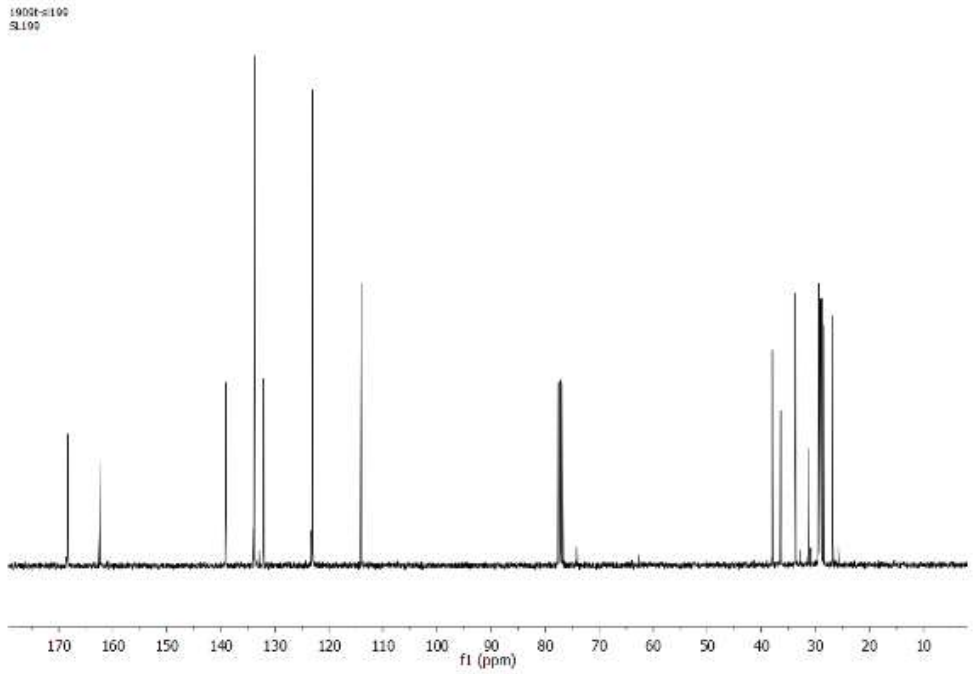

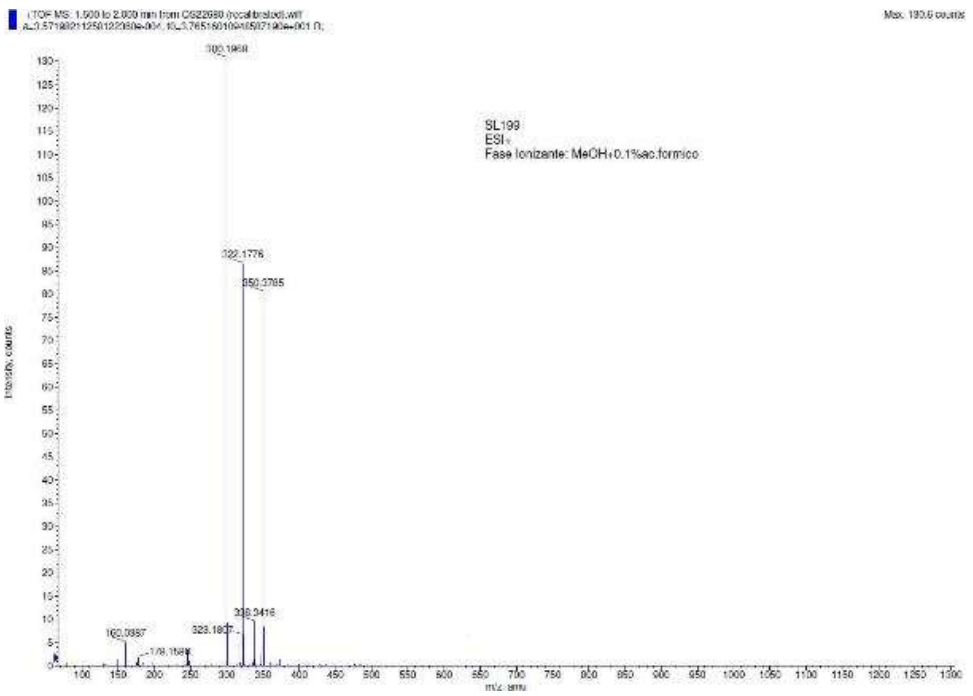

Compound 8 a-c: The previously obtained solid (5 g, 16.7 mmol) was dissolved in a mixture of THF/Ethanol (120 ml/120 ml), the hydrazine monohydrate (3.2 g, 100.2 mmol) was added and the reaction was heated at 83^0C during 2h. The solvent was removed in vacuo and the residue was poured onto NaOH 1M (30ml). The mixture was extracted with DCM. The organic layer was dried with sodium sulfate and the solvent was removed in vacuo afforded a yellow oil 83-87% yield.

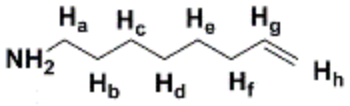

Compound 8a: ^{1}H NMR (300 MHz, $CDCl_3$) δ 5.76 (m, $1H_g$), 5.17 (m, $2H_h$), 2.71 (t, *J* = 6.9 Hz, $2H_a$), 2.11 (m, $2H_f$), 1.58 (m, $8H_{b,c,d,e}$), ^{13}C NMR (75 MHz, $CDCl_3$) δ 138.98, 114.21, 42.08, 33.71, 33.51, 28.93, 28.86, 26.71. MS m/z calculated for $C_8H_{17}N$ [M-H$^+$] 128.14 found MALDI TOF 128.15.

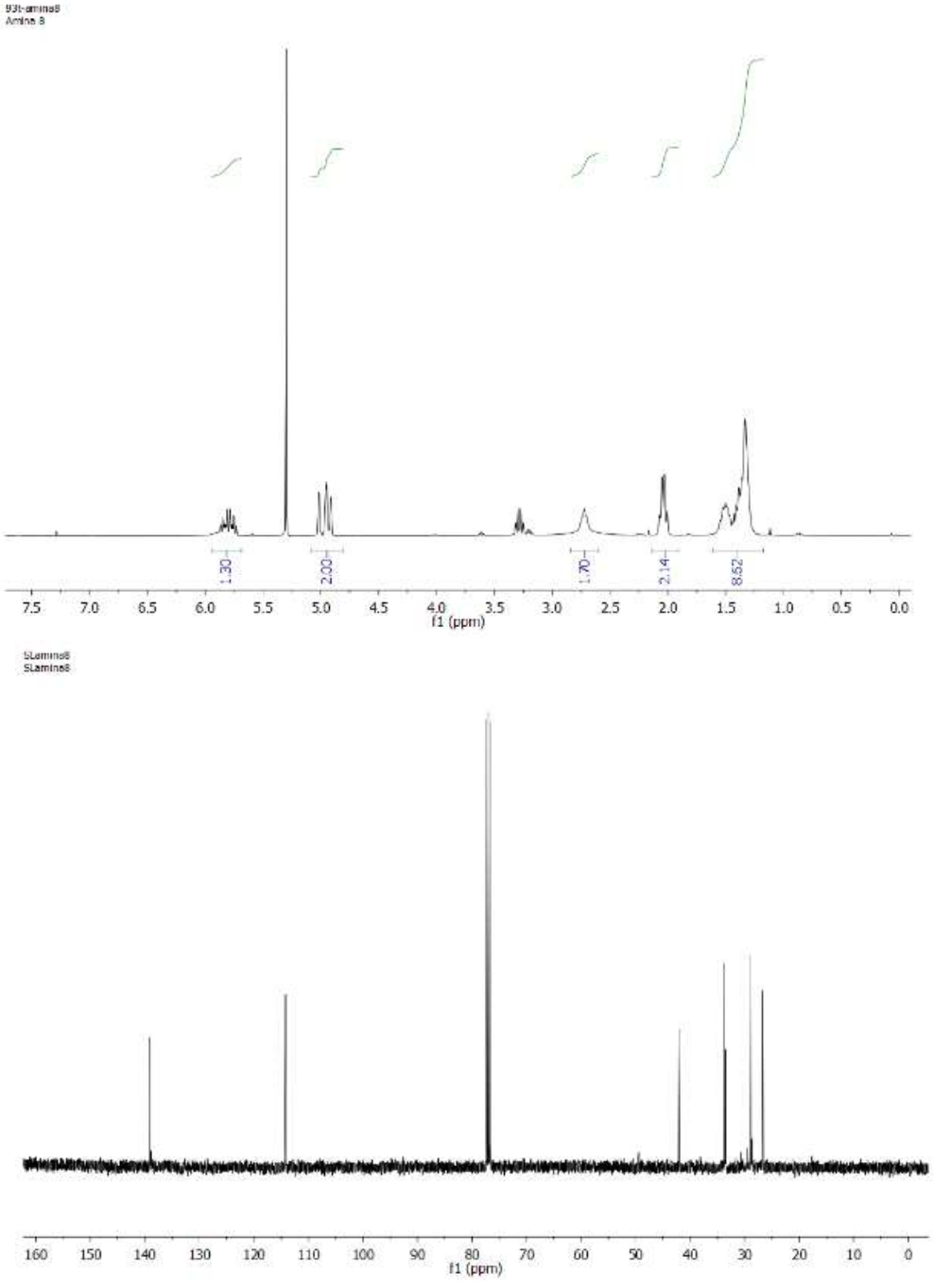

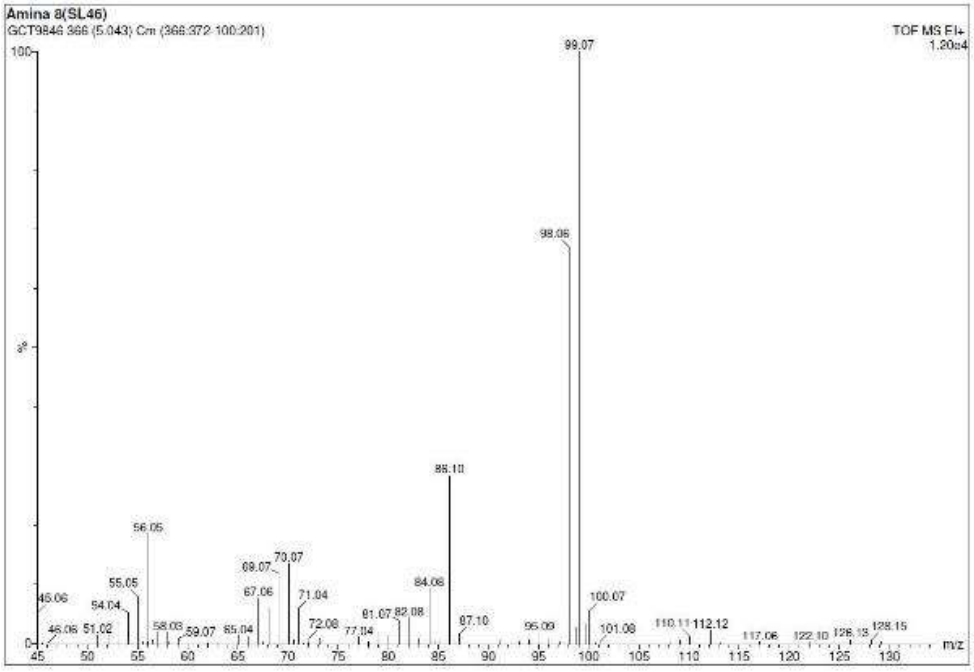

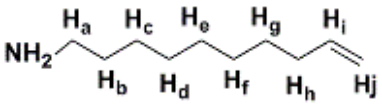

Compound 8b: ^{1}H NMR (300 MHz, $CDCl_3$) δ 6.06 (m, $1H_i$), 5.13 (m, $2H_j$), 2.68 (t, *J*= 6.9 Hz, $2H_a$), 2.04 (m, $2H_h$), 1.58 (m, $12H_{c,d,e,f,g}$),^{13}C NMR (75 MHz, $CDCl_3$) δ 139.17, 114.09, 42.19, 33.77, 33.75, 29.44, 29.43, 29.06, 28.90, 26.86. MS m/z calculated for $C_{10}H_{21}N$ [M-H^+] 156.17 found MALDI TOF 156.17.

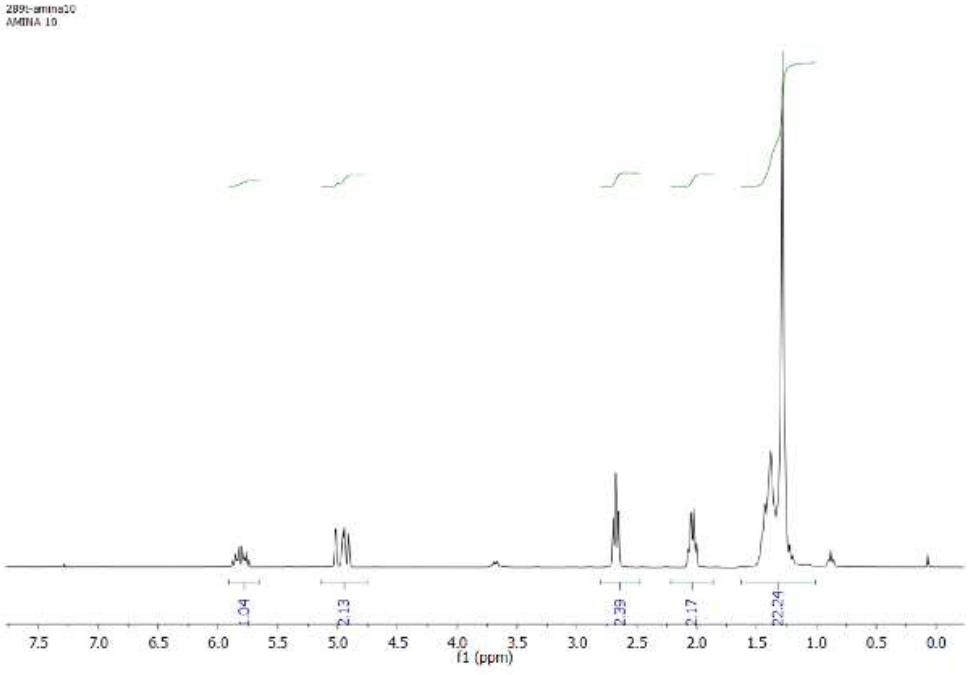

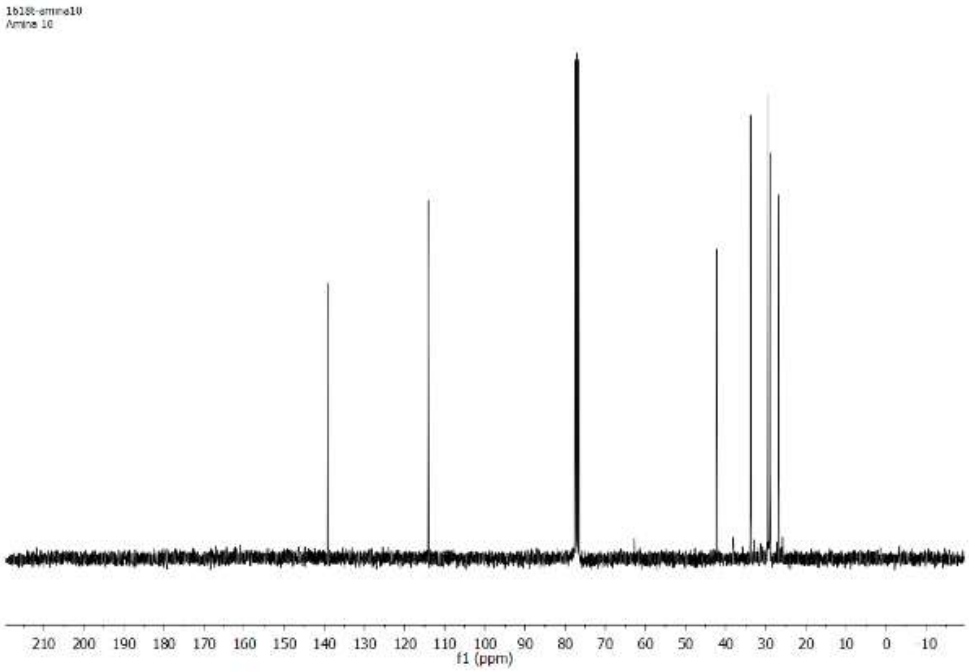

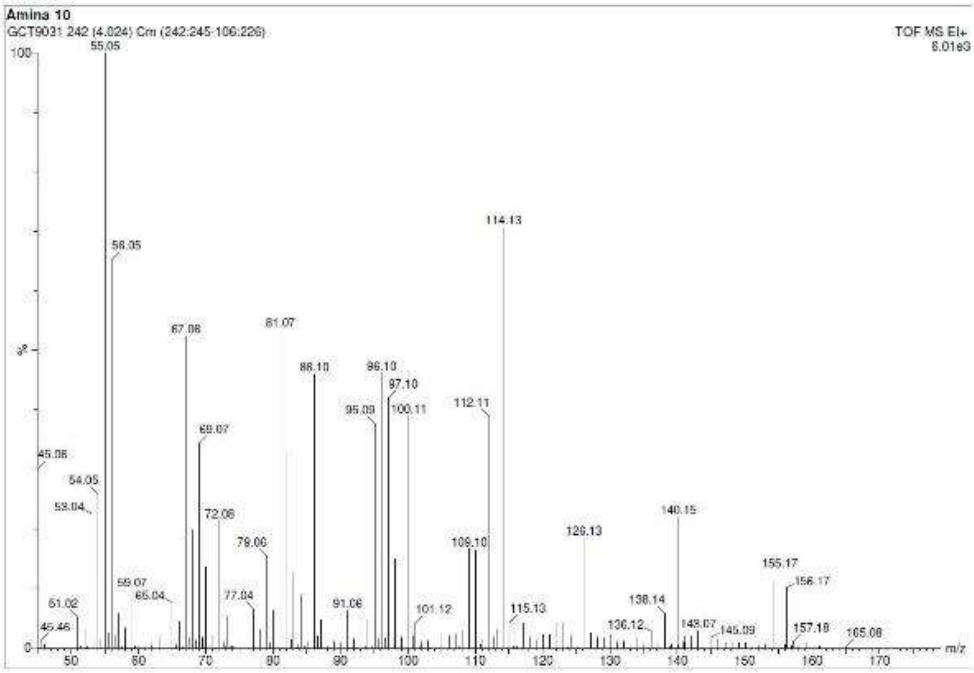

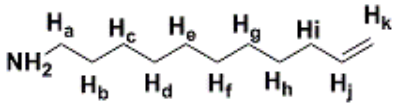

Compound 8c: ^{1}H NMR (300 MHz, $CDCl_3$) δ 5.91 (m, 1H_j), 5.06 (m, 2H_k), 2.64 (t, *J* = 6,9 Hz, 2H_b), 2.05 (m, 2H_i), 1.55 (m, 14H $_{c,d,e,f,g,h}$), ^{13}C NMR (75 MHz, $CDCl_3$) δ 139.14, 114.16, 40.07, 33.78, 29.37, 29.35, 29.06, 29.01, 28.91, 28.05, 26.55. MS m/z calculated for $C_{11}H_{23}N$ [M-H^+] 169.18 found MALDI TOF 169.18.

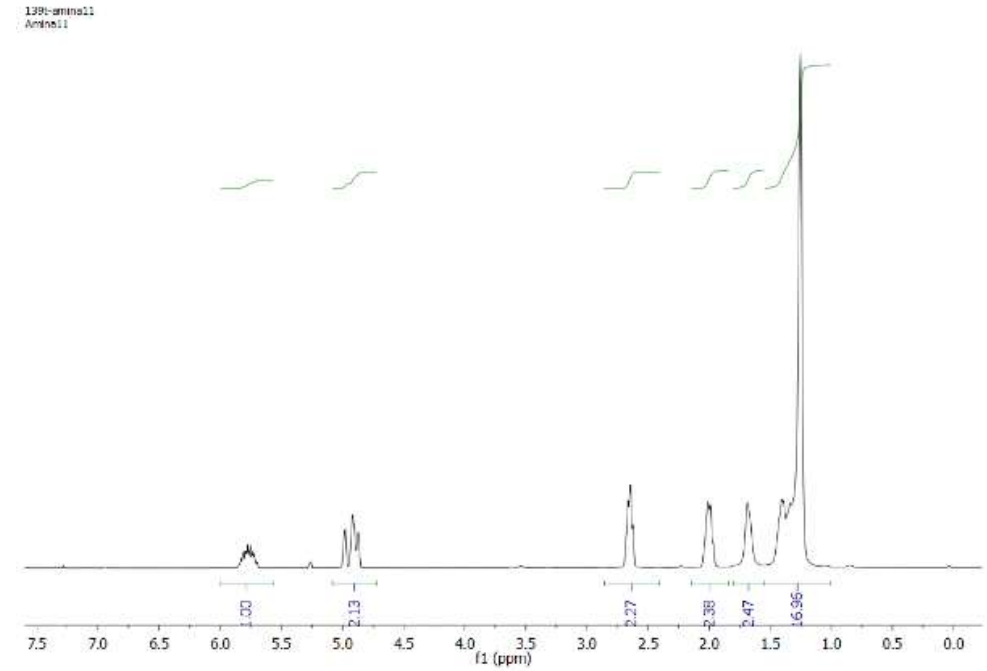
1.00
2.13
2.27
2.38
2.47
16.96
f1 (ppm)

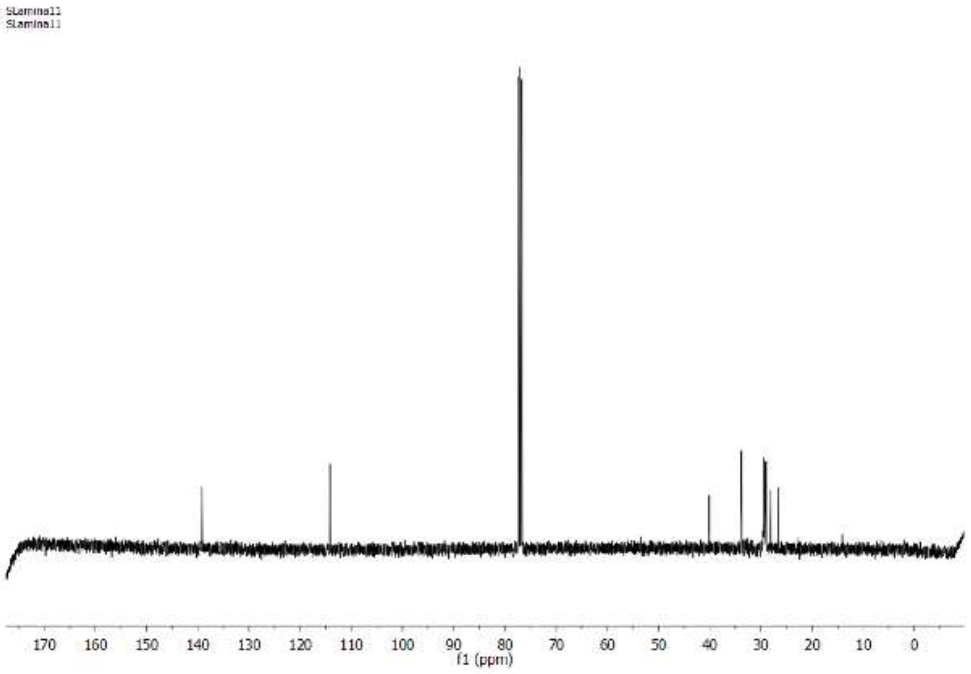
f1 (ppm)

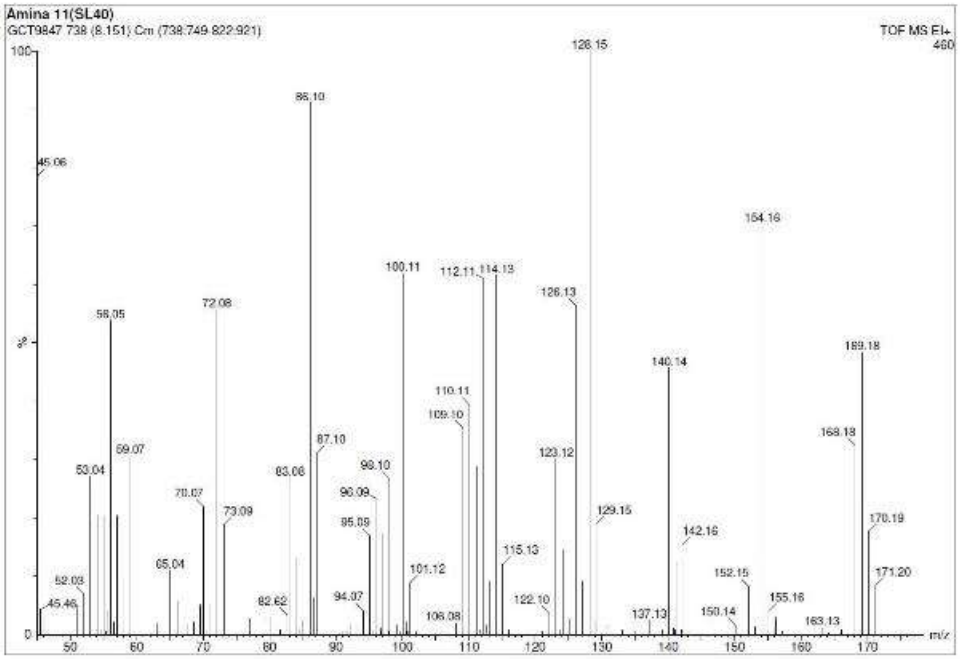
Amina 11(SL40)
GCT9847 738 (8.151) Cm (738:749-822:921)
TOF MS EI+
100
%
0
126.15
86.10
45.06
164.16
100.11
112.11
114.13
72.08
126.13
58.05
169.18
140.14
110.11
109.10
87.10
168.18
59.07
123.12
53.04
99.10
83.08
96.09
70.07
73.09
129.15
95.09
170.19
142.16
115.13
65.04
101.12
171.20
52.03
152.15
45.46
82.62
94.07
122.10
155.16
106.08
137.13
150.14
163.13
50
60
70
80
90
100
110
120
130
140
150
160
170
m/z

General procedure to the synthesis of aromatic spacer

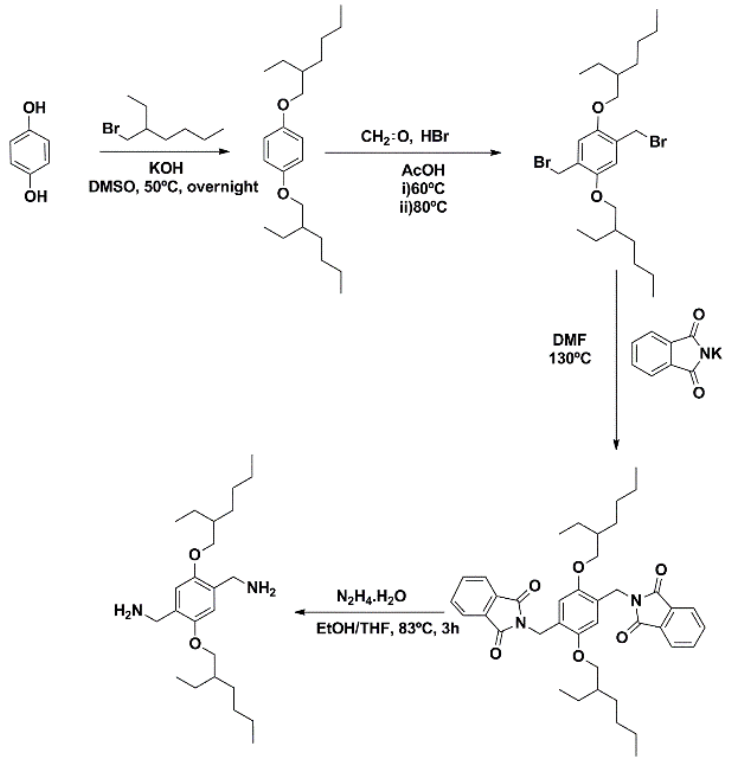

The compound 1,4-Bis (2-ethyl-hexyloxy)-benzene and the 1,4-Dibromo-2, 5-bis-(2-ethyl-hexyloxy)-benzene (II) were synthetized as described in Macromolecules **2012**, 45, 5051-5057.

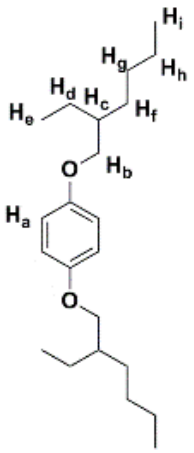

Compound 9. ^{1}H NMR (300 MHz, $CDCl_3$) δ 6.82 (s, $4H_a$), 3.78 (dd, *J* = 5.8, 1.2 Hz, $4H_b$), 1.69 (sep, *J* = 6.1 Hz, $2H_c$), 1.28-1.54 (m, $16H_{d,e,f,g}$) 0.92 (m, $4H_h$), ^{13}C NMR (75 MHz, $CDCl_3$) δ 153.43, 115.35, 71.20, 39.47, 30.53, 29.09, 23.86, 23.06, 14.08, 11.09. HR-MS m/z calculated for $C_{22}H_{38}O_2$ 334.2812 found HR-MS 334.2873.

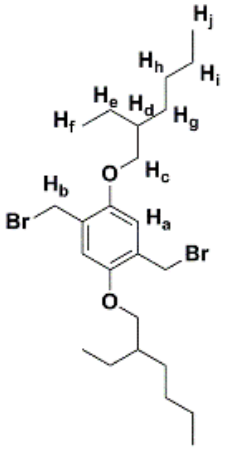

Compound 10. ^{1}H NMR (300 MHz, $CDCl_3$, ppm) δ 6.85 (s, $2H_a$), 4.52 (s, $4H_b$), 3.87 (d, *J* = 5.4 Hz, $4H_c$), 1.75 (sep, J = 6.2 Hz, $2H_d$), 1.61 – 1.29 (m, 16H $_{e,g,h,i}$), 0.97 – 0.89 (m, $12H_{f,\ j}$), ^{13}C NMR (75 MHz, $CDCl_3$) δ 150.69, 127.36, 114.21, 70.91, 39.59, 30.62, 29.10, 28.73, 24.01, 23.04, 14.08, 11.23.MS m/z calculated for $C_{24}H_{40}Br_2O_2$ 518.139 found MALDI TOF 518.139.

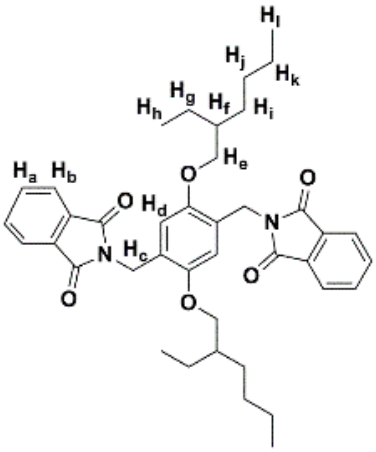

Compound 11 : the previously product (5g, 9.6 mmol) and the potassium phthalamide (7g, 38.4mmol) were charged in a flask N,N-dimethylformamide (80 ml) was added and the reaction was heated at 100^{0}C during 2h. The solution was then allowed to come back to room temperature and filtered over celite and the filtrate concentrate in vacuo to give a pale white solid (80%). ^{1}H NMR (300 MHz, $CDCl_3$) δ 7.82 – 7.68 (m, $8H_{a,b}$), 6.77 (s, $2H_d$), 4.85 (s, $4H_c$), 3,77 (m, $4H_e$), 1.75 (sep, J = 6.2 Hz, $2H_f$), 1.61 (m, $16H_{g,i,j,k}$), 0.97 (m, $12H_{h,l}$), ^{13}C NMR (75 MHz, $CDCl_3$) δ 168.09, 151.79 , 150.59, 133.97, 133.66, 124.95, 124.46, 123.35, 123.02, 113.29, 111.12, 71.41, 39.52, 37.17, 35.40, 30.54, 29.16, 23.94, 23.17, 14.22, 11.22. MS m/z calculated for $C_{40}H_{48}N_2O_6$ [M^+ Na^+] 675.3410 found HR-MS 675.3434.

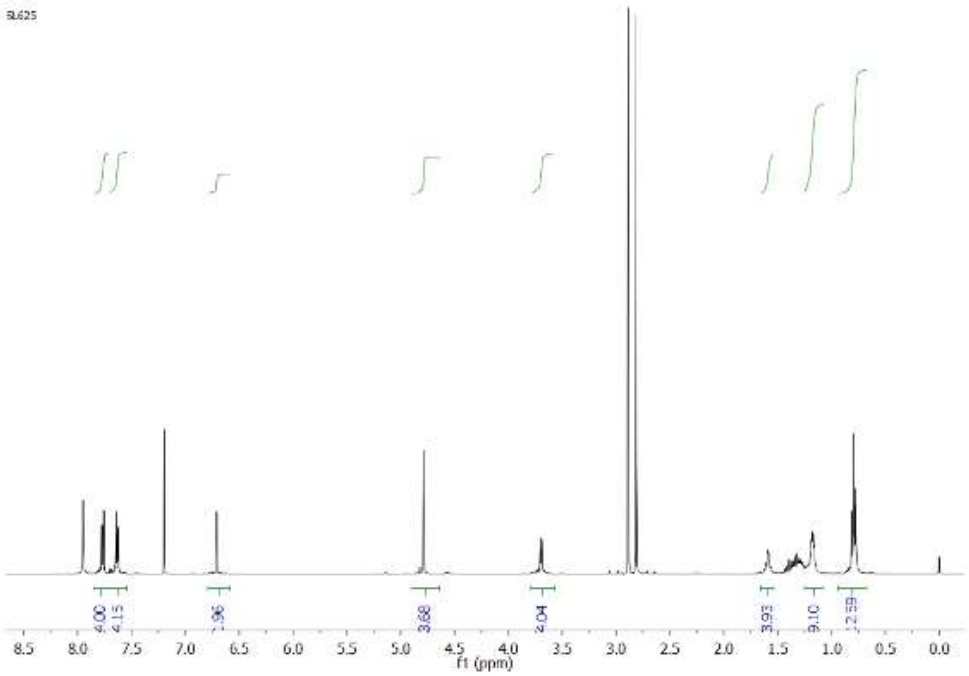
SL625
4.00
4.15
1.96
3.68
2.04
3.93
9.10
12.59
8.5 8.0 7.5 7.0 6.5 6.0 5.5 5.0 4.5 4.0 3.5 3.0 2.5 2.0 1.5 1.0 0.5 0.0
f1 (ppm)

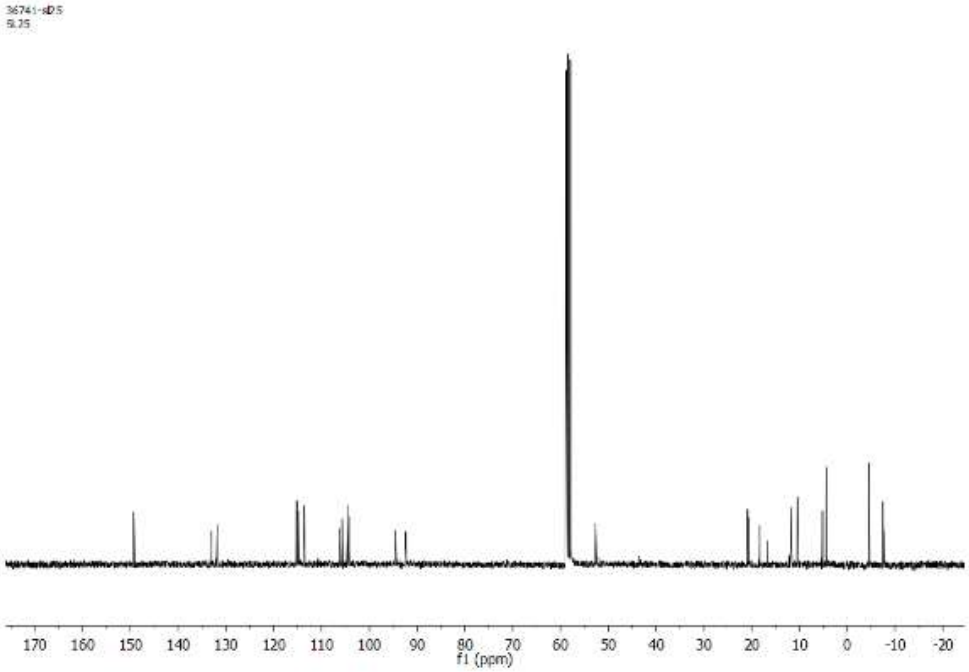
36741-sD5
SL25
170 160 150 140 130 120 110 100 90 80 70 60 50 40 30 20 10 0 -10 -20
f1 (ppm)

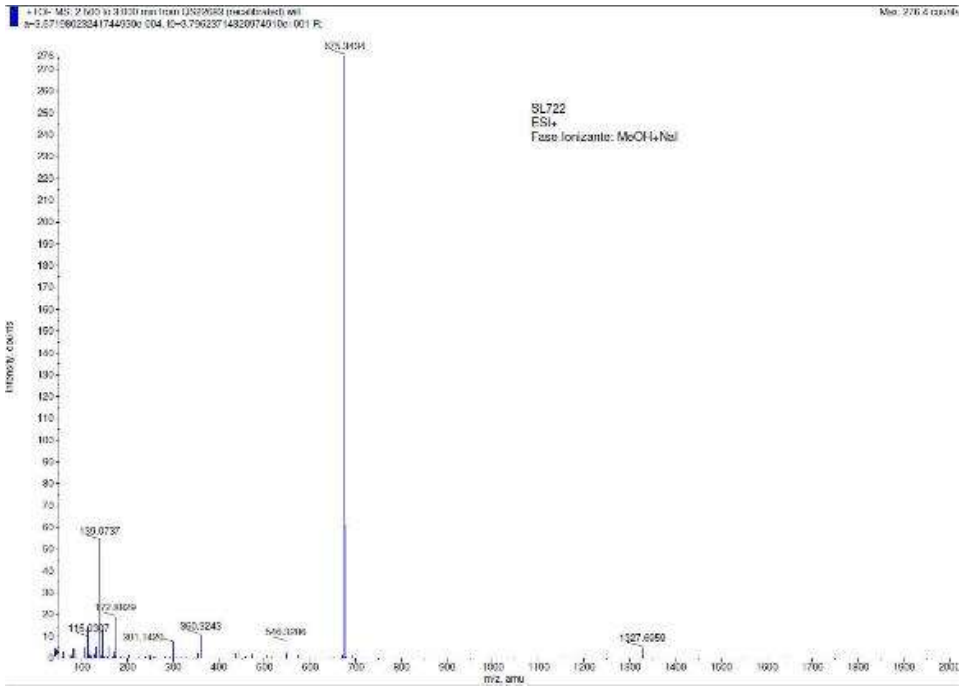

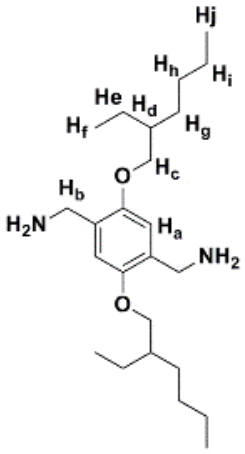

Compound 12: The previously obtained solid (4g, 6.1mmol) was dissolved in a mixture of THF/Ethanol (15ml/15ml), the hydrazine monohydrate (2.5g, 79.3 mmol) was added and the reaction was heated at 83ºC during 2h. The solvent was removed in vacuo and the residue was poured onto NaOH 1M (30ml). The mixture was extracted with DCM. The organic layer was dried with sodium sulfate and the solvent was removed in vacuo afforded 3,4 mg of a brown oil (92%). ^{1}H NMR (300 MHz, $CDCl_3$) δ 6.68 (s, $2H_a$), 3.87 (m, $4H_c$), 3.74 (s, $4H_b$), 1.75 (sep, J = 6.2 Hz, $2H_d$), 1.61 – 1.29 (m, $16H_{e,g,h,i,}$), 0.97 – 0.89 (m, $12H_{f,j}$), ^{13}C NMR (75 MHz, $CDCl_3$) δ 151.25, 150.14, 130.77, 112.20, 110.41, 70.66, 67.91, 42.71, 39.61, 30.72, 29.09, 25.58 , 24.12, 23.02 , 14.04, 11.17. MS m/z calculated for $C_{24}H_{44}N_2O_2$ 392.34 found MALDI TOF 392.4.

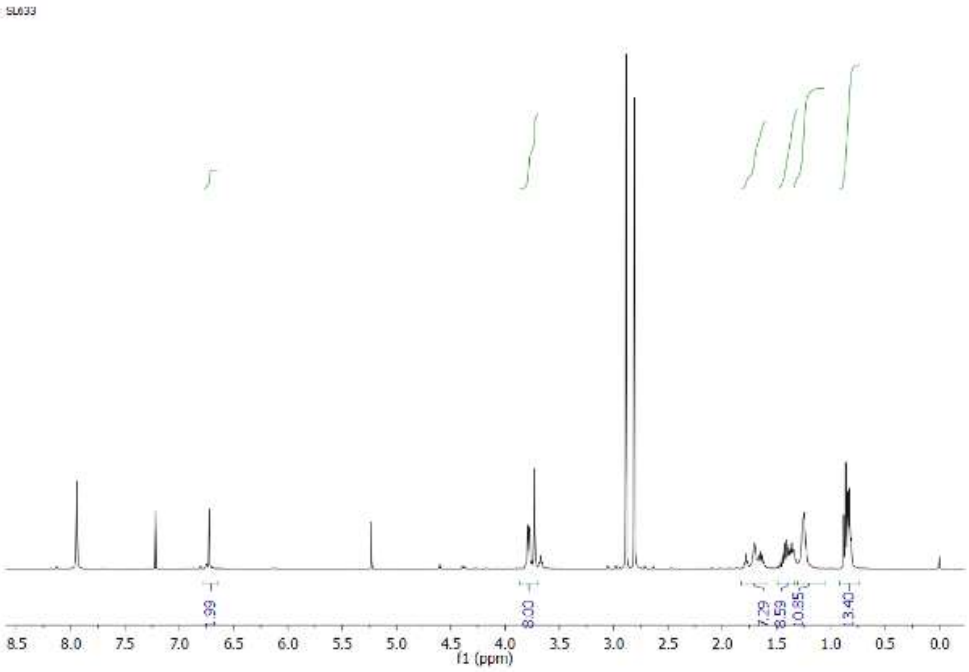
SL033
1.99
8.00
7.29
8.59
10.35
13.40
8.5 8.0 7.5 7.0 6.5 6.0 5.5 5.0 4.5 4.0 3.5 3.0 2.5 2.0 1.5 1.0 0.5 0.0
f1 (ppm)

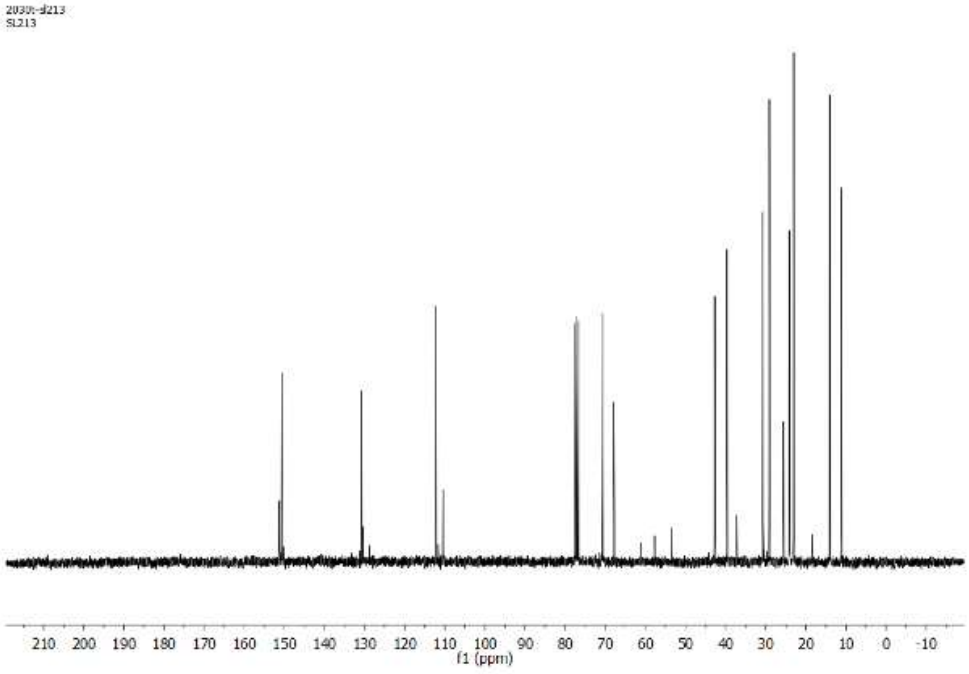
2030-sl213
SL213
210 200 190 180 170 160 150 140 130 120 110 100 90 80 70 60 50 40 30 20 10 0 -10
f1 (ppm)

General procedure Synthesis linear receptor

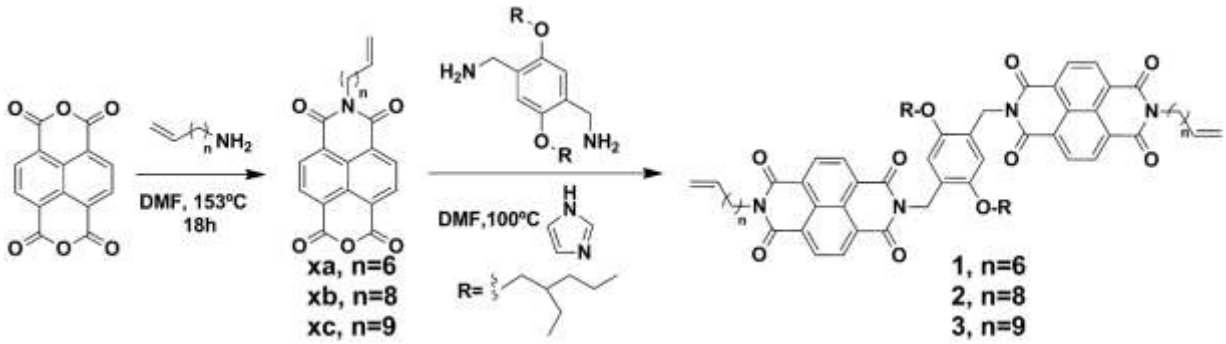

The compounds **13 a-c** were synthetized as described in *J. Phys. Chem*. **2001**, *105*, 7216-7219.

Compound 13 a-c:

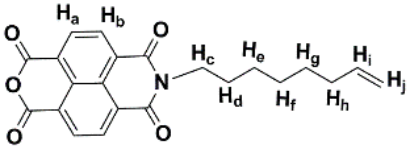

Compound 13a: ^{1}H NMR (300MHz, $CDCl_3$) δ 8.83 (s, $4H_{a,b}$), 5.65 (m, $1H_j$), 4.97 (m, $2H_i$), 4.17 (m, $2H_c$), 2.08 (m, $2H_h$), 1.76 (m, $2H_d$),1,33 (m, $6H_{e,f,g}$), ^{13}C NMR (75 MHz, $CDCl_3$) δ 162.04 (C=O), 158.51 (C=O), 139.11, 133.13, 130.80, 128.77 , 127.91, 126.84 , 122.81, 114.01, 41.15, 33.64, 28.50, 27.95, 26.88. MS m/z calculated for $C_{22}H_{19}NO_5$ 377.1 found MALDI TOF 377.2.

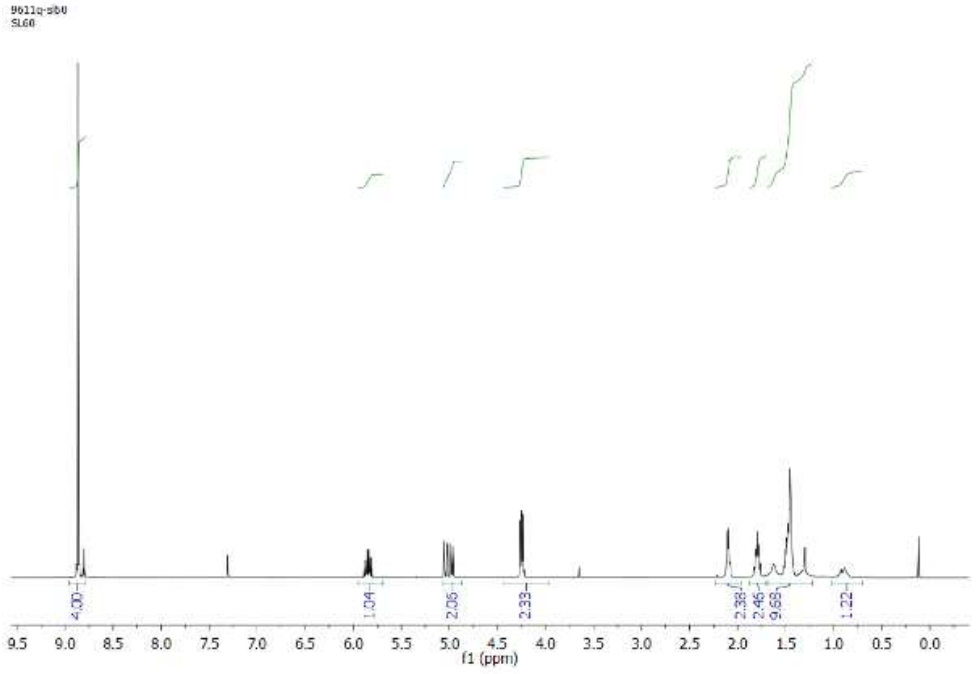

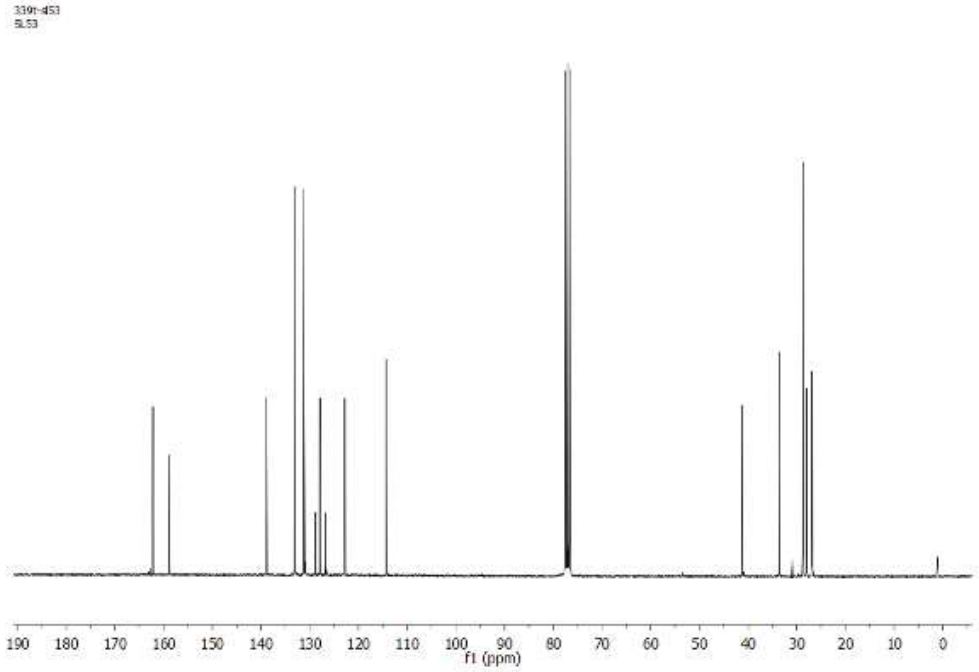

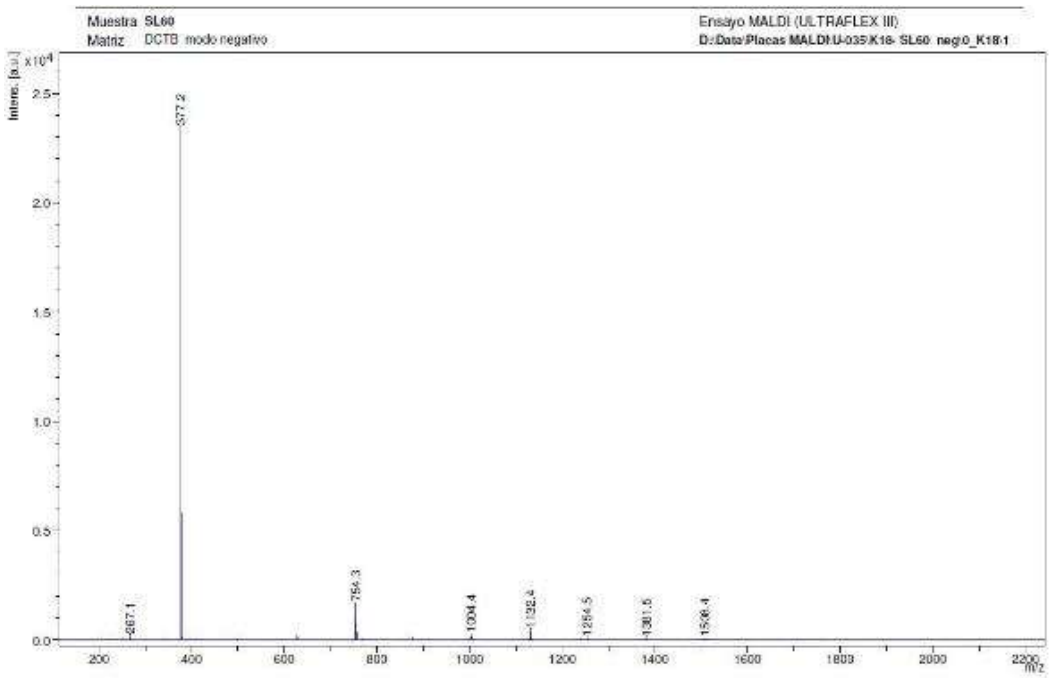

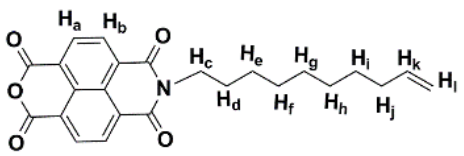

Compound 13b: ^{1}H NMR (300 MHz, $CDCl_3$) δ 8.84 (s, $4H_{a,b}$), 5.83 (m, $1H_k$), 4.83 (m, $2H_l$), 4.22 (m, $2H_c$), 2.06 (m, $2H_j$), 1.77 (m, $2H_d$), 1.36 (m, $10H_{e,f,g,h,i}$),^{13}C NMR (75 MHz, $CDCl_3$) δ 162.18 (C=O), 158.82 (C=O), 139.13, 133.13, 131.18, 128.86, 127.93, 126.84, 122.80, 114.15, 53.42, 41.19, 33.75, 28.00, 27.02. MS m/z calculated for $C_{24}H_{23}NO_5$ 405.1576 found HR-MS 406.1657.

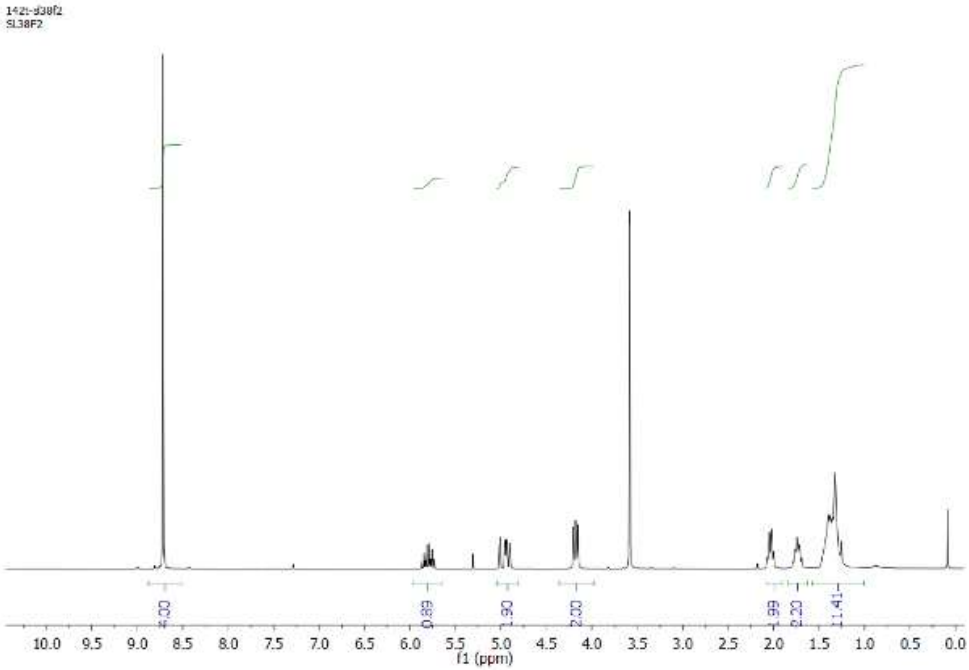
1421-s38f2
SL38F2
4.00
0.89
1.90
2.00
1.99
2.20
11.41
10.0 9.5 9.0 8.5 8.0 7.5 7.0 6.5 6.0 5.5 5.0 4.5 4.0 3.5 3.0 2.5 2.0 1.5 1.0 0.5 0.0
f1 (ppm)

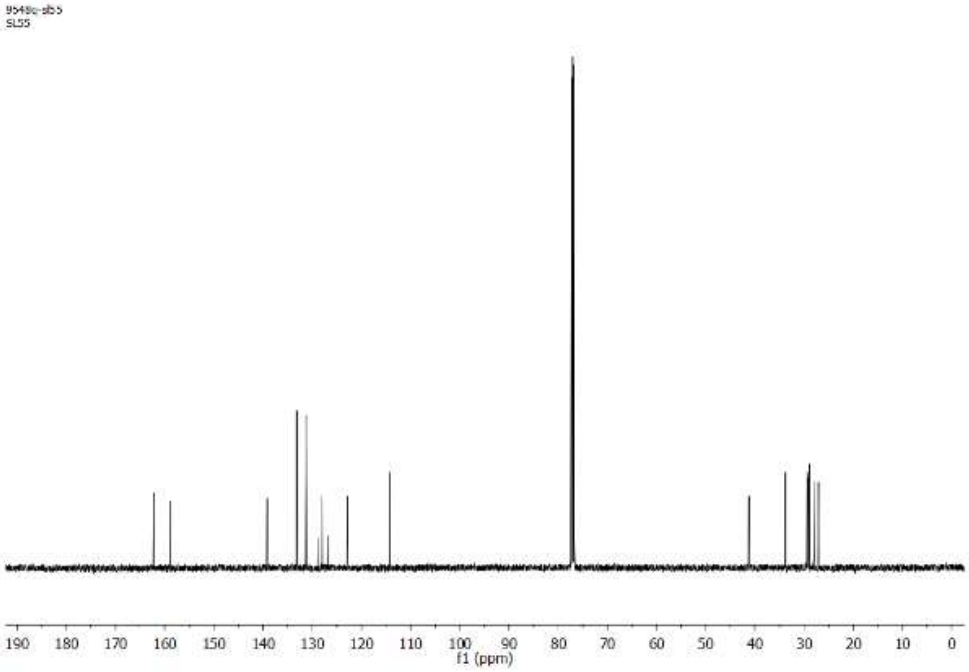
9548c-sb5
SL55
190 180 170 160 150 140 130 120 110 100 90 80 70 60 50 40 30 20 10 0
f1 (ppm)

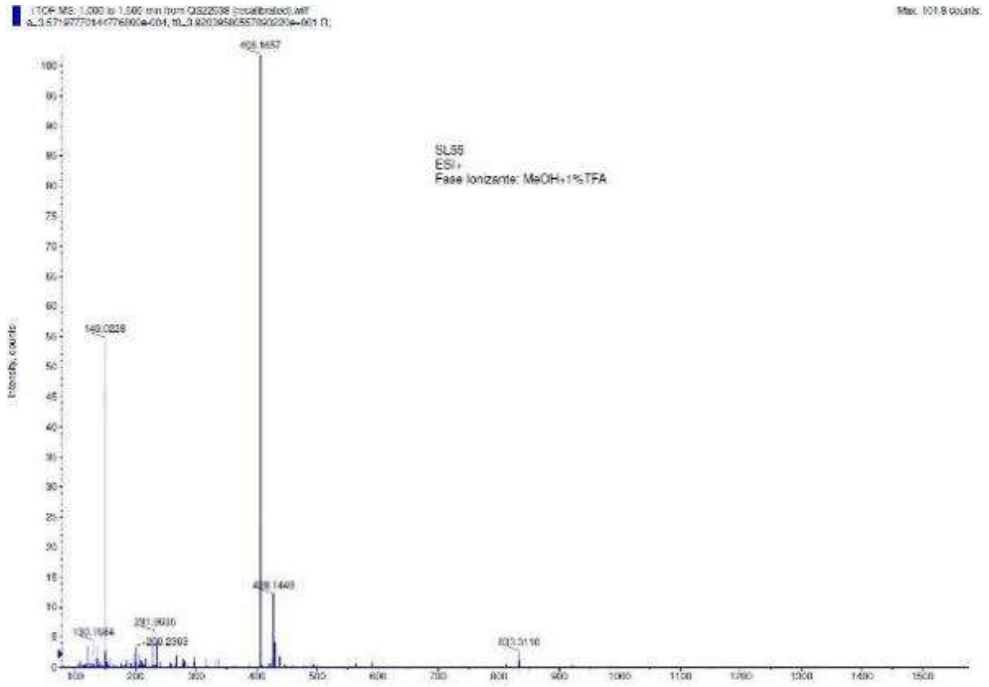

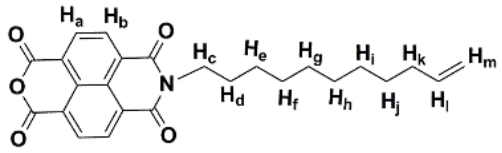

Compound 13c: ^{1}H NMR (300 MHz, $CDCl_3$) δ 8.98 (s, $4H_{a,b}$), 5.81 (m, $1H_l$), 4.84 (m, $2H_m$), 4.21 (m, $2H_c$), 2.09 (m, $2H_k$), 1.75 (m, $2H_d$), 1.53 (m, 12H $_{e,f,g,h,i,j}$),^{13}C NMR (75 MHz, $CDCl_3$) δ 162.35 (C=O), 158.83 (C=O), 139.09, 133.12, 131.18, 128.79, 127.92, 126.83, 122.80, 114.01, 41.19, 33.77, 30.90, 29.39, 29.24, 29.06 (s), 28.88 (s), 28.00, 27.02. MS m/z calculated for $C_{25}H_{25}NO_5$ 419.1733 found HR-MS 420.1789.

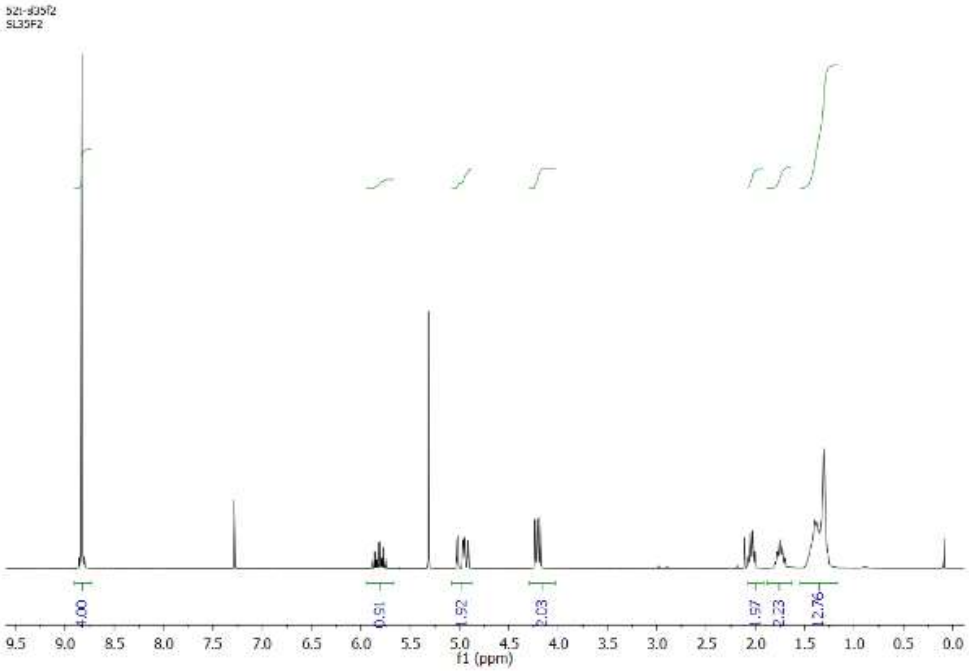
521-d35f2
SL35F2
4.00
0.51
1.92
2.03
1.97
2.23
2.76
9.5 9.0 8.5 8.0 7.5 7.0 6.5 6.0 5.5 5.0 4.5 4.0 3.5 3.0 2.5 2.0 1.5 1.0 0.5 0.0
f1 (ppm)

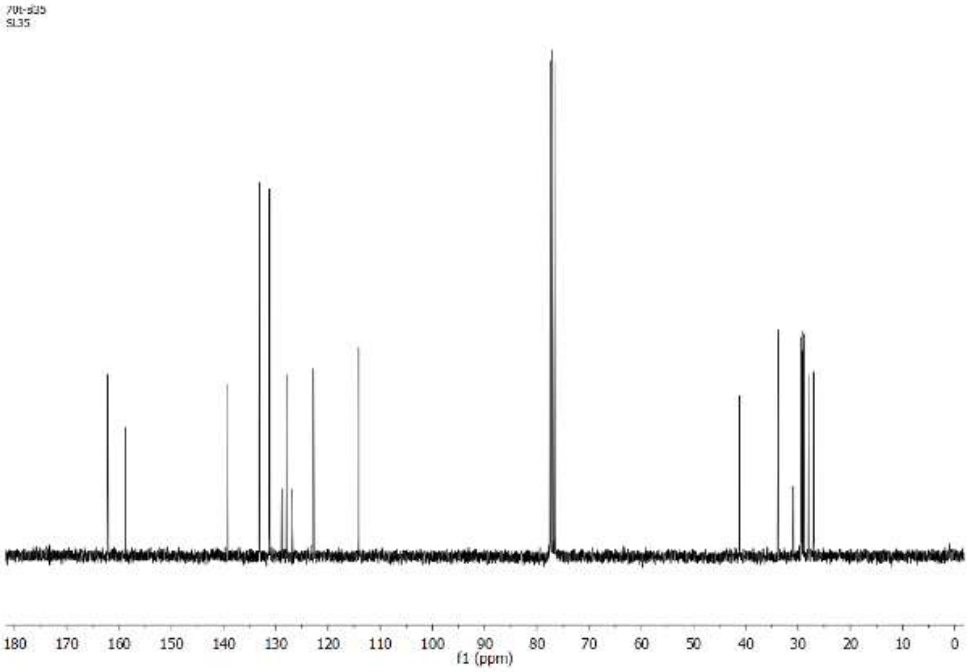
701-d35
SL35
180 170 160 150 140 130 120 110 100 90 80 70 60 50 40 30 20 10 0
f1 (ppm)

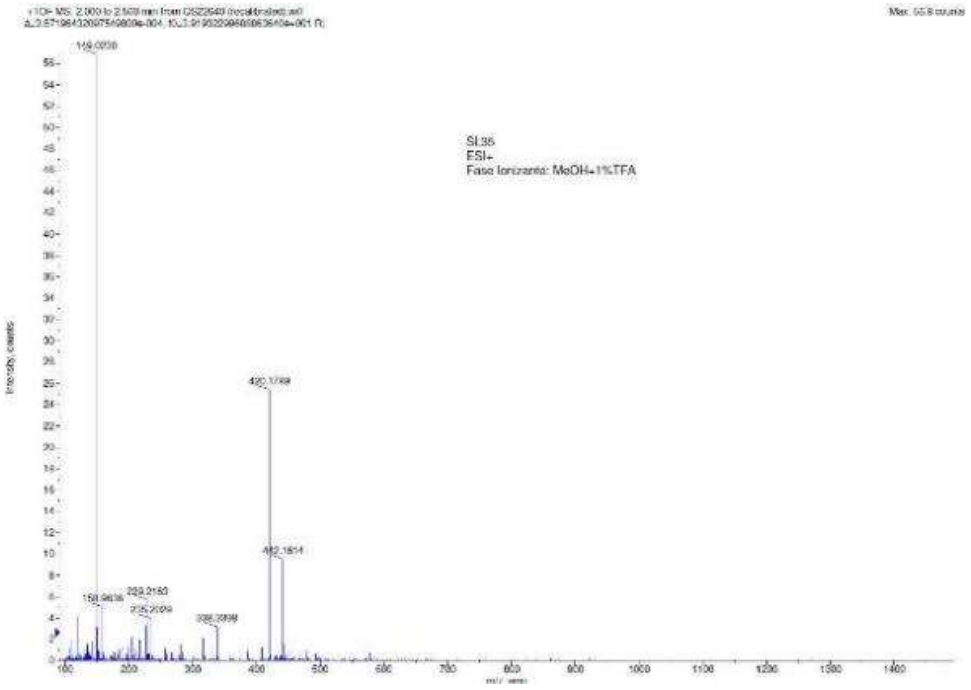

Compound 1-3: The previously obtained solid (200 mg, 0.47 mmol) was dissolved N, N-dimethylformamide (8ml), the imidazole (630 mg, 9.4 mmol) and the compound **12** (92mg, 0.23mmol) were added and the mixture was stirred at 130^{0}C during 5 h. The reaction was cooled to room temperature and it was poured onto HCl 1M. The solid was filtered and the crude was purified by Flash chromatography on silica (eluent: DCM) afforded a pink solid (76-80 %).

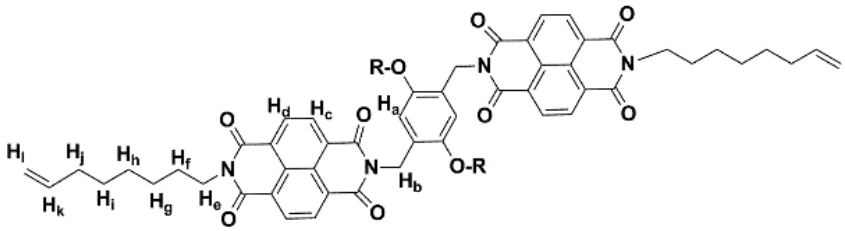

Compound 1: ^{1}H NMR (300 MHz, $CDCl_3$) δ 8.54 (m, 8H$_{c,d}$), 6.77 (s, 2H$_a$), 5.82 (m, 2H$_k$),5.40 (s, 4H$_b$) 4.97 (m, 4H$_l$), 4.42 (t, J = 5.6 Hz, 4H$_e$), 3.73 (m, 4H$_R$), 2.04 (m, 4H$_j$), 1.71 (m, 2H$_R$), 1.61 (m, 4H$_f$), 1.58 (m, 16H$_R$), 1.26 (m, 12H$_{g,h,i}$), 0.81 (12H$_R$), ^{13}C NMR (75 MHz, $CDCl_3$) δ 162.80 (C=O), 162.68 (C=O), 150.76, 138.95, 131.04, 130.92, 126.71, 126.66, 124.47, 114.28, 112.81, 77.43, 77.21, 77.01, 76.59, 71.48, 40.94, 39.75, 39.48, 33.66, 30.39, 28.99, 28.75, 28.02, 26.92, 23.73, 22.98, 14.02, 11.13. MS m/z calculated for $C_{68}H_{78}N_4O_{10}$ 1110.5718 found HR-MS 1110.5882. ε (λ_{max}=380) = 25555 $M^{-1}cm^{-1}$.

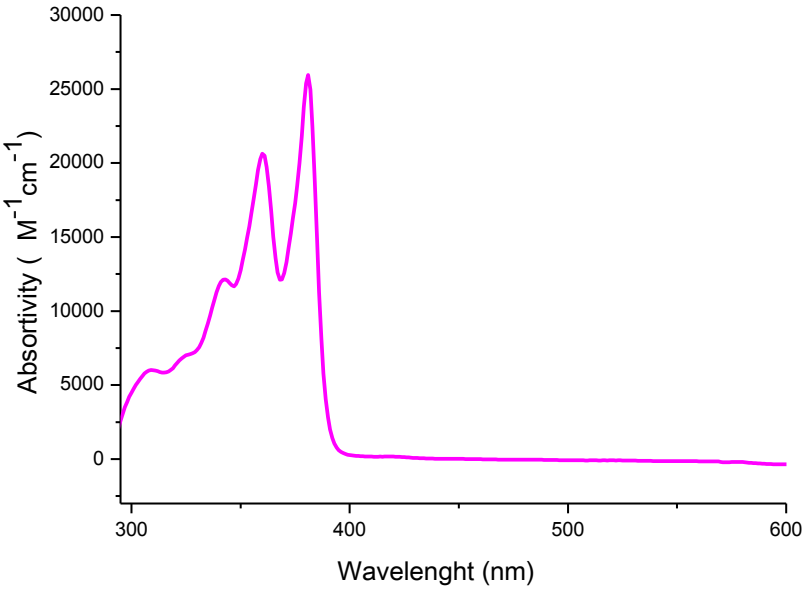
30000
25000
20000
15000
10000
5000
0
Absortivity (M-1cm-1)
300
400
500
600
Wavelenght (nm)

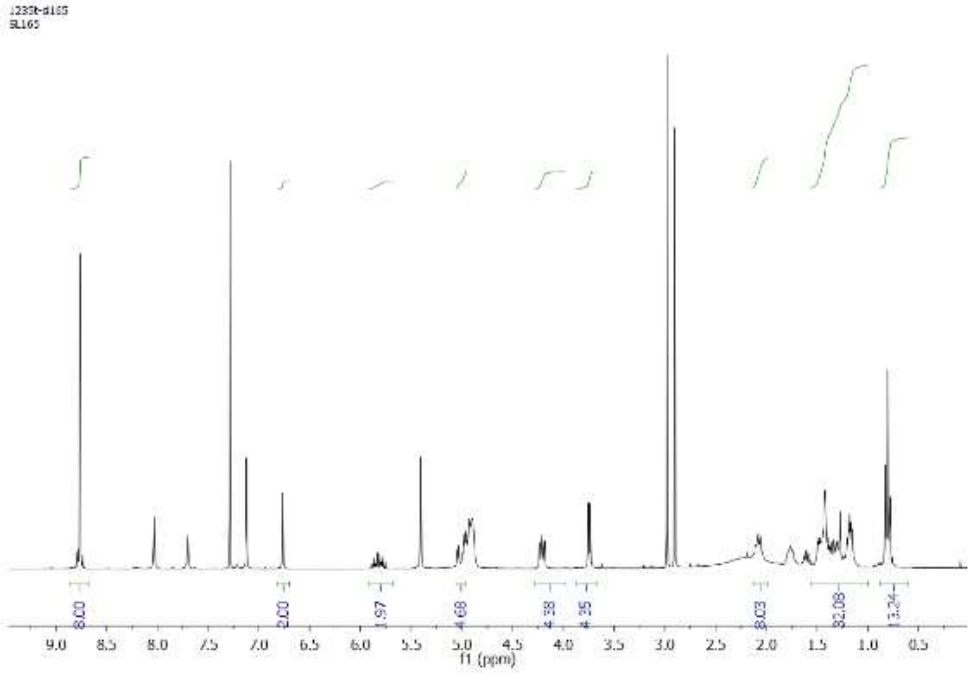
8.00
2.00
1.97
4.68
4.38
4.35
8.03
32.08
13.24
9.0
8.5
8.0
7.5
7.0
6.5
6.0
5.5
5.0
4.5
4.0
3.5
3.0
2.5
2.0
1.5
1.0
0.5
f1 (ppm)

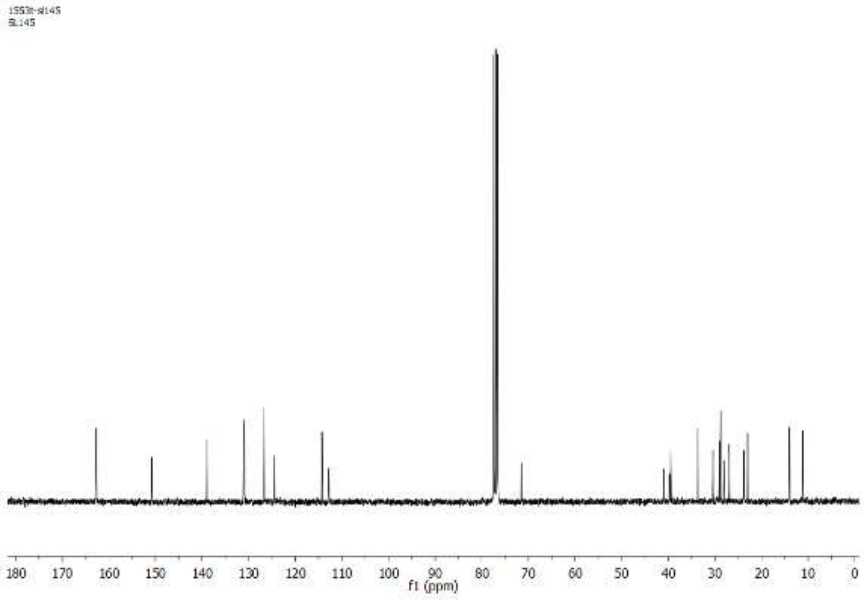

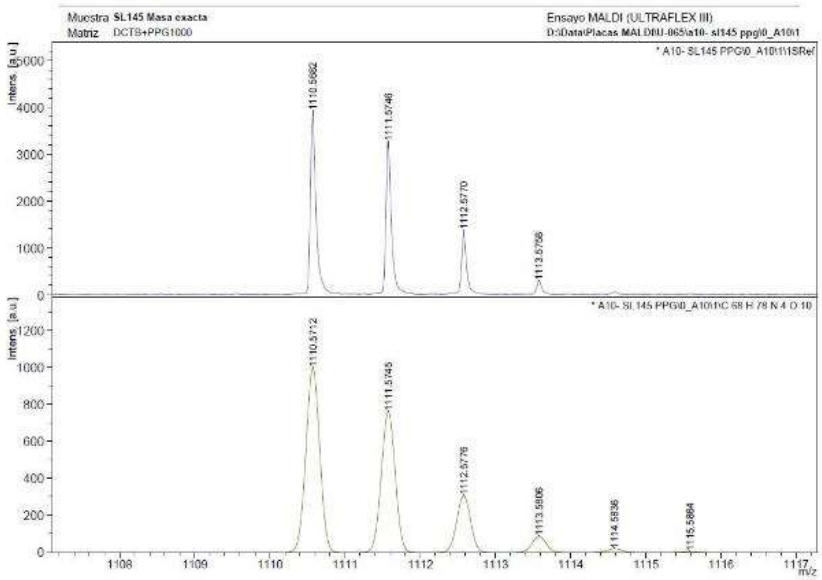

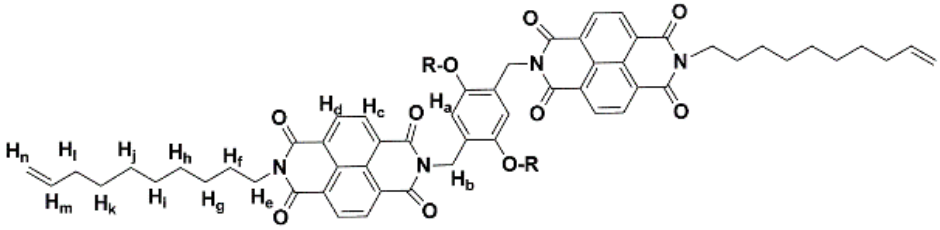

Compound 2: ^{1}H NMR (300 MHz, $CDCl_3$) δ 8.79 (m, 8$H_{c,d}$), 6.79 (s, 2H_a), 5.85 (m, 2H_m), 5.43 (s, 4H_b), 4.84 (m, 4H_n), 4.29 (d, J = 5.6 Hz, 4H_e), 3.65 (m, 4H_R), 2.08 (m, 4H_j), 1.78 (m, 2H_R), 1.63 (m, 4H_f), 1.57 (m, 16H_R), 1.28 (m, 20$H_{g,h,i,j,k}$), 0.84 (12H_R), ^{13}C NMR (75 MHz, $CDCl_3$) δ 162.83 (C=O), 162.71 (C=O), 150.78, 139.18, 131.01, 127.57, 125.83, 124.49, 114.16, 112.82, 71.50, 41.00, 39.77, 39.50, 33.79, 30.41, 29.36, 29.27, 29.06, 29.01, 28.89, 28.09, 27.08, 23.75, 23.00, 14.05, 11.15. MS m/z calculated for $C_{72}H_{86}N_4O_{10}$ 1166. 6344 found HR-MS 1166.6338. ε (λ_{max}=380nm) = 22399 $M^{-1}cm^{-1}$.

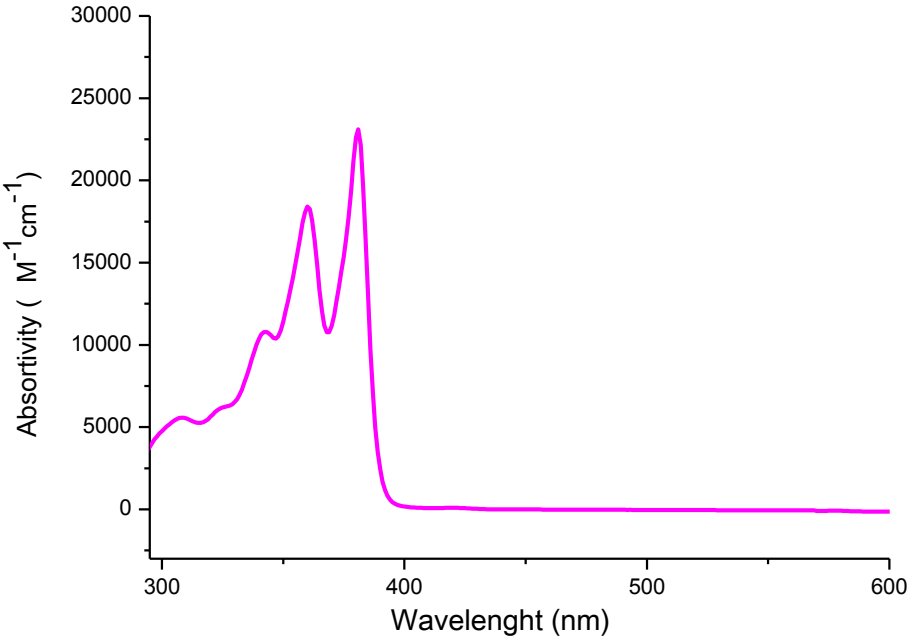
30000
25000
20000
15000
10000
5000
0
Absortivity (M-1cm-1)
300
400
500
600
Wavelenght (nm)

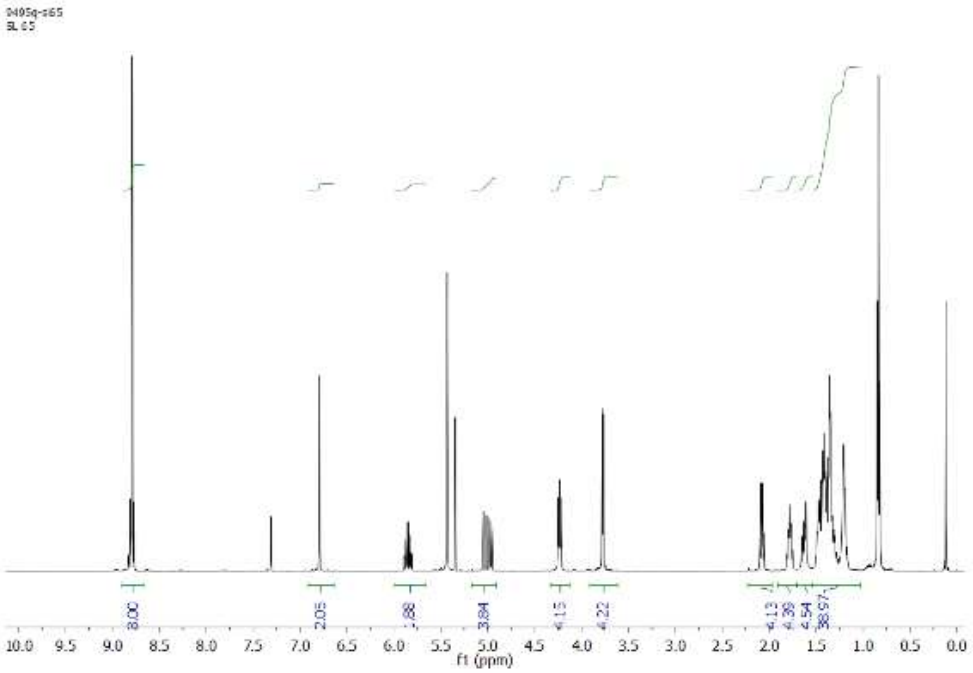
8.00
2.05
2.88
3.84
4.15
4.22
10.0
9.5
9.0
8.5
8.0
7.5
7.0
6.5
6.0
5.5
5.0
4.5
4.0
3.5
3.0
2.5
2.0
1.5
1.0
0.5
0.0
f1 (ppm)

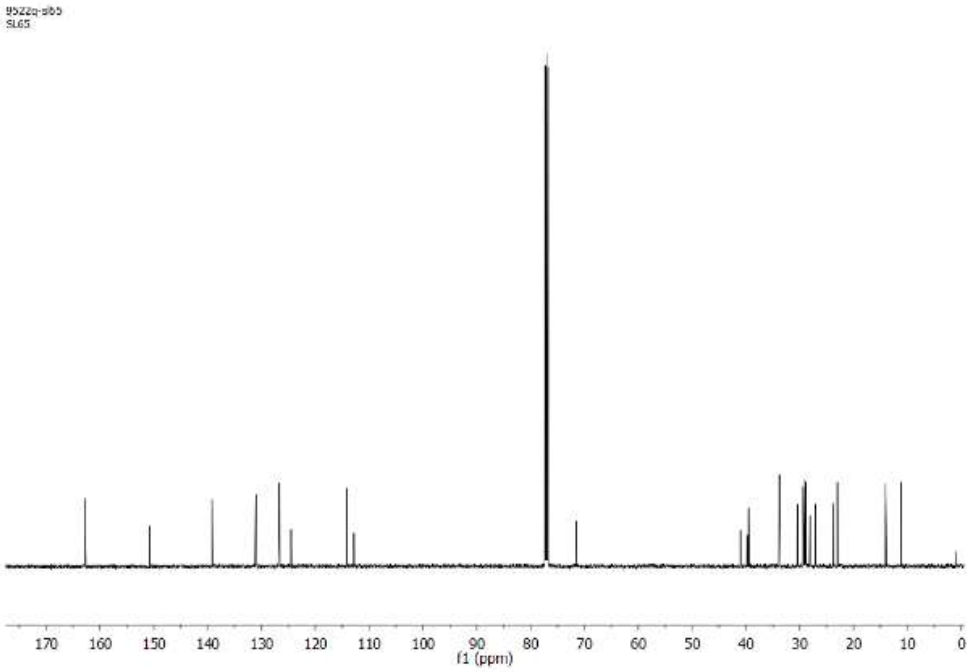

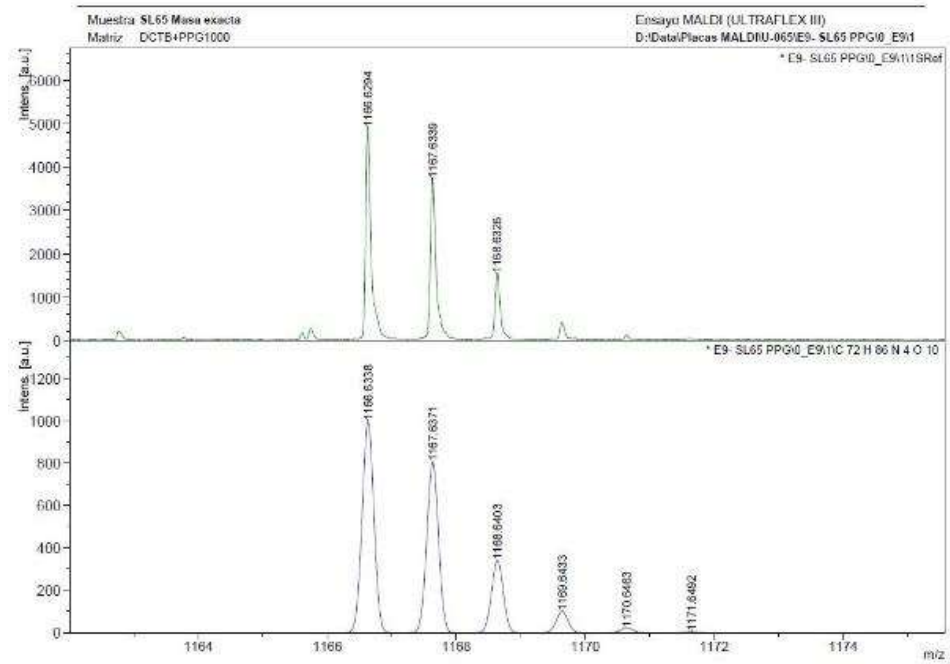

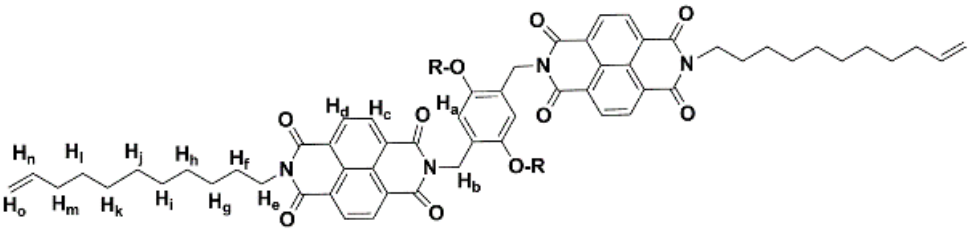

Compound 3: ^{1}H NMR (300 MHz, $CDCl_3$) δ 8.79 (s, 8$H_{c,d}$), 6.77 (s, 2H_a), 5.83 (m, 2H_n), 5.42 (s, 4H_b), 4.41 (m, 4H_o), 4.21(d, J = 5.6 Hz, 4H_e), 3.76 (m, 4H_R), 2.04 (m, 4H_j), 1.76 (m, 2H_R), 1.61 (m, 4H_f), 1.38 (m, 16H_R), 1.17(m, 24$H_{g,h,i,j,k,l}$), 0.81 (12H_R), ^{13}C NMR (75 MHz, $CDCl_3$) δ 162.75 (C=O),

150.75, 139.20, 130.99, 126.70, 124.47, 114.10, 112.80, 71.48, 40.99, 39.75, 39.48, 33.79, 30.39, 28.08, 27.06, 23.73, 22.97, 14.02, 11.13. MS m/z calculated for $C_{74}H_{90}N_4O_{10}$ 1194.6657 found HR-MS 1194.6598. ε (λ_{max}=380nm) = 22355 $M^{-1}cm^{-1}$.

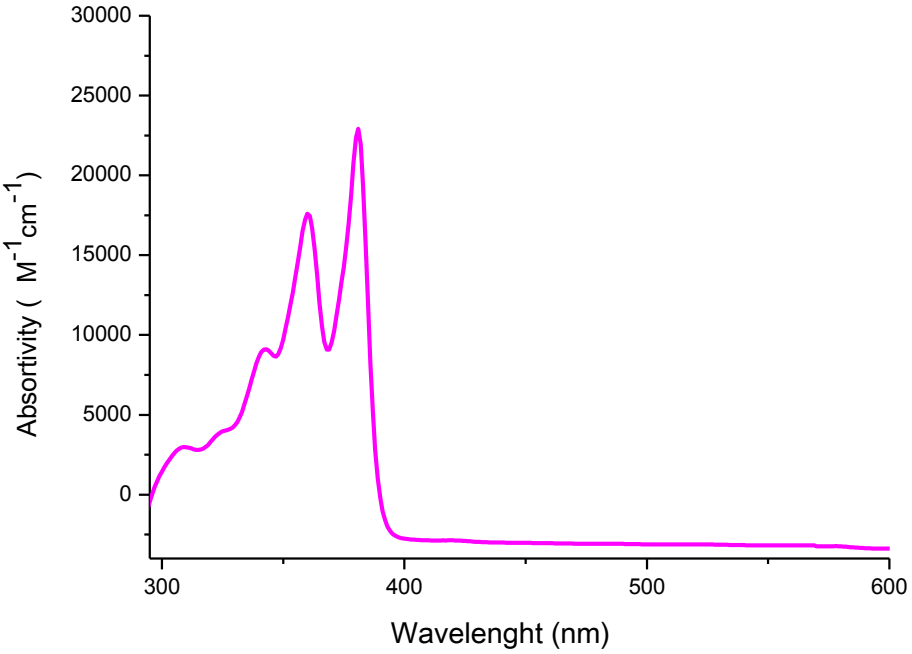

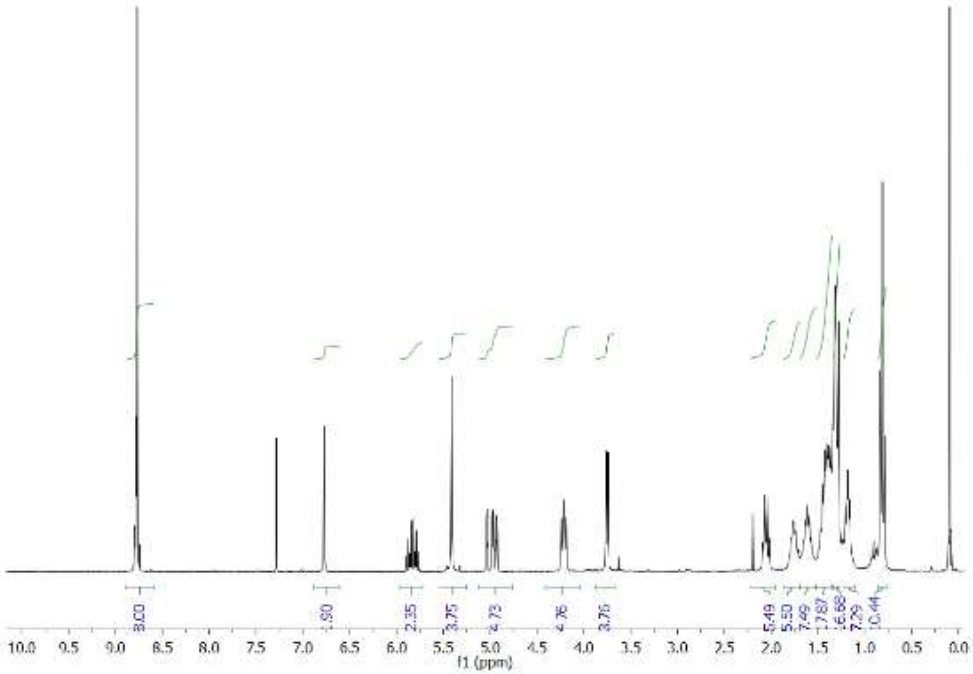

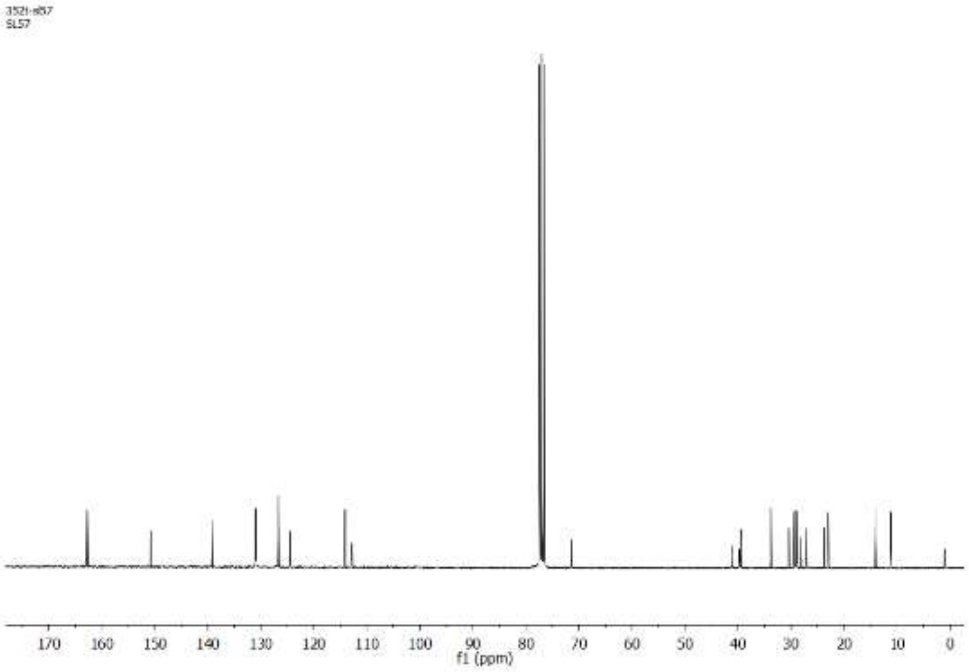
352l-s57
SL57
170 160 150 140 130 120 110 100 90 80 70 60 50 40 30 20 10 0
f1 (ppm)

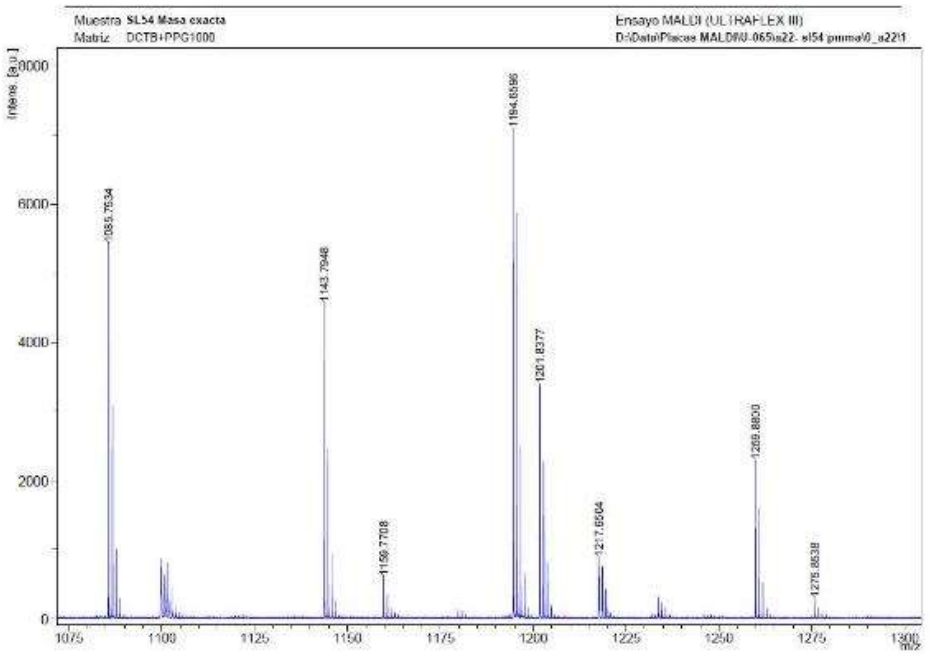
Muestra SL54 Masa exacta
Matriz DCTB+PPG1000
Ensayo MALDI (ULTRAFLEX III)
D:\Data\Placas MALDI\0-065\s22- sl54 pnrma\0_a221
Intens. [a.u.]
8000
6000
4000
2000
0
1085.7634
1143.7948
1159.7708
1184.6586
1201.8377
1217.6504
1269.8800
1276.8538
1075 1100 1125 1150 1175 1200 1225 1250 1275 1300
m/z

General procedure for the metathesis reaction.

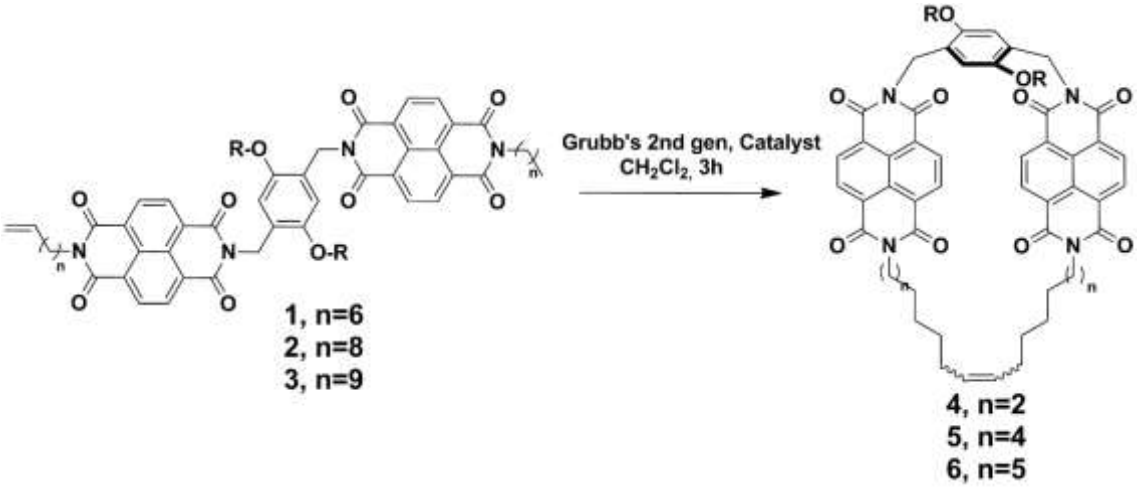

A 10^{-4} M solution of linear receptor **4-6** was prepared in dichloromethane and was degassed by nitrogen bubbling during 30 minutes. Then, a catalytic amount of Grubb's 2nd generation catalyst was introduced and the mixture was stirred for three hours at room temperature. The mixture was filtered on celite and concentrated in vacuo. The desired macrocycles were finally isolated by silica gel chromatography (eluent: CH_2Cl_2) afforded a pink solid in 82-85% yield.

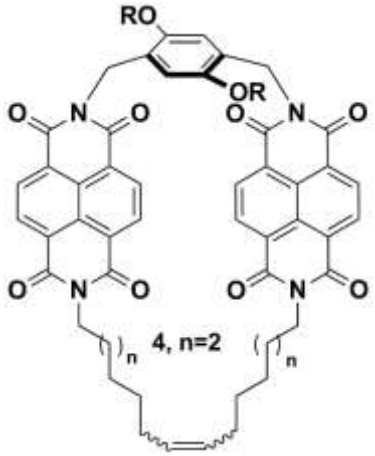

Compound 4: ^{1}H NMR (300 MHz, $CDCl_3$) δ 8.72 (m, 8H), 6.91 (s, 2H), 5.24 (m, 2H), 4.23 (m, 4H), 3.73 (m, 4H), 1.84 (m, 12H), 1.41 (m, 28H), 1.08 (m, 14H). ^{13}C NMR (75 MHz, $CDCl_3$) δ 162.80 (C=O), 162.41 (C=O), 150.98, 130.83, 130.79, 130.74, 129.90, 126.85, 126.58, 126.52, 126.28, 125.03, 115.20, 72.09, 53.41, 40.73, 39.45, 39.35, 32.63, 30.25, 29.48, 29.32, 28.99, 28.00, 26.71, 23.64, 23.00, 22.35, 14.09, 11.08. MS m/z calculated for $C_{66}H_{74}N_4O_{10}$ 1082.5405 found HR-MS 1082.5359. ε (λ_{max}=380nm) = 20210 $M^{-1}cm^{-1}$.

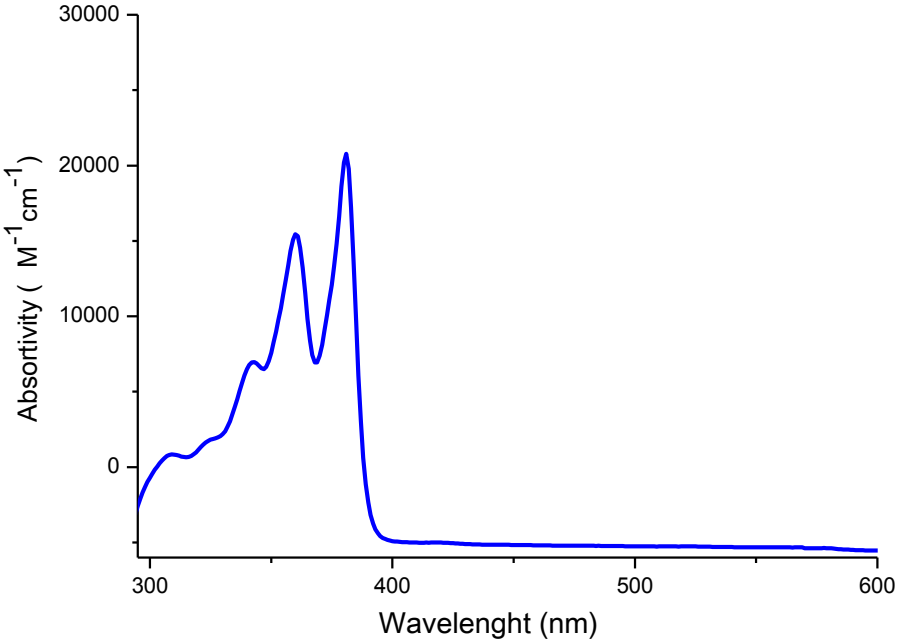
30000
20000
10000
0
Absortivity (M-1cm-1)
300
400
500
600
Wavelenght (nm)

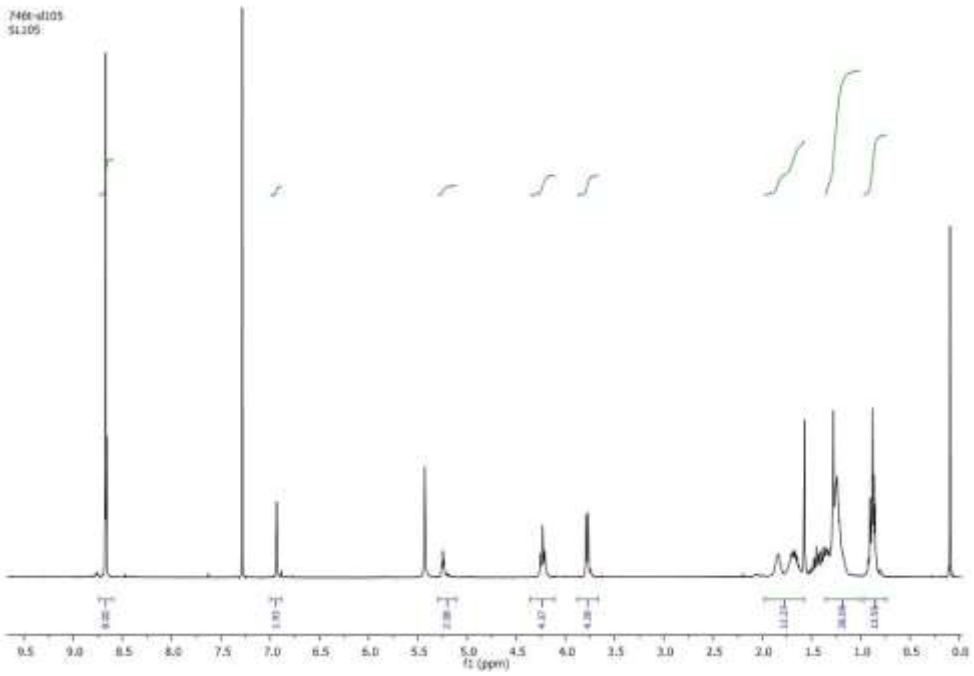

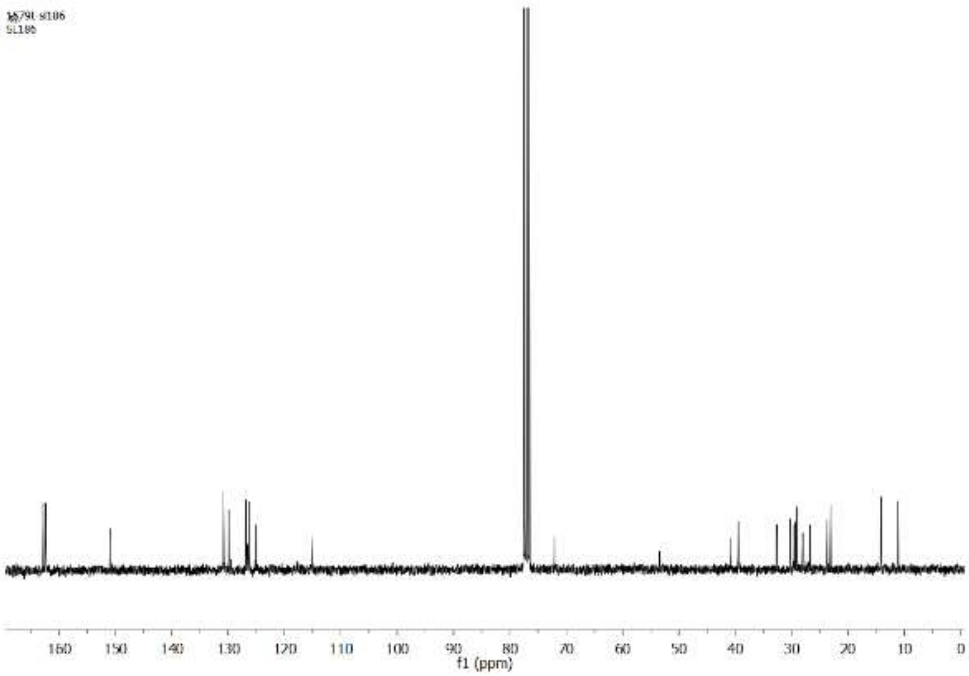
160
150
140
130
120
110
100
90
80
70
60
50
40
30
20
10
0
f1 (ppm)

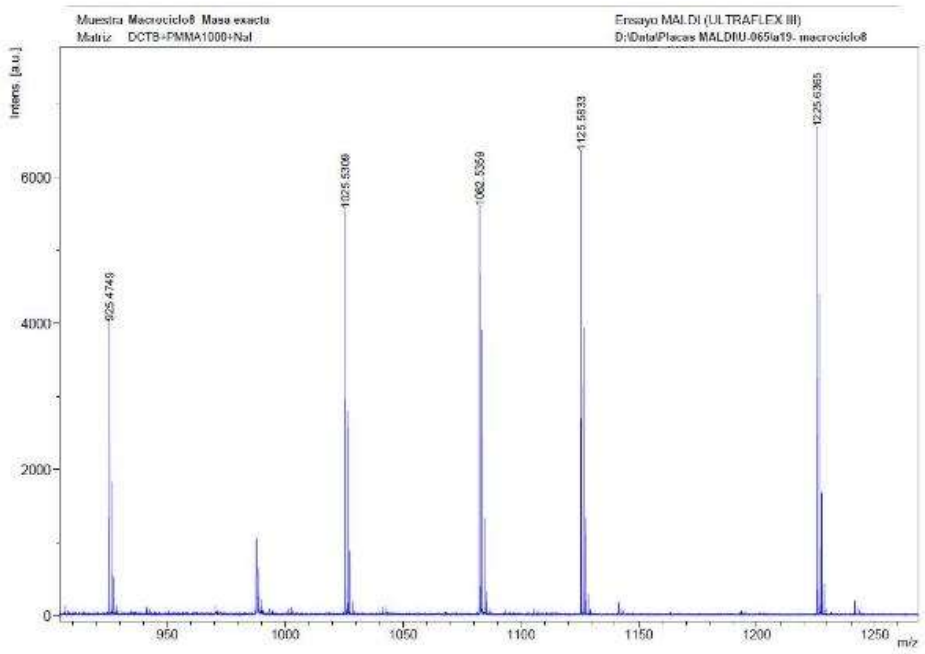
Muestra Macrociclo8 Masa exacta
Matriz DCTB+PMMA1000+NaI
Ensayo MALDI (ULTRAFLEX III)
D:\Data\Placas MALDI\U-065\a19- macrociclo8
Intens. [a.u.]
6000
4000
2000
0
925.4748
1025.5306
1082.5359
1125.5833
1225.6365
950
1000
1050
1100
1150
1200
1250
m/z

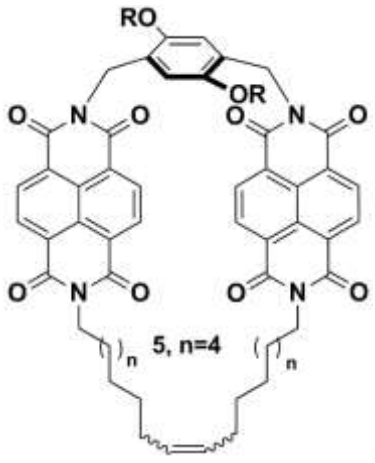
RO
OR
O
N
O
5, n=4
n

Compound 5: ^{1}H NMR (300 MHz, $CDCl_3$) δ 8.87 (s, 8H), 6.86 (s, 2H), 5.32 (m, 2H), 4.21 (m, 4H), 3.78 (m, 4H), 1.88 (m, 4H), 1.57 (m, 2H), 1.55 (m, 44H), 1.00 (m, 12H), ^{13}C NMR (75 MHz, $CDCl_3$) δ 162.79 (C=O), 162.48 (C=O), 150.88, 130.85, 130.08, 126.79, 126.4, 124.61, 71.77, 40.83, 39.86, 39.43, 32.50, 30.91, 30.27, 29.64, 29.40, 29.30, 29.11, 28.96, 28.02, 26.88, 23.63, 22.99, 14.05, 11.08. MS m/z calculated for $C_{70}H_{82}N_4O_{10}$ 1138.6031 found HR-MS 1138.5971. ε (λ_{max}=380nm) = 19955 $M^{-1}cm^{-1}$.

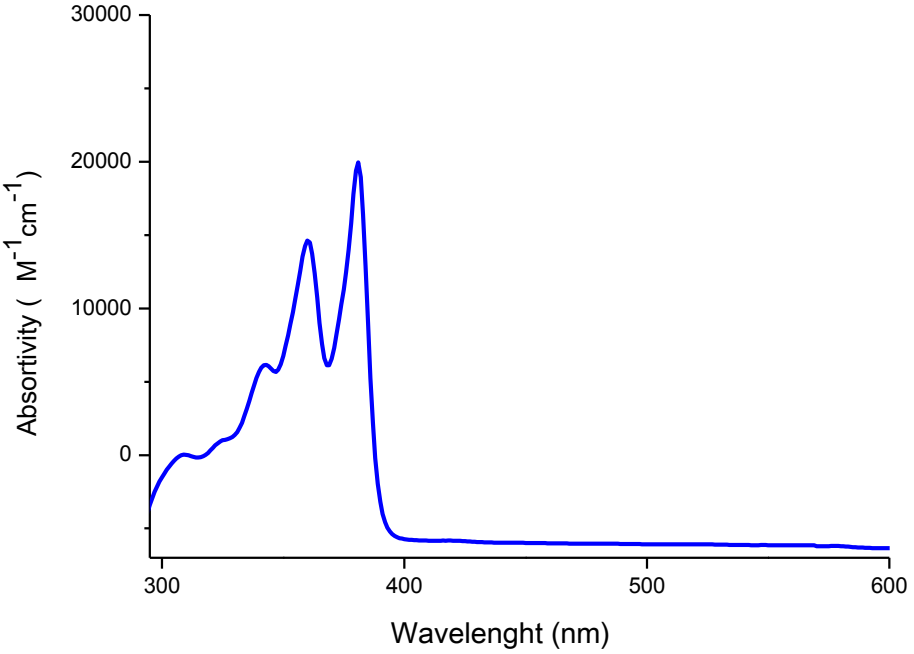

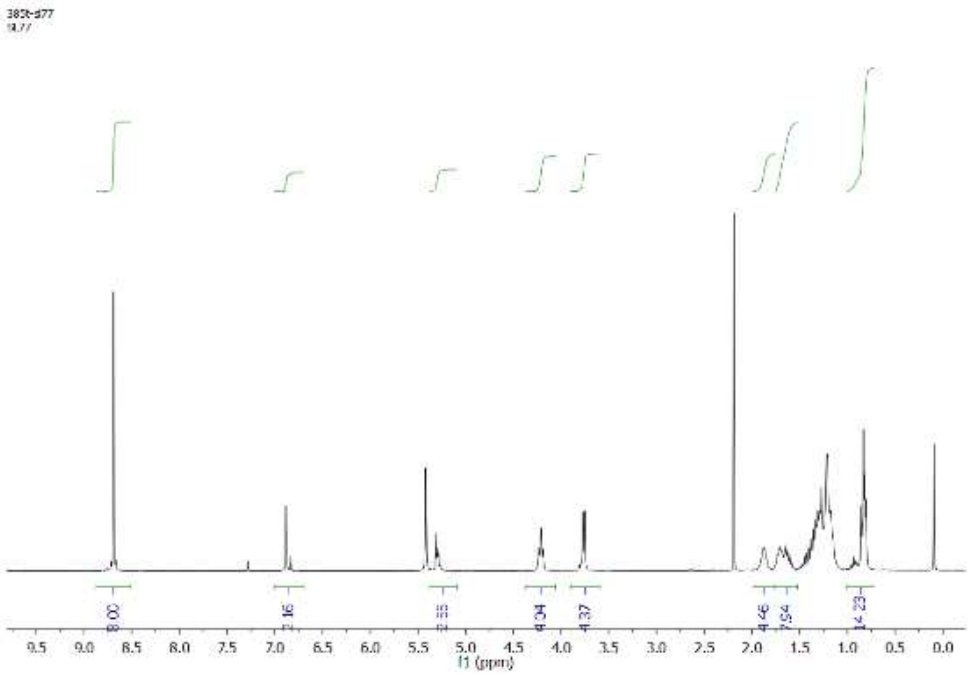

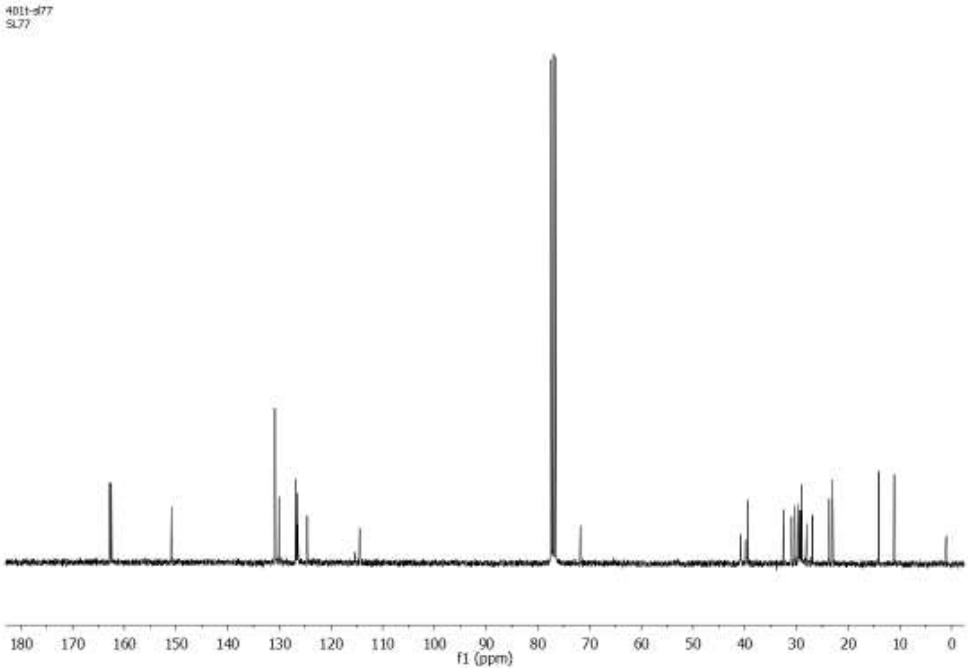
401t-sl77
SL77
180 170 160 150 140 130 120 110 100 90 80 70 60 50 40 30 20 10 0
f1 (ppm)

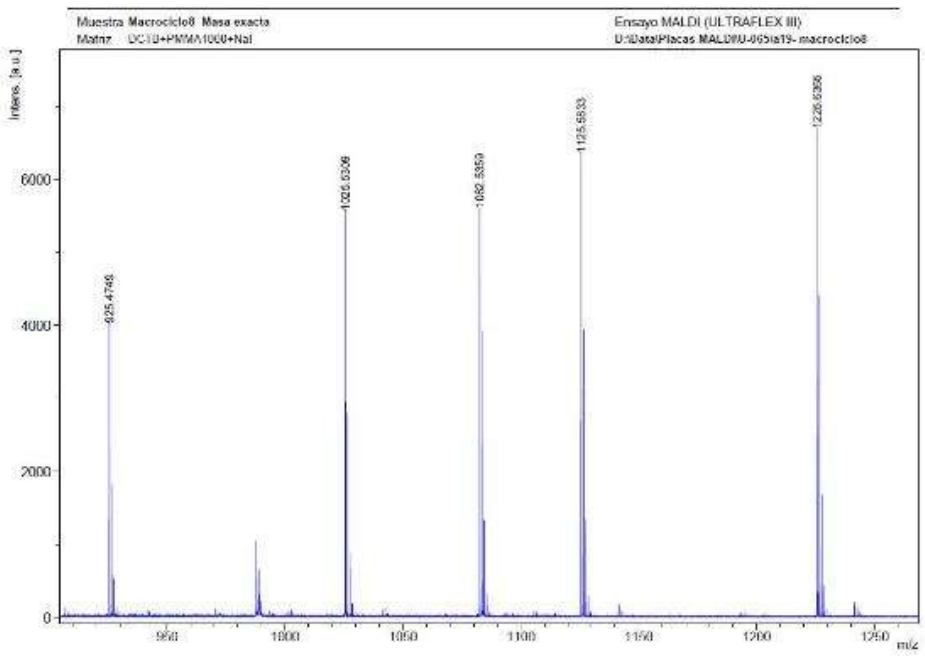
Muestra Macrociclo8 Masa exacta
Matriz DCTB+PMMA1000+NaI
Ensayo MALDI (ULTRAFLEX III)
D:\Data\Placas MALDI\U-065\a19- macrociclo8
Intens. [a.u.]
6000
4000
2000
0
925.4748
1026.6309
1082.5859
1125.5833
1226.6386
950
1000
1050
1100
1150
1200
1250
m/z

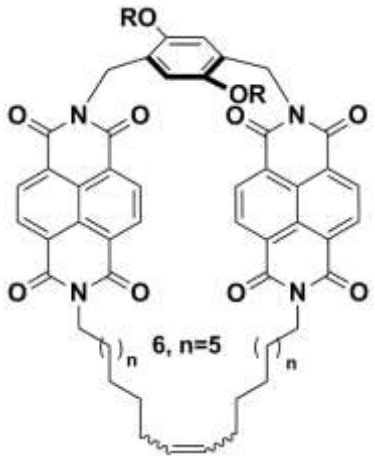
RO
OR
O
N
O
6, n=5
n

Compound 6: ^{1}H NMR (300 MHz, $CDCl_3$) δ 8.78 (m, 8H), 6.90 (s, 2H), 5.36 (m, 2H), 4.24 (m, 4H), 3.78 (m, 4H), 1.90 (m, 4H), 1.77 (m, 2H), 1.53 (m, 48H), 1.04 (m, 12H), ^{13}C NMR (75 MHz, $CDCl_3$) δ 162.84 (C=O), 162.55 (C=O), 130.89, 130.27, 126.79, 126.51, 77.32, 77.21, 77.00, 76.69, 39.43, 32.55, 30.28, 29.43, 29.29, 29.14, 28.96, 28.90, 26.82, 23.63, 22.98, 14.04, 11.08. MS m/z calculated for $C_{72}H_{86}N_4O_{10}$ 1166.6344 found HR-MS 1166.6295. ε (λ_{max}=380nm)= 19066 $M^{-1}cm^{-1}$.

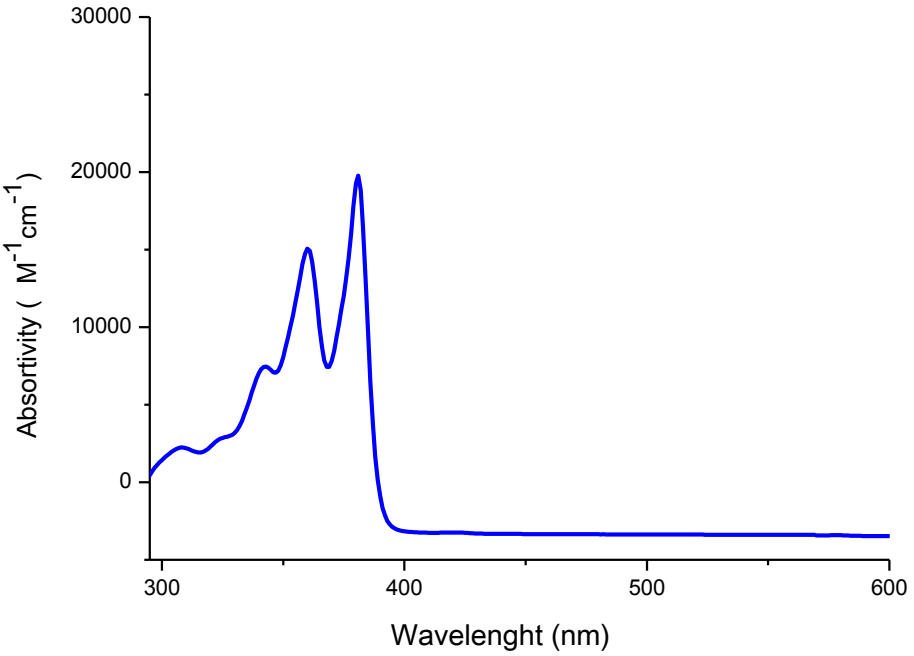

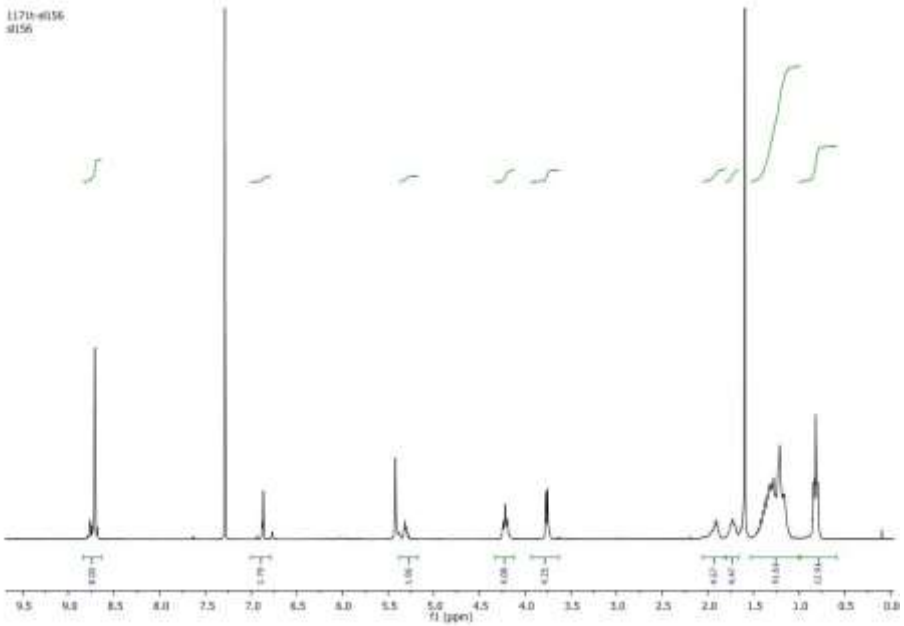

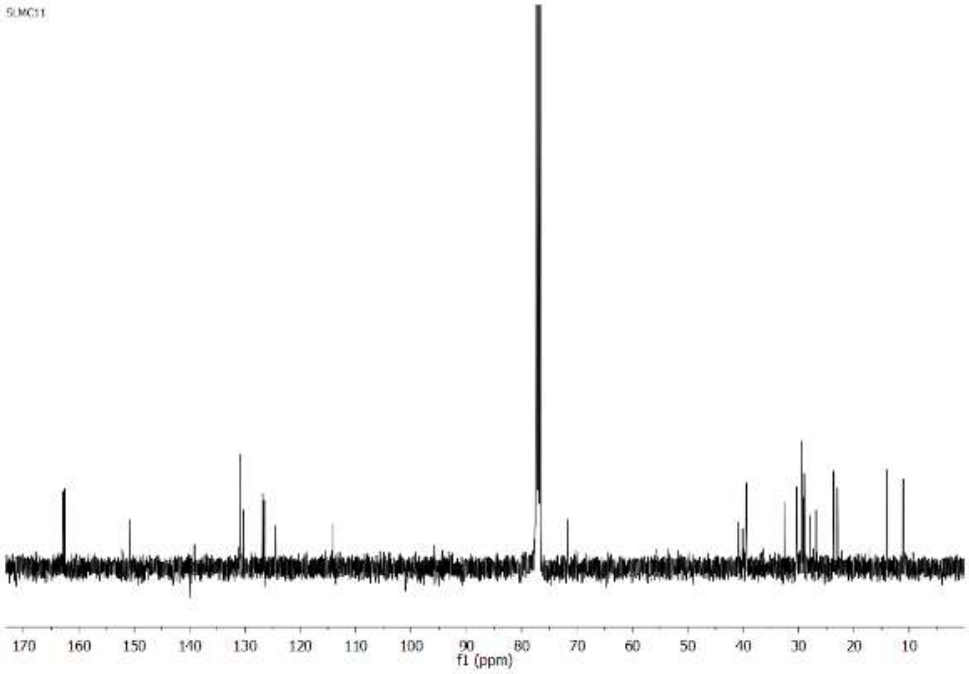
SLMC11
170
160
150
140
130
120
110
100
90
80
70
60
50
40
30
20
10
f1 (ppm)

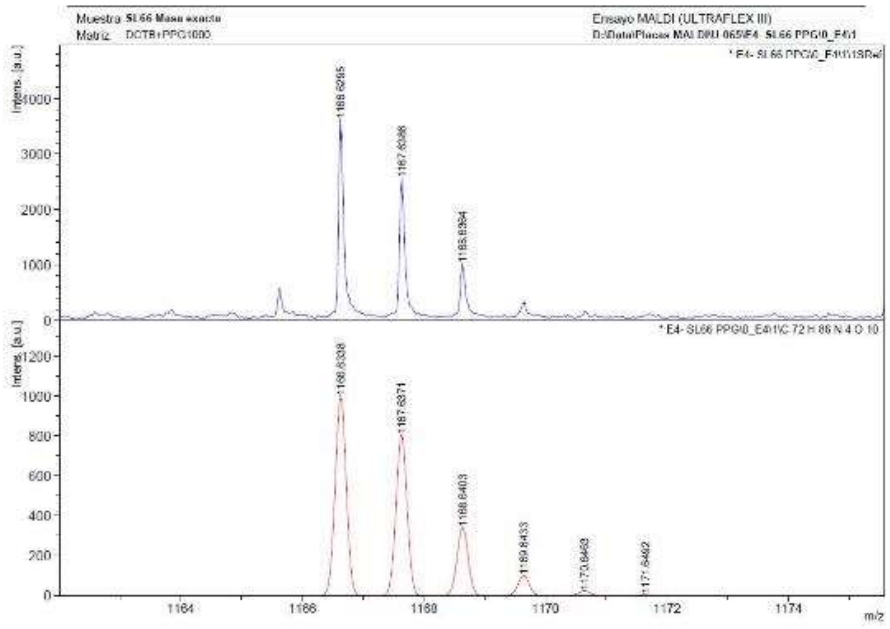
Muestra SL66 Masa exacta
Matriz DCTB+PPG1000
Ensayo MALDI (ULTRAFLEX III)
Intens. [a.u.]
1168.6265
1167.6398
1166.6394
* E4- SL66 PPG10_E4(1)C 72 H 86 N 4 O 10
1168.6338
1167.6371
1166.6403
1169.6433
1170.6468
1171.6492
1164
1166
1168
1170
1172
1174
m/z

General procedure for SWNTs functionalization.

The nanotubes (5mg) were suspended in 5 ml of either tetrachloroethane (TCE) or N, N-dimethylformamide (DMF) through sonication during 10 min. After sonication the linear precursor **4-6** was added and the mixture was degasified during 20 min, the Grubb's 2nd generation catalyst was added and the mixture was stirred at room temperature for 72 h. The suspension was filtered through a PTFE membrane of 0.2 µm pore size and the solid washed with dichloromethane (DMC). The solid was re-suspended in 20 ml of DMC through sonication during 10 min and filtered through PTFE membrane again. This washing was repeated three times.

General Procedure for SWNTs Functionalization varying the relative c concentration of 5 with respect to SWNTs.

The nanotubes (1mg /1ml) were suspended in TCE and DMF through sonication (10 min) and mixed with the linear precursor 5 (0.044 mM, 2.3 mM, 4.5 mM) and Grubb's 2ndgeneration catalyst at room temperature for 72h. The suspension was filtered and washed using the same procedure described above.

General Procedure for SWNTs Functionalization (control experiment).

The nanotubes (5mg) were suspended in 5 ml of tetrachloroethane (TCE) and N, N-dimethylformamide (DMF) through sonication during 10 min. After sonication the solvent was the linear precursor **1-3** or macrocycle **4-6** was added and the mixture was degasified during 20 min, the Grubb's 2nd generation catalyst was added and the mixture was stirred at room temperature for 72 h. The suspension as filtered through a PTFE membrane of 0.2 µm pore size and the solid washed with dichloromethane (DMC). The solid was re-suspended in 20 ml of DMC through sonication during 10 min and filtered through PTFE membrane again. This washing was repeated three times.

General Procedure for de-threading Functionalized SWNTs.

The functionalized nanotubes (2mg) were suspended in 5 ml of TCE by sonication for 5 min and then heated to reflux (bp = 146^{0}C) for 30 min. The suspension was filtered through a PTFE of 0.2 µm pore size and the solid washed profusely with DCM. De-threading was observed by TGA.

Chirality	Diameter	CNT (kJ/mol)	SYS (kJ/mol)	CMB (kJ/mol)	Eb (kJ/mol)	Eb (kcal/mol)	Atoms
(6,5)	7.4700E-01	2.2188E+04	6.8350E+02	2.2870E+04	-8.9600E-01	-2.1410E-01	476
(7,5)	8.1800E-01	2.5372E+04	1.1134E+03	2.6601E+04	1.1613E+02	2.7749E+01	548
(7,6)	8.8200E-01	2.8622E+04	1.4844E+03	3.0707E+04	6.0060E+02	1.4351E+02	620
(8,3)	7.7100E-01	2.3386E+04	8.1166E+02	2.4234E+04	3.6141E+01	8.6358E+00	500
(8,4)	8.2900E-01	2.5733E+04	1.1975E+03	2.7066E+04	1.3618E+02	3.2540E+01	560
(9,5)	9.6220E-01	3.2656E+04	2.3079E+03	3.5807E+04	8.4292E+02	2.0141E+02	716
(8,6)	9.5300E-01	3.2153E+04	2.2418E+03	3.5205E+04	8.0949E+02	1.9343E+02	704
(9,3)	8.4700E-01	2.6900E+04	1.3427E+03	2.8410E+04	1.6697E+02	3.9897E+01	580
(11,0)	8.6100E-01	1.6413E+04	1.4627E+03	1.8065E+04	1.8949E+02	4.5278E+01	420
(10,2)	8.7200E-01	2.8180E+04	1.5678E+03	2.9959E+04	2.1138E+02	5.0509E+01	608

Table 1.4: Dataset interaction energies of a series of SWNTs with macrocycle **6**.

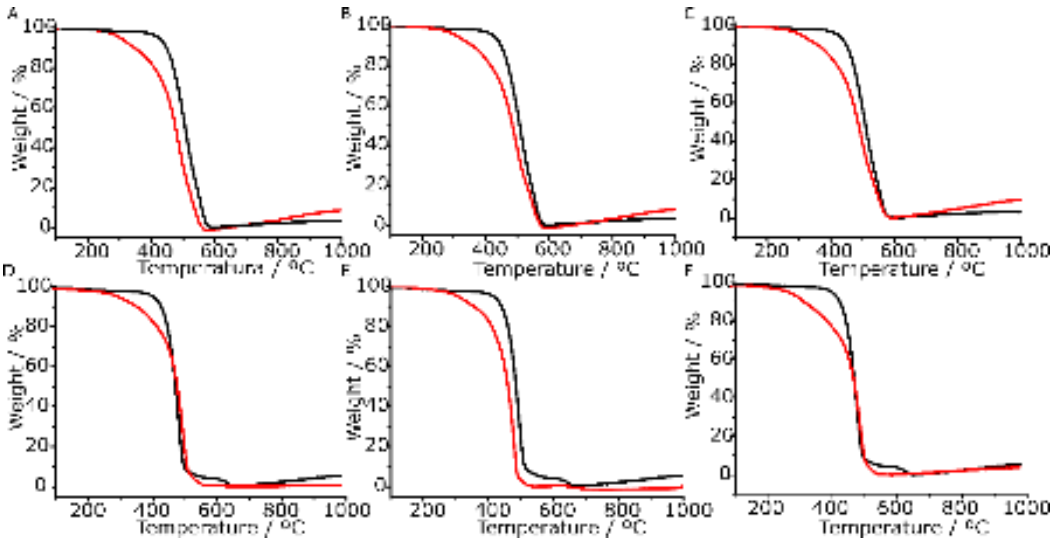

Figure 1.25:A-F: TGA (air, 10 C min^{-1}) of: **a)** (6,5) SWNTs (Black line), **1**-(6,5)-TCE (red line), **b)** (6,5) SWNTs (Black line), **2**-(6,5)-TCE (red line), **c)** (6,5) SWNTs (Black line), **3**-(6,5)-TCE (red line), **d)** (7,6) SWNTs (Black line), **1**-(7,6)-TCE (red line), **e)** (7,6) SWNTs (Black line), **2**-(7,6)-TCE (red line), **f)** (7,6) SWNTs (Black line), **3**-(7,6)-TCE (red line).

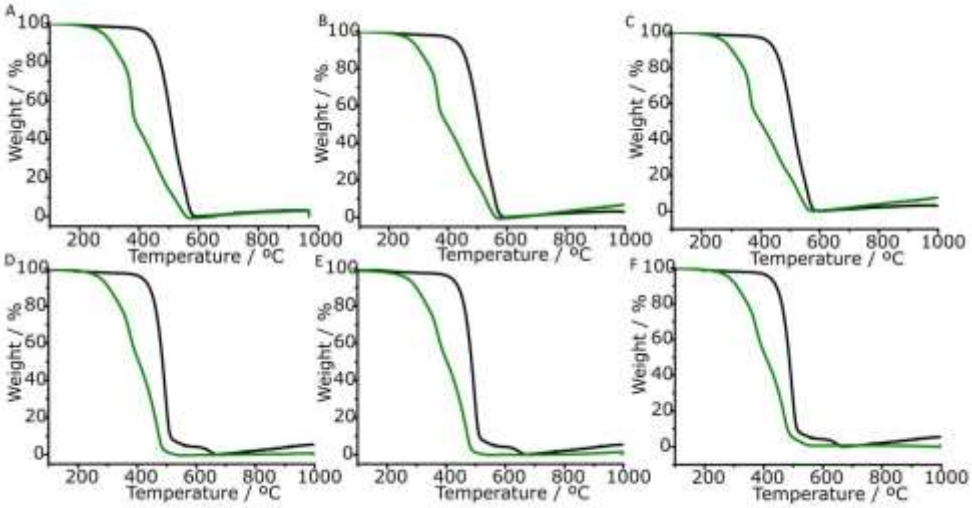

Figure 1.26: A-F: TGA (air, 10 C min^{-1}) of: **a)** (6,5) SWNTs (Black line), **1**-(6,5)-DMF (green line), **b)** (6,5) SWNTs (Black line), **2**-(6,5)-DMF (green line), **c)** (6,5) SWNTs (Black line), **3**-(6,5)-DMF (green line), **d)** (7,6) SWNTs (Black line), **1**-(7,6)-DMF (green line), **e)** (7,6) SWNTs (Black line), **2**-(7,6)-DMF (green line), **f)** (7,6) SWNTs (Black line), **3**-(7,6)- TCE (green line).

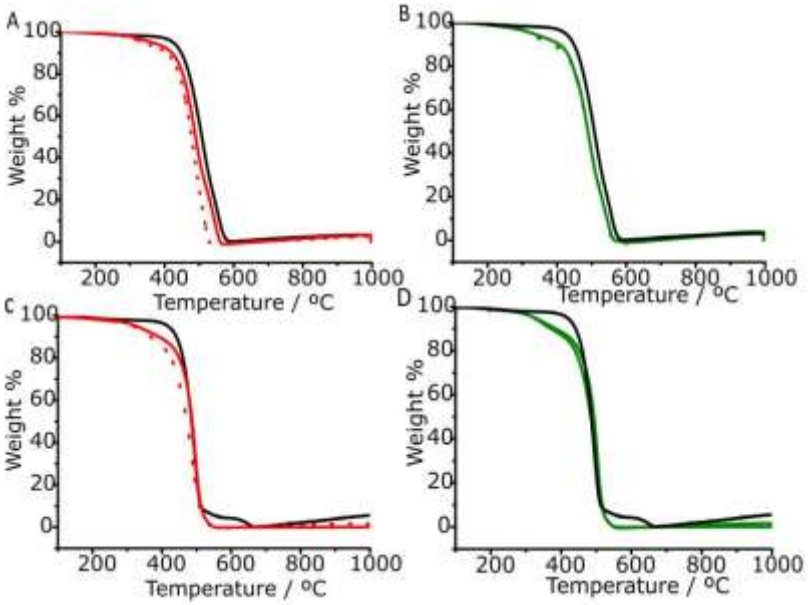

Figure 1.27: A-D: TGA (air, 10 C min^{-1}) of: **a)** **2**-(6,5)-TCE reaction with catalyst (Black line), **2**-(6,5)-TCE without catalyst (solid red line), **2**-(6,5)-TCE (dashed red line) **b)** **2**-(6,5)-DMF reaction with catalyst (Black line), **2**-(6,5)-DMF without catalyst (solid green line), **2**-(6,5)-DMF (dashed green line), **c)** **3**-(7,6)-TCE reaction with catalyst (Black line), **3**-(7,6)-TCE without catalyst (solid red line), **3**-(7,6)-TCE (dashed red line), **d)** **3**-(7,6)-DMF reaction with catalyst (Black line), **3**-(7,6)-DMF without catalyst (solid green line), **3**-(7,6)-DMF (dashed green line).

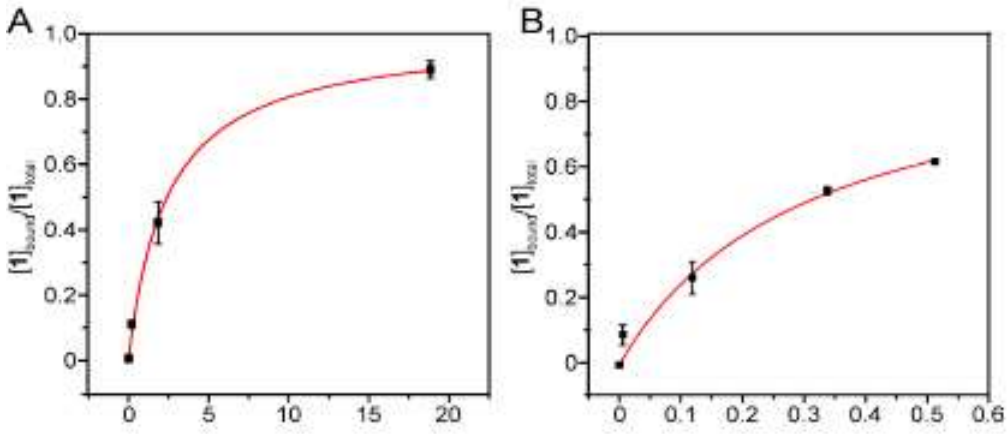

Figure 1.28: Titration of **3** *vs* (6,5)-SWNTs in a) TCE (K_a = 2.6 ± 0.1 M^{-1}, r^2= 0.9967) and b) DMF K_a = 3.5 ± 0.2 M^{-1}, r^2 = 0.8713).

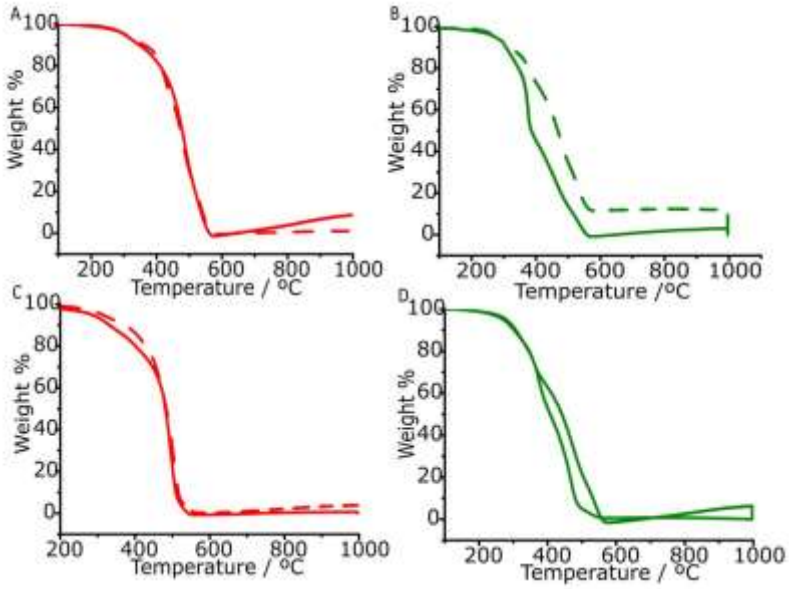

Figure 1.29: A-D: TGA (air, 10 C min^{-1}) of: **a) 1**-(6,5)-TCE (solid red line), **1**-(6,5)-TCE after heating at reflux in TCE for 30 min (dashed red line),**b) 1**-(6,5)-DMF (solid green line), **1**-(6,5)-DMF after heating at reflux in TCE for 30 min (dashed green line), **c) 3**-(7,6)-TCE (solid red line), **3**-(7,6)-TCE after heating at reflux in TCE for 30 min (dashed red line), **d) 3**-(7,6)-DMF (solid green line), **3**-(7,6)-DMF after heating at reflux in TCE for 30 min (dashed green line).

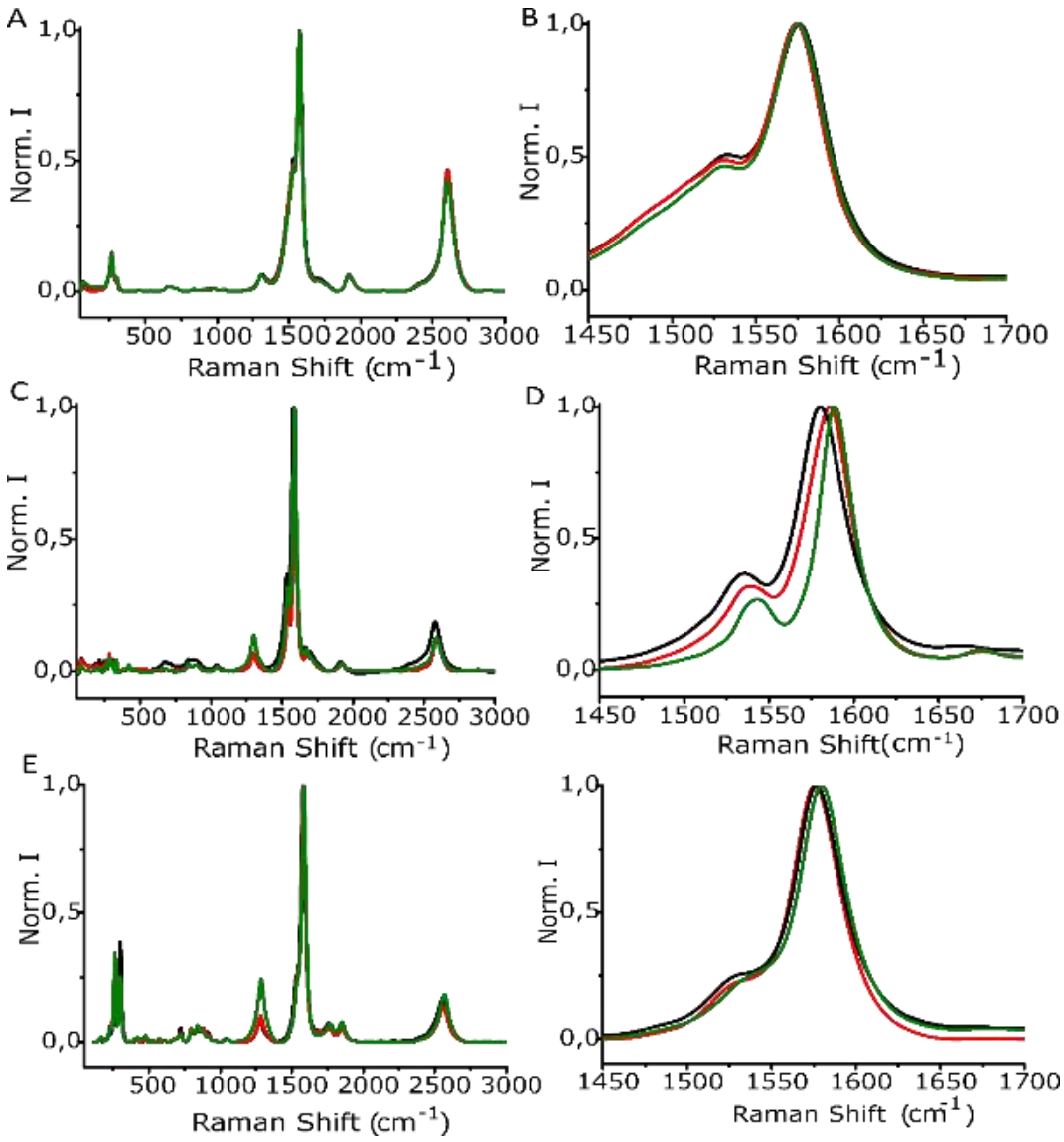

Figure 1.30 A-F: Raman spectra (λ_{exc} = 532 nm) of **a)** (6,5) SWNTs (black line), **1**-(6,5)-TCE (red line) and **1**-(6,5)-DMF (green line), **b)** Zoom in of the G band of the spectra, Raman spectra (λ_{exc} = 633 nm) of **c)** (6,5) SWNTs (black line), **1**-(6,5)-TCE (solid red line) and **1**-(6,5)-DMF (green line), **d)** Zoom in of the G band of the spectra, Raman spectra (λ_{exc} = 785 nm) of **e)** (6,5) SWNTs (black line), **1**-(6,5)-TCE (solid red line) and **1**-(6,5)-DMF (green line), **f)** Zoom in of the G band of the spectra.

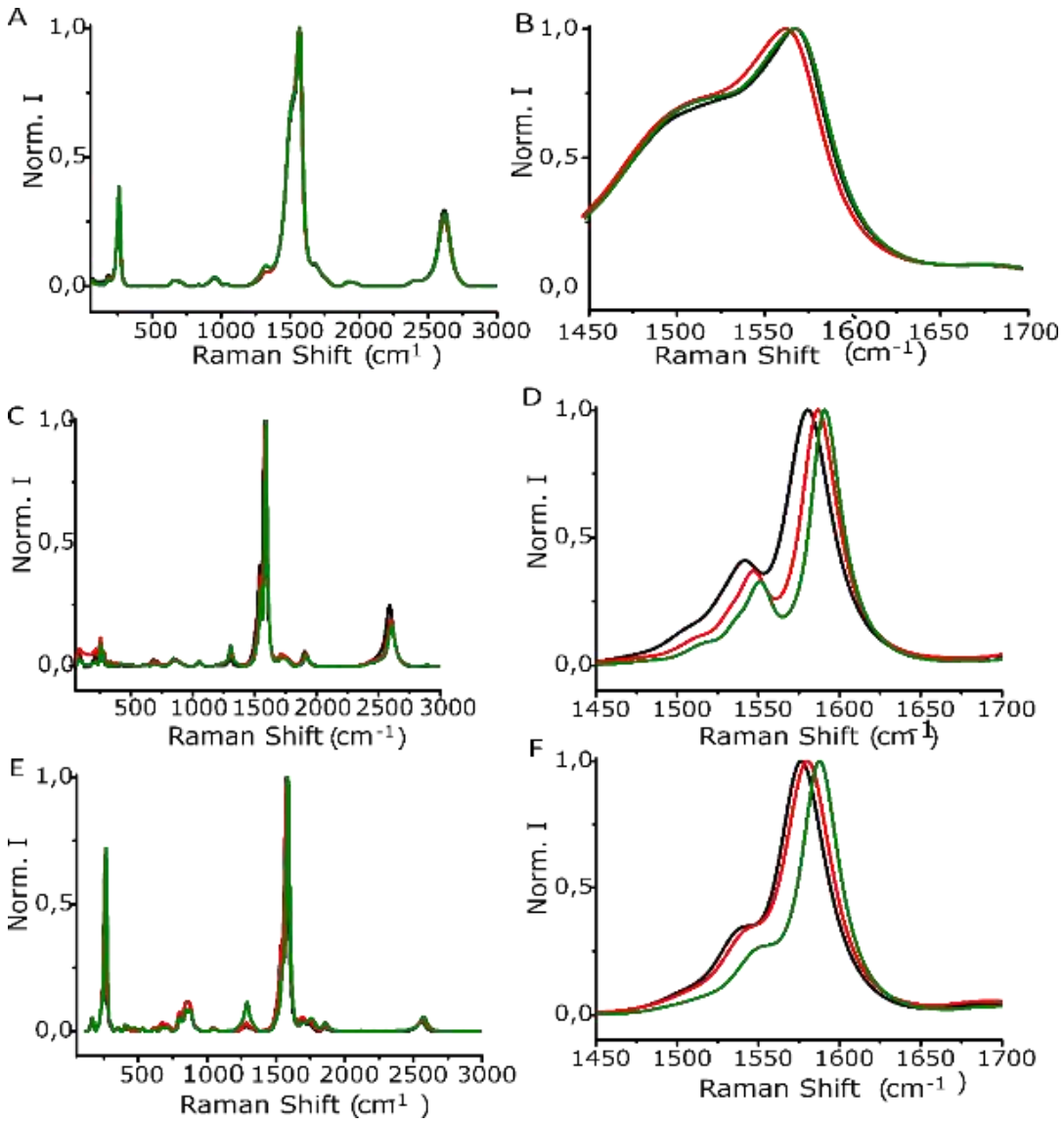

Figure 1.31 A-F: Raman spectra (λ_{exc} = 532 nm) of **a)** (7,6) SWNTs (black line), **1**-(7,6)-TCE (red line) and **1**-(7,6)-DMF (green line), **b)** Zoom in of the G band of the spectra, Raman spectra (λ_{exc} = 633 nm) of **c)** (7,6) SWNTs (black line) and **1**-(7,6)-TCE (solid red line), **1**-(7,6)-DMF (green line), **d)** Zoom in of the G band of the spectra, Raman spectra (λ_{exc} = 785 nm) of **e)** (7,6) SWNTs (black line), **1**-(7,6)-TCE (solid red line) and **1**-(7,6)-DMF (green line), **f)** Zoom in of the G band of the spectra.

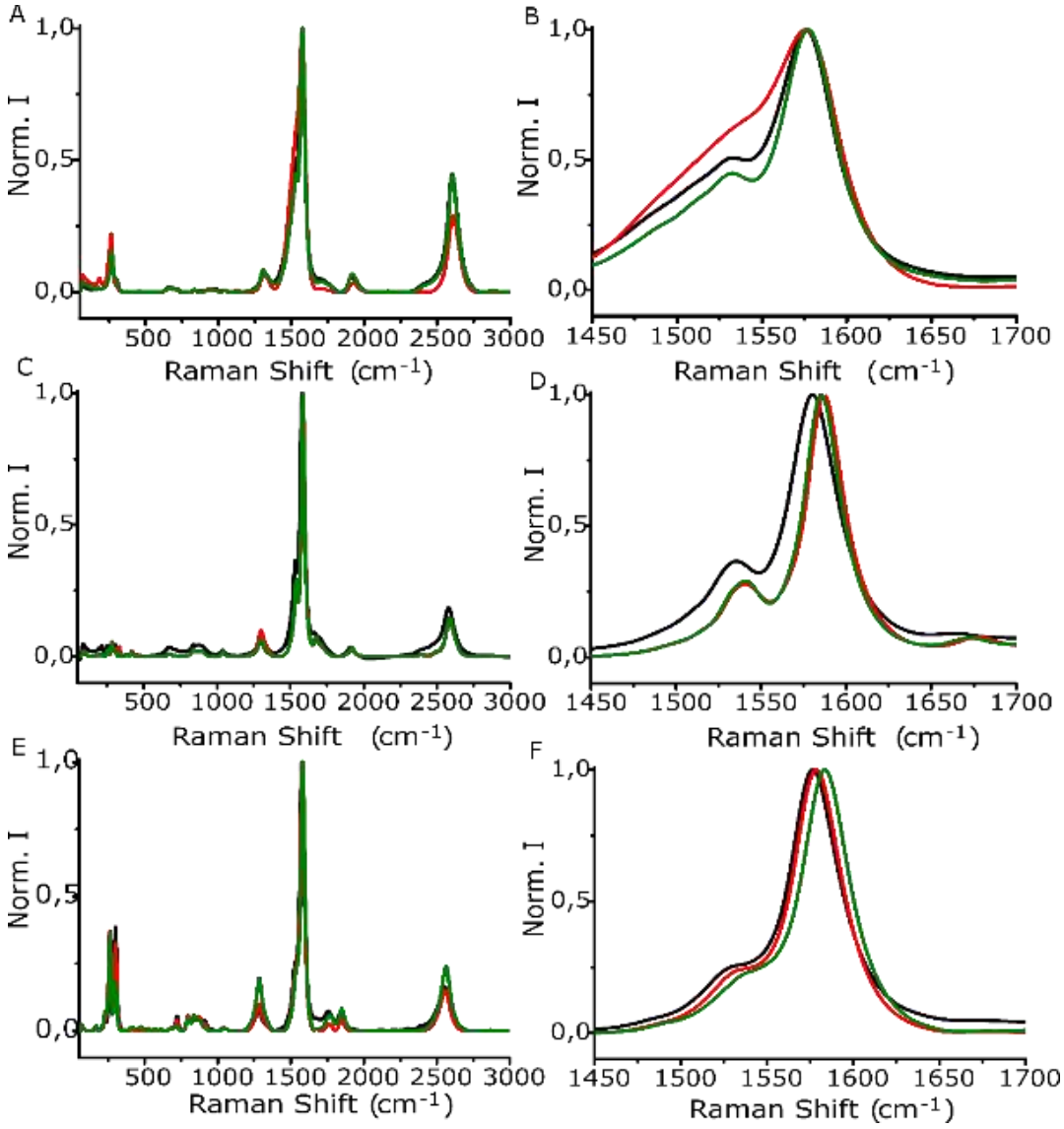

Figure 1.32 A-F: Raman spectra (λ_{exc} = 532 nm) of **a)** (6,5) SWNTs (black line), **2**-(6,5)-TCE (red line) and **2**-(6,5)-DMF (green line), **b)** Zoom in of the G band of the spectra, Raman spectra (λ_{exc} = 633 nm) of **c)** (6,5) SWNTs (black line), **2**-(6,5)-TCE (solid red line) and **2**-(6,5)-DMF (green line), **d)** Zoom in of the G band of the spectra, Raman spectra (λ_{exc} = 785 nm) of **e)** (6,5) SWNTs (black line), **2**-(6,5)-TCE (solid red line) and **2**-(6,5)-DMF (green line), **f)** Zoom in of the G band of the spectra.

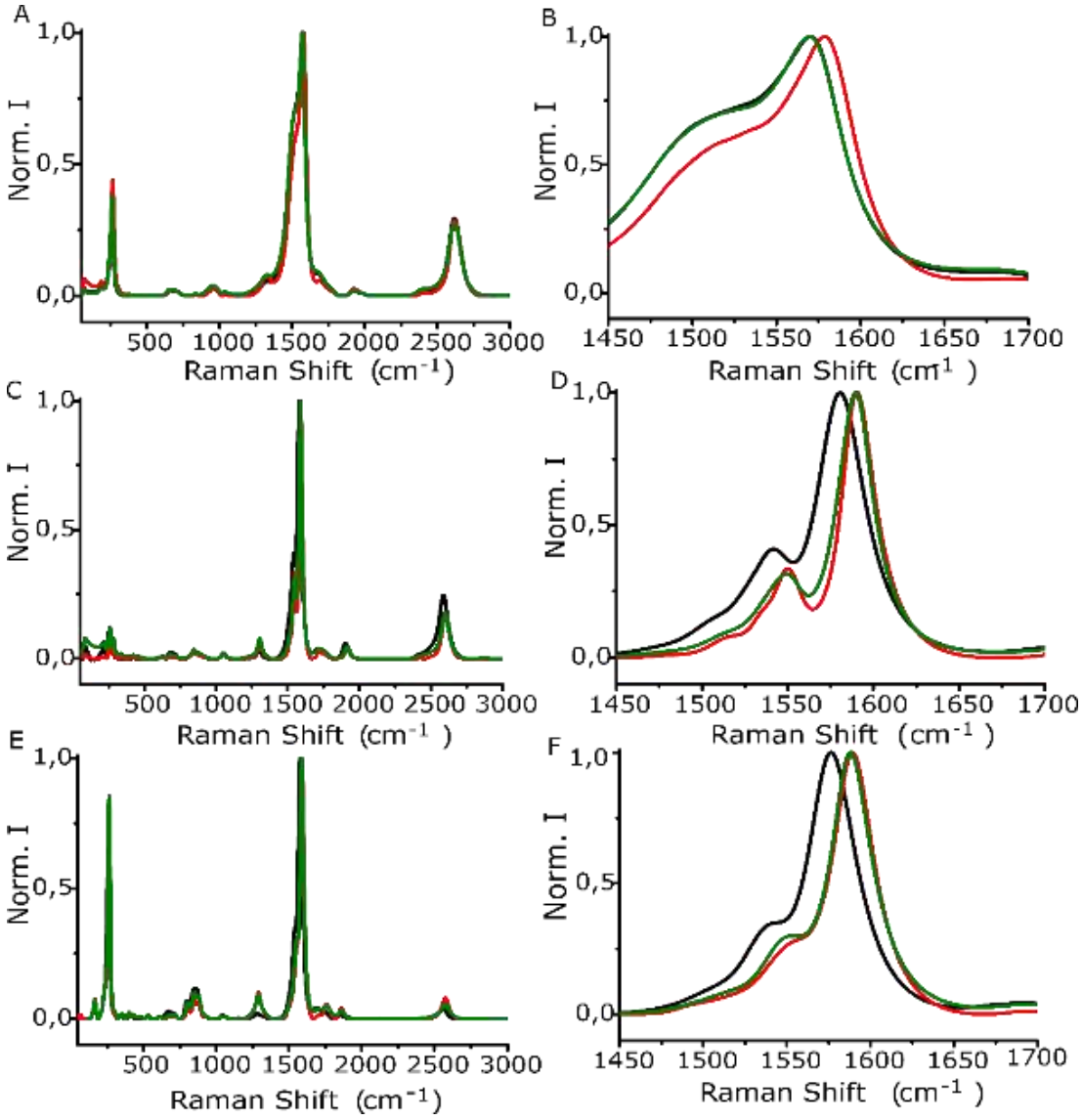

Figure 1.33 A-F: Raman spectra (λ_{exc} = 532 nm) of **a)** (7,6) SWNTs (black line), **2**-(7,6)-TCE (red line) and **2**-(7,6)-DMF (green line), **b)** Zoom in of the G band of the spectra, Raman spectra (λ_{exc} = 633 nm) of **c)** (7,6) SWNTs (black line), **2**-(7,6)-TCE (solid red line) and **2**-(7,6)-DMF (green line). **d)** Zoom in of the G band of the spectra, Raman spectra (λ_{exc} = 785 nm) of **e)** (7,6) SWNTs (black line), **2**-(7,6)-TCE (solid red line) and **2**-(7,6)-DMF (green line), **f)** Zoom in of the G band of the spectra.

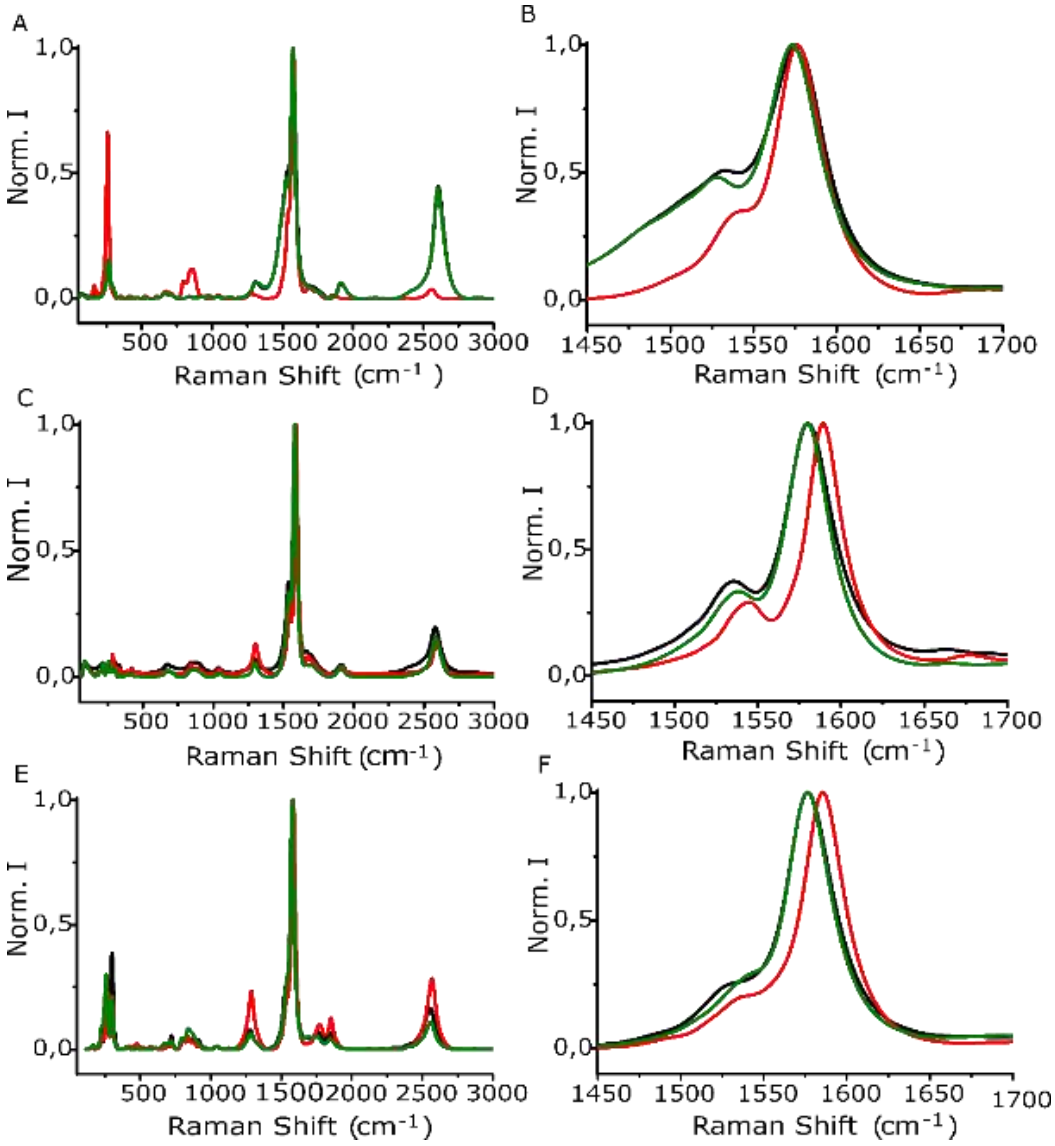

Figure 1.34 A-F: Raman spectra (λ_{exc} = 532 nm) of **a)** (6,5) SWNTs (black line), **3**-(6,5)-TCE (red line), **3**-(6,5)-DMF (green line). **b)** Zoom in of the G band of the spectra, Raman spectra (λ_{exc} = 633 nm) of **c)** (6,5) SWNTs (black line) and **3**-(6,5)-TCE (solid red line), **3**-(6, 5)-DMF (green line). **d)** Zoom in of the G band of the spectra, Raman spectra (λ_{exc} = 785 nm) of **e)** (6,5) SWNTs (black line) and **3**-(6,5)-TCE (solid red line), **3**-(6,5)-DMF (green line), **f)** Zoom in of the G band of the spectra.

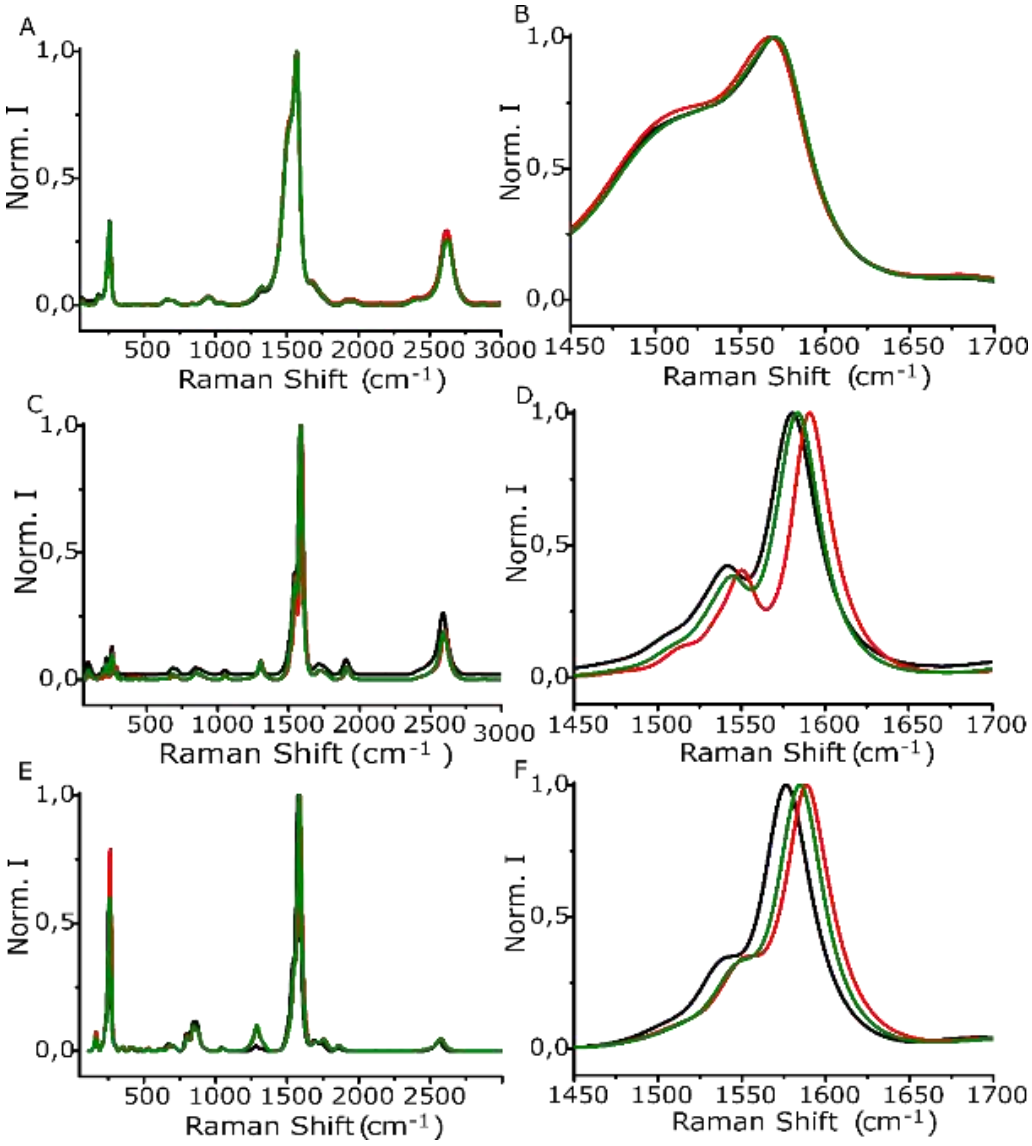

Figure 1.35 A-F: Raman spectra (λ_{exc} = 532 nm) of **a)** (7,6) SWNTs (black line), **3**-(7,6)-TCE (red line) and **3**-(7,6)-DMF (green line), **b)** Zoom in of the G band of the spectra, Raman spectra (λ_{exc} = 633 nm) of **c)** (7,6) SWNTs (black line), **3**-(7,6)-TCE (solid red line) and **3**-(7,6)-DMF (green line), **d)** Zoom in of the G band of the spectra, Raman spectra (λ_{exc} = 785 nm) of **e)** (7,6) SWNTs (black line), **3**-(7,6)-TCE (solid red line) and **3**-(7,6)-DMF (green line), **f)** Zoom in of the G band of the spectra.

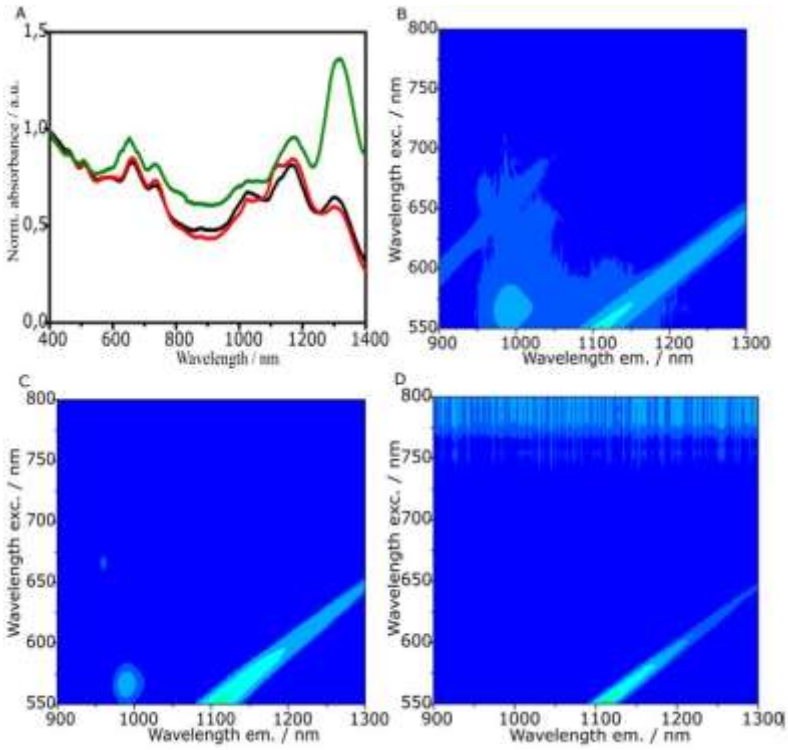

Figure 1.36 A-D: a) UV-vis-NIR absorption spectra (D_2O, 1% SDS, room temperature) of pristine (6,5)-enriched SWNTs (black), and the products of their reactions with **3** in TCE (red) and DMF (green). PLE intensity maps (D_2O, 1% SDS, room temperature) of **b)** pristine (6,5) enriched SWNTs, **c) 3**-(6,5)-TCE and **d) 3**-(6,5)-DMF.

5. References

1. H. W. Kroto, J. R. Heath, S. C. O'Brien, R. F. Curl, R. E. Smalley, *Nature*, **1985**, *318*, 162.
2. (a) K. S. Novoselov, A. K. Geim, S. V. Morozov, D. Jiang, Y. Zhang, S. V. Dubonos, I. V. Grigorievam and A. A. Firsov, Science 2004, 306, 666-669. (b) A. K. Geim and K. S. Novoselov, Nat. Mater. 2007, 6, 183-191.
3. L. V. Radushkevich, V. M. Lukyanovich, Zurn. Fisic. Chim. 1952, 26, 88-95.
4. S. Iijima, Nature 1991, 356, 56-58.
5. a) S. Iijima, T. Ichihashi, Nature 1993, 363, 603-605; b) D. S. Bethune, C. H. Kiang, M. S. De Vries, G. Gorman, R. Savoy, J. Vázquez, Nature, 1993, 363, 605-607.
6. Y. Ando, X. Zhao, T. Sugai and M. Kumar, Mater. Today, 2004, 7, 22-29.
7. T. Guo, P.Nikolaev, A. Thess, D. T. Colbert, R. E. Smalley; Chem. Phys. Lett., 1995, 243, 49-54.
8. M. José-Yacamán, M. Miki-Yoshida, L. Rendón, J. G. Santiesteban, Appl. Phys. Lett., 1993, 62, 657-659.
9. M. Kumar and Y. Ando, J. Nanosci. Nanotechnol., 2010, 10, 3739.
10. H. W. Zhu, C. L. Xu1, D. H. Wu, B. Q. Wei, R. Vajtai, P. M. Ajayan, *Science*, **2003**, *296*, 884-886.
11. R. Saito, M. Fujita, G. Dresselhaus and M. S Dresselhaus *Appl. Phys. Lett*. **1992**, *60*, 2204-2206.
12. a) L. C. Qin, *Rep. Prog. Phys*., **2006**, *69*, 2761-2816. b) L. C. Qin, *Phys. Chem. Chem. Phys.*, **2007**, *9*, 31-48.
13. M. S. Dresselhaus, G. Dresselhaus, and P. C. Eklund, *Science of Fullerenes and Carbon Nanotubes* (Academic, San Diego, **1996**).
14. M. S. Arnold, S. I. Stupp and M. C. Hersam*, Nano Lett*., **2005**, *5*, 713-718.
15. R. Krupke, F. Hennrich, M. M. Kappes and H. V. Lohneysen, *Nano Lett*.,**2004**, *4*, 1395-1399.
16. A. M. Rao, E. Richter, S. Bandow, B. Chase, P. C. Eklund, K. A. Willams, S. Fang, K. R. Subbaswamy, M. Menon, A. Thess, R. E. Smalley, G. Dresselhaus and M. S. Dresselhaus, *Science***, 1997**, *275*, 187-191.
17. A. Jorio, M. A. Pimenta, A. G. Souza, R. Saito, G. Dresselhaus and M. S. Dresselhaus, *New J. Phys*., **2003**, *5*, 139.
18. S. M. Bachilo, M. S. Strano, C. Kittrell, R. H. Huage, R. E. Smalley and R. B. Weisman, *Science*, **2002**, *298*, 2361-2366.
19. M. S. Strano, S. K. Doorn, E. H. Haroz, C. Kittrell, R. H. Huage and R. E. Smalley, *Nano Lett*., **2003**, *3*, 1091-1096.
20. M. S. Dresselhaus, A. Jorio, M. Hofmann, G. Dresselhaus and R. Saito, *Nano Lett*., **2010**, *10*, 751-758.
21. A. Kasuya, Y. Sasaki, Y. Saito, K. Tohji and Y. Nishina, *Phys. Rev. Lett*., **1997**, *78*, 4434-4437.
22. L. M. Malard, M. A. Pimenta, G. Dresselhaus and M. S. Dresselhaus, *Phys. Rep*., **2009**, *473*, 51-87.
23. Z. H. Ni, T. Yu, Y. H. Lu, Y. Y. Wang, Y. P. Feng and Z. X. Shen, *ACS Nano,* **2008**, *2*, 2301-2305.
24. M. J. O'Connell, S. M. Bachilo, C. B. Huffman, V. C. Moore, M. S. Strano, E. H. Haroz, K. L. Rialon, P. J. Boul, W. H. Noon, C. Kittrell, J. P. Ma, R. H. Hauge, R. B. Weisman and R. E. Smalley, *Science*, **2002**, *297*,593-596.
25. T. Hertel, A. Hagen, V. Talalaev, K. Arnold, F. Hennrich, M. Kappes, S. Rosenthal, J. McBride, H. Ulbricht and E. Flahaut, *Nano Lett.*, **2005**, *5*, 511-514.
26. P. L. McEuen and J. Y. Park, *MRS Bulletin*, **2004**, *72*.
27. M. Y. Sfeir, T. Beetz, F. Wang, L. Huang, X. M. Huang, M. Huang, J. Hone, S. O'Brien, J. A. Misewich, T. F. Heinz, L. Wu, Y. Zhu and L. E. Brus, *Science*, **2006**, *312*, 554-556.
28. A. Hirsch, *Angew. Chem. Int. Ed*., **2002**, *41*, 1853.
29. P. Avouris, *Acc. Chem. Res.*, **2002,** *35*, 1026-1034.
30. J. Liu, A. G. Rinzler, H. Dai, J. H. Hafner, R. K. Bradley, P. J. Boul, A. Lu, T. Iverson, K. Shelimov, C. B. Huffman, F. Rodriguez-Macias, Y. S. Shon, T. R. Lee, D. T. Colbert and R. E. Smalley, *Science*, **1998**, *280*, 1253-1256.
31. E. T. Mickelson, C. B. Huffman, A. G. Rinzler, R. E. Smalley, R. H. Hauge and J. L. Margrave, *Chem. Phys. Lett*, **1998**, *296*, 188-194.
32. P. J. Boul, J Liu, E. T. Mickelson, C. B. Huffman, L. M. Ericson, I. W. Chiang, K. A. Smith, D. T. Colbert, R. H. Hauge, J. L. Margrave and R. E. Smalley*, Chem. Phys. Lett.,* **1999**, *310*, 367.
33. Y. M. Ying, R. K. Saini, F. K. Liang, A. Sadana and W. E. Billups, *Org. Lett*., **2003**, *5*, 1471-1473.
34. H. Murakami, T. Nomura and N. Nakashima, *Chem. Phys. Lett.,* **2003,** *378,* 481-485.
35. X. Wang, S. Tao and B. Xing, *Environ. Sci. Technol.,* **2009,** *43,* 6214-6219.

36. J. N. Coleman, A. B. Dalton, S. Curran, A. Rubio, A. P. Davey, A. Drury, B. McCarthy, B. Lahr, P. M. Ajayan, S. Roth, R. C. Barklie and W. J. Blau, *Adv. Mater.*, **2000**, *1*, 213.
37. A. Star, J. F Stoddart, D. Steuerman, M. Diehl, A. Boukai, E. W. Wong, X. Yang, S. W. Chung, H. Choi and J. R. Heath, *Angew. Chem. Int. Ed*., **2001**, *40*, 1721-1725.
38. K. S. Chichak, A. Star, M. V. P. Altoe and J. F. Stoddart, *Small*, **2005**, *4*, 452-461.
39. D. S. Hecht, R. J. A. Ramirez, M. Briman, E. Artukovic, K. S. Chichak, J. F. Stoddart and G. Gruner, *Nano Lett*., **2006**, *6*, 2031-2036.
40. T. Schuettfort, H. J. Snaith, A. Nish and R. J. Nicholas, *Nanotechnology*, **2010**, *21*, 025201.
41. X. Peng, N. Komatsu, T. Kimura, and A. Osuka, *ACS Nano*, **2008**, *2*, 2045-2050.
42. F. Toshimitsu and N. Nakashima**,** *Nat. Commun***.**, **2014**, *5*, 5041.
43. M. T. Martínez, Y. C. Tseng, J. P. Salvador, M. P. Marco, N. Ormategui, I. Loinaz and J. Bokor*, ACS Nano*., **2010**, *41*, 473-480.
44. B. S. Wong, S. L. Yoong, A. Jagusiak, T. Panczyk, H. K. Ho, W. H. Ang and G. Pastorin, Adv. *Drug Del. Rev*., **2013**, *65*, 1964-2015.
45. A. A. Bhirde , V. Patel, J. Gavard, G. Zhang , A. A. Sousa, A. Masedunskas, R. D. Leapman, R. Weigert, J. S. Gutkind and J. F. Rusling, *ACS Nano*, **2009**, *3*, 307-316.
46. J. Liu, A.G. Rinzler, H. Dai, J.H. Hafner, R. K. Bradley, P. J. Boul, A. Lu, T. Iverson, K. Shelimov, C. B. Huffman, F. Rodriguez-Macias, Y. S. Shon, T. R. Lee, D. T. Colbert, R. E. Smalley, *Science*, **1998**, *280*, 1253-1256.
47. N. Nakashima, Y. Tomonari and H. Murakami, *Chem. Lett*., **2002**, *31*, 638.
48. Y. Tomonari, H. Murakami and N. Nakashima, *Chem. Eur. J.*, **2006**, *12*, 4027-4034.
49. B. C. Kim, I. Lee, S. J. Kwon, Y. Wee, K. Y. Kwon, C. Jeon, H. J. An, H. T. Jung, S. Ha, J. S. Dordick and J. Kim, *Scientific Reports*, **2017**, *7*, 40202.
50. L. C. Pauling*, the Nature of the Chemical Bond*, **1939**, Cornell University Press, Ithaca, New York.
51. E. Wasserman, *J. Am. Chem. Soc*., **1960**, *82*, 4433-4434.
52. J. P. Sauvage and C. Dietrich-Buchecker, *Wiley-VCH, Weinheim*, **1999**, *72*, 2265-2274.
53. D. B. Amabilino and J. F. Stoddart, *Chem. Rev*., **1995**, *95*, 2725-2828.
54. I. T. Harrison and S. Harrison, *J. Am. Chem. Soc.*, **1967**, *89***,** 5723-5724.
55. G. Schill and H. Zollenkopf, *Liebigs. Ann. Chem.,* **1969**, *721*, 53-74.
56. a) G. Wenz, *Angew. Chem. Int. Ed. Engl.,* **1994**, *33*, 803-822. b) D. B. Amabilino, J. F. Stoddart, *Chem. Rev*. **1995**, *95*, 2725-2828. c) M. C. T. Fyfe and J. F. Stoddart, *Acc. Chem. Res.*, **1997**, *30*, 393-401.
57. J. Cao, M. C. T. Fyfe, J. F. Stoddart, G. R. L. Cousins and P. T. J. Glink, *Org. Chem.,* **2000**, *65*, 1937-1946.
58. M. Händel, M. Plevoest, S. Gestermann and F. Vögtle, *Angew. Chem. Int. Ed*., **1997**, *36*, 1199.
59. J. M. Lehn, Angew. *Chem. Int. Ed.,* **1988**, *27*, 89-112.
60. D. J. Crowley, S. M. Goldup, A. L. Lee, D. A. Leigh and R. T. McBurney, *Chem. Soc. Rev***.**, **2009**, *38*, 1530-1541.
61. E. M. Pérez, L. Sánchez, G. Fernández and N. Martín, *J. Am. Chem. Soc.,* **2006,** *128*, 7172-7173.
62. H. Isla, M. Gallego, E. M. Pérez, R. Viruela, E. Ortí and N. Martín*, J. Am. Chem. Soc*., **2010**, *132*, 1772-1773.
63. A. de Juan, Y. Pouillon, L. Ruiz-González, A. Torres-Pardo, S. Casado, N. Martín, A. Rubio, and E. M. Pérez, *Angew. Chem. Int. Ed*., **2014**, *53*, 5394-5400.
64. A. López-Moreno and E. M. Pérez, *Chem. Commun.,* **2015**, *51*, 5421-5424.
65. S. Iijima and T. Ichihashi., *Nature,* **1993**, *363*, 603-605.
66. D. S. Bethune, C. H. Kiang, M. S. de Vries, G. Gorman, R. Savoy, J. Vazquez and R Beyers, *Nature* **1993**, *363*, 605-607.
67. J. M. Schnorr and T. M. Swager, *Chem. Mater.,* **2011**, *23*, 646-657.
68. M. F. L. De Volder, S. H. Tawfick, R. H. Baughman and A. J. Hart, *Science,* **2013**, *339*, 535-539.
69. Y. Cao, Y. Che, J. W. T Seo, H. Gui, M. C. Hersam and C. Zhou, *Appl. Phys. Lett.,* **2016**, *108*, 233105.
70. J. G. Weis, J. B. Ravnsbaek, K. A .Mirica and T. M. Swager, *ACS Sensors,* **2016**, *1*, 115-119.
71. S. Ishihara, J. M. Azzarelli, M. Krikorian and T. M. Swager, *J. Am. Chem. Soc.,* **2016**, *138*, 8221-8227.
72. Q. Cao, S.-J. Han, J. Tersoff, A. D. Franklin, Y. Zhu, Z. Zhang, G. S. Tulevski, J. Tang and W. Haensch, Science, **2015**, *350*, 68-72.

73. W. Qin, M. Gong, X. Chen, T. A. Shastry, R. Sakidja, G. Yuan, M. C. Hersam, M. Wuttig and S. Ren, *Adv. Mater.*, **2015**, *27*, 734-739.
74. S. F. Liu, A. R. Petty, G. T. Sazama and T. M. Swager, Angew. *Chem., Int. Ed.*, **2015**, *54*, 6554-6557.
75. P. Singh, S. Campidelli, S. Giordani, D. Bonifazi, A. Bianco and M. Prato, *Chem. Soc. Rev.*, **2009**, *38*, 2214-2230.
76. E. Bekyarova, S. Sarkar, F. Wang, M. E. Itkis, I. Kalinina, X. Tian and R. C. Haddon, *Acc. Chem. Res.*, **2013**, *46*, 65-76.
77. Y. L. Zhao and J. F. Stoddart, *Acc. Chem. Res.*, **2009**, *42*, 1161-1171.
78. K. Dirian, M. A. Herranz, G. Katsukis, J. Malig, L. RodríguezPérez, C. Romero-Nieto, V. Strauss, N. Martín and D. M. Guldi, *Chem. Sci.*, **2013**, *4*, 4335-4353.
79. S. Marchesan, M. Melchionna and M. Prato, *ACS Nano*, **2015**, *9*, 9441-9450.
80. H. Kwon, A. o. Furmanchuk, M. Kim, B. Meany, Y. Guo, G. C. Schatz and Y. H. Wang, *J. Am. Chem. Soc.*, **2016**, *138*, 6878-6885.
81. M. Barrejon, H. B. Gobeze, M. J. Gomez-Escalonilla, J. L. G. Fierro, M. Zhang, M. Yudasaka, S. Iijima, F. D'Souza and F. Langa, *Nanoscale*, **2016**, *8*, 14716-14724.
82. J. Chen, J. H. Walther and P. Koumoutsakos, *Adv. Funct. Mater.*, **2015**, *25*, 7539-7545.
83. I. Pochorovski, H. Wang, J. I. Feldblyum, X. Zhang, A. L. Antaris and Z. Bao, *J. Am. Chem. Soc.*, **2015**, *137*, 4328-4331.
84. A. Feng, L. Peng, B. Liu, S. Liu, S. Wang and J. Yuan, *ACS Appl. Mater. Interfaces*, **2016**, *8*, 11024-11030.
85. M. Mollahosseini, E. Karunaratne, G. N. Gibson, J. A. Gascon and F. Papadimitrakopoulos, *J. Am. Chem. Soc.*, **2016**, *138*, 5904-5915.
86. G. Clavé, G. Delport, C. Roquelet, J.-S. Lauret, E. Deleporte, F. Vialla, B. Langlois, R. Parret, C. Voisin, P. Roussignol, B. Jousselme, A. Gloter, O. Stephan, A. Filoramo, V. Derycke and S. Campidelli, *Chem. Mater.*, **2013**, *25*, 2700-2707.
87. I. Hijazi, T. Bourgeteau, R. Cornut, A. Morozan, A. Filoramo, J. Leroy, V. Derycke, B. Jousselme and S. Campidelli, *J. Am. Chem. Soc.*, **2014**, *136*, 6348-6354.
88. T. Lei, X. Chen, G. Pitner, H. S. P. Wong and Z. Bao, *J. Am. Chem. Soc.*, **2016**, *138*, 802-805.
89. A. de Juan, Y. Pouillon, L. Ruiz-González, A. Torres-Pardo, S. Casado, N. Martín, A. Rubio and E. M. Pérez, *Angew. Chem. Int. Ed.*, **2014**, *53*, 5394-5400.
90. A. López-Moreno and E. M. Pérez, *Chem. Commun.*, **2015**, *51*, 5421-5424.
91. A. de Juan, M. Mar Bernal and E. M. Pérez, *ChemPlusChem,* **2015**, *80*, 1153-1157.
92. E. Martínez-Periñán, A. de Juan, Y. Pouillon, C. Schierl, V. Strauss, N. Martín, A. Rubio, D. M. Guldi, E. Lorenzo and E. M. Pérez, *Nanoscale*, **2016**, *8*, 9254-9264.
93. Rotaxanes and pseudorotaxanes are both topologically trivial and, mathematically speaking, neither is mechanically interlocked, since they can be converted into the macrocycle-dumbell or macrocycle-thread pairs by shrinking the stoppers and/or stretching out the macrocycle to allow dissociation. From a chemical perspective, this would require that the species withstand the shrinking or stretching without breaking a covalent bond. This, we believe, is a more adequate criterion than the presence or absence of stoppers to decide if the species are mechanically interlocked or not (see: A. de Juan and E. M. Pérez, *Nanoscale*, **2013**, *5*, 7141). Since MINTs require breaking of covalent bonds to dissociate, we consider them mechanically interlocked.
94. S. V. Bhosale, C. H. Jani and S. J. Langford, *Chem. Soc. Rev.*, **2008**, *37*, 331-342.
95. X. Zhan, A. Facchetti, S. Barlow, T. J. Marks, M. A. Ratner, M. R. Wasielewski and S. R. Marder, *Adv. Mater.*, **2011**, *23*, 268-284.
96. H. E. Katz, A. J. Lovinger, J. Johnson, C. Kloc, T. Siegrist, W. Li, Y. Y. Lin and A. Dodabalapur, *Nature*, **2000**, *404*, 478-481.
97. M. Sommer, *J. Mater. Chem. C*, **2014**, *2*, 3088-3098.
98. R. Kim, P. S. K. Amegadze, I. Kang, H. J. Yun, Y. Y. Noh, S.-K. Kwon and Y. H. Kim, *Adv. Funct. Mater.*, **2013**, *23*, 5719-5727.
99. V. Senkovskyy, R. Tkachov, H. Komber, M. Sommer, M. Heuken, B. Voit, W. T. S. Huck, V. Kataev, A. Petr and A. Kiriy, *J. Am. Chem. Soc.,* **2011**, *133*, 19966-19970
100. S. L. Suraru and F. Wurthner, *Angew. Chem. Int. Ed.*, **2014**, *53*, 7428-7448.

101. P. Ballester, *Acc. Chem. Res*., **2012**, *46*, 874-884.
102. S. Guha, F. S. Goodson, L. J. Corson and S. Saha, *J. Am. Chem. Soc.*, **2012**, *134*, 13679-13691.
103. S. Guha and S. Saha, *J. Am. Chem. Soc*., **2010**, *132*, 17674-17677.
104. V. Gorteau, G. Bollot, J. Mareda, A. Pérez-Velasco and S. Matile, *J. Am. Chem. Soc*., **2006**, *128*, 14788-14789.
105. N. Ponnuswamy, G. D. Pantos, M. M. J. Smulders and J. K. M. Sanders, *J. Am. Chem. Soc*., **2012**, *134*, 566-573.
106. A. R. Stefankiewicz, E. Tamanini, G. D. Pantos and J. K. M. Sanders, *Angew. Chem., Int. Ed*., **2011**, *50*, 5725-5728.
107. Z. Hu, G. D. Pantos, N. Kuganathan, R. L. Arrowsmith, R. M. J. Jacobs, G. Kociok-Koehn, J. O'Byrne, K. Jurkschat, P. Burgos, R. M. Tyrrell, S. W. Botchway, J. K. M. Sanders and S. I. Pascu, *Adv. Funct. Mater*., **2012**, *22*, 503-518.
108. E. M. Pérez and N. Martín, *Chem. Soc. Rev*., **2008**, *37*, 1512-1519.
109. Our method is based on the direct measurement of the concentration of bound and free host molecule in the equilibrium, so that the "concentration" of SWNTs does not need to be known. See: A. de Juan, A. López-Moreno, J. Calbo, E. Ortí and E. M. Pérez, *Chem. Sci*., **2015**, *6*, 7008-7014.
110. C. Fantini, M. L. Usrey and M. S. Strano, *J. Phys. Chem. C*, **2007**, *111*, 17941-17946.
111. S. M. Bachilo, M. S. Strano, C. Kittrell, R. H. Hauge, R. E. Smalley and R. B. Weisman, *Science*, **2002**, *298*, 2361-2366.
112. S. Hüfner, Photoelectron Spectroscopy. Principles and Applications, Springer, Berlin Heidelberg, 3 edn., **2003**.
113. P. Chen, X. Wu, X. Sun, J. Lin, W. Ji and K. L. Tan, *Phys. Rev. Lett*., **1999**, *82*, 2548-2551.
114. M. Scardamaglia, C. Struzzi, F. J. Aparicio Rebollo, P. De Marco, P. R. Mudimela, J.-F. Colomer, M. Amati, L. Gregoratti, L. Petaccia, R. Snyders and C. Bittencourt, *Carbon*, **2015**, *83*, 118-127.
115. A. López-Moreno, B. Nieto-Ortega, M. Moffa, A. de Juan, M. M. Bernal, J. P. Fernández-Blázquez, J. J. Vilatela, D. Pisignano and E. M. Pérez, *ACS Nano*, **2016**, *10*, 8012- 8018.

CHAPTER 2

1. Introduction

1.1 Graphene structure

The hypothetical study of graphite[1] prior to the isolation of graphene was widely used to describe properties of carbon based forms including zero dimensional fullerenes, and one-dimensional carbon nanotubes. It was not until 2004 when Andre Geim and Konstantin Novoselov[2] isolated the first graphene films by simply peeling down graphite with Scotch tape. Very briefly, a flake of graphite was put on a piece of tape and then the tape was peeled and re-stuck together many times, spreading the thinned-down flake over the surface of the tape. Graphene can be described in a simple way as one single layer of graphite; a layer of sp^2 bonded carbon atoms arranged in a honeycomb (hexagonal) lattice, with a thickness of only one C atom (0.335 nm). The bidimensional structure is responsible of the excellent physicochemical properties and applications of this material.[3] The limit between 2D (few layers of graphene) and 3D materials (graphite) is considered to be at 10 layers.[4]

The discovery of graphene supposed a revolution in the field of materials science due to its outstanding electronic, optical, mechanical and thermal properties.[5] It is the first truly two-dimensional material, being only one atom thick (the π orbitals span approximately 0.34 nm). This leads to a specific surface area of ~2600 m^2/g.[6] It exhibit a carrier mobility that can be as high as 10^5 cm^2 / Vs at ambient temperature and 10^6 cm^2 / Vs at low temperature.[7] In addition, the Young's modulus of graphene has been found to be as high as ~ 1 TPa which makes graphene the strongest material discovered so far.[8] Graphene shows the record thermal conductivity of ~5000 W/mK.[9] It is also almost transparent (it absorbs ~2.3 % of any visible wavelength).[10]

[1] P. R. Wallace, The band theory of graphite, *Phys. Rev.*, **1947**, *71*, 622.
[2] K. S. Novoselov, A. K. Geim, S. V. Morozov, D. Jiang, Y. Zhang, S. V. Dubonos, I. V. Grigorieva and A. A. Firsov, *Science*, **2004,** *306*, 666.
[3] A. K. Geim and K. S. Novoselov, *Nat. Mater.,* **2007,** *6*,183-191.
[4] B. Partoens and F. M. Peeters, *Physical Review B,* **2006,** *74*, 075404.
[5] Y. Zhang, Y. W. Tan, H. L. Stormer and P. Kim, *Nature,* **2005**, *438*, 201.
[6] M. D. Stoller, S. J. Park, Y. W. Zhu, J. H. An, and R. S. Ruoff, *Nano Lett.*, **2008**, *8*, 3498-3502,
[7] A. S. Mayorov, R. V. Gorbachev, S. V. Morozov, L. Britnell, R. Jalil, L. A. Ponomarenko, P. Blake, K. S. Novoselov, K. Watanabe, T. Taniguchi, and A. K. Geim, *Nano Lett*., **2011**, *11*, 2396-2399.
[8] C. Lee, X. Wei, J. W. Kysar and J. Hone, *Science*, **2008**, *321*, 385-388.
[9] A. A. Balandin, S. Ghosh, W. Bao, I. Calizo, D. Teweldebrhan, F. Miao and C. N. Lau, *Nano Lett*., **2008**, *8*, 902-907
[10] R. R. Nair, P. Blake, A. N. Grigorenko, K. S. Novoselov, T. J. Booth, T. Stauber, N. M. R. Peres and A. K. Geim, *Science*, **2008**, *320*, 1308.

In terms of electronic properties, graphene is a promising candidate for a wide range of applications including, chemical sensors[11,12] and transparent conducting electrodes.[13,14,15] The first publications in graphene in 2004 proved the possibility to control the carrier density in the graphene sheet by simple application of a gate voltage despite having zero band gap, this behavior comes from its particular valence and conduction band structure, which cross in the Dirac point (see Figure 2.1).

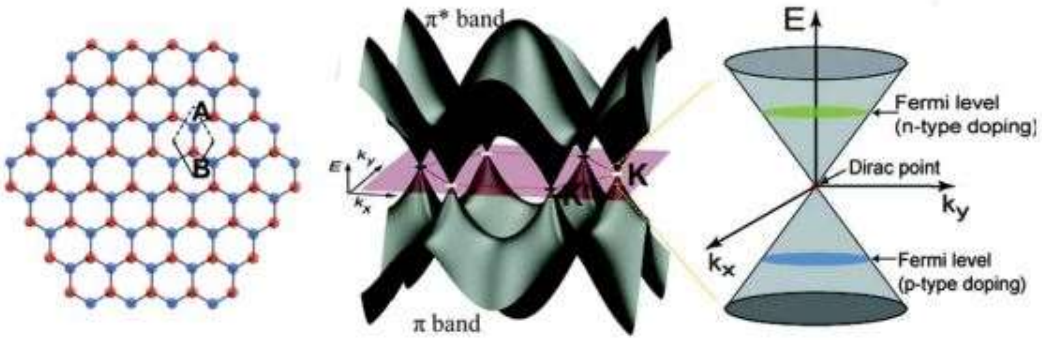

Figure 2.1. Scheme of the hexagonal lattice of graphene, the π and π^* bands in graphene and the band structure at the Dirac point.

The absence of bandgap makes difficult the potential use of graphene in semiconductor technologies, therefore the modification of graphene in order to obtain a sizeable band gap has attracted significant number of investigations.[16,17,18] This zero band gap is a result of the identical environment of the two carbons atoms in the graphene unit cell thus to open up a bandgap its necessary to break the lateral in-plane lattice symmetry by chemical modification or by structural modifications, e.g., stacking two graphene layers.

[11] F. *Schedin*, *A. K. Geim*, *S. V. Morozov*, *E. W. Hill*, *P.* Blake, *M.I. Katsnelson*, *Nature materials*, **2007**, *6*, 652-655.
[12] J. T. Robinson, F. K. Perkins, E. S. Snow, Z. Wei and P. E. Sheehan *Nano Lett.,* **2008**, *8*, 3137-3140.
[13] S. Watcharotone, D. A. Dikin, S. Stankovich, R. Piner, I. Jung, G. H. B. Dommett, G. Evmenenko, S. E. Wu, S. F. Chen, C. P. Liu, S. T. Nguyen and R. S. Ruoff, *Nano Lett*. **2007**, *7*, 1888-1892.
[14] X. Wang, L. Zhi and K. Müllen, *Nano Lett*., **2008**, *8*, 323–327.
[15] K. S. Kim, Y. Zhao, H. Jang, S. Y. Lee, J. M. Kim, K. S. Kim, J. H. Ahn, P. Kim, J. Y. Choi and B. H. Hong, *Nature*, **2009**, *457*, 706-710.
[16] S. Y. Zhou, G. H. Gweon, A. V. Fedorov, P. N. First, W. A. De Heer, D. H. Lee, F. Guinea, A. H. Castro Neto and A. Lanzara, *Nature Mater*., **2007**, *6*, 770.
[17] F. N. Xia, D. B. Farmer, Y. M. Lin and P. Avouris, *Nano Lett.*, **2010**, *10*, 715–718.
[18] H. Liu, Y. Liu and D. Zhu, J. *Mater. Chem*., **2011**, *21*, 3335-3345.

1.2 Graphene fabrication

During the last decade many techniques for fabricating graphene have been developed. Within these techniques, we can highlight the fabrication by liquid phase exfoliation (LPE),[19,20] mechanical exfoliation[21,22] or chemical vapor deposition,[23,24,25] all these techniques present their own limitations. The most common fabrication method is mechanical exfoliation, it is cheap and versatile technique that allows obtaining high quality graphene flakes, but this method is not scalable and results in small numbers of flakes that can be thinned down to the single layer. If we consider the low cost and abundance of graphite flakes, the LPE of graphite to graphene seem to fit all the requirements, except that the quality of graphene is still an issue because of the high quantity of defects, and the lack of absolute control over the number of layers of the final product, usually anywhere from 1-10. With all these factors in mind, mechanical exfoliation remains the technique of choice to produce high-quality graphene for proof-of-concept experiments, while LPE is adequate for applications that requires large amounts of low-quality FLG. Perhaps the most promising graphene production techniques for industrial and commercial purposes are those based on chemical vapor deposition (CVD) on metal catalyst. It involves the catalytic decomposition of hydrocarbons on metal catalyst (Cu, Ni, Pt, Ru and Ir) under a pressure of 1×10^{-7}mbar condition. In CVD, a substrate is exposed to one or several precursor gases containing reactive elements. These elements are made to react by heating the chamber to high temperature. In graphene CVD, typically methane or ethylene are introduced into the chamber (see Figure 2.2) in which there is a catalytic metal at high temperature, the C-C and C-H bonds are broken and the carbon radicals combine form a graphene lattice on the surface of the substrate. Today this method is used to grow epitaxial graphene layers in a controlled way. The specific parameters vary depending of the metal, but the mechanism involved is the same: the dehydrogenation of hydrocarbons on the surface of the catalytic metal leads to the formation of the sp^2-hybridized graphene honeycomb lattice.

[19] V. C. Vincent, C. Tung, M. J. Matthew, J. Allen, Y. Yang, R. B. Richard and B. Kaner*, Nat. Nanotechnol*., **2009,** *4*, 25-29.
[20] M. Lotya, Y. Hernandez, P. J. King, R. J. Smith, V. Nicolosi, L. S. Karlsson, F. M. Blighe, S. De, Z. Wang, I. T. McGovern, G. S. Duesberg and J. N. Coleman*, J. Am. Chem. Soc*., **2009**, *131*, 3611-3620.
[21] Y. T. Liang and M. C. Hersam, *J. Am. Chem. Soc*., **2010**, *132*, 17661.
[22] Y. Zhu, S. Murali, W. Cai, X. Li, J. W. Suk and J. R. Potts, *Adv. Mater*., **2010**, *22*, 3906.
[23] Q. Yu, J. Lian, S. Siriponglert, H. Li, Y. P. Chen, and S. Pei*, Appl. Phys. Lett*., **2008**, *93*, 113103.
[24] X. Li, W. Cai, J. An, S. Kim, J. Nah, D. Yang, R. Piner, A. Velamakanni, I. Jung, E. Tutuc, S. K. Banerjee, L. Colombo and R. S. Ruoff, *Science*, **2009**, *324*, 1312.
[25] S. Bae, H. Kim, Y. Lee, X. Xu, J. Park, Y. J. Zheng, J. Balakrishnan, T. Lei, H. Ri Kim, Y. I. Song, Y. J. Kim, K. S. Kim, B. Özyilmaz, J. H. Ahn, B. H. Hong and S. Iijima, *Nat. Nanotechnol*., **2010**, *5*, 574.

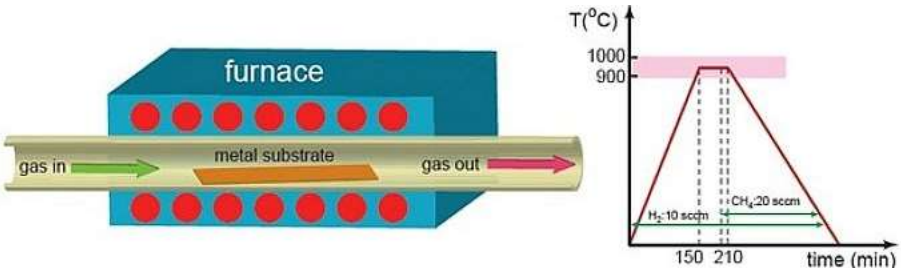

Figure 2.2. a) Experimental set up for CVD of graphene. **b)** Typical growth process.

CVD has proven to be an efficient method to growth large-area graphene on many metal substrates, such as Ru,[26] Co,[27] Ir,[28] Ni,[29] Pt[30] and Cu.[31,32] While it is possible to obtain large-area high quality graphene with this technique, requires the transfer of graphene from the metal to an arbitrary substrate using a manual method,[33] the general transfer method can be described as follows (see Figure 2.3):

- Protecting the graphene layer with a polymer layer.
- Etching chemically the metal catalyst in an etchant solution to release the film in the liquid. Fe, Co, Ni and Cu can be etched by their etchants easily.
- Rinsing with deionized water, and finally transferring it to the target substrate.
- Removing the polymer, washing with acetone.

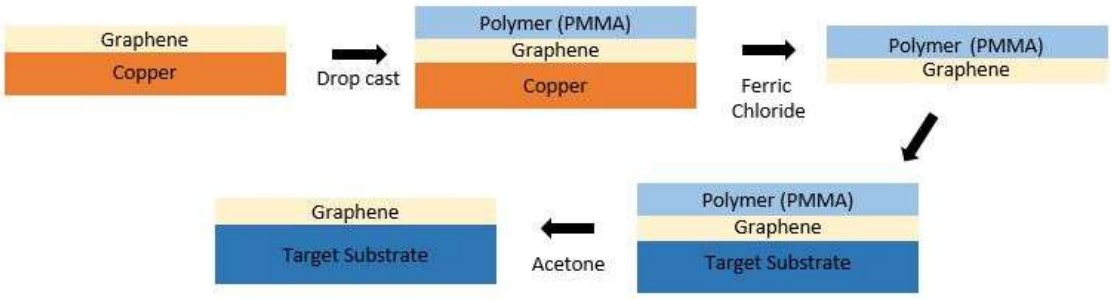

Figure 2.3. Schematic diagram of the transfer process to an arbitrary substrate.

[26] E. Sutter, P. Albrecht and P. Sutter, *Appl. Phys. Lett.*, **2009**, *95*, 133109.
[27] J. Vaari, J. Lahtinen and P. Hautojarvi, *Catal. Lett.*, **1997**, *44*, 43–49.
[28] C. Vo-Van, A. Kimouche, A. Reserbat-Plantey, O. Fruchart, P. Bayle-Guillemaud, N. Bendiab and J. Coraux, *Appl. Phys. Lett*., **2011**, *98*, 181903.
[29] T. Iwasaki, H. J. Park, M. Konuma, D. S. Lee, J. H. Smet, and U. Starke, *Nano lett*., **2011**, *11*, 79.
[30] D. E. Starr, E. M Pazhetnov, A. I. Stadnichenko, A. I. Boronin and S. K. Shaikhutdinov, *Surf. Sci.,* **2006**, *600*, 2688–2695.
[31] K. S. Kim, Y. Zhao, H. Jang, S. Y. Lee, J. M. Kim, K. S. Kim, J. H. Ahn, P. Kim, J. Y. Choi and B. H. Hong, *Nature*, **2009**, *457*, 706.
[32] X. Li, W. Cai, L. Colombo and R. S. Ruoff, *Nano Lett*., **2009**, *9*, 4268-4272.
[33] The Journal of Physical Chemistry C, **2008**, *112*, 17741.

This method is simple and cost-effective, but also time-consuming and requires handling skills, affecting the yield and reproducibility of the transfer process, for this reason the search for better techniques of graphene production, in particular a transfer-free production method, has intensified in recent years.[34] One of the main goals of this thesis is the controlled chemical modification of high-quality graphene monolayer. In particular, we use Ru(0001) as a substrate to grow graphene.

1.3 Graphene on Ru (0001) moiré structure

Ru(0001) is one of the best catalysts for the epitaxial growth of graphene, and it is easy to obtain a single-crystal surface with an orientation of (0001). The difference in lattice parameter between graphene and the different metal substrates causes the appearance of moiré patterns with a range of apparent vertical corrugations and lateral periodicities with respect to the basic graphene structure.[35,36,37,38] The CVD graphene grown on Ru(0001) presents strong chemisorption interactions due to the hybridization of the d-orbital of Ru and the Cp_z orbital. The lattice mismatch of graphene (0.246nm) and ruthenium (0.271nm), which is also rotated by 0.5^o produces a periodic repetition of three different regions (see Figure 2.4) including ridges, valleys, and medium heights.[39,40,41] The resulting moiré cell corresponds roughly to 11(10) unit cells of C (Ru). The structural and electronic properties of this system are responsible for the subsequent functionalization of graphene with periodicity at the nanometer scale.

[34] S. Jiang, Y. Zeng, W. Zhou, X. Miao and Y. Yu., *Nature*, **2016**, *6*, 19313.
[35] S. Marchini, S. Günthera and J. Wintterlin, *Phys. Rev. B,* **2007**, *76*, 075429.
[36] A.T. N'Diaye, S. Bleikamp, P.J. Feibelman and T. Michely, *Phys. Rev. Lett*. **2006**, *97*, 215501.
[37] J. Coraux, A.T. N'Diaye, C. Busse and T. Michely, *Nano Lett*. **2008**, *8*, 565.
[38] T. Fujita, W. Kobayashi and C. Oshima, *Surf. Interface. Anal*., **2005**, *37*, 120.
[39] A. Vázquez de Parga, F. Calleja, B. Borca, M. C. G. Passeggi, Jr., J. Hinarejos, F. Guinea and R. Miranda, *Phys. Rev. Lett*. **2008**, *100*, 056807.
[40] B. Borca, S. Barja, M. Garnica, D. Sánchez-Portal, V. Silvino, E. Chulkov, F. Hermanns, J. Hinarejos, A. Vázquez de Parga, A. Arnau, P. Echenique and R. Miranda, *Physical Review Letters,* **2010**, *105*, 036804.
[41] B. Borca, S. Barja, M. Garnica, M. Minniti, A. Politano, F. J. M. R. García, J. Hinarejos, D. Farías, A. Vázquez de Parga, and R. Miranda, *New journal of Physics,* **2010**, *12*, 093018.

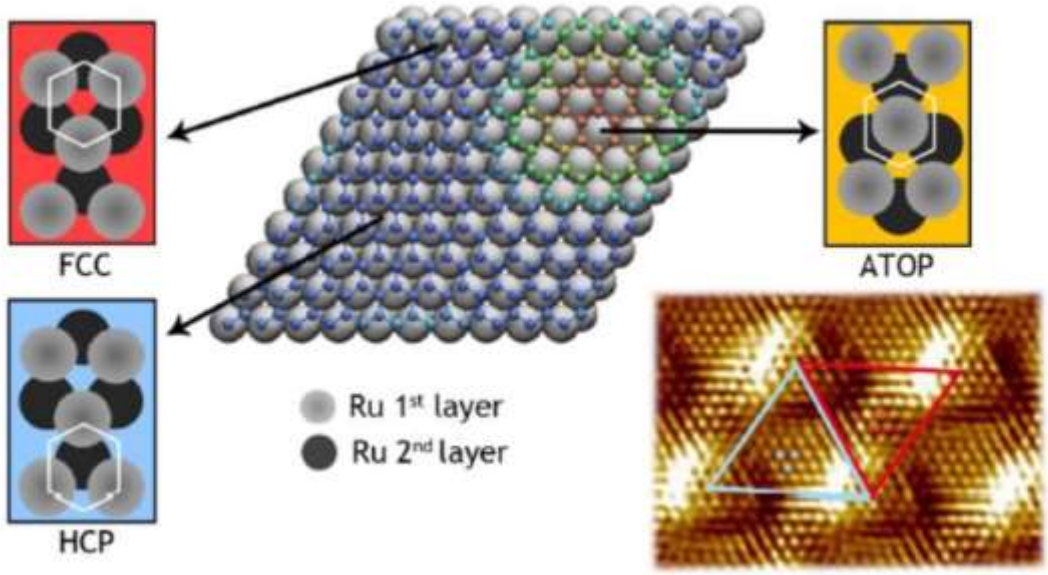

Figure 2.4. Calculated ground-state geometry of graphene/Ru(0001) with a 11Cx11C/10Rux10Ru periodicity. There are four different regions forming the moiré superstructure, namely atop, HCP, FCC and bridge (areas between HCP and FCC). A STM topographic image with atomic resolution showing the different parts of the moiré.

In-situ scanning tunneling microscopy (STM) imaging of graphene monolayers on Ru(0001) reveals periodic corrugations with (12×12),[42,43,44] and surface x-ray diffraction (XRD) experiments give a (25×25) periodicity based on the distortion of the first Ru layer under the graphene.[45] The carbon atoms on the gr/Ru(0001) are electronically inequivalent as reflected in the x-ray photoelectron spectroscopy C 1s core levels, which show two peaks, i.e. two differently bonded C atoms.[46] Due to the magnifying effect of the moiré pattern,[47] the misalignment of the C and Ru lattices can be determined with high precision from the observed angles between the moiré superstructure and the Ru or C lattices. This small rotation might explain the contradiction between the periodicity (25×25) obtained with XRD by measuring the deformation of the last ruthenium layers and the moiré periodicity obtained from the STM images.

[42] S. Marchini, S. Günthera and J. Wintterlin, *Phys. Rev. B*, **2007**, *76*, 075429.
[43] A. L. Vázquez de Parga, F. Calleja, B. Borca, J. J. Hinarejos, M. G. C. Passeggi, F. Guinea and R. Miranda, *Phys. Rev. Lett.*, **2008**, *100*, 056807.
[44] P. W. Sutter, J. I. Flege and E. A. Sutter, *Nature Mater.*, **2008**, *7*, 406.
[45] D. Martoccia, P. R. Willmott, T. Brugger, M. Björck, S. Günther, C. M. Schlepütz, A. Cervellino, S. A. Pauli, B. D. Patterson, S. Marchini, J. Wintterlin, W. Moritz and T. Greber, *Phys. Rev. Lett.*, **2008**, *101*, 126102.
[46] A. B. Preobrajenski, M. L. Ng, A. S. Vinogradov and N. Martensson, *Phys. Rev. B*, **2008**, *78*, 073401.
[47] A. T. N'Diaye, J. Coraux, T. N. Plasa, C. Busse and T. Michely, *New J. Phys.*, **2008**, *10*, 043033.

1.4 Graphene Modification

Chemical functionalization and dispersion of graphene sheets is one of the many solutions to address the challenges of graphene and take advantage of all its properties. In this work we use high-quality CVD grown graphene so it is not necessary a strategy to disperse the graphene but we need a way to modulate the energy bandgap. In the literature we found two main strategies to modify graphene: the covalent and the non-covalent approach (see Figure 2.5).

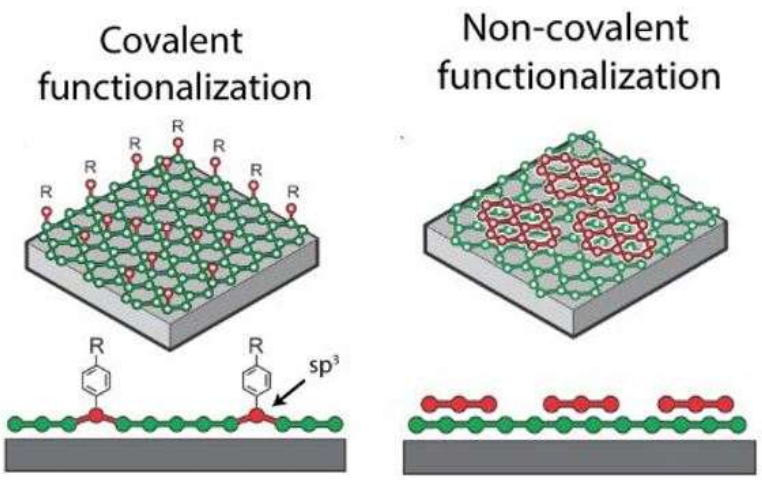

Figure 2.5. Representation functionalization of graphene via chemical methods to control its properties.

The non-covalent modification[48,49] is a simple and versatile method for modification. Within this type of modification we find exploit weak non-covalent forces, such as van der Waals forces, it is employed when the graphene's electrical conductivity and large surface are required, so it is necessary to keep the sp^2 network of C atoms intact. The use of these non-covalent interactions can also help to generate single layer graphene and few layer graphene.[50,51,52,53] On the other hand, covalent binding provides the opportunity to permanently modify graphene sheets, at the expense of saturating some of the C-C double bonds.[54,55,56,57] This offers the potential to modulate the electrical properties opening a band gap. However this functionalization is accompanied by *structural* modification due to the

[48] Q. H. Wang and M. C. Hersam, *Nat. Chem*., **2009**, *1*, 206.
[49] F. Schedin, A. K. Geim, S. V. Morozov, E. W. Hill, P. Blake, M. I. Katsnelson and K. S. Novoselov, *Nat. Mater*., **2007**, *6*, 652.
[50] J. *Malig, A. W. I. Stephenson*, *P. Wagner*, *G. G. Wallace*, *D. L. Officer* and *D. M. Guldi, Chem*. *Commun.,* **2012***, 48, 8745-8747.*
[51] F. Zhang, X. Chen, R.A. Boulos, F. Md Yasin, H. Lu, C. Raston and H. Zhang, *Chem. Commun*., **2013**, *49*, 4845–4847.
[52] W. Wang, Y. Zhang and Y. B. Wang, *J. Chem. Phys.*, **2014**, *140*, 094302.
[53] M. M. Bernal and E. M. Pérez, *Int. J. Mol. Sci*., **2015**, *16*, 10704-10714.
[54] V. Georgakilas, M. Otyepka, A. B. Bourlinos, V. Chandra, N. Kim, K. C. Kemp, P. Hobza, R. Zboril and K. S. Kim, *Chem. Rev*., **2012**, *112*, 6156.
[55] L. Yan, Y. B. Zheng, F. Zhao, S. Li, X. Gao, B. Xu, P. S. Weiss and Y. Zhao, *Chem. Soc. Rev*., **2012**, *41*, 97–114.
[56] K. P. Loh, Q. Bao, P. K. Ang and J. Yang, *J. Mater. Chem*., **2010**, *20*, 2277.
[57] Q. Tang, Z. Zhou and Z. Chen, *Nanoscale*, **2013**, *5*, 4541.

conversion of sp^2 into sp^3 carbon, a selective spatial control of the covalent attachment would allow to obtain samples with an excellent quality without introducing defects in a random fashion. In the following subsection a brief explanation of the current methods for covalent modification of graphene is provided.

1.4.1 Covalent modification of graphene/substrate

Haddon and co-workers were the first to carry out the covalent attachment of free radicals to epitaxial graphene grown on SiC wafers.[58] The radical addition reactions are one of the best ways to functionalize graphene, they lead to high functionalization degrees and also have the advantage of being tolerant with a variety of conditions. More recently Strano and co-workers have used these radical reactions to demonstrate that the substrate on which graphene rests strongly influences in the chemical reaction on graphene.[59] They transferred CVD-grown graphene onto different substrates and it was covalently functionalized with aryl diazonium salts. Raman spectroscopy was used to follow the reaction, the measurement taken before and after functionalization revealed a high degree of functionalization in graphene transferred to SiO_2 and Al_2O_3 substrates (see Figure 2.6).

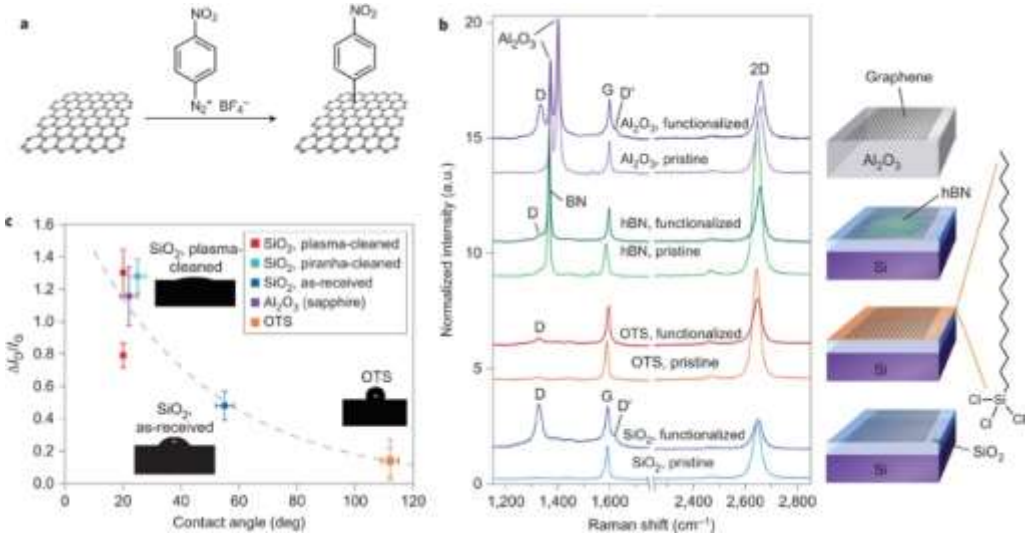

Figure 2.6. a) Scheme of covalent chemical functionalization of graphene by 4-nitrobenzenediazonium tetrafluoroborate. **b)** Representative Raman spectra of CVD-grown graphene deposited on different substrate materials before and after diazonium functionalization, normalized to the G peak height. **c)** Change in intensity ratio of Raman D and G peaks (I_D/I_G) after diazonium functionalization plotted as a function of water contact-angle of the substrate before graphene deposition. Reproduced with permission from reference 59 (Copyright © 2012 Nature publishing group).

[58] E. Bekyarova, M. E. Itkis, P. Ramesh, C. Berger, M. Sprinkle, W. A. de Heer and R. C. Haddon, *J. Am. Chem. Soc.*, **2009**, *131*, 1336.
[59] Q. H. Wang, Z. Jin, K. K. Kim, A. J. Hilmer, G. L. C. Paulus, C. J. Shih, M. H. Ham, J. D. Sanchez-Yamagishi, K. Watanabe, T. Taniguchi, J. Kong, P. Jarillo-Herrero and M. S. Strano, *Nat. Chem*. **2012**, *4*, 724.

In addition, Ruoff and co-workers reported a way to control the graphene layer deformations to obtain regions of high curvature and prove how the graphene curvature can influence the degree of functionalization in different regions.[60] The graphene was transferred onto SiO_2 decorated with nanoparticles to introduce local curvature, and then exposed to aryl radicals to determine the degree of functionalization in the curved and planar regions (see Figure 2.7). The reaction at the planar or wrinkled sites was followed by Raman spectroscopy showing the presence of D band in both sites. However, the intensity of the D band at the wrinkled sites was significantly larger. This experiment demonstrates how the deformation of graphene in well-defined areas can control the functionalization, and opened the door to future investigation using corrugated epitaxial graphene. At the same time, Hiroki Ago and co-workers developed a new strategy to introduce corrugation in the graphene layers by mechanical strain. To this end, polydimethylsiloxane (PDMS) was used as a flexible substrate, obtaining a reversible, non-homogeneous, and damage-free deformation of graphene. This stained graphene was functionalized with different aryl diazonium molecules showing a reactivity that was up to ten times higher than that of the unstrained samples.[61]

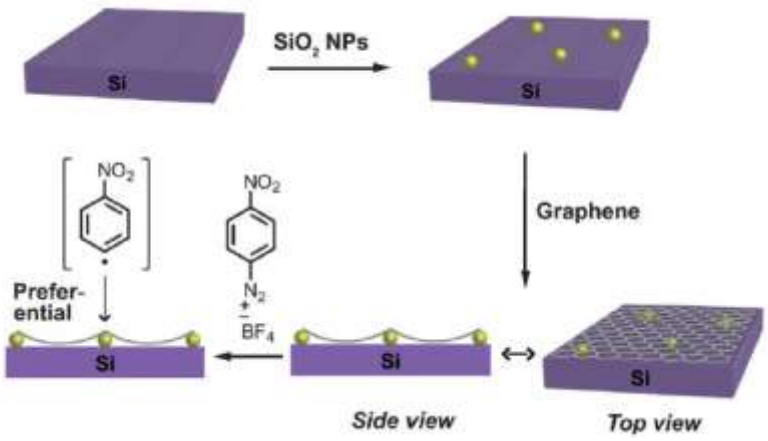

Figure 2.7. Transferring graphene onto a substrate decorated with SiO_2 NPs facilitated the selective functionalization with aryl radicals in regions of high local curvature. Reproduced with permission from reference 60 (Copyright © 2013 Royal Society of Chemistry).

[60] Q. Wu, Y. Wu, Y. Hao, J. Geng, M. Charlton, S. Chen, Y. Ren, H. Ji, H. Li, D. W. Boukhvalov, R. D. Piner, C. W. Bielawski and R. S. Ruoff, *Chem. Commun.*, **2013**, *49*, 677.
[61] M. A. Bissett, S. Konabe, S. Okada, M. Tsuji and H. Ago, *ACS Nano*, **2013**, *7*, 10335.

All these research works show that the rate and yield of functionalization can be affected by the supporting substrate,[59] the numbers of layers[62] and graphene curvature.[63] In order to study reactions on surfaces at the atomic or molecular scale, the ability to precisely control the environment and condition of the surface at hand is an absolute prerequisite. From this perspective, ultra-high vacuum (UHV) is a fundamental tool which allows to keep the surfaces free of contaminants. Recently, CVD growth of graphene in UHV conditions has been successfully applied to metals such as Ru,[64,65] Ir[66] and Pt[67] and results in a high quality corrugated graphene which is single crystalline in wide areas of the substrate. In this chapter we will focus on the functionalization of graphene grown over Ru in UHV conditions.

1.5 Scanning Tunneling microscopy

Scanning tunneling microscopy (STM) is an experimental technique based on the principles of quantum tunneling of electrons between two electrodes separated by a potential barrier, typically used for imaging surfaces of materials with sub-atomic resolution. It was in 1982 when Binning and Rohrer, at the Zurich research laboratory of the International Business Machine (IBM) cooperation, discovered this powerful surface analytical technique, a scanning tunneling microscope (STM) was a tool to look individual atoms on the surface of a material. Gerd Binning and Heinrich Rohrer, won 1986 Nobel Prize in physics for their brilliant invention (see Figure 2.8).[68] Most of the theoretical approaches to the tunneling process occurring in an STM system are based on the formalism developed by J. Bardeen[69] to explain the tunneling processes in metal-insulator-metal junctions. It describes the current flowing between two tunneling electrodes from their wave functions and unperturbed energies. In the case of our STM, the two electrodes are the STM tip and the surface of the sample, and the insulating layer is the vacuum gap between them.

[62] R. Sharma, J. H. Baik, C. J. Perera, and M. S. Strano, *Nano Lett.*, **2010**, *10*, 398-405.
[63] *M. A. Bissett*, *M. Tsuji* and *H. Ago*, *Phys. Chem. Chem. Phys.*, ***2014***, *16*, *11124*-11138.
[64] P. W. Sutter, J. I. Flege, and E. A. S. Er, *Nature Mater.*, **2008**, *7*, 406.
[65] Y. Pan, H. G. Zhang, D. X. Shi, J. T. Sun, S. X. Du, F. Liu, and H. J. Gao, *Adv. Mater.*, **2009**, *21*, 2777.
[66] A. T. N'Diaye, J. Coraux, T. N. Plasa, C. Busse, and T. Michely, *New J. Phys.,* **2008**, *10*, 043033.
[67] T. A., Michely, T. Behm, R. J. Hemminger and J. C. Comsa. *Surf. Sci.*, **1992**, *264*, 261.
[68] G. Binnig, H. Rohrer, Ch. Gerber and E. Weibel, *Phys. Rev. Lett.*, **1982**, *49*, 57.
[69] J. Bardeen, *Phys. Rev. Lett.,* **1961**, *6*, 57.

Figure 2.8. Nobel laureates Gerd Binning (left) and Heinrich Rohrer (right).

The basics component of this microscope are:

- The sample to study.
- A sharp conducting tip which is scanned a flat conducting sample.
- A high precision positioning system to control the location on the tip in the x-y plane parallel to the sample surface.
- A feedback loop to control of the tip above the sample (the z-axis).

The STM is become one of most widespread technology for scanning materials surfaces with sub-nanometric resolution in the three spatial dimensions that allow to observe the individual atoms or molecules on material surfaces. When a bias voltage V_h is applied between tip and sample, a current can be flow, and it can be measured as a function of (x, y) location (see Figure 2.9).

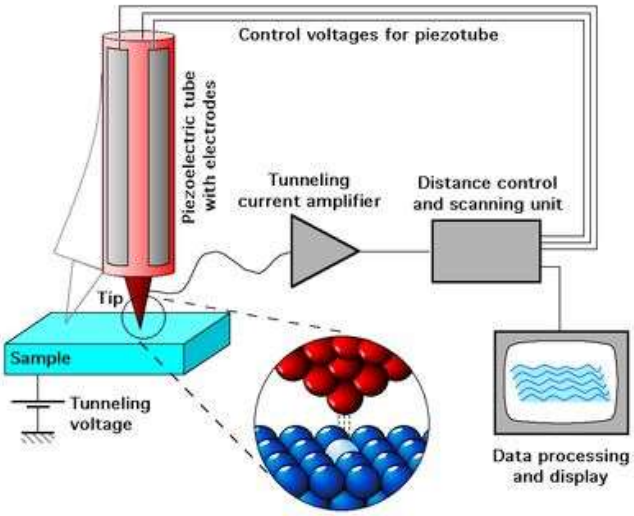

Figure 2.9. Schematic view of a STM.

The metallic tip is placed into close proximity to the surface of conducting samples by means of a high precision positioning system thanks to a piezoelectric scanning stage able to achieve picometric precision when applying high voltages between the different pairs of electrodes. It allows movement in the X-Y plane, as well as in the Z direction. The most common operation mode is the constant current mode, in which a feedback system controls the tip-sample distance by moving the scanner in the Z direction in order to keep the tunneling current constant, while recording the vertical displacement of the tip. The resulting image is formed by representing the vertical displacement of the tip at each point of the X-Y plane, and it represents a convolution between the actual topography of the sample and its electronic structure at fixed voltage.

1.5.1 Local Density of states: What an STM measures

STM is able to measure the local density of states the surface below the tip so in order to understand the tunneling current, first we have to talk about density of states (DOS), it gives information about the number of electron allowed per energy lever as a function if which energy level you consider. This density can vary as a function of position in the crystal, so we can define a local density of states (LDOS) so it gives the density of electrons of a certain energy at that particular spatial location. The tunneling current is thus expressed as:

$$I_t\ (V) \propto \int_{E_F}^{E_{F+eV}} \rho_t\,(E - eV)\rho_s\,(E)T(z, E, eV)dE$$

Where ρ_t and ρ_s represent, respectively, the tip and surface density of states. The factor T (z, E, eV) reveals the dependence of the transmission coefficient on the tips sample distance (z), the energy E, and the bias voltage V. Following this equation the tunneling between tip and surface depends, on three interconnected parameters: the tunneling current (I_t), the bias voltage (V) and the tip-sample distance (z). By applying a bias voltage a tunneling current occurs as show the Figure 2.10.

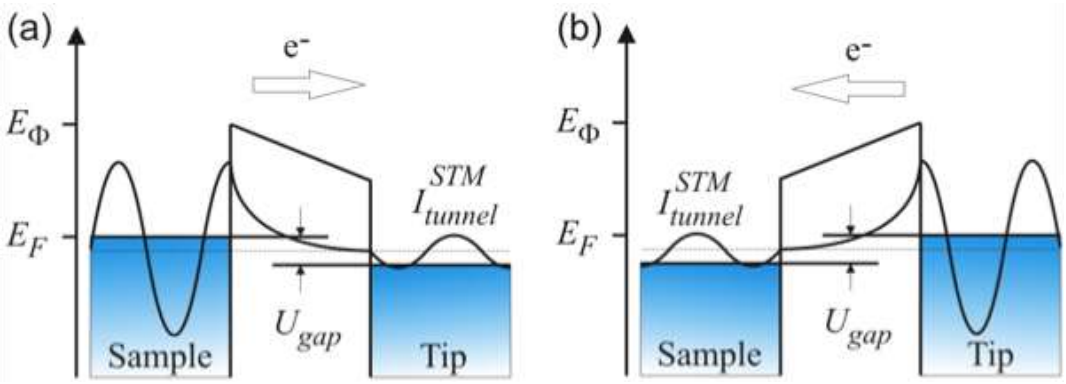

Figure 2.10. One-dimensional diagram of a tip-sample junction **a)** negative bias U has been applied to the sample, electrons tunnel from the occupied states of the sample into the unoccupied states of the tip, **b)** when a positively biased sample, electrons tunnel from the occupied states of the tip to the unoccupied states of the sample.

1.5.2 Scanning tunneling spectroscopy

Before the first successful STM images of organic molecules were reported,[70,71] the scientific began to speculate about possible uses of the instrument for imaging molecules on surfaces. The idea of imaging molecules on surfaces with atomic resolution has implications for the determination of molecular absorption sites and the study of chemical reactions on surfaces. In the last decade strongly chemisorbed molecules, mostly containing aromatic rings, have been observed on metal substrate in ultrahigh vacuum (UHV). STM images carry information about the chemical molecule-surface bonding that only throughout detailed theoretical simulations can be extracted[72,73,74] but STM images are not only topography it can also be a spectroscopic tool for measurements of the local electronic structure which may be deduced from current-voltage curves between tip and sample. This technique of scanning tunneling spectroscopy (STS) has been applied to atomic adsorbates on semiconductors[75] and metals.[76] In this way Hossain and co-workers[77] employed both techniques, the UHV-STM for assessing the morphology of EG/SiC after covalent modification using 4-NBD and the scanning tunneling spectroscopy (STS) to understand the electronic structure of the grafted substrates as show Figure 2.11.

[70] J. K. Gimzewski, E. Stoll and R. R. Schlitter, *Surf. Sci.*, **1987**, *181*, 267.
[71] T. Sleator and R. Tycko, *Phys. Rev. Lett.*, **1988**, *60*, 1418.
[72] P. S. Weiss and D. M. Eigler, Phys. *Rev. Lett.*, **1993**, *71*, 3139.
[73] G. S. McCarty and P. S. Weiss, *J. Phys. Chem. B*, **2002**, *106*, 8005.
[74] A. Kuhnle, T. R. Linderoth, B. Hammer and F. Basenbacker, *Nature*, **2002**, *415*, 891.
[75] I. W. Lyo and P. Avouris, *Science*, **1989**, *245*, 1369.
[76] M. F. Crommie, C. P. Lutz, and D. M. Eigler, *Phys. Rev. B*, **1993**, *48*, 2851.
[77] M. Z. Hossain, M. A. Walsh and M. C. Hersam, *J. Am. Chem. Soc.*, **2010**, *132*, 15399.

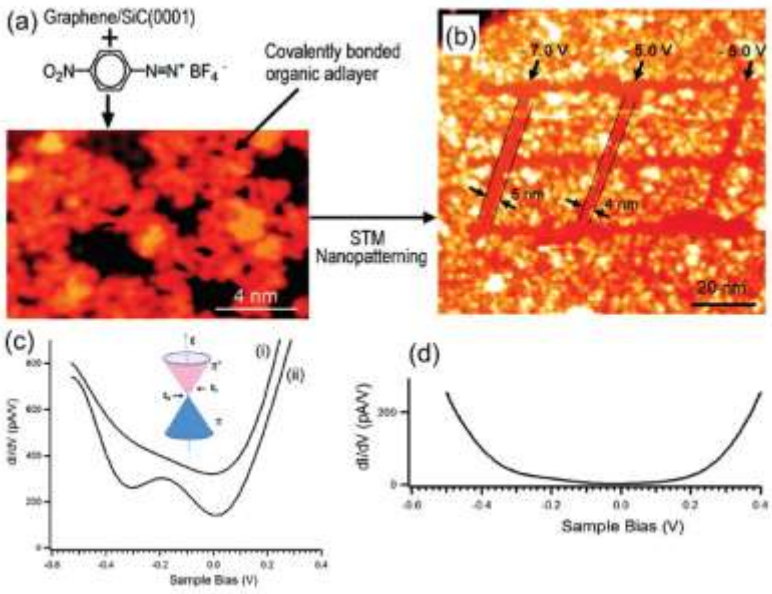

Figure 2.11. a) STM image of the nitrophenyl modified graphene surface. **b)** Bias-dependent nanopatterning of the aryl grafted graphene surface using STM. **c)** dI/dV spectra obtained on the (i) aryl grafted regions of graphene and (ii) clean (unmodified) regions of graphene. **d)** dI/dV spectrum showing the opening of a band gap in covalently modified graphene. Such STS spectra however represent a minority. Reproduced with permission. Reproduced with permission from reference 77 (Copyright © 2010 American Chemical Society).

Scanning Tunneling Spectroscopy (STS) measurements establishes the relations between these parameters by fixing one of them and determining the dependence between the other two. Hence, there are three modes of spectroscopy measurements: i) in I-z curves the variation of the current depending on the tip-sample distance is measured for a constant voltage V, ii) in V-z characteristics I_t is kept constant and the variations in z are measured for different values of V, and iii) in I-V characteristics V and I are varied while z is kept constant. I-V characteristics are the most widely used spectroscopic technique in the STM community. In order to take an I-V curve the feedback loop opens once the tip is positioned at a desired height. The voltage is ramped keeping a constant tip-sample distance and the tunneling current is recorded over the desired range of voltages. The changes in the slope of the obtained I-V curve reflect the conductance variations between the tip and the sample. Another spectroscopy tool is the spatial mapping of the dI/dV signal in a surface area. During a slow *constant current* topography image, the dI/dV signal is simultaneously recorded in each point of the XY matrix at a certain bias voltage V. As a result, we have a mapping that reflects the LDOS of a two-dimensional region at a defined energy eV.

2. Objectives

I have collaborated with IMDEA physicists in the functionalization and study of new 2D materials properties. As part of the study of these new materials we will investigate:

i) The synthesis of graphene/Ru(0001) with a topographic and electronic periodicity of ~3nm, we take advantage of this moiré pattern to carry out a periodic chemical modification of graphene at the nanoscale.

3. Organic covalent patterning of graphene with periodicity at the nanometer scale

3.1 Introduction

Graphene is a bidimensional network of sp^2-hybridized carbon atoms. The planar hexagonal arrangement of carbon in graphene, its chemical stability, and most significantly, its extraordinary physical properties all stem from the extended conjugation provided by the homogeneous sp^2 hybridization.[78] The chemical functionalization of graphene has been intensely pursued in the last years.[79,80] A significant part of the research efforts from the wet chemistry trench have focused on the covalent attachment of molecular fragments to graphene. Addition of malonate-type carbanions and radicals, acylations, and a wide variety of cycloadditions, including [2+1], [2+2], [3+2], and [4+2], have all been explored, among others.[81,82,83,84] Negative consequences of graphene's planar geometry are its insolubility and its tendency to reaggregate to form graphite through π-π and van der Waals interactions. Such issues can be solved using graphene on a suitable substrate.[85] It has been demonstrated that graphene grown or deposited on a substrate can physisorb or chemisorb molecules. Weakly attached adsorbates can act as donors or acceptors leading to changes in carrier concentration that allow the detection of single molecules[86] or the formation of intermolecular bands with long range magnetic order at low temperatures.[87] Beyond the supramolecular functionalization of epitaxial graphene, its covalent modification has been proposed as an ideal tool for adjusting the electronic, optical or magnetic properties. The chemical oxidation of graphene in ultra-high vacuum (UHV) conditions has also been demonstrated.[88,89] The attachment of hydrogen to each atomic site of the graphene lattice to create graphane was proposed,[90] resulting in a change in the hybridization of carbon atoms from sp^2 to sp^3 , as well as the opening a sizeable gap at the Dirac point.[91,92,93] In these experiments, all the atoms in

[78] A. K. Geim and K. S. Novoselov, *Nat. Mater*., **2007**, *6*, 183−191.
[79] V. Georgakilas, M. Otyepka, A. B. V. Chandra, N. Kim, K. C. Kemp, P. Hobza, R. Zboril and K. S. Kim. *Chem. Rev.,* **2012**, *112*, 6156-6214.
[80] C. K. Chua and M. Pumera, *Chem. Soc. Rev*., **2013**, *42*, 3222-3233.
[81] J. Park and M. Yan, *Acc. Chem. Res.,* **2013**, *46*, 181-189.
[82] T. Kuila, S. Bose, A. Mishra, P. Khanra, N. H. Kim and J. H. Lee, *Prog. Mater. Sci.*, **2012**, *57*, 1061-1105.
[83] Z. Sun, D. K. James and J. M. Tour, *J. Phys. Chem. Lett*., **2011**, *2*, 2425-2432.
[84] A. Criado, M. Melchionna, S. Marchesan and M. Prato, *Angew. Chem. Int. Ed*., **2015**, *54*, 10734-10750.
[85] A. Criado, M. Melchionna, S. Marchesan and M. Prato, *Angew. Chem., Int. Ed.,* **2015**, *54*, 2-19.
[86] F. Schedin, A. K. Geim, S. V. Morozov, E. W. Hill, P. Blake, M. I. Katsnelson and K. S. Novoselov*, Nat. Mater*., **2007**, *6*, 652-655.
[87] M. Garnica, D. Stradi, S. Barja, F. Calleja, C. Díaz, M. Alcamí, A. L. Vázquez de Parga, F. Martín and R. Miranda, *Nat. Phys.*, **2013**, *9*, 368-374.
[88] N. A. Vinogradov, K. Schulte, A. Mikkelsen, E. Lundgren, N. Mårtensson and A. B. J. Preobrajenski, *Phys. Chem. C*, **2011**, *115*, 9568-9577.
[89] M. Z. Hossain, J. E. Johns, K. H. Bevan, H. J. Karmel, Y. T. Liang, S. Yoshimoto, K. Mukai, T. Koitaya, J. Yoshinobu, M. Kawai, A. M. Lear, L. L. Kesmodel, S. L. Tait and M. C. Hersam, *Nat. Chem*., **2012**, *4*, 305-309.
[90] J. O. Sofo, A. S. Chaudhari and G. D. Barber, *Phys. Rev. B: Condens. Matter Mater. Phys*., **2007**, *75*, 153401.
[91] D. W. Boukhvalov, M. I. Katsnelson and A. I. Lichtenstein, *Phys. Rev. B: Condens. Matter Mater. Phys*., **2008**, 77, 035427.
[92] D. C. Elias, R. R. Nair, T. M. G. Mohiuddin, S. V. Morozov, P. Blake, M. P. Halsall, A. C. Ferrari, D. W. Boukhvalov, M. I. Katsnelson, A. K. Geim and K. S. Novoselov, *Science*, **2009**, *323*, 610-613.

the graphene lattice exhibit very similar reactivity and the only way to get an atomically well-defined long range order is to saturate all the atomic sites, creating a completely new material, e.g., graphane or graphene oxide. This lack of selectivity is a major drawback if the objective of the covalent modification is to modulate the electronic properties of graphene. It has been predicted that a periodic patterning of graphene would lead to new electronic properties[94] including a direct relation between the periodicity and the bandgap amplitude[95,96] Therefore the chemical functionalization of graphene in a periodic fashion with a periodicity in the range of 1 to 5 nm is highly desirable.There have been several approaches for obtaining site selectivity in the chemical functionalization of graphene. One approach relies on patterning the surface using an atomic force microscope (AFM).[97,98] The main drawback of this approach is the time needed to write the motifs and also the difficulty of scaling the process to millimeter size samples. Another approach relies on the fact that strain and curvature strongly enhance the local reactivity of the graphene[99,100] although so far no long range order has been achieved. Graphene grown on metallic substrates presents a moiré pattern due to the difference in lattice parameter between graphene and the substrate.[101] In particular, graphene grown on Ir(111) has been used to study the influence of a spatially ordered covalent functionalization in the graphene electronic structure.[102,103] Due to the weak interaction between the graphene and the Ir(111) substrate, the moiré pattern presents several rotational domains with different periodicities.[104,105] The weak interaction with the substrate also renders all the carbon atoms almost identical electronically and no distinct reactive sites are present in the system. To the best of our knowledge, there have been no reports of covalent functionalization of graphene with atomic-level selectivity.

---

[93] D. Haberer, D. V. Vyalikh, S. Taioli, B. Dora, M. Farjam, J. Fink; D. Marchenko, T. Pichler, K. Ziegler, S. Simonucci, M. S. Dresselhaus, M. Knupfer, B. Büchner and A. Grüneis, *Nano Lett*., **2010**, *10*, 3360-3366.

[94] C. H. Park, L. Yang, Y. W. Son, M. L. Cohen and S. G. Louie, *Nat. Phys*., **2008**, *4*, 213−217.

[95] F. P. Ouyang, S. L. Peng, Z. F. Liu, and Z. R. Liu. *ACS Nano,* **2011**, *5*, 4023−4030.

[96] M. Dvorak, W. Oswald and Z. Wu, *Sci. Rep*., **2013**, *3*, 2289.

[97] S. Bian, A. M. Scott, Y. Cao, Y. Liang, S. Osuna, K. N. Houk and A. B. Braunschweig, *J. Am. Chem. Soc*., **2013**, *135*, 9240-9243.

[98] M. Z. Hossain, M. A. Walsh and M. C. Hersam, *J. Am. Chem. Soc*., **2010**, *132*, 15399-15403.

[99] Q. Wu, Y. Wu, Y. Hao, J. Geng, M. Charlton, S. Chen, Y. Ren, H. Ji, H. Li, D. W. Boukhvalov, R. D. Piner, C. W. Bielawski and R. S. Ruoff, *Chem. Commun*., **2013**, *49*, 677-679.

[100] M. A. Bissett, S. Konabe, S. Okada, M. Tsuji and H. Ago, *ACS Nano***, 2013**, *7*, 10335-10343.

[101] A. L. Vázquez de Parga and R. Miranda In Graphene: Properties, preparation, characterization and devices; Chapter 6, V. Skakalova and A. B. Kaiser, *Eds.; Woodhead Publishhing*, **2014**.

[102] R. Balog, B. Jørgensen, L. Nilsson, M. Andersen, E. Rienks, M. Bianchi, M. Fanetti, E. Laegsgaard, A. Baraldi, S. Lizzit, Z. Sljivancanin, F. Besenbacher, B. Hammer, T. G. Pedersen, P. Hofmann and L. Hornekaer, *Nat. Mater*., **2010**, *9*, 315-319.

[103] R. Balog, M. Andersen, B. Jørgensen, Z. Slijvancanin, B. Hammer, A. Baraldi, R. Larciprete, P. Hofmann, L. Hornekaer and S. Lizzit, *ACS Nano* **2013**, *7*, 3823-3832.

[104] J. Coraux, A. T. N'Diaye, C. Busse and T. Michely, *Nano Lett.,* **2008**, *8*, 565-570.

[105] E. Loginova, S. Nie, K. Thurmer, N. C. Bartelt and K. F. McCarty, *Phys. Rev. B: Condens. Matter Mater. Phys*., **2009**, *80*, 085430.

3.1 Results and discussion

Here, we describe a method for the organic covalent modification of graphene with exquisite spatial periodicity at the atomic scale. We take advantage of the fact that the growth of graphene on lattice-mismatched metallic substrates allows us to tailor the geometric and electronic properties of the graphene overlayer in a periodic fashion. In particular, we use graphene grown on Ru(0001) that presents a moiré pattern with a periodicity of ≈ 3 nm. The moiré shows periodically distributed areas where the charge transfer due to the interaction between graphene and ruthenium is rather large and, as a consequence, these graphene areas present higher chemical reactivity. This point is illustrated by demonstrating that cyanomethyl radicals ($CH_2CN^{\bullet}$) produced by homolytic breaking of acetonitrile (CH_3CN) in UHV by electron bombardment bind to graphene preferentially at specific atomic sites with a nearly complete selectivity (>98%).

Growth of graphene through chemical vapor deposition (CVD) on a variety of metallic substrates is one of the preferred methods for the synthesis of high-quality graphene.[106,107,108,109] This method presents the additional advantage that the strength in the interaction between graphene and the metallic substrate can be tuned by varying the chemical nature of the latter.[110] In this respect some of us have previously reported the epitaxial growth of graphene on Ru(0001) (hereafter, gr/Ru(0001)) where due to the mismatch between the hexagonal lattices of graphene and Ru, the system presents a moiré pattern with a surface periodicity of 2.93 nm.[111] Figure 2.12a shows that three different areas can be distinguished inside the moiré unit cell depending on the registry between the carbon atoms and the last two ruthenium atomic layers, namely: the "atop" region where all carbon atoms are placed above threefold hollow sites of the Ru surface (vertex of the blue triangles in Fig.2.12a), the "HCP-Top" region where half of the carbon atoms are located on HCP threefold positions and the other half on top of Ru atoms (dashed blue triangle in Fig. 2.12a) and the "FCC-Top" region where half of the carbon atoms are located on FCC threefold positions and the other half on top of Ru atoms (solid blue triangle in Figure. 2.12a).

[106] S. J. C hae, F. Günes, K. K. Kim, E. S. Kim, G. H. Han, S. M. Kim, H. J. Shin, S. M. Yoon, J. Y. Choi, M. H. Yang, C. W. Park, D. Pribat and Y. H. Lee, *Adv. Mater*., **2009**, *21*, 2328-2333.
[107] A. Reina, X. Jia, J. Ho, D. Nezich, H. Son, V. Bulovic, M. S. Dresselhaus and J. Kong, *Nano Lett*., **2009**, *9*, 30-35.
[108] X. Li, X. Cai, J. An, S. Kim, J. Nah, D. Yang, R. Piner, A. Velamakanni, I. Jung, E. Tutuc, S. K. Banerjee, L. Ruoff and R. S. Colombo, *Science*, **2009**, *324*, 1312-1314.
[109] Y. Lee, S. Bae, H. Jang, S. Jang, S. E. Zhu, S. H. Sim, Y. I. Song, B. H. Hong and J. H. Ahn, *Nano Lett*., **2010**, *10*, 490-493.
[110] A. B. Preobrajensk, M. L. Ng, A. S. Vinogradov and N. Martensson, *Phys. Rev. B: Condens. Matter Mater. Phys*., **2008**, *78*, 073401.
[111] A. L. Vázquez de Parga, F. Calleja, B. Borca; J. J. Hinarejos, M. G. C. Passeggi, F. Guinea and R. Miranda, *Phys. Rev. Lett*., **2008**, *100*, 056807.

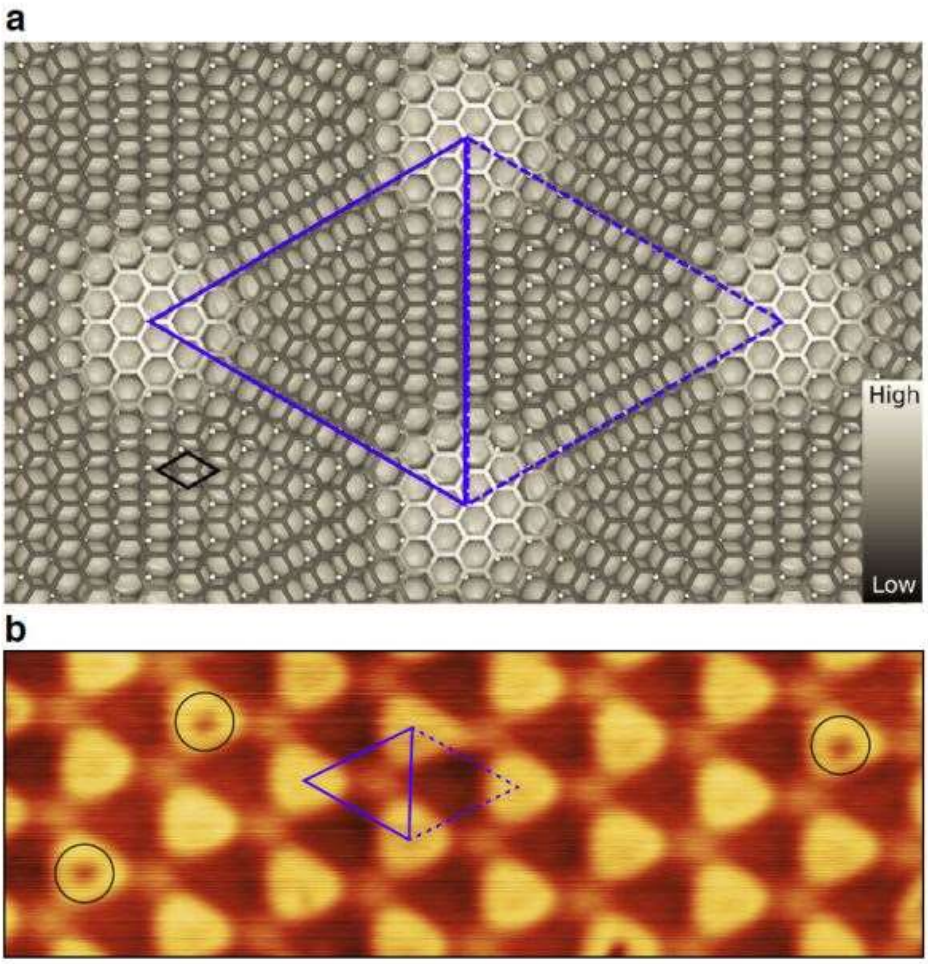

Figure 2.12. **a)** Ball model of the gr/Ru(0001) surface, where grey circles represent the Ru atoms of the first atomic layer. The graphene hexagonal lattice is shown in a black to white color scale to indicate the height of the carbon atoms respect to the Ru(0001) surface. The unit cell of the moiré pattern is highlighted by two blue triangles. At the vertices all carbon atoms fall on threefold hollow sites of the Ru(0001) surface. At the center of the solid (dashed) triangle one carbon sub-lattice falls on FCC-stacked (HCP-stacked) threefold hollow sites and the other one on top positions. These two regions are named "FCC-Top" and "HCP-Top" respectively. **b)** STM image acquired on pristine gr/Ru(0001) (24×7 nm², V_b= +1.5 V, I_t = 30 pA). The moiré pattern arising from the lattice mismatch is highlighted in blue. The HCP-Top area is marked with the dashed triangle and the FCC-Top area is marked the solid triangle. Four point defects on the top areas are indicated by black circles.

Figure 2.12b shows a Scanning Tunneling Microscope (STM) topographic image of the surface measured at +1.5V bias voltage. Under these bias conditions, the moiré appears as a hexagonal array of bumps with a small corrugation (~40 pm). The origin of the bumps is the change in registry within the moiré unit cell that produces a spatial modulation in the interaction between the C and Ru atoms, from weak van der Waals interaction in the high areas of the STM images to strong interaction in the lower areas.[112,113] This spatial variation of

[112] D. Stradi, S. Barja, C. Díaz, M. Garnica, B. Borca, J. J. Hinarejos, D. Sánchez-Portal, M. Alcamí, A. Arnau, A. L. Vázquez de Parga, R. Miranda and F. Martín, *Phys. Rev. B: Condens. Matter Mater. Phys.*, **2013**, *88*, 245401.
[113] D. Stradi, S. Barja, C. Díaz, M. Garnica, B. Borca, J. J. Hinarejos, D. Sánchez-Portal, M. Alcamí, A. Arnau, A. L. Vázquez de Parga, R. Miranda and F. Martín, *Phys. Rev. Lett.,* **2011**, *106*, 186102.

the interaction modulates all surface electronic properties, from the potential surface[114] to the electronic structure around the Fermi level,[111] which directly affects the chemical reactivity. The STM imaging conditions of Figure 2.12b also reveal the presence of four point defects on top of the ripples (marked with black circles), which we attribute to subsurface oxygen trapped during the graphene growth process. Recently, Ruoff, Bielawski and co-workers have introduced a method for the selective functionalization of graphene on areas with high local curvature.[99] Considering this, and the seminal work by Balog and co-workers on the patterned hydrogenation of graphene on Ir we reasoned that graphene on Ru(0001) seems an ideal playground to exploit a similar strategy for a periodic chemical modification of graphene with sub-nanoscale selectivity, due to the presence of the moiré-related corrugation. In addition to this corrugation the metal-graphene interaction in gr/Ru(0001) is sufficiently strong to affect the chemical reactivity of specific atomic sites of the graphene overlayer. Thus following the same approach of Ruoff, we treated gr/Ru(0001) with solution of 4-nitrophenyl diazonium tetrafluoroborate (NDA) in acetonitrile under a nitrogen atmosphere with concentrations varying from 1mg/mL to 0.01mg/mL changing the exposition time from 1h down to 1-2 seconds, washing the surface afterwards with CH_3CN to remove the unreacted aryl compound and dried it under a N_2 gas flow, the functionalization was carried out leaving a well-defined control area without NDA. The samples are then introduced in UHV system and explored by means of STM. As the Figure 2.13a shown the surface is covered by 'big mountains', to the point that the moiré pattern is no visible. The resulting micrographs are the same for all the concentrations and time exposure. Surprisingly we found indistinguishable STM images in the region where the graphene had not been exposed to the NDA, but only to acetonitrile during washing (Figure 2.13b).

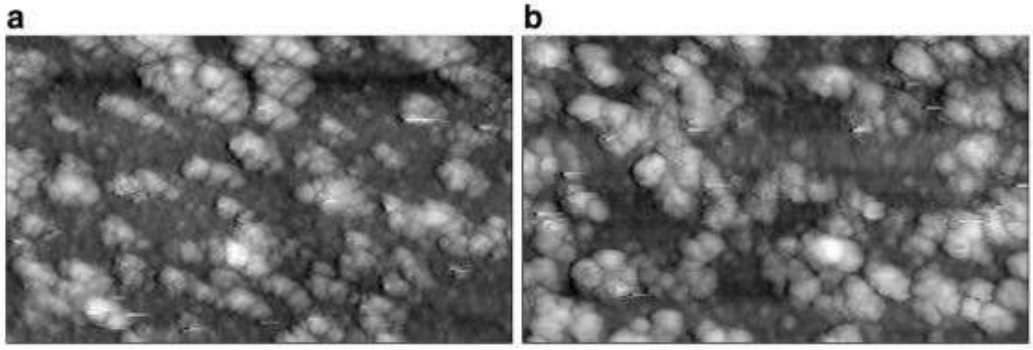

2.13. Wet chemistry treatment a) 70×40 nm² STM image (I_t = 10 pA, V_t = -4.0 V) obtained after dosing a drop of NDA and rinsing with acetonitrile. **b)** 70×40 nm² control image obtained outside the drop of NDA. Both images have been acquired at 80 K in UHV conditions after annealing the samples to 500 K also in UHV conditions.

[114] B. Borca, S. Barja; M. Garnica, D. Sánchez-Portal, V.M. Silkin, E. V. Chulkov, C. F. Hermanns, J. J. Hinarejos, A. L. Vázquez de Parga, A. Arnau, P. M. Echenique and R. Miranda, *Phys. Rev. Lett*., **2010**, *105*, 036804.

With these experimental results, we decided to investigate the absorption of CH_3CN on gr/Ru(0001) in ultra-high vacuum conditions. The sample was exposed to $1x10^{-6}$ Torr of CH_3CN for 3 minutes at room temperature discovered that gr/Ru(0001) can be functionalized by cyanomethyl radicals with exquisite spatial selectivity. Representative STM images are shown in Figure 2.14a-f, measured at 80 K as a function of the sample bias voltage after exposure of the sample at room temperature to 1×10^{-6} Torr of CH_3CN for 3 minutes, equivalent to 180 Langmuirs. Bright bumps related to the adsorption of acetonitrile, located exclusively at the valleys and the HCP-top sites are observed for voltages between +1.25 V and +2 V. The molecular attachments show an apparent height of 26 ± 2 pm and a lateral width of 560 ± 20 pm at +1.5 V. The shape and size of the molecular attachments are very similar to those measured on STM images taken of acetonitrile adsorbed on Pt(111).[115] Figure 2.14g shows Scanning Tunnelling Spectroscopy (STS) recorded on various positions of the moiré unit cell. The curves measured on top of the ripples and the ones measured on the (empty) low areas of the moiré show the well-known asymmetry between the occupied and empty density of states of gr/Ru(0001).[111] The curves measured on the molecular attachments present an additional peak at +1.6 eV identified as the Lowest Unoccupied Molecular Orbital (LUMO). The energy of the Highest Occupied Molecular Orbital (HOMO) is below -2.0 V and, therefore, out of the measured energy window. The images confirm that for bias voltages below +0.5 V the molecular attachments are not visible, since tunneling is being carried out in the gap between the HOMO and LUMO. For bias voltages larger than +2.5 V the reduction in the apparent corrugation of the moiré pattern and its subsequent inversion[116] hinders the precise identification of the adsorption site of the molecular attachments.

[115] S. Katano, Y. Kim, M. Trenary and M. Kawai, *Chem. Commun*., **2013**, *49*, 4679-4681.

[116] B. Borca, S. Barja, M. Garnica, M. Minniti, A. Politano, J. M. Rodríguez-García, J. J. Hinarejos, D. Farías, A. L. Vázquez de Parga and R. Miranda, *New J. Phys*., **2010**, *12*, 093018.

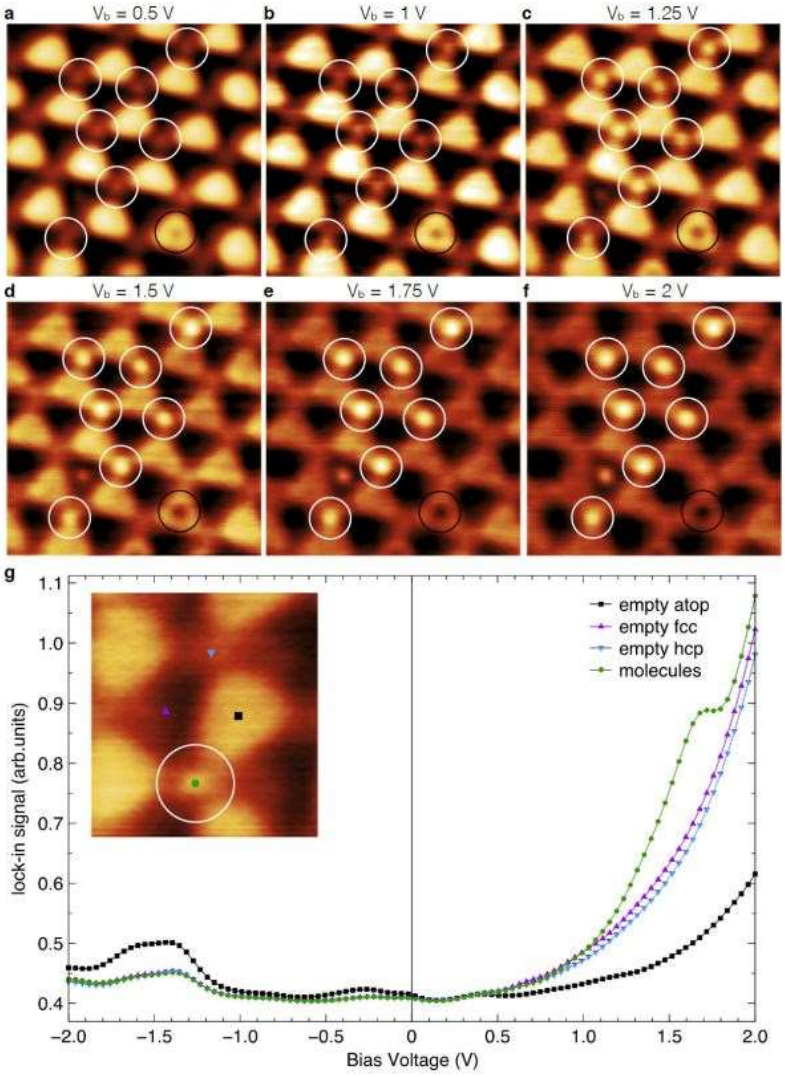

Figure 2.14. (a)-(f) 10×10 nm^2 STM images with different bias voltages acquired at 80 K after exposing gr/Ru(0001) to 180 Langmuir of acetonitrile at 300 K. Notice the related presence of seven bright bumps on HCP-Top sites (marked with a white circle), one on FCC-Top site and one graphene point defect (marked with a black circle). **(g)** Differential conductance, dI/dV, curves recorded at 80 K with the tip of the STM placed on top of the molecular attachments (green), the FCC-Top, HCP-Top (purple and blue, respectively) and the ripples (black) areas of the moiré pattern of gr/Ru(0001). The dI/dV individual curves were measured in open feedback loop conditions with the tunneling gap stabilized at +0.3V and 50 pA. The lock-in signal was acquired using a modulation in the bias voltage of 40 mV (rms), a frequency of 856 Hz and a time constant of 10 ms.

Remarkably, single molecular attachments can be observed exclusively at the valleys of the moiré pattern. Moreover, there is a strong preference for HCP-Top sites over FCC-top regions offering another level of selectivity. For higher coverages on the order of 0.50 acetonitrile molecules per moiré unit cell, 98.0 ± 1% of the HCP-Top and 2 ± 1% of the FCC-Top areas of the unit cells are occupied. The same site preference has been observed for TCNQ[117] and F4-TCNQ[118] molecules adsorbed on gr/Ru(0001) and can be understood considering the difference in the electronic structure between the FCC-Top and HCP-Top areas.[118]

In the present case, however, the bonding between the adsorbed molecular attachments and graphene relies on a strong C-C covalent bond, which modifies the sp^2 hybridization of a single C atom in graphene. This is demonstrated in Figure 2.15, in which a region containing three molecular attachments located in HCP-Top regions, encircled in white, is imaged with atomic resolution. The STM image has been taken in conditions where the molecular attachment is transparent (2 mV bias and 800 pA current) because the small bias voltage is probing the energy gap between HOMO and LUMO of the adsorbed molecule. Accordingly, the tip does not move up when is located on top of the molecules attached to the surface. Simultaneously, the C atoms with a modified hybridization where the three molecules are bonded appear as single atom "holes". Remarkably, the covalent attachments are located exclusively on crystallographically identical carbon atoms of the graphene overlayer. The inset shows the bright bumps of the molecules adsorbed in the "hole" sites by restoring a bias voltage where they can be imaged through their LUMO orbitals. In spite of the harsh imaging conditions all three molecules remain in place without any noticeable change in shape or position.

Going down to atomic resolution parameters without sweeping the molecular attachments away during the scan is contrary to what happens with physisorbed or even strongly chemisorbed isolated molecules, such as TCNQ9 or F4-TCNQ,[119] indicating the covalent nature of their attachment to graphene. In fact, the molecular attachments cannot be displaced from their adsorption sites by the STM tip following standard manipulation techniques.[120,121] Annealing the sample in UHV further confirms the strong bond between graphene and the molecular attachments. The sample remains unaltered up to 573 K.

[117] M. Garnica, D. Stradi, F. Calleja, S. Barja, C. Díaz, M. Alcamí, A. Arnau, A. L. Vázquez de Parga, F. Martín and R. Miranda, *Nano Lett.,* **2014**, *14*, 4560-4567.
[118] D. Stradi, M. Garnica, C. Díaz, F. Calleja, S. Barja, M. Alcamí, N. Martín, A. Arnau, A. L. Vázquez de Parga, R. Miranda and F. Martín, *Nanoscale*, **2014**, *6*, 15271-15279.
[119] S. Barja, M. Garnica, J. J. Hinarejos, A. L. Vázquez de Parga, N. Martín and R. Miranda, *Chem. Commun*., **2009**, *46*, 8198.
[120] J. A. Stroscio and D. M. Eigler, *Science,* **1991**, *254*, 1319-1326.
[121] Hla, S.-W. *J. Vac. Sci. Technol., B: Microelectron. Process. Phenom*., **2005**, *23*, 1351-1360.

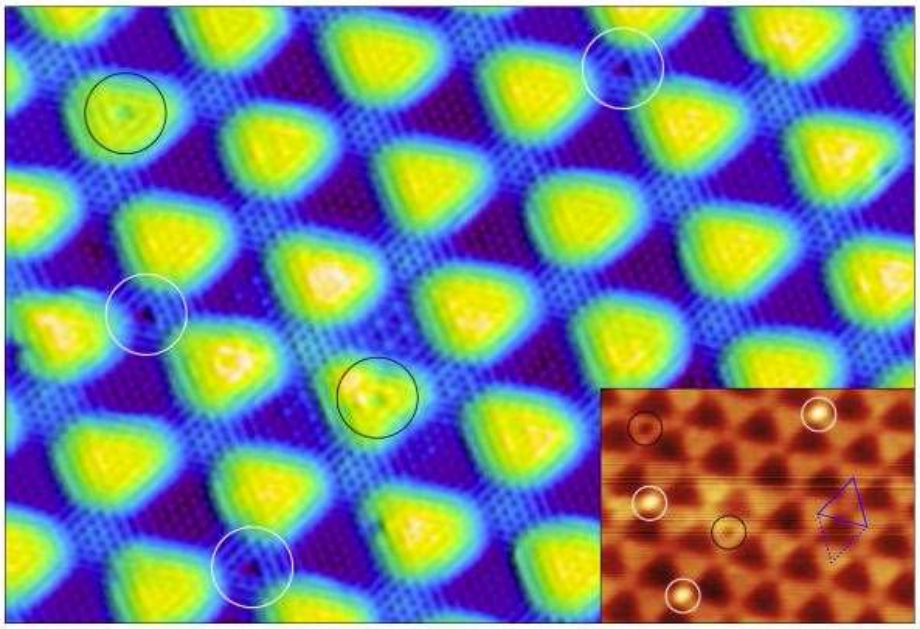

Figure 2.15. High resolution STM image (17×12 nm^2, V_b = 2 mV, I_t = 800 pA), acquired at 80 K on a region containing three molecular species (white circles) and two oxygen-related defects on graphene (black circles). Inset: Same region scanned afterwards with V_b= +1.7 V and I_t = 100 pA. All three molecular attachments are still in place. The moiré unit cell is highlighted in blue in the inset.

These facts confirm the selective covalent patterning of gr/Ru(0001) through treatment with CH_3CN beyond reasonable doubt. Given the relatively inert nature of CH_3CN, and knowing that under high-vacuum (10^{-6} Torr) conditions ion gauges produce and emit active chemical species through ionization of the residual gases in the vacuum chamber, which can be adsorbed onto graphene,[122] we reasoned the same process may take place during the exposure of the graphene surface to the acetonitrile molecules in UHV, since we use an ion gauge to measure the partial pressure of the acetonitrile gas. In order to gather experimental evidence of the molecular fragments that can be produced in the ion gauge during the CH_3CN exposition, we introduced in the UHV chamber the same partial pressure (1×10^{-6} Torr) of acetonitrile used during the graphene exposure and recorded the mass spectrum of the gas utilizing a quadrupole mass spectrometer (QMS). The ionization chamber of the QMS works under the same physical principle as the ion gauges and therefore the spectra measured is a reliable indicator of the chemical species produced in the ion gauge. The m/z pattern is perfectly consistent with a significant concentration of $CH_2CN^{\bullet}$. It is well known that $CH_2CN^{\bullet}$ can be generated directly from CH_3CN by homolytic cleavage of a C-H bond.[123,124,125] Moreover, the

[122] C. Caillier, D. K. Ki, Y. Lisunova, I. Gaponenko, P. Paruch and A. F. Morpurgo, *Nanotechnology*, **2013**, *24*,405201.
[123] J. Lalevee, X. Allonas and J. P. Fouassier, *J. Org. Chem*,. **2005**, *70*, 814.
[124] D. J. Henry, C. J. Parkinson, P. M. Mayer and L. J. Radom, *Phys. Chem. A,* **2001**, *105*, 6750.
[125] M. L. Coote, *J. Phys. Chem. A***, 2004**, *108*, 3865.

cyanomethyl radical ($CH_2CN^{\bullet}$) is known to react with C-C double bonds[126,127,128] and arenes[129] forming C-C bonds.

To provide further experimental evidence for this hypothesis we exposed the sample to 180 Langmuir of acetonitrile with the ion gauge in the preparation chamber turned *off* and under these conditions no molecular attachments were detected on the surface. The Figure 2.16a demonstrates that in these conditions no molecular attachments are detected on the surface. Only some oxygen related defects already present on the ripples of the moiré after the graphene growth are seen, and only one molecular attachment that could be related with the CH_3CN exposure. The same experiment was carried out under identical conditions, but with the ion gauge on and the sample located at a distance of 12 cm from the gauge during the exposition and molecular attachments are clearly detected (see Figure 2.16b). These results show that the degree of functionalization depends on the ionization induced by the electron filament of the gauge. The CH_3CN molecules are homolitically broken at the ion gauge by electron bombardment at the gauge, creating $CH_2CN^{\bullet}$ radicals. These radicals diffuse into the ultra-high vacuum chamber and some arrive to the gr/Ru(0001) surface and react with the chemically active atomic sites within the moiré unit cell. The carbon atom on the graphene atomic lattice changes its hybridization from sp^2 to sp^3, locally distorting the graphene atomic lattice and its local electronic structure.

[126] E. Kukk, R. Sankari, M. Huttula, A. Sankari, H. Aksela and S. J. Aksela, *Electron Spectrosc. Relat. Phenom.*, **2007**, *155*, 141.
[127] J. Q. Wu, I. Beranek and H. Fischer, *Helv. Chim. Acta*, **1995**, *78*, 94.
[128] M. W. Wong and L. J. Radom, *Phys. Chem*. **1995**, *99*, 8582.
[129] H. Yoshida, Y. Fujimura, H. Yuzawa, J. Kumagai and T. Yoshida, *Chem. Commun*., **2013**, *49*, 3793.

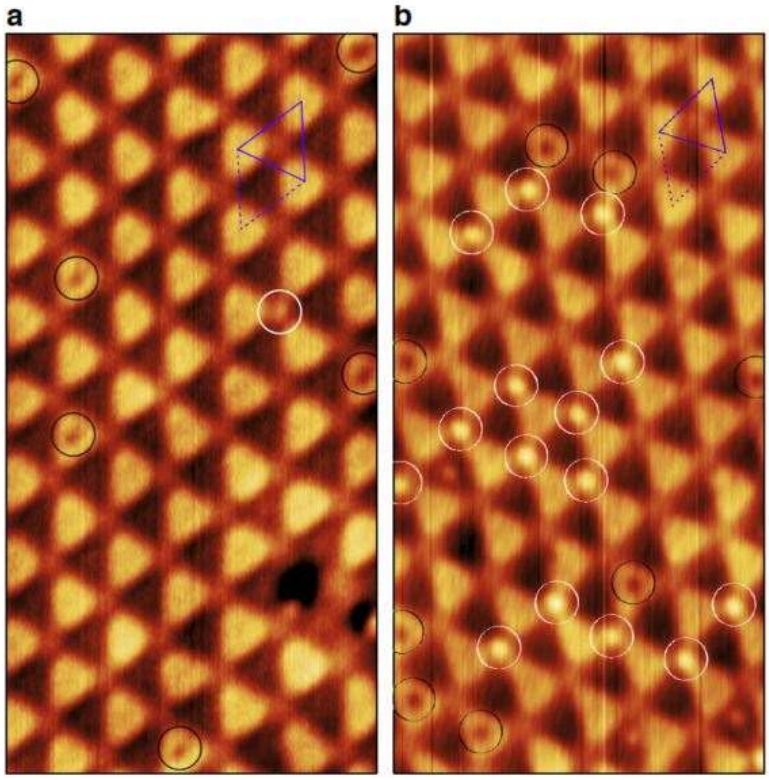

Figure 2.16. Influence of the ion gauge in the site-effective functionalization of gr/Ru(0001). 15×30 nm^2 STM images corresponding to 180 Langmuir exposure (3 min at 1×10^{-6} Torr) to CH_3CN with (a) the ion gauge off, and (b) with the ion gauge on and the sample at 12 cm. The molecular attachments are marked with white circles and the oxygen related defects with black circles. The moiré unit cell is highlighted in blue.

To gain atomic understanding of the reaction, we ran DFT calculations for the adsorption of $CH_2CN^{\bullet}$ on gr/Ru(0001). The results are summarized in Figure 2.17. In agreement with the experimental data, the adsorption energies are within the limits of a covalent bond (>2.1 eV) (see Figure 2.17a). Remarkably, the HCP-Top/FCC-Top preference we observe experimentally is also reproduced. The two most stable configurations, HCP-Top (1) and HCP-Top (4), with adsorption energies of 2.34 eV and 2.49 eV are shown in Figure 2.17b, and Figure 2.17c. In this case, it is the alkyl carbon atom of $CH_2CN^{\bullet}$ that lies closer to the graphene surface, as is observed in the cycanomethylation of arenes.[129] The graphene carbon atom immediately below the CH_2CN addend is clearly displaced from the graphene mesh. The shortest distance between an acetonitrile carbon atom and a graphene atom are 1.60 Å and 1.58 Å for the acetonitrile in the HCP-Top (1) and HCP-Top (4) adsorption geometries shown in Figure 2.17b and Figure 2.17c, in very good accordance with a C-C single bond, for which the textbook C-C distance is 1.54 Å.[130]

[130] T. L. Cottrell, The Strengths of Chemical Bonds, Butterworth Scientific, **1978**.

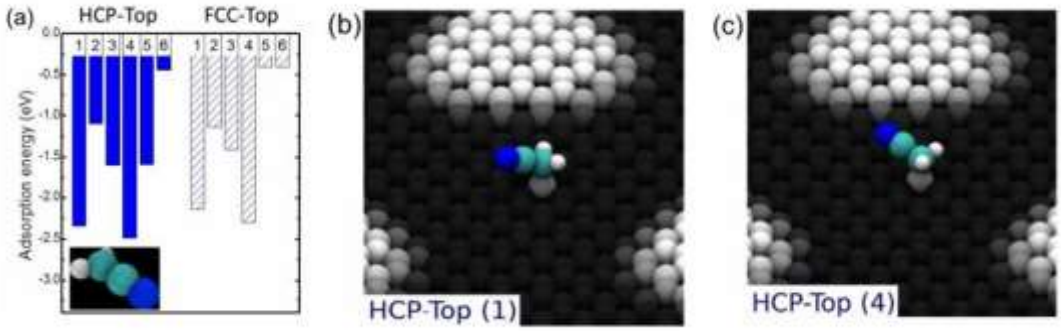

Figure 2.17. a) Adsorption energies calculated for the different configurations of CH_2CN on the HCP-top (solid boxes) and on the FCC-Top (empty boxes) regions of the gr/Ru(0001) moiré. The inset shows the ground state geometry of the corresponding molecule in the gas-phase. **(b)** and **(c)**, Ground state adsorption geometries of the two most stable configurations of CH_2CN adsorbed in the HCP-Top region of the gr/Ru(0001) moiré. Graphene atoms are colored from dark-gray to white depending on their height. Carbon, nitrogen and hydrogen atoms of the molecule are colored in cyan, blue and white.

To investigate the role of the Ru metallic substrate we synthesized graphene on Ir(111). Graphene on Ir(111) presents a moiré pattern[131] with a periodicity of 9.3 × 9.3, very similar to the one presented on the gr/Ru(0001) system but with almost negligible[132] charge transfer and interaction between the carbon and iridium. Exposing gr/Ir(111) CH_3CN for three minutes with a partial pressure of 3×10^{-6} Torr, with the ion gauge on and the sample in the closest position, no $CH_2CN^{\bullet}$ attachments were observed, confirming that the strong interaction between Ru and the graphene over layer plays a fundamental role in the covalent functionalization (see Figure 2.18).

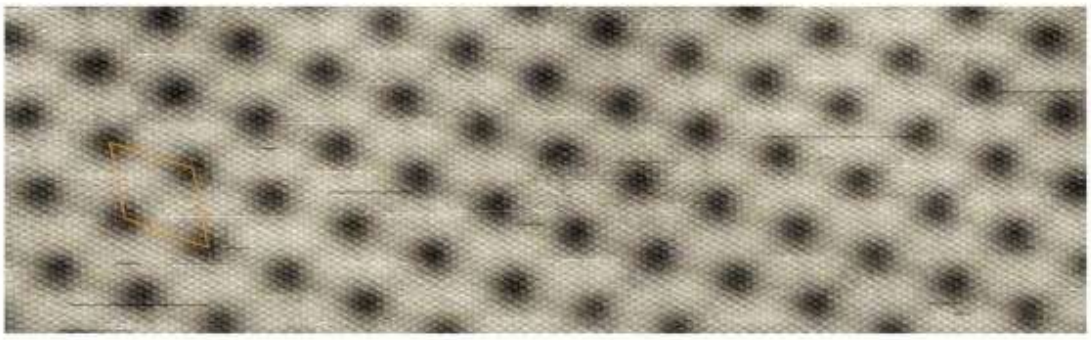

Figure 2.18. 36×11 nm^2 atomic resolution STM image measured on a gr/Ir(111) surface exposed to 3×10^{-6} Torr of acetonitrile for three minutes. Imaging conditions 25 mV bias voltage and 2 nA of tunneling current. The moiré unit cell is highlighted in orange.

[131] A. T. N'Diaye, J. Coraux, T. N. Plasa, C. Busse and T. Michely, *New J. Phys*., **2008**, *10*, 043033.
[132] X. Li, X. Cai, J. An, S. Kim, J. Nah, D. Yang, R. Piner, A. Velamakanni, I. Jung, E. Tutuc, S. K. Banerjee, L. Ruoff and R. S. Colombo, *Science,* **2009**, *324*, 1312.

Due to the strong interaction between graphene and the Ru(0001) surface, the moiré pattern not only presents specific atomic sites with high chemical reactivity but long range order as well. In this system it is possible to grow graphene layers presenting lateral domain sizes exceeding 300 nm.[116,133] The large domain size together with the exquisite spatial selectivity of our functionalization method ensures the long range order of the functionalized surface. Figure 2.19 shows a 66 x 40 nm^2 STM image of the functionalized gr/Ru(0001). In the image 50% of the moiré unit cells are occupied by one chemically bonded – CH_2CN molecule. Of those 98.6% are bonded in the HCP-Top areas, while only 1.4% of the – CH_2CN are bonded to the FCC-TOP areas.

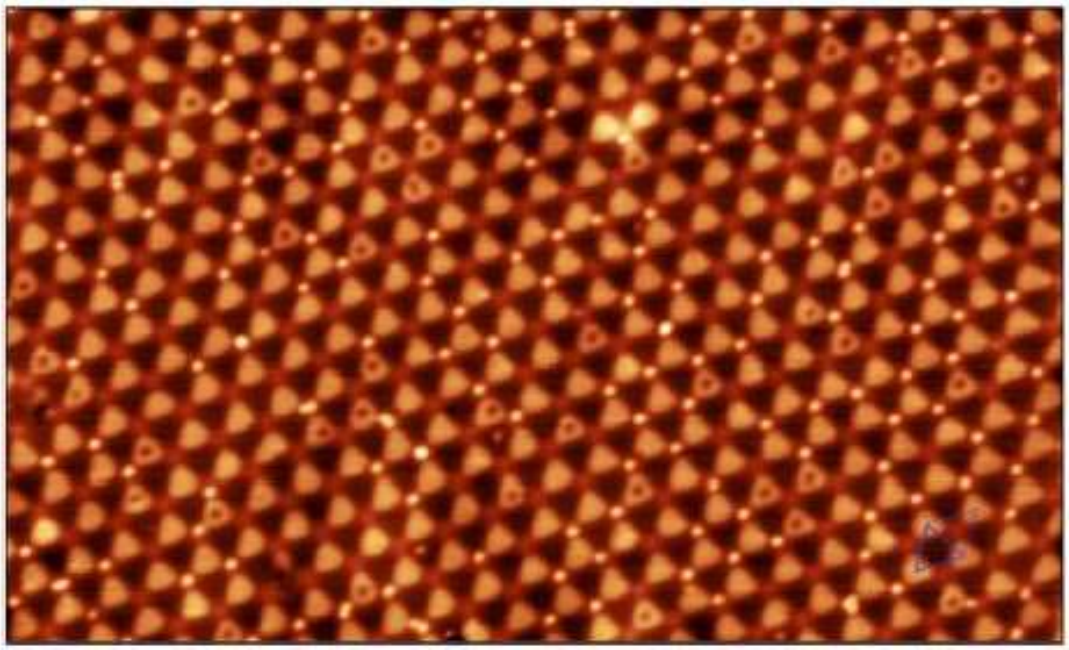

Figure 2.19. STM image (66×40 nm^2, V_b = 1.7 V, I_t = 30 pA) acquired at 80 K on a high coverage sample, prepared by exposing the gr/Ru(0001) surface to 600 Langmuir of acetonitrile at 300 K. The moiré unit cell is highlighted in blue.

In order to test the generality of our functionalization method we repeat the experiments with different molecules, namely CH_3CH_2CN, $(CH_3)_2CHCN$ and Ph-CH_2CN. Figure 2.20 shows the coverage obtained counting on the corresponding STM images the molecular attachments after the exposition of the gr/Ru(0001) clean surface to a partial pressure of 1×10^{-6} Torr during 3 minutes (equivalent to 180 Langmuir) of the different molecular species compared to the acetonitrile results. The sensitivity to each molecule is expected to be different, depending not only on the relative concentration of the corresponding radical, but also on its reactivity, and therefore the actual exposition of the surface to the molecules may vary. Even with this uncertainty the graph shows that the functionalization mechanism proposed in this work is rather general and gives consistent result for different molecules.

[133] P. W. Sutter, J. I. Flege and E. A. Sutter, *Nat. Mater.,* **2008**, *7*, 406.

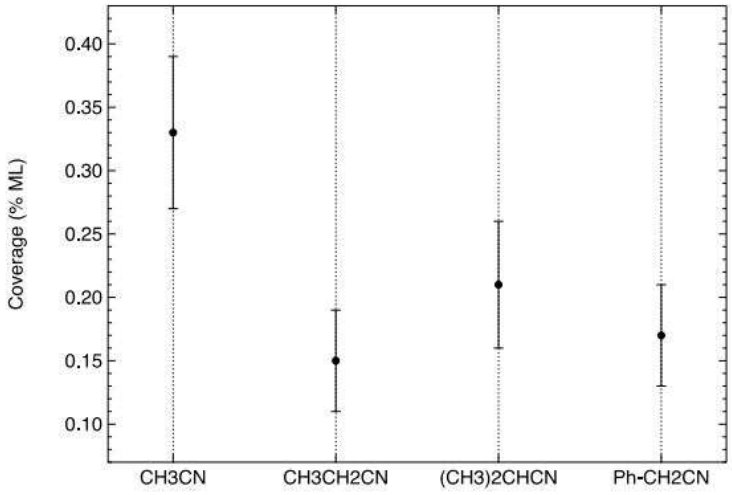

Figure 2.20. Local coverage measured on different STM images after exposing a clean gr/Ru(0001) surface during 3 minutes to a partial pressure of 1×10^{-6} Torr of the different molecules.

3.2 Conclusions

In conclusion, we take advantage of the nanostructuration induced on graphene grown on Ru(0001) to chemically functionalize the graphene overlayer with atomic-level selectivity and exquisite spatial periodicity. The comparison between graphene grown on Ir(111) and graphene on Ru(0001) shows the importance of the interaction between the graphene and the metallic substrate that spatially modulates the properties of the graphene. Acetonitrile is homolytically broken by electron bombardment producing cyanomethyl radicals that react with the nanostructured graphene in a spatially modulated fashion. These results offer the possibility for tuning the graphene electronic, optic or magnetic properties trough an adequate covalent functionalization of single layer graphene with long-range order on the order of hundreds of nanometers and a periodicity of almost 3 nm. Moreover, identical results were obtained for propionitrile, isobutyronitrile and 2-phenylacetonitrile, establishing a benchmark for the attachment of more complex molecular structures to specific atomic sites on graphene.

3.3 Experimental section

Two different UHV systems have been used, first the growth of epitaxial graphene on Ru(0001) was performed at a UHV system equipped with a variable-temperature STM (VT-STM) located at the Surface Physics Department of the Universidad Autónoma de Madrid (UAM) and the functionalization and characterization of gr/Ru(0001) were carried out using a UHV system equipped with a low-temperature STM (LT-STM) located at the Scanning Probe Microscopies and Surfaces Laboratory at the Madrid Institute for Advanced Studies in Nanoscience (IMDEA-Nanoscience) (see Figure 2.21).

Figure 2.21. LT-STM of IMDEA Nanoscience.

The design and fabrication of the fast entry and preparation chamber were carried out at the UAM. Both the VT-STM and LT-STM chambers are commercial systems from Omicron.[134] For the LT-STM it was used the electronics provided by Omicron, whereas for controlling the VT-STM was used Omicron-compatible electronics designed by Specs.[135] Both systems are mounted on an aluminum frame resting on active pneumatic damping systems (Newport I-2000) to decouple the systems from external vibrations. All experiments were performed in an UHV chamber with a base pressure of 5×10^{-11} Torr equipped with a low-temperature STM and facilities for tip and sample preparation. All the STM measurements were carried out at 80 K. The graphene layer was prepared by keeping the Ru crystal at 1150 K in UHV while exposing it to an ethylene partial pressure of 8×10^{-8} Torr for 10 min. Acetonitrile was introduce in the UHV chamber via a leak valve to produce a partial pressure of 1×10^{-6} Torr.

[134] Omicron NanoTechnology, GmbH, [Online]. Available: http://www.omicron.de.
[135] Specs, [Online]. Available: http://www.specs.de.

A.- Graphene on Ru(0001) sample

Figure 2.22 shows a typical STM image of the gr/Ru(0001) surface after annealing the clean graphene surface at 600 K in a partial pressure of O_2. As can be seen in the inset there are areas of the moiré pattern destroyed. In the areas where the moiré is still visible, the upper part of the ripples present a variable number of individual depressions. Based on this result we tentatively attribute the single defects that are present on the clean gr/Ru(0001) surface to the residual oxygen atoms present in the sample holder and in the vacuum chamber during the preparation of the graphene overlayer. The Ru(0001) surface is annealed in an oxygen partial pressure that produces a well-known 2×2 reconstruction that passivates the surface.[136,137] After this the oxygen is evacuated from the ultra-high vacuum (UHV) chamber and the Ru(0001) surface is flash annealed at 1500 K to remove the 2×2 reconstruction and produce an atomically clean surface. To avoid the contamination of the highly reactive Ru(0001) immediately after the flash annealing the graphene overlayer is grown. Therefore we cannot exclude presence of small amount of oxygen during the graphene growth process.

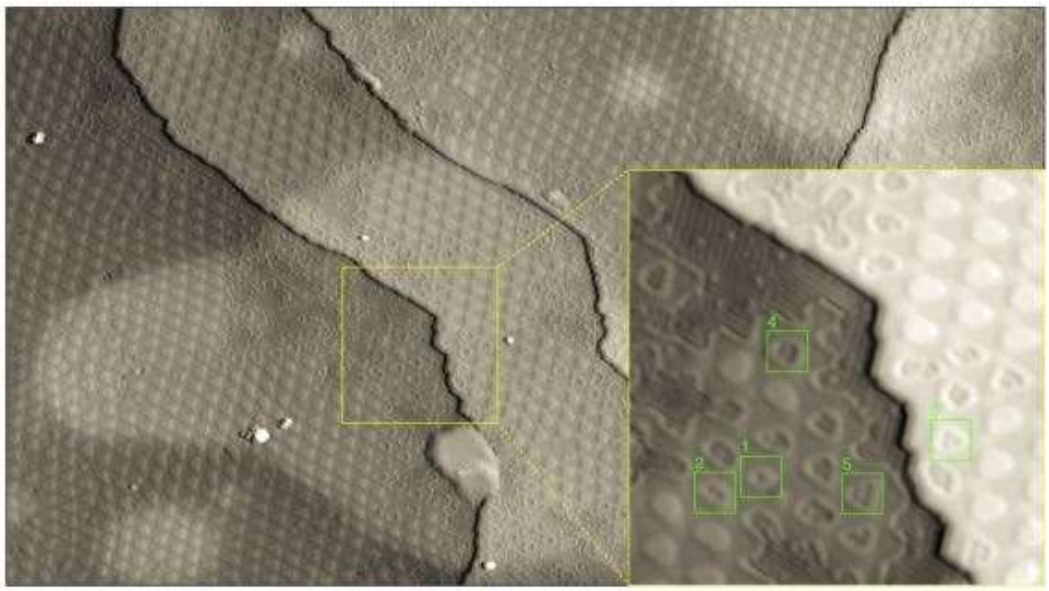

Figure 2.22. 160×90 nm^2 STM image measured on gr/Ru(0001) after annealing the sample at 600 K in a O_2 partial pressure of 3×10^{-7} Torr during 5 minutes. The inset shows a zoom of the region highlighted in yellow. Several atop regions affected by oxygen are marked in green. The numbers indicate the individual defects found at every ripple. Both STM images have been recorded at 80 K.

[136] F. Calleja, A. Arnau, J. J. Hinarejos, A. L. Vázquez de Parga, W.A. Hofer, P. M. Echenique and R. Miranda, *Phys. Rev. Lett*., **2004**, *92*, 206101.
[137] B. Borca, F. Calleja, J. J. Hinarejos, A. L. Vázquez de Parga and R. Miranda, *J. Phys. Condens. Matter*, **2009**, *21*,134002.

B.- Wet chemistry

In a first attempt to reproduce the reaction conditions described by Wu et al.,[138] we treated gr/Ru(0001) with a solution of 4-nitrophenyl diazonium tetrafluoroborate (NDA) in acetonitrile (1 mg/mL). After exposure for 1 h, we washed the gr/Ru(0001) sample with CH_3CN to remove unreacted aryl compound, dried it under a N_2 current, and observed it under STM. The resulting micrographs show densely covered graphene, to the point that the moiré pattern is no longer visible, with no apparent selectivity (Figure 2.23). The addends could not be removed by heating under the high vacuum conditions of STM. In fact, prolonged heating led to the destruction of graphene, confirming the covalent nature of the attachments. In order to decrease the degree of functionalization, we reduced the exposure to the NDA solution to 30 seconds, and observed no significant differences. Surprisingly, the same results were obtained even after washing the gr/Ru(0001) sample immediately after exposure to the reagent (1-2 seconds). Finally, diluting the NDA by two orders of magnitude (0.01 mg/mL), did not lead to a decrease in the functionalization either. Moreover, we observed that even the regions of graphene that had not been exposed to the diazonium solution, but only to acetonitrile vapours, were also heavily functionalized.

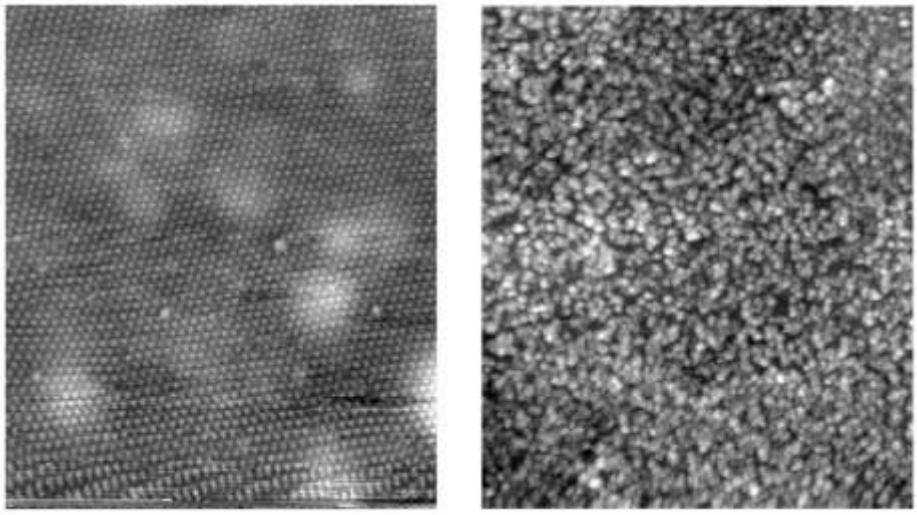

Figure 2.23: 70x40 nm^2 STM image obtained before functionalization and after dosing a drop of NDA and rinsing with acetonitrile.

[138] S. Bian, A. M. Scott, Y. Cao, Y. Liang, S. Osuna, K. N. Houk and A. B. J. Braunschweig, J. *Am. Chem. Soc.*, **2013**, *135*, 9240.

C.- Relative abundance of the cyanomethyl radical ($CH_2CN^{\bullet}$) vs acetonitrile (CH_3CN); $CH_3CHCN^{\bullet}$ vs CH_3CH_2CN; and $(CH_3)_3CCN^{\bullet}$ vs $(CH_3)_2CHCN$

A quadrupole mass spectrometer (QMS) has three main components, an ionization chamber, the quadrupole mass filter and an ion detector. The working principle of the ionization chamber is very similar to an ion gauge. The gas molecules are ionized by bombardment with high energy electrons (~100 eV) and then the ions are injected into the quadrupole mass filter that allows for the selection of the q/m ratio.

Finally they are detected measuring the current needed to electrically neutralize them. In this kind of spectrometer the expected m/z peaks are M+, where M is the molecular mass of the analyte. Figure 2.24 shows the experimental QMS spectra obtained with a partial pressure of acetonitrile of 10^{-6} Torr. The main peak appears at an atomic mass of 41 that corresponds to acetonitrile (CH_3CN). The second peak in intensity appears at an atomic mass of 40 and corresponds to the cyanomethyl radical ($CH_2CN^{\bullet}$). The appearance of this peak in the spectra requires two consecutive collisions between the high energy electrons and the molecules. The first collision produces the homolytic breaking of the acetonitrile molecule producing the cyanomethyl radicals, and then a second collision is needed to remove one electron from the radical and allow the detection by means of the QMS. The two consecutive collisions needed for the detection of the cyanomethyl radical is much less probable than the single collision needed for the detection of the acetonitrile specie, suggesting a very high abundance of the cyanomethyl radical. The peaks at 39 and 38 m/z demonstrate that all three hydrogens of the methyl group can be removed. Other experimental results show that the homolytic breaking of the acetonitrile molecule is a rather common process when the acetonitrile molecule is bombarded with high energy electrons or ions.[139,140] Similar results are obtained for propionitrile and isobutyronitrile.

[139] C. Caillier, D. K. Ki, Y. Lisunova, I. Gaponenko, P. Paruch and A. F. Morpugo, *Nanotechnology*, **2013**, *24*, 405201.
[140] E. Kukk, R. Sankari, M. Huttula, A. Sankari, H. Aksela and S. J. Aksela, *Electron Spectrosc. Relat. Phenom.*, **2007**, *155*, 141.

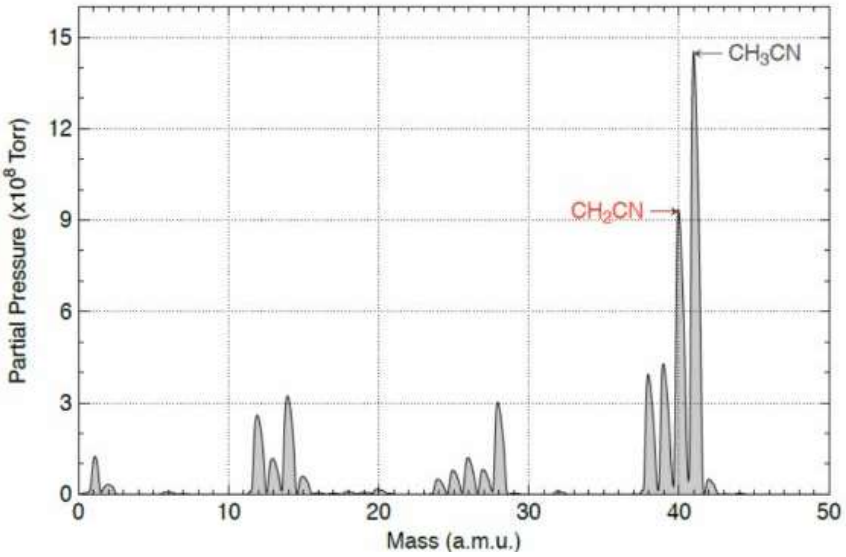

Figure 2.24. QMS spectrum obtained with an acetonitrile partial pressure of 10^{-6} Torr. In addition to the acetonitrile peak at 41 there is a strong peak at 40 that corresponds to $CH_2CN^{\bullet}$ (marked in red). It is worth mentioning that the appearance of this peak requires two consecutive collisions between the high energy electrons and the corresponding molecules or radicals. The first one is necessary for the hemolytic breaking of the acetonitrile and the second one for producing the CH_2CN^- ion. This means that the relative abundance of $CH_2CN^{\bullet}$ is much higher than the corresponding peak in the spectrum.

Figure 2.25 shows a comparison between the experimental QMS spectra obtained with a partial pressure of each nitrile compound of 10^{-6} Torr (in black) and the calculated isotopic distribution for the molecular peak (in red). Unfortunately, the mass range of our QMS set up did not allow for the measurement of the mass spectrum of phenylacetonitrile.

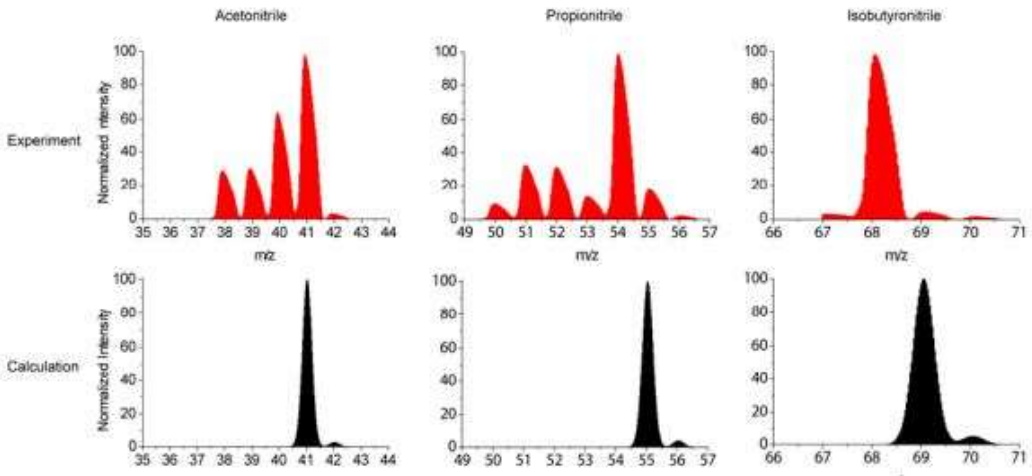

Figure 2.25. Experimental QMS spectra obtained with a partial pressure of the corresponding nitrile of 10^{-6} Torr (red). The calculated isotopic distributions for the molecular species are shown below (black).

D.- Theoretical calculations

D.1.- Computational details

Density Functional Theory (DFT) calculations have been performed using the Vienna ab initio simulation package.[141] To describe the exchange-correlation energy of the electrons, we have used the generalized gradient approximation (GGA) and the Perdew-Burke-Ernzerhof[142] (PBE) functional. Dispersion interactions have been described using the DFT+D2 semi-empirical method of Grimme.[143] The projector augmented wave[144] (PAW) method has been used to describe the ionic cores. The one-electron Kohn-Sham orbitals have been expanded in a plane-waves basis set, and the energy cutoff for the plane waves expansion has been set to 400 eV. The Brillouin zone has been sampled at the Γ-point only. Geometry optimizations have been performed using a convergence threshold of 0.01 eV/A^3.

D.2.- Cyanomethyl radical energy formation

The bond dissociation energy (BDE) for the CH_3CN, $CH_2CN^{\bullet}$ +$H^{\bullet}$ reaction has been calculated by placing the molecule at the center of a cubic box of 25Å × 25Å × 25Å, and by performing a constrained minimization for different values of the distance $d_{H\cdots CH2CN}$ between the abstracted H atom and the cyanomethyl radical fragment. Starting from the optimized geometry of the CH_3CN molecule in the gas-phase, one of the H atoms of the methyl group has been displaced stepwise $\Delta d_{H\cdots CH2CN}$ = 0.52 Å from the rest of the molecule. At each step, the position of the abstracted H atom and that of the C atom of the $CH_2CN^{\bullet}$ methylene group have been kept frozen, whereas all the remaining molecular degrees of freedom have been allowed to relax. The BDE at that value of $d_{H\cdots CH2CN}$ has been then calculated as the energy difference between the total energy of the resulting optimized geometry and that of the optimized geometry of the CH_3CN molecule ($d_{H\cdots CH2CN}$ = 1.62 Å). The resulting curve of the BDE as a function of $d_{H\cdots CH2CN}$ is shown in Figure 2.26. Above $d_{H\cdots CH2CN}$ = 6.29 Å, the difference in energy between two consecutive configurations is lower than 5×10^{-2} kcal mol^{-1}, i.e., the two fragments can be essentially considered as non-interacting. Following these considerations, the value BDE = 92.431 kcal mol^{-1} reported in the main text has been calculated as the difference in total energy between the configuration at $d_{H\cdots CH2CN}$ = 1.62 Å and that at $d_{H\cdots CH2CN}$ = 11.48 Å. This BDE value is in good agreement with previous calculations.[145,146]

[141] G. Kresse and J. Hafner, *Phys. Rev. B*, **1993**, *47*, 588(R).
[142] J. P. Perdew, K. Burke and M. Ernzerhof, *Phys. Rev. Lett*., **1997**, *77*, 3865.
[143] S. J. Grimme, *Comp. Chem.*, **2006**, *27*, 1787.
[144] G. Kresse and D. Joubert, *Phys. Rev. B*, **1999**, *59*, 1758.
[145] D.J. Henry, C.J. Parkinson, P. M. Mayer, L. J. Radom, Phys. Chem. A, **2001**, *105*, 6750.
[146] M. L. Coote, *J. Phys. Chem. A*, **2004**, *108*, 3865.

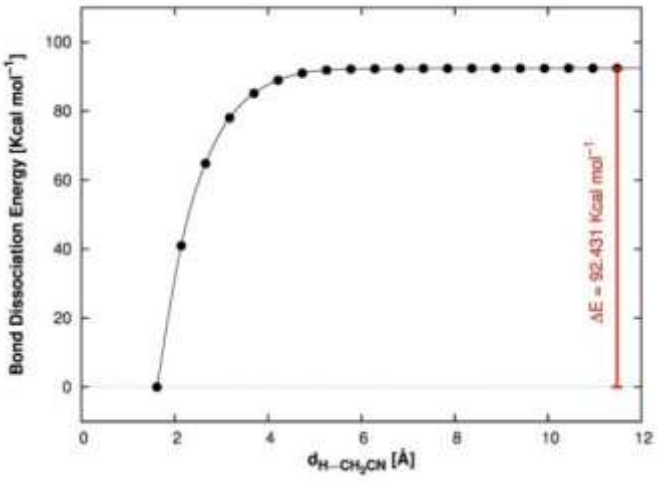

Figure 2.26. Bond dissociation energy (BDE) of CH_3CN in the gas-phase as a function of the distance $d_{H\cdots CH2CN}$ between the abstracted H atom and the C atom of the $CH_2CN^{\bullet}$ methylene group.

D.3.- Cyanomethyl and acetonitrile radical adsorption energy

DFT calculations have been performed for the acetonitrile molecule, and the corresponding cyanomethyl radical, adsorbed on gr/Ru(0001). The surface of gr/Ru(0001) has been described using an 11×11 graphene sheet adsorbed on a 10×10 Ru(0001) 3-layer slab.[147] In the first step, the gr/Ru(0001) surface has been optimized by allowing the graphene and the topmost Ru(0001) layer to relax. In the second step, the molecule has been positioned over the surface, and the structure has been relaxed again. During this geometry optimization, the molecular as well as the graphene degrees of freedom have been allowed to relax, while the Ru(0001) surface atoms have been kept frozen. The adsorption energies have been calculated as the difference between the total energy of the optimized geometry of the molecule adsorbed on the surface, and that of the optimized geometries of the two non-interacting molecular and gr/Ru(0001) fragments. Following the experimental observations, we have studied the adsorption of $CH_2CN^{\bullet}$ radical on the strongly interacting areas of the gr/Ru(0001) moiré. Both the HCP-Top and FCC-Top areas have been considered, since they exhibit distinct surface electronic structures as a consequence of the stacking order between the graphene atoms and the atoms of the Ru(0001) surface underneath.[148] For each area, several initial configurations of the molecule over the gr/Ru(0001) surface have been considered, corresponding to situations in which: (i) the molecule long axis lies parallel to the surface, with the C-N bond aligned along a graphene C-C bond, and the N atom pointing either in the direction of the graphene atom at the FCC (HCP) position or in the direction of the graphene atom at the Top position; (ii) the molecule long axis is normal to the surface, above either the graphene atom at the FCC (HCP) position or the graphene atom at the Top position, with the N atom pointing

[147] D. Stradi, S. Barja, C. Díaz, M. Garnica, B. Borca, J. J. Hinarejos, D. Sánchez Portal, M. Alcamí, A. Arnau, A. L. Vázquez de Parga, R. Miranda and F. Martín, *Phys. Rev. Lett*., **2011**, *106*, 186102.
[148] M. Garnica, D. Stradi, F. Calleja, S. Barja, C. Díaz, M. Alcamí, A. Arnau, A. L. Vázquez de Parga, F. Martín and R. Miranda, *Nano Lett*., **2014**, *4*, 4560.

towards the surface; (iii) the molecule long axis lies parallel to the surface, with the C-N bond above one of the graphene honeycomb rings, and the N atom pointing either to the graphene atom at the FCC (HCP) position or to that at the Top position. The adsorption energies calculated for each configuration of $CH_2CN^{\bullet}$ adsorbed on gr/Ru(0001) are listed in Table 2.1, and the corresponding optimized geometries are shown in Figure 2.27. The average adsorption energy of $CH_2CN^{\bullet}$ on gr/Ru(0001) is higher at the HCP-Top area (1.58 eV) compared to the FCC-Top area (1.3 eV), in agreement with the experimental observation that molecular adsorption occurs preferentially at the HCP-Top area of the gr/Ru(0001) moiré. The enhanced reactivity of the HCP-Top area, compared to the FCC-Top area, can be traced back to the higher density of electronic states available in the graphene layer close to the Fermi level.[23] The strong interaction of the $CH_2CN^{\bullet}$ radical with the graphene is also reflected in the geometry of the system. On the one hand, the molecule lies considerably closer to the graphene, with an average distance between the graphene and the lowest atom of $CH_2CN^{\bullet}$ of 1.57 Å, i.e., similar to the distance given by the sum of the covalent radio of either two sp^3 carbon (1.54 Å) or an sp^3 carbon atom and a nitrogen atom (1.54 Å). On the other hand, the graphene atom that binds directly to the $CH_2CN^{\bullet}$experiences an out-of-plane buckling, which can be associated with a change its orbital hybridization from sp^2 to sp^3. These results point at the formation of a covalent bond between the $CH_2CN^{\bullet}$ radical and the gr/Ru(0001) surface. The covalent binding of the cyanomethyl radical to the graphene has a direct influence on the electronic properties of the latter (see Figure 2.28). The PDOS on the graphene atom binding directly to the molecule is strongly quenched with respect to that of the same atom in the bare gr/Ru(0001) surface, especially close to the Fermi level EF. However, this electronic perturbation in the graphene lattice decays very rapidly, as the PDOS on the graphene atoms that do not bind directly to the molecule remains similar to that of the same atoms in the bare gr/Ru(0001) surface. This local modification in the graphene electronic structure, due to the covalent attachment of $CH_2CN^{\bullet}$, provides an explanation for the experimental observation that only those atoms binding directly to the molecule appear as “holes” in the STM topographic images measured with atomic resolution within the molecular HOMO-LUMO gap. Therefore, the present calculations indicate that the $CH_2CN^{\bullet}$ radical is chemisorbed on gr/Ru(0001), and that this covalent attachment can be associated with a reduced electronic density in the graphene atom that binds to the molecule, in agreement with the experimental results reported in the main text. For comparison, the same calculations have been performed for CH_3CN. The adsorption energies calculated for each configuration of CH_3CN adsorbed on gr/Ru(0001) are listed in Table 2.2, and the corresponding optimized geometries are shown in Figure 2.29. The small adsorption energy, which varies only slightly among the different adsorption configurations, and the large average distance between the graphene and the lowest atom of CH_3CN (3.04 Å), indicate that the molecule is weakly bound to the surface, contrary to what happen with the $CH_2CN^{\bullet}$ radical. The presence of such a weak interaction is further confirmed by the analysis of the projected density of states (PDOS) on the graphene atoms lying below the adsorbed molecule. Figure 2.30 shows the results for the most stable configuration calculated for CH_3CN on gr/Ru(0001) – HCP-Top(3) in Figure 2.29. The PDOS calculated in the presence of the adsorbed molecule is very similar to that calculated on the same atoms in the bare gr/Ru(0001) surface. This fact indicates that the perturbation induced on the graphene

atoms by the adsorption of CH_3CN is negligible, which further support the conclusion that the interaction between the molecule and the gr/Ru(0001) surface is weak. Overall, these results indicate that the CH_3CN molecule is essentially physisorbed on gr/Ru(0001).

Configuration	Adsorption Energy (eV) / (Kcal mol^{-1})	Configuration	Adsorption Energy (eV) / (Kcal mol^{-1})
HCP-Top (1)	-2.34 / -53.910	FCC-Top (1)	-2.14 / -49.38
HCP-Top (2)	-1.1 / -25.58	FCC-Top (2)	-1.14 / -26.20
HCP-Top (3)	-1.60 / -37.00	FCC-Top (3)	-1.41 / -32.51
HCP-Top (4)	-2.49 / -57.38	FCC-Top (4)	-2.30 / -52.99
HCP-Top (5)	-1.59 / -36.76	FCC-Top (5)	-0.40 / -9.34
HCP-Top (6)	-0.44 / 10.14	FCC-Top (6)	-2.34 / -9.22

Table 2.1. Calculated adsorption energies of $CH_2CN^{\bullet}$ on gr/Ru(0001) at different positions on the strongly bound areas (HCP-Top and FCC-Top) of the gr/Ru(0001) moiré.

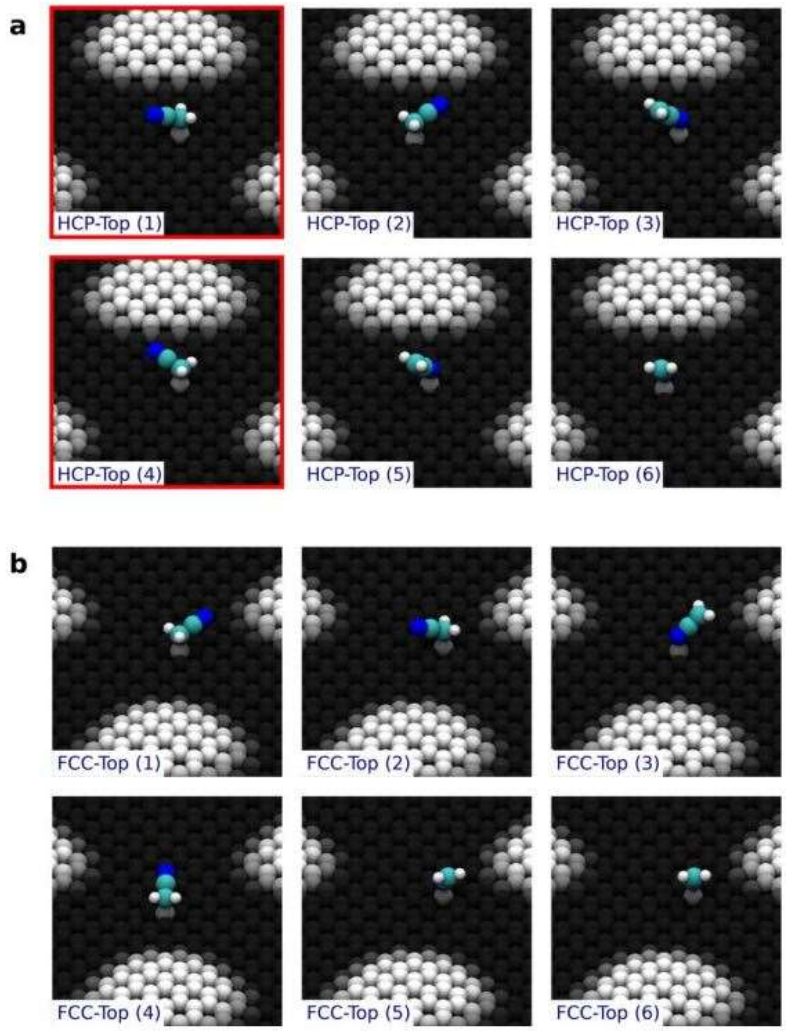

Figure 2.27. a) Adsorption configurations for cyanomethyl radical ($CH_2CN^{\bullet}$) on HCP-Top and **b)** FCC-Top areas considered in this study. The corresponding adsorption energies are show in Table 2.1.

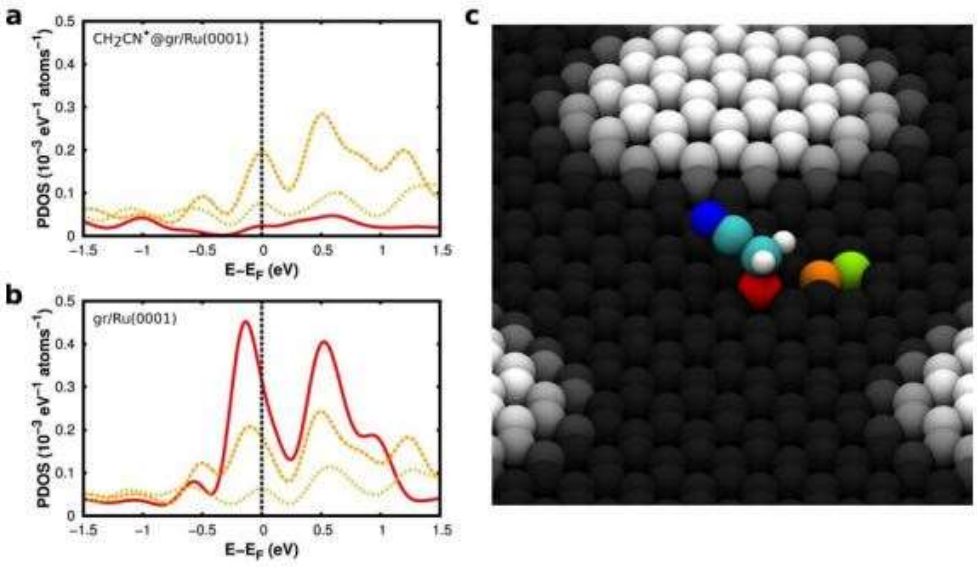

Figure 2.28. Projected density of states (PDOS) over selected graphene atoms of the gr/Ru(0001) moiré, in the presence **(a)** or absence **(b)** of an adsorbed $CH_2CN^{\bullet}$ molecule. The red (solid), orange (dashed) and yellow (dotted) lines indicate the PDOS calculated on the graphene atoms shown in the corresponding colors in **(c).**

Configuration	Adsorption Energy (eV) / (Kcal mol^{-1})	Configuration	Adsorption Energy (eV) / (Kcal mol^{-1})
HCP-Top (1)	-0.41 / -9.50	FCC-Top (1)	-0.42 / -9.60
HCP-Top (2)	-0.40 / -9.30	FCC-Top (2)	-0.41 / -9.34
HCP-Top (3)	-0.45 / -10.44	FCC-Top (3)	-0.45 / -10.48
HCP-Top (4)	-0.45 / -10.44	FCC-Top (4)	-0.44 / -10.23
HCP-Top (5)	-0.41 / -9.38	FCC-Top (5)	-0.41 / -9.42
HCP-Top (6)	-0.39 / -9.04	FCC-Top (6)	-0.42 / -9.80

Table 2.2. Calculated adsorption energies of CH_3CN on gr/Ru(0001) at different positions on the strongly bound areas (HCP-Top and FCC-Top) of the gr/Ru(0001) moiré.

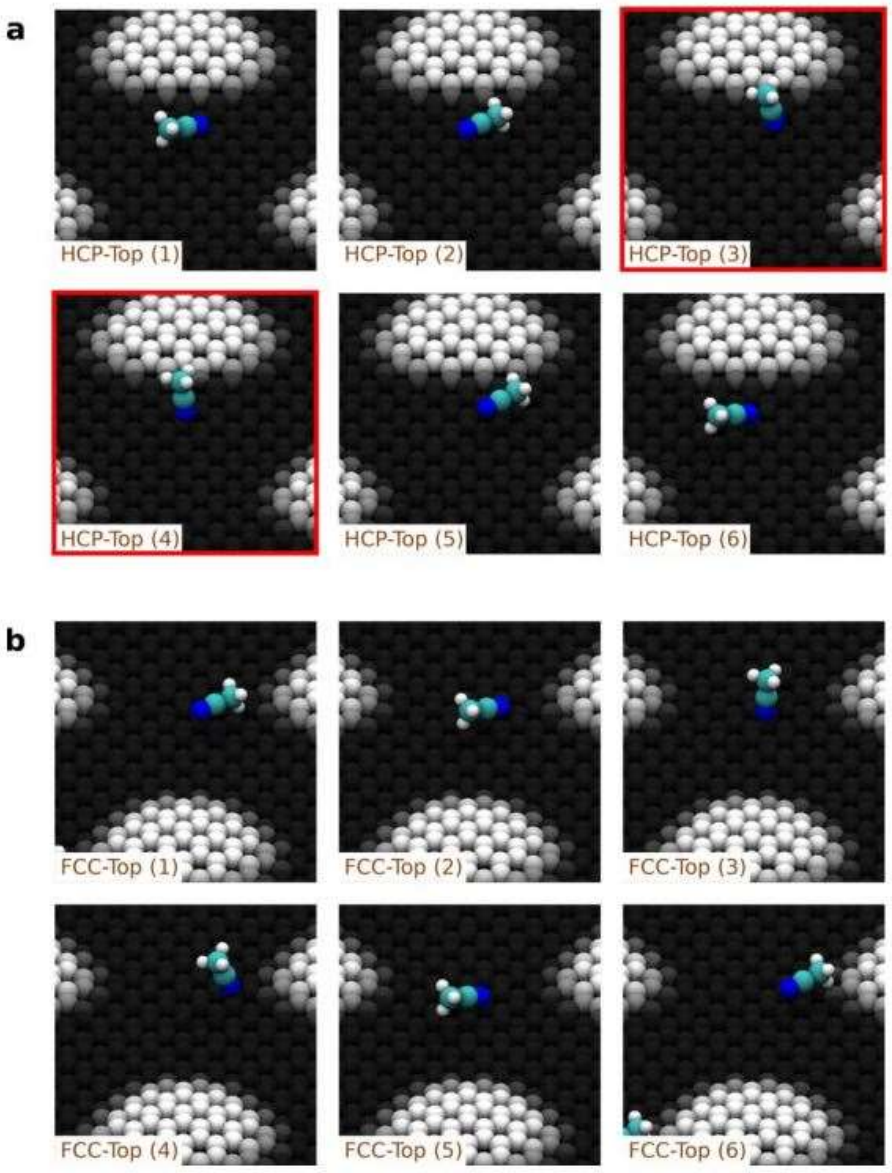

Figure 2.29. a) Adsorption configurations for acetonitrile (CH_3CN) on HCP-Top and **b)** FCC-Top areas considered in this study. The configurations marked in red are the most stable. The corresponding adsorption energies are show in Table 2.2.

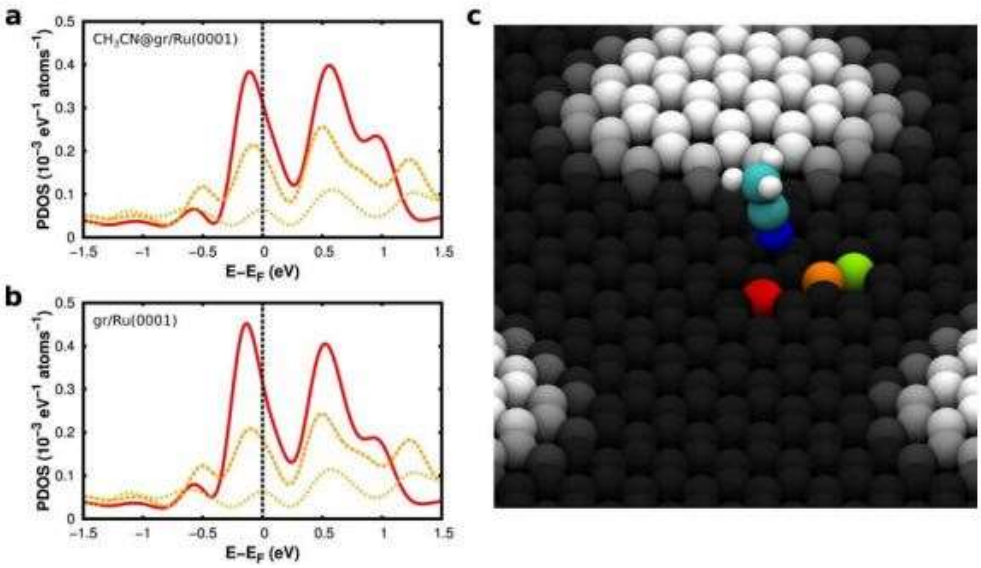

Figure 2.30. Projected density of states (PDOS) over selected graphene atoms of the gr/Ru(0001) moiré, in the presence **(a)** or absence **(b)** of an adsorbed CH_3CN molecule. The red (solid), orange (dashed) and yellow (dotted) lines indicate the PDOS calculated on the graphene atoms shown in the corresponding colors in **(c)**.

4. References

1 P. R. Wallace, The band theory of graphite, *Phys. Rev*., **1947**, *71*, 622.

2. K. S. Novoselov, A. K. Geim, S. V. Morozov, D. Jiang, Y. Zhang, S. V. Dubonos, I. V. Grigorieva and A. A. Firsov, *Science*, **2004,** *306*, 666.

3. A. K. Geim and K. S. Novoselov, *Nat. Mater.,* **2007,** *6*,183-191.

4. B. Partoens and F. M. Peeters, *Physical Review B,* **2006,** *74*, 075404.

5. Y. Zhang, Y. W. Tan, H. L. Stormer and P. Kim, *Nature* **2005**, *438*, 201.

6. M. D. Stoller, S. J. Park, Y. W. Zhu, J. H. An, and R. S. Ruoff, *Nano Lett.*, **2008**, 8, 3498-3502.

7. A. S. Mayorov, R. V. Gorbachev, S. V. Morozov, L. Britnell, R. Jalil, L. A. Ponomarenko, P. Blake, K. S. Novoselov, K. Watanabe, T. Taniguchi, and A. K. Geim, *Nano Lett*., **2011**, 11, 2396-2399.

8. C. Lee, X. Wei, J. W. Kysar and J. Hone, *Science*, **2008**, *321*, 385-388.

9. A. A. Balandin, S. Ghosh, W. Bao, I. Calizo, D. Teweldebrhan, F. Miao and C. N. Lau, *Nano Lett*., **2008**, *8*, 902-907.

10. R. R. Nair, P. Blake, A. N. Grigorenko, K. S. Novoselov, T. J. Booth, T. Stauber, N. M. R. Peres and A. K. Geim, *Science*, **2008**, *320*, 1308.

11. F. *Schedin*, *A. K. Geim*, *S. V. Morozov*, *E. W. Hill*, *P.* Blake, *M.I. Katsnelson*, *Nature materials*, **2007**, *6*, 652-655.

12. J. T. Robinson, F. K. Perkins, E. S. Snow, Z. Wei and P. E. Sheehan *Nano Lett.,* **2008**, *8*, 3137-3140.

13. S. Watcharotone, D. A. Dikin, S. Stankovich, R. Piner, I. Jung, G. H. B. Dommett, G. Evmenenko, S. E. Wu, S. F. Chen, C. P. Liu, S. T. Nguyen and R. S. Ruoff, *Nano Lett*. **2007**, *7*, 1888-1892.

14. X. Wang, L. Zhi and K. Müllen, *Nano Lett*., **2008**, *8*, 323-327.

15. K. S. Kim, Y. Zhao, H. Jang, S. Y. Lee, J. M. Kim, K. S. Kim, J. H. Ahn, P. Kim, J. Y. Choi and B. H. Hong, *Nature*, **2009**, *457*, 706-710.

16. S. Y. Zhou, G. H. Gweon, A. V. Fedorov, P. N. First, W. A. De Heer, D. H. Lee, F. Guinea, A. H. Castro Neto and A. Lanzara, *Nature Mater*., 2007, *6*, 770.

17. F. N. Xia, D. B. Farmer, Y. M. Lin and P. Avouris, *Nano Lett.*, **2010**, *10*, 715-718.

18. H. Liu, Y. Liu and D. Zhu, J. *Mater. Chem*., **2011**, *21*, 3335-3345.

19. V. C. Vincent, C. Tung, M. J. Matthew, J. Allen, Y. Yang Yang, R. B. Richard and B. Kaner*, Nat. Nanotechnol*., **2009,** *4*, 25-29.

20. M. Lotya, Y. Hernandez, P. J. King, R. J. Smith, V. Nicolosi, L. S. Karlsson, F. M. Blighe, S. De, Z. Wang, I. T. McGovern, G. S. Duesberg and J. N. Coleman*, J. Am. Chem. Soc*., **2009**, *131*, 3611-3620.

21. Y. T. Liang and M. C. Hersam, *J. Am. Chem. Soc*., **2010**, *132*, 17661.

22. Y. Zhu, S. Murali, W. Cai, X. Li, J. W. Suk and J. R. Potts, *Adv. Mater*., **2010**, *22*, 3906.

23. Q. Yu, J. Lian, S. Siriponglert, H. Li, Y. P. Chen, and S. Pei*, Appl. Phys. Lett*., **2008**, *93*, 113103.

24. X. Li, W. Cai, J. An, S. Kim, J. Nah, D. Yang, R. Piner, A. Velamakanni, I. Jung, E. Tutuc, S. K. Banerjee, L. Colombo and R. S. Ruoff, *Science*, **2009**, *324*, 1312.

25. S. Bae, H. Kim, Y. Lee, X. Xu, J. Park, Y. J. Zheng, J. Balakrishnan, T. Lei, H. Ri Kim, Y. I. Song, Y. J. Kim, K. S. Kim, B. Özyilmaz, J. H. Ahn, B. H. Hong and S. Iijima, *Nat. Nanotechnol*., **2010**, *5*, 574.

26. E. Sutter, P. Albrecht and P. Sutter, *Appl. Phys. Lett.*, **2009**, *95*, 133109.

27. J. Vaari, J. Lahtinen and P. Hautojarvi, *Catal. Lett.,* **1997**, *44*, 43-49.

28. C. Vo-Van, A. Kimouche, A. Reserbat-Plantey, O. Fruchart, P. Bayle-Guillemaud, N. Bendiab and J. Coraux, Appl. Phys. Lett., **2011**, 98, 181903.

29. T. Iwasaki, H. J. Park, M. Konuma, D. S. Lee, J. H. Smet, and U. Starke, *Nano lett*., **2011**, *11*, 79.

30. D. E. Starr, E. M Pazhetnov, A. I. Stadnichenko, A. I. Boronin and S. K. Shaikhutdinov, *Surf. Sci.,* **2006**, *600*, 2688-2695.

31. K. S. Kim, Y. Zhao, H. Jang, S. Y. Lee, J. M. Kim, K. S. Kim, J. H. Ahn, P. Kim, J. Y. Choi and B. H. Hong, *Nature*, **2009**, *457*, 706.

32. X. Li, W. Cai, L. Colombo and R. S. Ruoff, *Nano Lett*., **2009**, *9*, 4268-4272.

33. The Journal of Physical Chemistry C, **2008**, *112*, 17741.

34. S. Jiang, Y. Zeng, W. Zhou, X. Miao and Y. Yu., *Nature*, **2016**, *6*, 19313.

35. S. Marchini, S. Günthera and J. Wintterlin, *Phys. Rev. B,* **2007**, *76*, 075429.
36. A.T. N'Diaye, S. Bleikamp, P.J. Feibelman and T. Michely, *Phys. Rev. Lett*. **2006**, *97*, 215501.
37. J. Coraux, A.T. N'Diaye, C. Busse and T. Michely, *Nano Lett*. **2008**, *8*, 565.
38. T. Fujita, W. Kobayashi and C. Oshima, *Surf. Interface. Anal*., **2005**, *37*, 120.
39. A. Vázquez de Parga, F. Calleja, B. Borca, M. C. G. Passeggi, Jr., J. Hinarejos, F. Guinea and R. Miranda, *Phys. Rev. Lett*. **2008**, *100*, 056807.
40. B. Borca, S. Barja, M. Garnica, D. Sánchez-Portal, V. Silvino, E. Chulkov, F. Hermanns, J. Hinarejos, A. Vázquez de Parga, A. Arnau, P. Echenique and R. Miranda, *Physical Review Letters,* **2010**, *105*, 036804.
41. B. Borca, S. Barja, M. Garnica, M. Minniti, A. Politano, F. J. M. R. García, J. Hinarejos, D. Farías, A. Vázquez de Parga, and R. Miranda, *New journal of Physics,* **2010**, *12*, 093018.
42. S. Marchini, S. Günthera and J. Wintterlin, *Phys. Rev. B*, **2007**, 76, 075429.
43. A. L. Vázquez de Parga, F. Calleja, B. Borca, J. J. Hinarejos, M. G. C. Passeggi, F. Guinea and R. Miranda, *Phys. Rev. Lett*., **2008**, *100*, 056807.
44. P. W. Sutter, J. I. Flege and E. A. Sutter, *Nature Mater*., **2008**, *7*, 406.
45. D. Martoccia, P. R. Willmott, T. Brugger, M. Björck, S. Günther, C. M. Schlepütz, A. Cervellino, S. A. Pauli, B. D. Patterson, S. Marchini, J. Wintterlin, W. Moritz and T. Greber, *Phys. Rev. Lett.,* **2008**, *101*, 126102.
46. A. B. Preobrajenski, M. L. Ng, A. S. Vinogradov and N. Martensson, *Phys. Rev. B*, **2008**, *78*, 073401.
47. A. T. N'Diaye, J. Coraux, T. N. Plasa, C. Busse and T. Michely, *New J. Phys.*, **2008**, *10*, 043033.
48. Q. H. Wang and M. C. Hersam, *Nat. Chem*., **2009**, *1*, 206.
49. F. Schedin, A. K. Geim, S. V. Morozov, E. W. Hill, P. Blake, M. I. Katsnelson and K. S. Novoselov, *Nat. Mater*., **2007**, *6*, 652.
50. J. *Malig, A. W. I. Stephenson*, *P. Wagner*, *G. G. Wallace*, *D. L. Officer* and *D. M. Guldi, Chem*. *Commun.,* **2012***, 48,* 8745-8747.
51. F. Zhang, X. Chen, R.A. Boulos, F. Md Yasin, H. Lu, C. Raston and H. Zhang, *Chem. Commun*., **2013**, *49*, 4845-4847.
52. W. Wang, Y. Zhang and Y. B. Wang, *J. Chem. Phys.*, **2014**, *140*, 094302.
53. M. M. Bernal and E. M. Pérez, *Int. J. Mol. Sci*., **2015**, *16*, 10704-10714.
54. V. Georgakilas, M. Otyepka, A. B. Bourlinos, V. Chandra, N. Kim, K. C. Kemp, P. Hobza, R. Zboril and K. S. Kim, *Chem. Rev*., **2012**, *112*, 6156.
55. L. Yan, Y. B. Zheng, F. Zhao, S. Li, X. Gao, B. Xu, P. S. Weiss and Y. Zhao, *Chem. Soc. Rev*., **2012**, *41*, 97-114.
56. K. P. Loh, Q. Bao, P. K. Ang and J. Yang, *J. Mater. Chem*., **2010**, *20*, 2277.
57. Q. Tang, Z. Zhou and Z. Chen, *Nanoscale*, **2013**, *5*, 4541.
58. E. Bekyarova, M. E. Itkis, P. Ramesh, C. Berger, M. Sprinkle, W. A. de Heer and R. C. Haddon, *J. Am. Chem. Soc.*, **2009**, *131*, 1336.
59. Q. H. Wang, Z. Jin, K. K. Kim, A. J. Hilmer, G. L. C. Paulus, C. J. Shih, M. H. Ham, J. D. Sanchez-Yamagishi, K. Watanabe, T. Taniguchi, J. Kong, P. Jarillo-Herrero and M. S. Strano, *Nat. Chem*. **2012**, *4*, 724.
60. Q. Wu, Y. Wu, Y. Hao, J. Geng, M. Charlton, S. Chen, Y. Ren, H. Ji, H. Li, D. W. Boukhvalov, R. D. Piner, C. W. Bielawski and R. S. Ruoff, *Chem. Commun.*, **2013**, *49*, 677-679.
61. M. A. Bissett, S. Konabe, S. Okada, M. Tsuji and H. Ago, *ACS Nano***, 2013**, *7*, 10335.
62. R. Sharma, J. H. Baik, C. J. Perera, and M. S. Strano, *Nano Lett*., **2010**, *10*, 398-405.
63. *M. A. Bissett*, *M. Tsuji* and *H. Ago*, *Phys*. *Chem*. *Chem*. *Phys.*, ***2014***, *16*, *11124*-11138.
64. P. W. Sutter, J. I. Flege, and E. A. S. Er, *Nature Mater*., **2008**, *7*, 406.
65. Y. Pan, H. G. Zhang, D. X. Shi, J. T. Sun, S. X. Du, F. Liu, and H. J. Gao, *Adv. Mater*., **2009**, *21*, 2777.
66. A. T. N'Diaye, J. Coraux, T. N. Plasa, C. Busse, and T. Michely, *New J. Phys.,* **2008**, *10*, 043033.
67. T. A., Michely, T. Behm, R. J. Hemminger and J. C. Comsa. *Surf. Sci*., **1992**, *264*, 261.
68. G. Binnig, H. Rohrer, Ch. Gerber and E. Weibel, *Phys. Rev. Lett*., **1982**, *49*, 57.
69. J. Bardeen, *Phys. Rev. Lett.,* **1961**, *6*, 57.
70. J. K. Gimzewski, E. Stoll and R. R. Schlitter, *Surf. Sci*., **1987**, *181*, 267.
71. T. Sleator and R. Tycko, *Phys. Rev. Lett*., **1988**, *60*, 1418.
72. P. S. Weiss and D. M. Eigler, Phys. *Rev. Lett*., **1993**, *71*, 3139.

73. G. S. McCarty and P. S. Weiss, *J. Phys. Chem. B*, **2002**, *106*, 8005.
74. A. Kuhnle, T. R. Linderoth, B. Hammer and F. Basenbacker, *Nature*, **2002**, *415*, 891.
75. I. W. Lyo and P. Avouris, *Science*, **1989**, *245*, 1369.
76. M. F. Crommie, C. P. Lutz, and D. M. Eigler, *Phys. Rev. B*, **1993**, *48*, 2851.
77. M. Z. Hossain, M. A. Walsh and M. C. Hersam, *J. Am. Chem. Soc*., **2010**, *132*, 15399.
78. A. K. Geim and K. S. Novoselov, *Nat. Mater*., **2007**, *6*, 183-191.
79. V. Georgakilas, M. Otyepka, A. B. V. Chandra, N. Kim, K. C. Kemp, P. Hobza, R. Zboril and K. S. Kim. *Chem. Rev.,* **2012**, *112*, 6156-6214.
80. C. K. Chua and M. Pumera, *Chem. Soc. Rev*., **2013**, *42*, 3222-3233.
81. J. Park and M. Yan, *Acc. Chem. Res.,* **2013**, *46*, 181-189.
82. T. Kuila, S. Bose, A. Mishra, P. Khanra, N. H. Kim and J. H. Lee, *Prog. Mater. Sci.*, **2012**, *57*, 1061-1105.
83. Z. Sun, D. K. James and J. M. Tour, *J. Phys. Chem. Lett*., **2011**, *2*, 2425-2432.
84. A. Criado, M. Melchionna, S. Marchesan and M. Prato, *Angew. Chem. Int. Ed*., **2015**, *54*, 10734-10750.
85. A. Criado, M. Melchionna, S. Marchesan and M. Prato, *Angew. Chem., Int. Ed.,* **2015**, *54*, 2-19.
86. F. Schedin, A. K. Geim, S. V. Morozov, E. W. Hill, P. Blake, M. I. Katsnelson and K. S. Novoselov*, Nat. Mater*., **2007**, *6*, 652-655.
87. M. Garnica, D. Stradi, S. Barja, F. Calleja, C. Díaz, M. Alcamí, A. L. Vázquez de Parga, F. Martín and R. Miranda, *Nat. Phys.*, **2013**, *9*, 368-374.
88. N. A. Vinogradov, K. Schulte, A. Mikkelsen, E. Lundgren, N. Mårtensson and A. B. J. Preobrajenski, *Phys. Chem. C*, **2011**, *115*, 9568-9577.
89. M. Z. Hossain, J. E. Johns, K. H. Bevan, H. J. Karmel, Y. T. Liang, S. Yoshimoto, K. Mukai, T. Koitaya, J. Yoshinobu, M. Kawai, A. M. Lear, L. L. Kesmodel, S. L. Tait and M. C. Hersam, *Nat. Chem*., **2012**, *4*, 305-309.
90. J. O. Sofo, A. S. Chaudhari and G. D. Barber, *Phys. Rev. B: Condens. Matter Mater. Phys*., **2007**, *75*, 153401.
91. D. W. Boukhvalov, M. I. Katsnelson and A. I. Lichtenstein, *Phys. Rev. B: Condens. Matter Mater. Phys*., **2008**, 77, 035427.
92. D. C. Elias, R. R. Nair, T. M. G. Mohiuddin, S. V. Morozov, P. Blake, M. P. Halsall, A. C. Ferrari, D. W. Boukhvalov, M. I. Katsnelson, A. K. Geim, K. S. Novoselov, *Science*, **2009**, *323*, 610-613.
93. D. Haberer, D. V. Vyalikh, S. Taioli, B. Dora, M. Farjam, J. Fink; D. Marchenko, T. Pichler, K. Ziegler, S. Simonucci, M. S. Dresselhaus, M. Knupfer, B. Büchner and A. Grüneis, *Nano Lett*., **2010**, *10*, 3360-3366.
94. C. H. Park, L. Yang, Y. W. Son, M. L. Cohen and S. G. Louie, *Nat. Phys*., **2008**, *4*, 213−217.
95. F. P. Ouyang, S. L. Peng, Z. F. Liu, and Z. R. Liu. *ACS Nano,* **2011**, *5*, 4023−4030.
96. M. Dvorak, W. Oswald and Z. Wu, *Sci. Rep*., **2013**, *3*, 2289.
97. S. Bian, A. M. Scott, Y. Cao, Y. Liang, S. Osuna, K. N. Houk and A. B. Braunschweig, *J. Am. Chem. Soc*., **2013**, *135*, 9240-9243.
98. M. Z. Hossain, M. A. Walsh and M. C. Hersam, *J. Am. Chem. Soc*., **2010**, *132*, 15399-15403.
99. Q. Wu, Y. Wu, Y. Hao, J. Geng, M. Charlton, S. Chen, Y. Ren, H. Ji, H. Li, D. W. Boukhvalov, R. D. Piner, C. W. Bielawski and R. S. Ruoff, *Chem. Commun*., **2013**, *49*, 677-679.
100. M. A. Bissett, S. Konabe, S. Okada, M. Tsuji and H. Ago, *ACS Nano***, 2013**, *7*, 10335-10343.
101. A. L. Vázquez de Parga and R. Miranda In Graphene: Properties, preparation, characterization and devices; Chapter 6, V. Skakalova and A. B. Kaiser, *Eds.; Woodhead Publishhing*, **2014**.
102. R. Balog, B. Jørgensen, L. Nilsson, M. Andersen, E. Rienks, M. Bianchi, M. Fanetti, E. Laegsgaard, A. Baraldi, S. Lizzit, Z. Sljivancanin, F. Besenbacher, B. Hammer, T. G. Pedersen, P. Hofmann and L. Hornekaer, *Nat. Mater*., **2010**, *9*, 315-319.
103. R. Balog, M. Andersen, B. Jørgensen, Z. Slijvancanin, B. Hammer, A. Baraldi, R. Larciprete, P. Hofmann, L. Hornekaer and S. Lizzit, *ACS Nano* **2013**, *7*, 3823-3832.
104. J. Coraux, A. T. N'Diaye, C. Busse and T. Michely, *Nano Lett.,* **2008**, *8*, 565-570.
105. E. Loginova, S. Nie, K. Thurmer, N. C. Bartelt and K. F. McCarty, *Phys. Rev. B: Condens. Matter Mater. Phys*., **2009**, *80*, 085430.
106. S. J. C hae, F. Günes, K. K. Kim, E. S. Kim, G. H. Han, S. M. Kim, H. J. Shin, S. M. Yoon, J. Y. Choi, M. H. Yang, C. W. Park, D. Pribat and Y. H. Lee, *Adv. Mater*., **2009**, *21*, 2328-2333.

107. A. Reina, X. Jia, J. Ho, D. Nezich, H. Son, V. Bulovic, M. S. Dresselhaus and J. Kong, *Nano Lett*., **2009**, *9*, 30-35.
108. X. Li, X. Cai, J. An, S. Kim, J. Nah, D. Yang, R. Piner, A. Velamakanni, I. Jung, E. Tutuc, S. K. Banerjee, L. Ruoff and R. S. Colombo, *Science*, **2009**, *324*, 1312-1314.
109. Y. Lee, S. Bae, H. Jang, S. Jang, S. E. Zhu, S. H. Sim, Y. I. Song, B. H. Hong and J. H. Ahn, *Nano Lett*., **2010**, *10*, 490-493.
110. A. B. Preobrajensk, M. L. Ng, A. S. Vinogradov and N. Martensson, *Phys. Rev. B: Condens. Matter Mater. Phys*., **2008**, *78*, 073401.
111. A. L. Vázquez de Parga, F. Calleja, B. Borca; J. J. Hinarejos, M. G. C. Passeggi, F. Guinea and R. Miranda, *Phys. Rev. Lett*., **2008**, *100*, 056807.
112. D. Stradi, S. Barja, C. Díaz, M. Garnica, B. Borca, J. J. Hinarejos, D. Sánchez-Portal, M. Alcamí, A. Arnau, A. L. Vazquez de Parga, R. Miranda and F. Martín, *Phys. Rev. B: Condens. Matter Mater. Phys*., **2013**, *88*, 245401.
113. D. Stradi, S. Barja, C. Díaz, M. Garnica, B. Borca, J. J. Hinarejos, D. Sánchez-Portal, M. Alcamí, A. Arnau, A. L. Vazquez de Parga, R. Miranda and F. Martín, *Phys. Rev. Lett.,* **2011**, *106*, 186102.
114. B. Borca, S. Barja; M. Garnica, D. Sánchez-Portal, V.M. Silkin, E. V. Chulkov, C. F. Hermanns, J. J. Hinarejos, A. L. Vazquez de Parga, A. Arnau, P. M. Echenique and R. Miranda, *Phys. Rev. Lett*., **2010**, *105*, 036804.
115. S. Katano, Y. Kim, M. Trenary and M. Kawai, *Chem. Commun*., **2013**, *49*, 4679-4681.
116. B. Borca, S. Barja, M. Garnica, M. Minniti, A. Politano, J. M. Rodríguez-García, J. J. Hinarejos, D. Farías, A. L. Vazquez de Parga and R. Miranda, *New J. Phys*., **2010**, *12*, 093018.
117. M. Garnica, D. Stradi, F. Calleja, S. Barja, C. Díaz, M. Alcamí, A. Arnau, A. L. Vázquez de Parga, F. Martín and R. Miranda, *Nano Lett.,* **2014**, *14*, 4560-4567.
118. D. Stradi, M. Garnica, C. Díaz, F. Calleja, S. Barja, M. Alcamí, N. Martín, A. Arnau, A. L. Vázquez de Parga, R. Miranda and F. Martín, *Nanoscale*, **2014**, *6*, 15271-15279.
119. S. Barja, M. Garnica, J. J. Hinarejos, A. L. Vázquez de Parga, N. Martín and R. Miranda, *Chem. Commun*., **2009**, *46*, 8198.
120. J. A. Stroscio and D. M. Eigler, *Science,* **1991**, *254*, 1319-1326.
121. Hla, S.-W. *J. Vac. Sci. Technol., B: Microelectron. Process. Phenom*., **2005**, *23*, 1351-1360.
122. C. Caillier, D. K. Ki, Y. Lisunova, I. Gaponenko, P. Paruch and A. F. Morpurgo, *Nanotechnology*, **2013**, *24*,405201.
123. J. Lalevee, X. Allonas and J. P. Fouassier, *J. Org. Chem*,. **2005**, *70*, 814.
124. D. J. Henry, C. J. Parkinson, P. M. Mayer and L. J. Radom, *Phys. Chem. A,* **2001**, *105*, 6750.
125. M. L. Coote, *J. Phys. Chem. A***, 2004**, *108*, 3865.
126. E. Kukk, R. Sankari, M. Huttula, A. Sankari, H. Aksela and S. J. Aksela, *Electron Spectrosc. Relat. Phenom*., **2007**, *155*, 141.
127. J. Q. Wu, I. Beranek and H. Fischer, *Helv. Chim. Acta***, 1995**, *78*, 94.
128. M. W. Wong and L. J. Radom, *Phys. Chem*. **1995**, *99*, 8582.
129. H. Yoshida, Y. Fujimura, H. Yuzawa, J. Kumagai and T. Yoshida, *Chem. Commun*., **2013**, *49*, 3793.
130. T. L. Cottrell, The Strengths of Chemical Bonds, Butterworth Scientific, **1978**.
131. A. T. N'Diaye, J. Coraux, T. N. Plasa, C. Busse and T. Michely, *New J. Phys*., **2008**, *10*, 043033.
132. X. Li, X. Cai, J. An, S. Kim, J. Nah, D. Yang, R. Piner, A. Velamakanni, I. Jung, E. Tutuc, S. K. Banerjee, L. Ruoff and R. S. Colombo, *Science,* **2009**, *324*, 1312.
133. P. W. Sutter, J. I. Flege and E. A. Sutter, *Nat. Mater.,* **2008**, *7*, 406.
134. Omicron NanoTechnology, GmbH, [Online]. Available: http://www.omicron.de
135. Specs, [Online]. Available: http://www.specs.de.
136. F. Calleja, A. Arnau, J. J. Hinarejos, A. L. Vázquez de Parga, W.A. Hofer, P. M. Echenique and R. Miranda, *Phys. Rev. Lett*., **2004**, *92*, 206101.
137. B. Borca, F. Calleja, J. J. Hinarejos, A. L. Vázquez de Parga and R. Miranda, *J. Phys. Condens. Matter*, **2009**, *21*,134002.
138. S. Bian, A. M. Scott, Y. Cao, Y. Liang, S. Osuna, K. N. Houk and A. B. J. Braunschweig, *Am. Chem. Soc*., **2013**, *135*, 9240.

139. C. Caillier, D. K. Ki, Y. Lisunova, I. Gaponenko, P. Paruch and A. F. Morpugo, *Nanotechnology*, **2013**, *24*, 405201.
140. E. Kukk, R. Sankari, M. Huttula, A. Sankari, H. Aksela and S. J. Aksela, *Electron Spectrosc. Relat. Phenom*., **2007**, *155*, 141.
141. G. Kresse and J. Hafner, *Phys. Rev. B*, **1993**, *47*, 588(R).
142. J. P. Perdew, K. Burke and M. Ernzerhof, *Phys. Rev. Lett*., **1997**, *77*, 3865.
143. S. J. Grimme, *Comp. Chem.*, **2006**, *27*, 1787.
144. G. Kresse and D. Joubert, *Phys. Rev. B*, **1999**, *59*, 1758.
145. D.J. Henry, C.J. Parkinson, P. M. Mayer, L. J. Radom, Phys. Chem. A, **2001**, *105*, 6750.
146. M. L. Coote, *J. Phys. Chem. A*, **2004**, *108*, 3865.
147. D. Stradi, S. Barja, C. Díaz, M. Garnica, B. Borca, J. J. Hinarejos, D. Sánchez Portal, M. Alcamí, A. Arnau, A. L. Vázquez de Parga, R. Miranda and F. Martín, *Phys. Rev. Lett*., **2011**, *106*, 186102.
148. M. Garnica, D. Stradi, F. Calleja, S. Barja, C. Díaz, M. Alcamí, A. Arnau, A. L. Vázquez de Parga, F. Martín and R. Miranda, *Nano Lett*., **2014**, *4*, 4560.

CHAPTER 3

1. Introduction

1.1 Transition Metal Dichalcogenides band structure

Two-dimensional (2D) materials are currently one of the most extensively studied classes of materials due to the wealth of unusual physical phenomena that occur when charge and heat transport are confined to a plane. Graphene was theoretically studied by P. R. Wallace as early as in 1947[1] and experimentally isolated and characterized by K. Novoselov and A. Geim et al. in 2004.[2] As discussed in Chapter 2 the unique electronic, optical, mechanical and thermal properties found in graphene make it the most representative material member of the 2D material family. However some of graphene's properties can also be interpreted as drawbacks for certain applications, such as its zero band gap and its weak light absorption. These limitations have motivated the search for new 2D materials. One important class of 2D materials is layered transition metal dichalcogenides (TMDCs) that show a wide range of physical properties depending of material composition and thickness. Since the discovery of monolayer molybdenum disulfide (MoS_2)[3] and the development of the first single-layer MoS_2 transistor in 2011,[4] the performance of 2D-TMDCs materials has incited an incredible amount of work. Most remarkably the properties of the atomically thin crystals of TMDCs can drastically differ from their well-characterized bulk counterparts. In particular, monolayer TMDCs are particularly interesting because of their direct band gap and non-centrosymmetric lattice structure.[5,6]

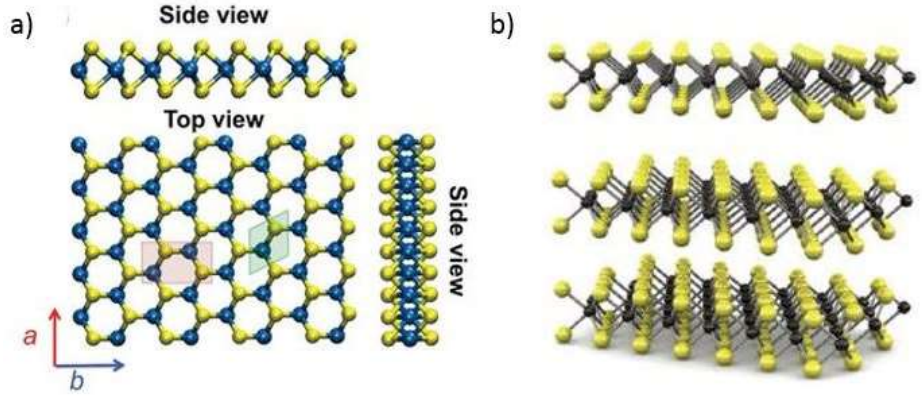

Figure 3.1. a) Optimized geometric structures of the MoS_2 monolayer from the top view and side view, **b)** three-dimensional schematic representation of a typical MX_2 structure, with the chalcogen atoms (X) in yellow and the metal atoms (M) in grey.

[1] P. R. Wallace, *Phys. Rev*., **1947**, *71*, 622-634.
[2] K. S. Novoselov, A. K. Geim, S. V. Morozov, D. Jiang, Y. Zhang, S. V. Dubonos, I. V. Grigorieva and A. A. Firsov, *Science* **2004,** *306*, 666-669.
[3] K. F. Mak, C. Lee, J. Hone, J. Shan and T. F. Heinz, *Physical Review Letters*, **2010**, *105*, 136805.
[4] B. Radisavljevic, A. Radenovic, J. Brivio, V. Giacometti and A. Kis, *Nat. Nanotechnol*., **2011**, *6*, 147-150.
[5] A. Splendiani, L. Sun, Y. Zhang, T. Li, J. Kim, C. Y. Chim, G. Galli and F. Wang, *Nano Lett*., **2010**, *10*, 1271-1275.
[6] K. F. Mak, K. He, J. Shan and T. F. Heinz, *Nat. Nanotechnol*., **2012**, *7*, 494-498.

TMDCs (e.g., MoS_2, WS_2, and $NbSe_2$) represent a large family of layered materials with the formula MX_2, where M is a transition metal element from group IV (Ti, Zr or Hf), group V (V, Nb or Ta) or group VI (Mo, W), and X is a chalcogen atom (S, Se or Te). The atom in 2D TMDCs are arranged in sheets so that M-atoms are sandwiched between two layers of X-atoms. Depending on the stacking sequence and the metal atom coordination the bulk crystal, layered TMDCs present different polymorphs, which vary in metal atom coordination (octahedral or trigonal) and polytypes that vary in stacking order (hexagonal or rhombohedral)(see Figure 3.2).

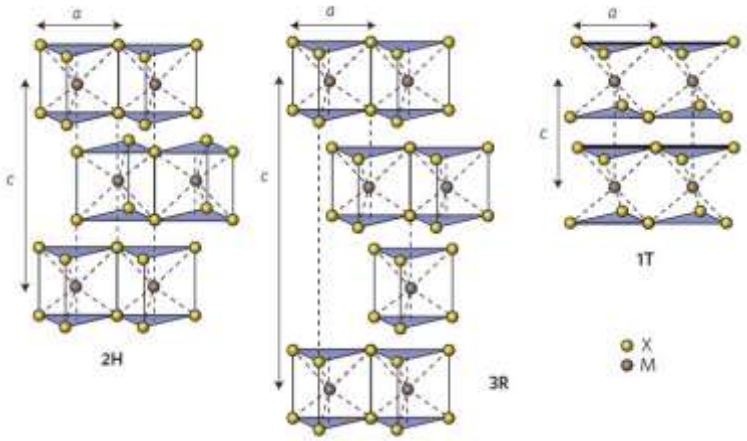

Figure 3.2. Schematics of the structural polytypes where the chalcogen atoms (X) are yellow and the metal atoms (M) are grey.

The geometry of metal coordination can have a significant influence on the electronic properties of TMDCs. For example when MoS_2 is coordinated in trigonal prismatic geometry and arranged in hexagonal or rhombohedral stacking, it is semiconducting whereas it is metallic in octahedral coordination. According to the ligand field theory, the semiconducting nature of trigonal prismatic MoS_2 is due to the completely filled dz_2 and empty dxy and $dx_2\_y_2$ orbitals while octahedral MoS_2 is metallic because of it is partially filled (dxy, dxz, dyz).[7,8] (see Figure 3.3)

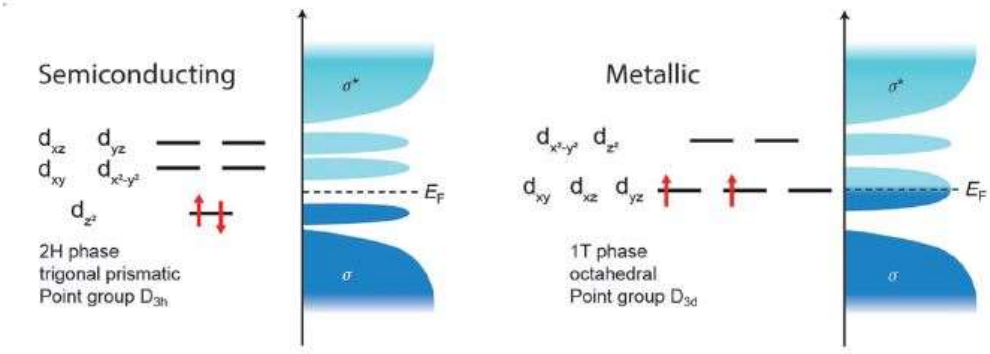

Figure 3.3. Energy bands in semiconductor and metallic MoS_2.

[7] L. F. Mattheiss, *Physical Review B*, **1973**, *8*, 3719.
[8] R. A. Bromley, *Physics Letters A*, **1970**, *33*, 242-243.

This electronic band structure is not only controlled by the coordination but also by the numbers of layers. As the intra-layer covalent bonds are much stronger than the interlayer Van der Waals forces, bulk TMDCs can be mechanically exfoliated obtaining monolayers of thickness of approximately 0.6-0.7 nm, Figure 3.4 shows the band structures obtained for bulk and few- to mono-layer MoS_2. The changes band structure with the number layer can be explained by interlayer orbital interactions.[9,10] The Density functional theory (DFT) calculations show that the uppermost states at the Γ-point at the valence band are originate mainly from d_{2z} orbitals on Mo atoms and contributions of p_z orbitals on S atoms. Due to the antibonding nature of these states, their energy diminishes with increasing interlayer distance and decreasing of the layer-layer interaction.[11] Conversely, the states at the top of the valence band and the bottom of the conduction band near the K-point, which are nearly exclusively dxy and dx_2-y_2 states for Mo, are accordingly unaffected by a change in the interlayer separation. In the case of single layer the gap is determined by the states at the K-point and a transition from an indirect gap (Γ →K) to a direct gap (K→K) semiconductor, this behavior was confirmed by Lebègue and co-workers.[12]

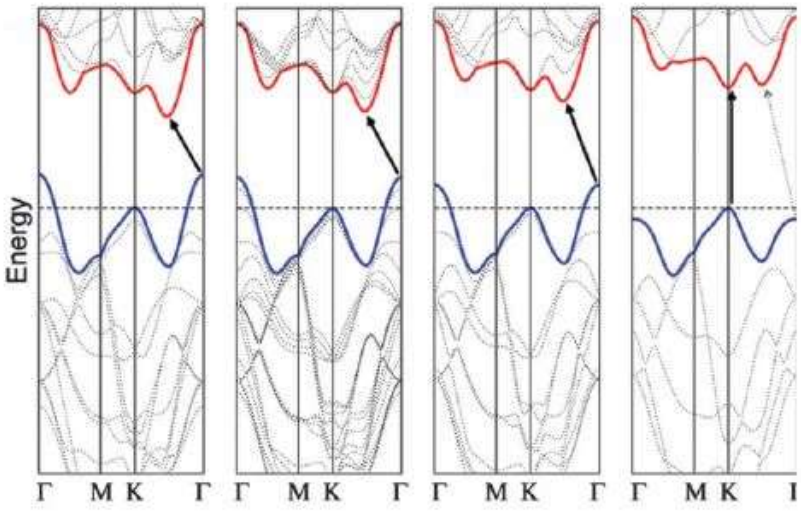

Figure 3.4. Band structure calculated from density functional theory (DFT) for bulk and monolayer MoS_2.

[9] K. F. Mak, C. Lee, J. Hone, J. Shan and T. F. Heinz*, Phys. Rev. Lett*., **2010**, *105*, 136805.
[10] J. A. Wilson and A. D. Yoffe, *Adv. Phys*., **1969**, *18*, 193.
[11] T. Li. and G. Galli. Journal of Physical Chemistry C, **2007**, 44, 16192-16196.
[12] S. Lebègue and O. Eriksson, *Physical Review B*, **2009**, *79*, 115409.

1.2 Electronic properties

Monolayer TMDCs are particularly interesting due to their direct energy band gaps and non-centrosymmetric lattice structure.[13,14] With a direct band gap of 1.8 eV and exceptional mechanical strength, 2D-TMDCs have become new candidates for the development ultra-thin semiconductors.[15] During the last years different strategies have been used for the design of new field effect transistors (FETs) that incorporate monolayer TMDCs. In this field we can highlight the group of Podzorov which reported one of the earliest works on field-effect transistors using WSe_2 crystal as semiconductor. In this work they obtained flexible inorganics FETs with high mobility values around 500 cm^2 /V s at room temperature, ambipolar behavior and high on/off ratios (≈10^4). After that, new devices were fabricated using thin layers of MoS_2 with a back-gate and top gate configuration. For the back gate mobility values in the range 0.1-10 cm^2 /V s were obtained[16,17] whereas for devices with a top gate configuration, the mobility values are increased up to 200 cm^2 /V s at room temperature. In addition, the top-gate geometry also increases the on/off ratios (≈10^8) and allows a reduction of the voltage necessary to switch the device (see Figure 3.5).

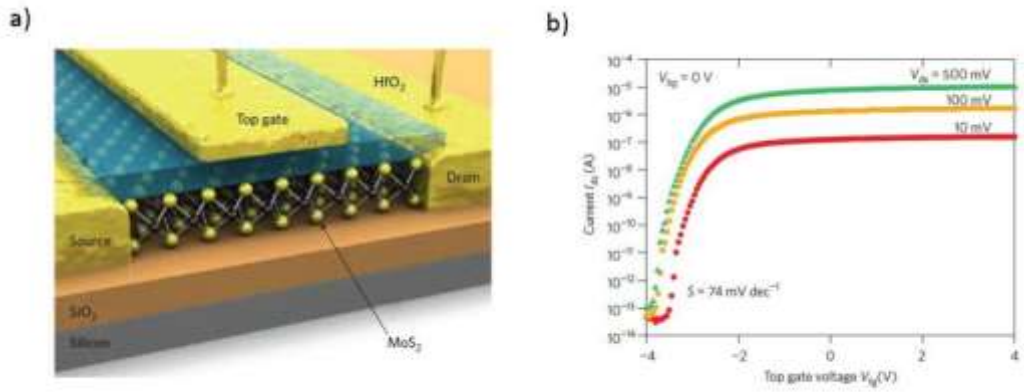

Figure 3.5. a) Schematic illustration of HfO_2-top-gated monolayer MoS_2 FET device. **b)** Source–drain current (I_{ds}) versus top gate voltage (V_{tg}) curve recorded from the top-gated device in **a** for a bias voltage ranging from 10 mV to 500 mV.

This work also explores the mechanical properties of single layer MoS_2, showing that it is 30 times as strong as steel and can be deformed up to 11% before breaking.[18] All these results suggest MoS_2 as an excellent alternative for low-cost flexible electronics. However some of the limitations of TMDCs as high effective mass of carriers and relatively low carrier mobility values[19] could restrict certain high-performance applications.

[13] A. Splendiani, L. Sun, Y. Zhang, T. Li, J. Kim, C. Y. Chim, G. Galli and F. Wang, *Nano Lett.*, **2010**, *10*, 1271-1275.
[14] K. F. Mak, K. He, J. Shan and T. F. Heinz, *Nat. Nanotechnol.*, **2012**, *7*, 494-498.
[15] B. Radisavljevic, A. Radenovic, J. Brivio, V. Giacometti and A. Kis, *Nat. Nanotechnol.*, **2011**, *6*, 147-150.
[16] K. S. Novselov, D. Jiang, F. Schedin, V. V. Khotekevich, S. V. Morozov and A. K. Geim, *Proc. Natl. Acad. Sci. U. S. A.* **2005**, *102* 10451-10453.
[17] A. Ayari, E. Cobas, O. Ogundadegbe and M. S. Fuhrer, *J. Appl. Phys.*, **2007,** *101*, 014507.
[18] S. Bertolazzi, J. Brivio and A. Kis, *ACS Nano*, **2011**, *5*, 9703-9709.
[19] Y. Yoon, K. Ganapathi and S. Salahuddin, *Nano Lett.,* **2011**, *11*, 3768-3773.

1.3 Photophysical Properties

Both theoretical work[20,21,22] and experiments[23,24] suggest that optical transitions in ultrathin TMDCs samples are dominated by excitons rather than direct interband transitions. In 2010 Mak and co-workers[25] and Splendiani and co-workers[26] reported on the optical transitions, photoluminescence (PL) and photoconductivity spectroscopy on monolayer and few layers MoS_2 samples. The optical absorption spectrum of thin layer MoS_2 exhibits two prominent peaks at 670 and 627 nm assigned to A and B excitons, at the expected energies of the band gap energies at the K-point point. This absorption peaks for the direct excitonic states exhibit little change with layer thickness. This is due to the small energy difference between the direct and the indirect excitonic transitions (~ 1 eV) (see Figure 3.6a). Unlike optical absorption, photoluminescence shows a strong dependence with the layer thickness. The photoluminescence emission of monolayer MoS_2 is in striking contrast to its absence in bulk MoS_2 (see Figure 3.6b).

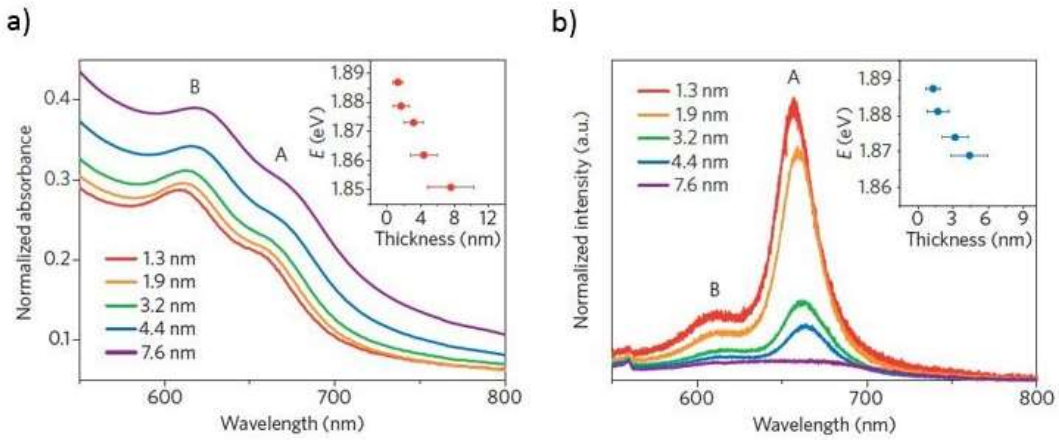

Figure 3.6. Optical absorption **(a)** and photoluminescence spectra **(b)** of different thin layer MoS_2.

Thus, with direct band gaps in the visible region of the electromagnetic spectrum, large exciton binding energies, and strong photoluminescence, monolayer semiconducting TMDCs are a promising material for optoelectronic applications. In order to optimize the photoresponsivity of mono- and multilayer MoS_2 devices, during the last years a great number of strategies have been developed to modulate these optical properties, among the strategies applied we can highlight chemical and physical modification.

[20] T. Cheiwchanchamnangij and W. R. Lambrecht, *Phys. Rev. B,* **2012**, *85*, 205302.
[21] A. Ramasubramaniam, *Phys. Rev. B*, **2012**, *86*, 115409.
[22] *M. Ye*, *D. Winslow, D. Zhang*, *R. Pandey and Y. K. Yap, Photonics*, **2015,** *2*, 288-307.
[23] J. S. Ross, S. Wu, H. Yu, N. J. Ghimire, A. M. Jones, G. Aivazian, J. Yan, D. G. Mandrus, D. Xiao and W. Yao, *Nat. Commun*., **2013**, *4*, 1474.
[24] T. Korn, S. Heydrich, M. Hirmer, J. Schmutzler and C. Schüller, *Appl. Phys. Lett*., **2011**, *99*, 102109.
[25] K. F. Mak, C. Lee, J. Hone, J. Shan and T. Heinz, *Phys. Rev. Lett*., **2010**, *105*, 136805.
[26] A. Splendiani, L. Sun., Y. Zhang, T. Li, J. Kim, C. Y. Chim, G. Galli and F. Wang, Nano Lett., **2010**, 10, 1271-1275.

1.4 Physical modification

Among the different physical methods developed to modify TMDCs we can mention strain-engineering,[27,28,29] field effect doping,[30] or artificial stacking of different 2D materials.[31,32] In this way Bolotin and co-workers[27] used the previous work with corrugated graphene to perturb[33] the band structure of MoS_2 by mechanical strain. They studied the influence of uniaxial tensile strain from 0% to 2.2% on the phonon spectra and band gaps of both monolayer and bilayer MoS_2. As the strain increase, the Raman peak corresponding to the in-plane E_{2g} phonon mode is divided into two distinct peaks and the photoluminescence signal exhibits a linear redshift (see Figure 3.7).

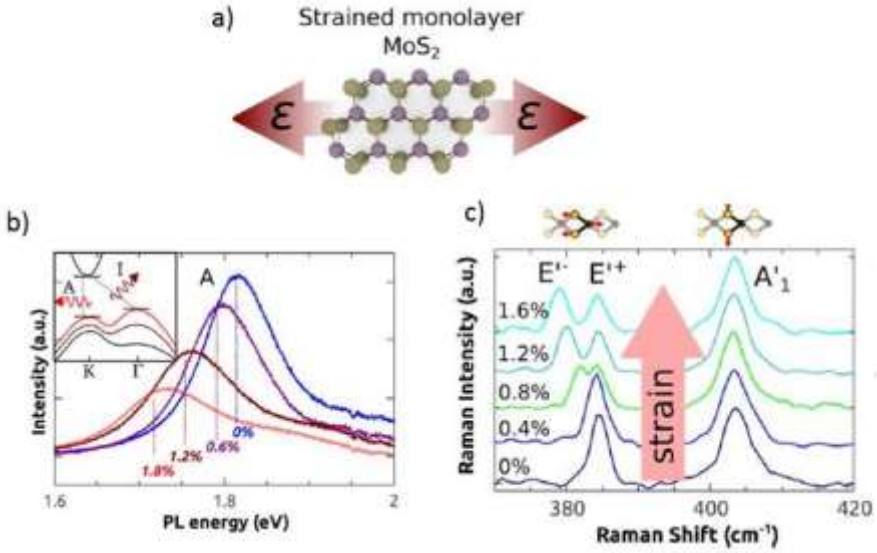

Figure 3.7 a) Scheme strained monolayer MoS_2 **b)** Evolution of the Raman spectrum as a device is strained from 0 to 1.6%, **c)** PL spectra of a representative monolayer device as it is strained from 0 to 1.8%. Strain independent PL background was subtracted.

[27] H. J. Conley, B. Wang, J. I. Ziegler, R. F. Haglund, S. T. Pantelides and K. I. Bolotin, *Nano Lett.,* **2013,** *13*, 3626-3630.
[28] A. Castellanos-Gomez, R. Roldán, E. Cappelluti, M. Buscema, F. Guinea, H. S. J. van der Zant and G. A. Steele, *Nano Lett.*, **2013**, *13*, 5361-5366.
[29] R. Das, B. Rakshit, S. Debnath and P. Mahadevan, *Physical Review B*, **2014**, 89, 115201.
[30] Q. H. Wang, K. Kalantar-Zadeh, A. Kis, J. N. Coleman and M. S. Strano, *Nat. Nanotechnol.*, **2012**, *7*, 699.
[31] C. H. Lee, G. H. Lee, M. van der Zande, W. Chen, Y. Li, M. Han, X. Cui, G. Arefe, C. Nuckolls, T. F. Heinz, J. Guo, J. Hone and P. Kim, *Nat. Nanotechnol.*, **2014**, *9*, 676-681.
[32] M. M. Furchi, A. Pospischil, F. Liebisch, J. Burgdörfer and T. Mueller, *Nano Lett.*, **2014**, *14*, 4785-4791.
[33] T. Mohiuddin, A. Lombardo, R. Nair, A. Bonetti, G. Savini, R. Jalil, N. Bonini, D. Basko, C. Galiotis, N. Marzari, K. Novoselov, A. Geim, A. Ferrari, *Phys. Rev. B*, **2009**, *79*, 1-8.

Following the results obtained for other 2D semiconductors,[34] the influence of the field effect doping in the optical properties of the TMDCs was also investigated.[35,36] The doping via FET setup changes the band structure considerably as exemplified in Figure 3.8, which shows the band structures for different electron and hole doping levels for mono and trilayer MoS_2, respectively.

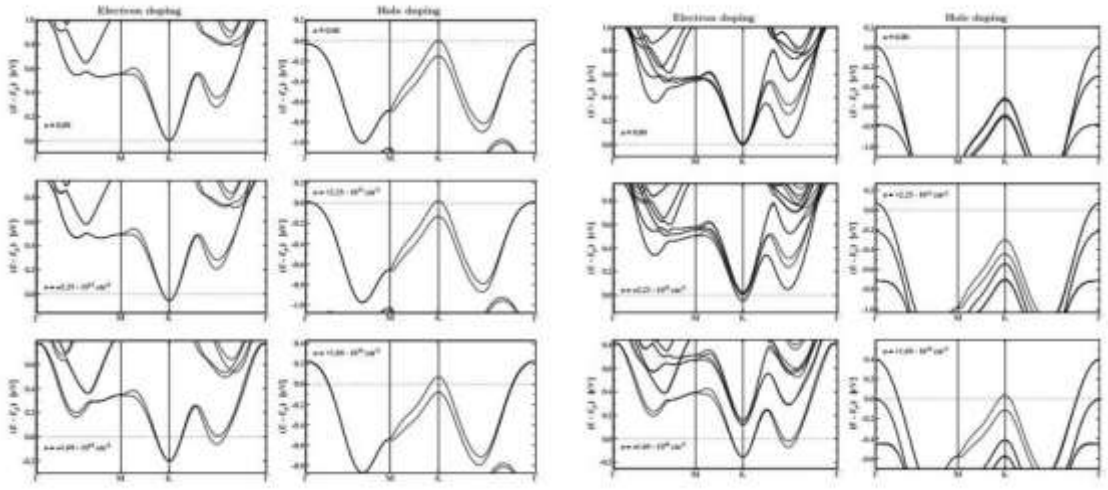

Figure 3.8. Band structure for different FET induced doping of monolayer (a) and trilayer MoS_2 (b).

An other way to modify the optical properties of TMDCs is through building van der Waals heterostructures with other atomically thin materials.[37] Making use of this methodology, Philip et al. carried out the development of p–n junction heterostructures, combining p-type tungsten diselenide (WSe_2) and n-type molybdenum disulphide (MoS_2).[38] The interlayer tunnelling recombination of the majority carriers across the van der Waals interface, which can be tuned by gating, is found to influence significantly the electrical and optoelectronic properties of the junction due to the rapid separation of charge carriers in the junction region (see Figure 3.9).

[34] F. Xia, H. Wang, D. Xiao and M. Dubey, *Nat. Photon.*, **2014**, *8*, 899-907.
[35] S. Tongay, J. Zhou, C. Ataca, J. Liu, J. S. Kang, T. S. Matthews, L. You, J. Li, J.C. Grossman and J. Wu, *Nano Lett.*, **2013**, *13*, 2831-2836.
[36] B. Chakraborty, A. Bera, D. V. S. Muthu, S. Bhowmick, U.V. Waghmare and A. K. Sood, *Phys. Rev. B*, **2012**, 161403(R).
[37] L. Britnell, R. V. Gorbachev, R. Jalil, B. D Belle, F. Schedin, A. Mishchenko, T. Georgiou, M. I. Katsnelson, L. Eaves, S. V. Morozov, N. M. R Peres, J. Leist, A. K Geim, K. S Novoselov and L. A. Ponomarenko, *Science*, **2012**, *335*, 947-950.
[38] C. H. *Lee*, G. H. *Lee*, *A. M. van der Zande*, *W. Chen*, Y. Li, *M. Han*, *X. Cui*, *G. Arefe*, *C. Nuckolls*, *T. F. Heinz*, *J. Guo*, *J. Hone*, *P. Kim Nat. Nanotechnol.*, **2014**, *9*, 676-681.

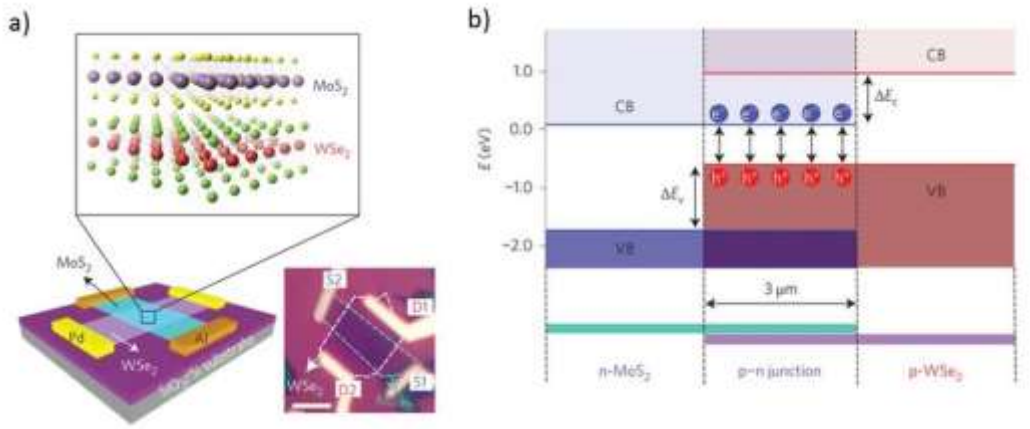

Figure 3.9. a) Bottom left: Schematic diagram of a van der Waals-stacked MoS_2/WSe_2 heterojunction device with lateral metal contacts. **Top**: enlarged crystal structure, with purple, red, yellow and green spheres representing Mo, S, W and Se atoms, respectively. **Bottom right**: Optical image of the fabricated device, where D1 and D2 (S1 and S2) indicate the metal contacts for WSe_2 (MoS_2). Scale bar, 3 μm. b) Band profiles in the lateral directions, obtained from electrostatic simulations. Under forward bias (V_{ds} = 0.6 V), electrons in the conduction band (CB) of MoS_2 and holes in the valence band (VB) of WSe_2 undergo interlayer recombination (black arrows). Reproduced by permission from ref 38 (Copyright © 2014 Nature publishing group).

1.5 Chemical Modification

Surface modification strategies offer additional ways to tune the properties of this TMDCs. Javey et al. paved the way of chemical modification through charge-transfer using gases[39] and metal atoms.[40] They were the first group to report the use of NO_2 molecules as effective p-dopants of monolayer and multi-layer WSe_2 obtaining high-performance ML-FETs (see Figure 3.10).

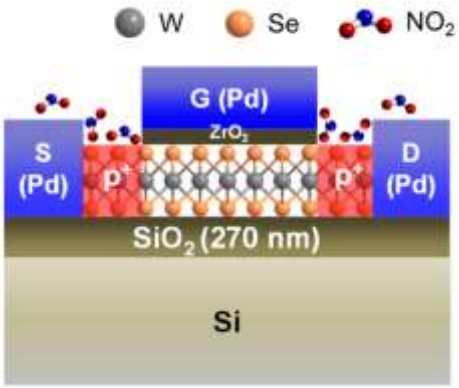

Figure 3.10. Schematic of a top-gated WSe_2 ML-FET with chemically p-doped S/D contacts by NO_2 exposure. The top-gate acts as a mask that protects the active channel from NO_2 doping. Reproduced by permission from ref 39 (Copyright © 2012 American Chemical Society).

[39] H. Fang, S. Chuang, T. C. Chang, K. Takei, T. Takahashi and A. Javey, *Nano Lett.*, **2012**, *12*, 3788-3792.
[40] H. Fang, M. Tosun, G. Seol, T. C. Chang, K. Takei, J. Guo and A. Javey, *Nano Lett.*, **2013**, *13*, 1991-1995.

The p-doping was followed by the first n-doping of MoS_2 and WSe_2 using metals, such as potassium. After K vapor exposure the electron conduction at the positive gate voltage increases drastically by several orders of magnitude, due to the lowering of the contact resistance. Specifically, the current value after 120 min of doping using the specified condition is $\sim 10^5$ × higher than the undoped device, this n-type WSe_2 FETs with high mobilities complement those obtained for previously reported p-type WSe_2 FETs.

Continuing with the chemical doping, the use of organic molecules opens the door for new surface charge transfer doping, this doping concepts is similar to that used with other material such as graphene, carbon nanotubes and fullerenes. In this way it was also Javey and co-workers[41] who carried out the development of air stable dopants for TMDCs. They studied the benzyl viologen (BV) as a donor in few-layer MoS_2 crystals. After doping with the BV molecule the gate dependence of the current decreased while the on current level increased by an order of magnitude, these changes confirm the air stable n-doping of MoS_2 crystals (see Figure 3.11). Following the same strategy others groups have developed new photodetectors using organic dyes with different structures[42,43,44] to modify the MoS_2 surface. These studies with both n-and p-type organic semiconductors, show higher values of photoresponsivity and photodetectivity with respect the pristine device, and suggest that stacking organic semiconductors is a valid approach to create MoS_2 heterostructures that result efficient photodetecting devices

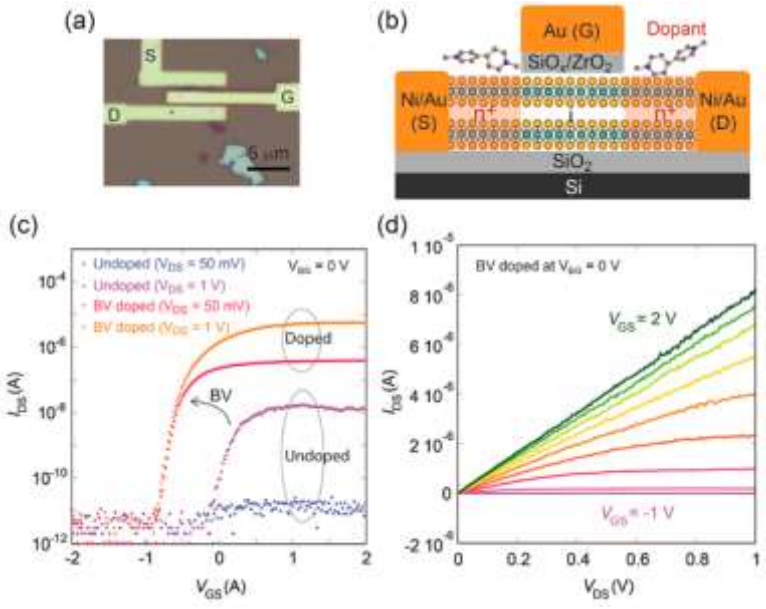

Figure 3.11. a) Optical microscope image **(b)** Schematic illustration of a back-gated MoS_2 device used for BV surface charge transfer doping studies. The phenyl rings have been omitted in the schematics of BV

[41] D. Kiriya, M. Tosun, P. Zhao, J. S. Kang and A. Javey, *J. Am. Chem. Soc*., **2014**, *136*, 7853-7856.

[42] S. H. Yu, Y. Lee ,S. K Jang, J. Kang, J. Jeon, C. Lee, J. Y. Lee, H. Kim, E. Hwang, S. Lee and J. H. Cho, *ACS Nano,* **2014**, *8*, 8285-8291.

[43] Y. Huang, W. Zheng, Y. Qiu, and P. Hu, *ACS Appl. Mater. Interfaces*, **2016**, *8*, 23362-23370.

[44] J. Pak, J. Jang, K. Cho, T. Y. Kim, J. K. Kim, Y. Song, W. K. Hong, M. Min, H. Lee and T. Lee, *Nanoscale,* **2015**, *7*, 18780-18788.

molecules for simplification. **(c)** Transfer characteristic curves of the device before doping (green), right after BV doping (purple), and after the doped device was kept in air for 1 day (blue) at V_{DS} = 1 V. d) output characteristic of the devices after BV doping measured at gate voltage increments of 0.3 V.

1.6 Sample preparation

The need for high-quality, large-area monolayer materials has incited an incredible amount of work on thin film synthesis. The reliable synthesis of single and few-layer 2D materials is an essential first step for characterizing the layer dependent changes in their properties, as well as providing pathways for their integration into a multitude of applications. It was in 1963 when the work by Frindt and Yoffe[45] demonstrated that layered van der Waals materials, such as layered metal dichalcogenides, could be mechanically and chemically exfoliated[46,47] into few and single layers,[48,49] as well as the Chemical Vapor Deposition (CVD) growth.[50]

1.6.1 Mechanical exfoliation and deterministic transfer

In this particular case the mechanical exfoliation is the best way to obtain cleanest, highly crystalline and atomically thin nanosheets to be transferred onto suitable substrate using deterministic transfer. After exfoliation we can use different methods to control the location of the flakes on substrate. Within these, we can highlight three transfer methods: the wedging method,[51] the polyvinylalcohol (PVA) method[52] and the evalcite method.[53] These methods involve wet process steps, which can compromise the stability and quality of the transferred material either by chemical reaction with the material itself or by leaving residues on the surface. In order to preserve the original properties and avoid the contamination of the fabricated structures Castellanos-Gomez et al [54]developed a new method based on the use of polydimethylsiloxane (PDMS), a commercially available silicone-based viscoelastic material. The method, called *deterministic transfer by all-dry viscoelastic stamping*, gives the possibility to choose a flake among all the exfoliated material and accurately transfer it to an arbitrary substrate in the desired exact position of the substrate.

---

[45] R. F. Frindt*, J. Appl. Phys*., **1966**, *37*, 1928.

[46] J. Kim, S. Kwon, D. H. Cho, B. Kang, H. Kwon, Y. Kim, S. O. Park, G. Y. Jung, E. Shin, W. G. Kim, H. Lee, G. H. Ryu, M. Choi, T. H. Kim, J. Oh, S. Park, S. K. Kwak, S. W. Yoon, D. Byun, Z. Lee and C. Lee, *Nat. Commun.,* **2015**, *6*, 8294.

[47] G. Eda, H. Yamaguchi, D. Voiry, T. Fujita, M. Chen and M. Chhowalla, *Nano Lett.,* **2011**, *11*, 5111-5116.

[48] P. Joensen, R. F. Frindt and S. R. Morrison, *Mater. Res. Bull***. 1986**, *21*, 457-461.

[49] V. Nicolosi, M. Chhowalla, M. G. Kanatzidis, M. S. Stranoa and J. N. Coleman, *Science*, **2013**, *340*, 1226419-1226437.

[50] Y. H. Lee, X. Q. Zhang, W. Zhang, M. T. Chang, C. T. Lin, K. D. Chang, Y. C. Yu, J. T. Wang, C. S. Chang, L. J. Li and T. W. Lin, *Adv Mater,* **2012**, *24*, 2320-2325.

[51] G. F. Schneider, V. E. Calado, H. Zandbergen, L. M. K. Vandersypen and C. Dekker., *Nano Lett*., **2010**, *10*, 1912-1916.

[52] C. R. Dean, A. F. Young, I. Meric, C. Lee, L. Wang, S. Sorgenfrei, K. Watanabe, T. Taniguchi, P. Kim, K. L. Shepard and J. Hone, *Nat. Nanotechnol*., **2010**, *5*, 722-726.

[53] P. Zomer, S. Dash, N. Tombros, B. van Wees, Appl. Phys Lett., **2011**, *99*, 232104.

[54] A. Castellanos-Gomez, M. Buscema, R. Molenaar, V. Singh, L. Janssen, H. S. J. van der Zant and G. A. Steele, *2D Materials*, **2014**, *1*, 011002.

1.6.2 Mechanical exfoliation

Since the development of this methodology to isolate graphene from bulk graphite, it has been widely used for the exfoliation of other layered materials, such as TMDCs. The crystals are first peeled off from their bulk crystals by using adhesive tape. The step by step method is as follow: a piece of adhesive tape put into contact with the bulk material and peeled off fast in such a way that several pieces of material with different thicknesses are detached from the bulk material, remaining stuck to the tape. The process is then repeated as many times as necessary to reduce the thickness of the exfoliated material (see Figure 3.12).

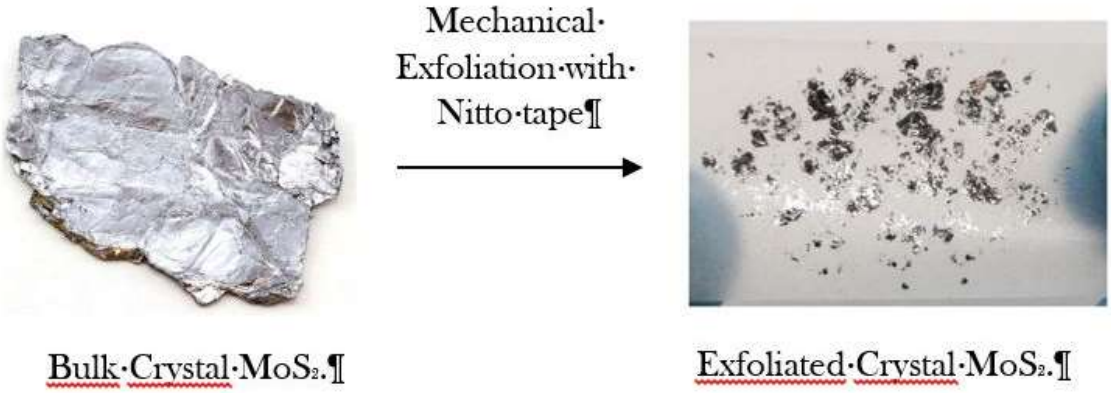

Figure 3.12. Scheme of the scotch tape method with the bulk material and the exfoliated MoS_2 crystal on a Nitto tape.

The exfoliated crystals are deposited from the Nitto tape onto PDMS, which is a thin layer of commercially available viscoelastic material. At this point two different procedures can be followed to remove the Nitto tape, the usual procedure consists in peeling off the stamp fast, living high density of flakes on the PDMS stamps. On the other hand, the adhesive tape can be removed slowly leaving less material on the stamp (see Figure 3.13). The procedure to follow depends on the material and the size of exfoliated crystals.

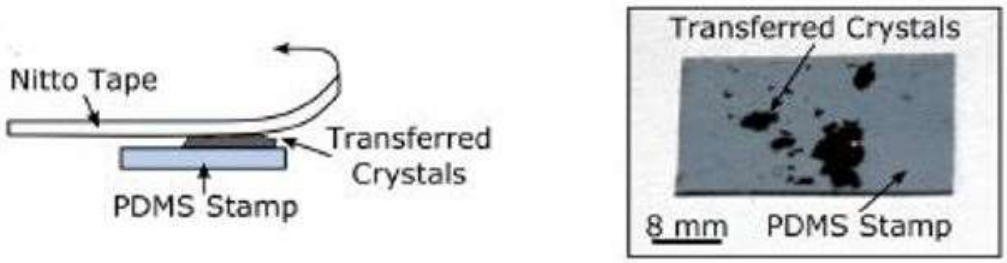

Figure 3.13. Artistic representation transfer exfoliated flakes to a PDMS stamp.

Once the crystals are transferred to the PDMS stamp, the exfoliated MoS_2 is inspected under an optical microscope in transmission mode to select the thinner flakes, according to their contrast under illumination, the amount of light each flakes absorbs depends on the number of layers, resulting in a different color for each thickness. The thickness can also be determined by measuring the Raman spectra.[55] Thanks to the optical microscope we can quickly and easily find a flake with a suitable area and thickness to transfer onto the substrate.

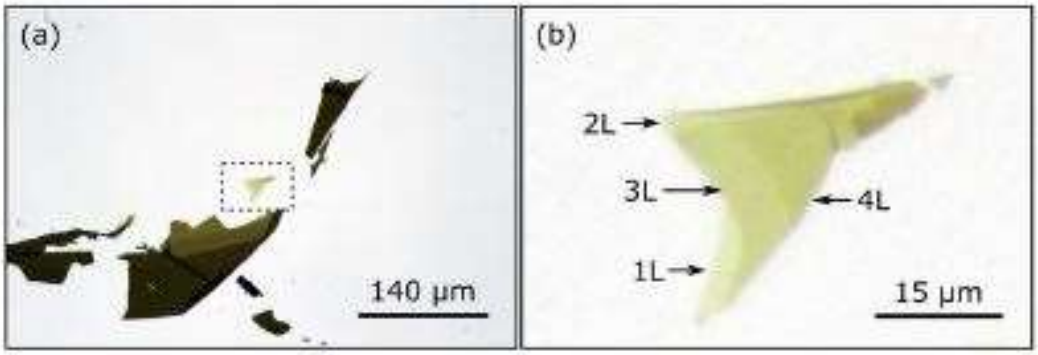

Figure 3.14. a) Optical microscopy image in transmission mode of several MoS_2 flakes transferred to a PDMS stamp with different thickness. **b)** Zoom of the region highlighted with a dashed square in (a) where it is shown a MoS_2 flake with different thickness ranging from 1 to 4 layers.

[55] C. Lee, H. Yan, L. E. Brus, T. F. Heinz, J. Hone and S. R. Yu, *ACS Nano*, **2010**, *4*, 2695-2700.

1.6.3 Deterministic transfer

Once we have found the flake that gathers the characteristics that we are looking for (thickness and area), we place one of the edges of the PDMS stamp on the edge of a glass slide. The glass slide is then placed in the stamping setup shown in Figure 3.15, which presents the following elements: a XYZ micromanipulator that holds the glass slide containing the stamp, a rotational XY stage which is used to place the substrate, and a zoom lens with a camera attached to it and connected to a LED screen. All of these components are placed on an optical breadboard, simplifying the alignment of the different elements. The step-by-step procedure goes as follows:

1. The glass slide with the PDMS stamp stuck to it is placed in the XYZ micromanipulator upside down in such a way that the flakes on the stamp surface face the substrate

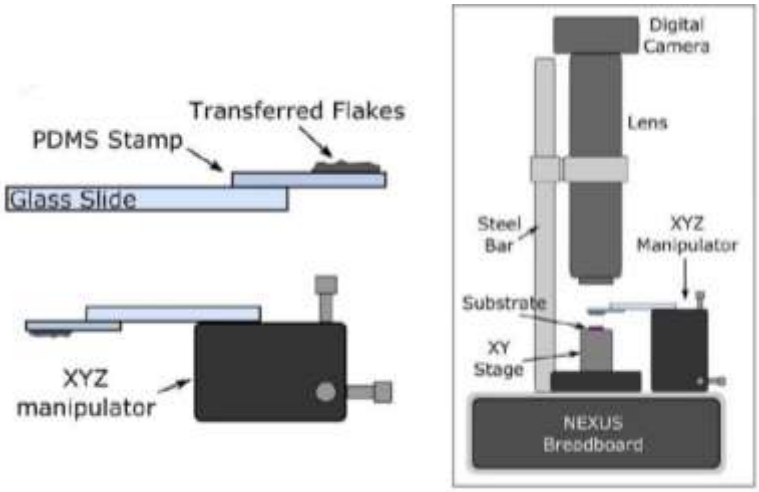

Figure 3.15. Scheme of the glass slide placed in the XYZ micromanipulator and drawing of the setup used to perform the deterministic transfer of the exfoliated flakes.

2. Through the transparent PDMS stamp, we can see and focus on the back side of the flakes with the zoom lens. Now we can look around in the PDMS to find the flake previously selected in the optical microscope.

3. Once we localize the desired flake in the PDMS stamp, we start to slowly approach the stamp to the substrate using the XYZ micromanipulator. If the substrate presents some pre-patterned structure, moving the rotational XY stage that holds the substrate we can align the flake and the substrate during the approach. During the approach, one might need to alternatively focus, on the substrate and on the PDMS stamp, to accurately align the pattern and the flake.

4. We keep approaching until the stamp gets in contact with the substrate. We will know that both of them are in contact because of a change in the color. This fact can be seen by comparing the central panel with the right panel in Figure 3.16.

5. The PDMS stamp is separated slowly by moving up the XYZ micromanipulator transferring the desired flake onto the substrate. This part of the process must be done really slowly in order to take advantage of the viscoelastic nature of PDMS that allows the stamp to behave as an elastic solid at short time scales, [56] so that it detaches from the flake that adheres to the substrate. In Figure 3.16 there is a sequence of pictures that shows this part of the process.

6. Finally, the desired flake is transferred and the PDMS stamp completely separate from the substrate.

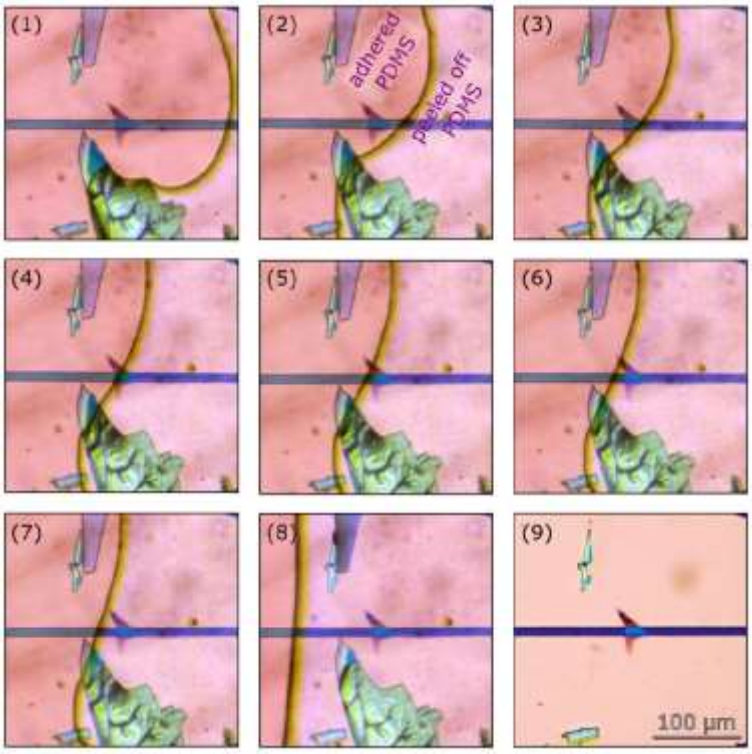

Figure 3.16. From **(1)** to **(9)** Sequence of optical microscopy images of the part of the process while the PMDS stamp is slowly peeled off to transfer the flake. The color difference allows differences the part of the PDMS which is already peeled off from the one that is still in contact with the substrate. The line that moves from one picture to the next one is the meniscus that separates both parts. Once the meniscus has passed the flake, we can completely remove the stamp.

This method can be applied to transfer any kind of exfoliate material with a yield of ~ 100%, as well as being especially useful when the substrate presents pre-patterned structures, like evaporated metallic electrodes, in order to fabricate electronic devices by van der Waals heterostructures or simply to transfer any layered material that requires careful transfer as large-scale two-dimensional materials.

[56] M. A. Meitl, Z. T. Zhu, V. Kumar, K. J. Lee, X. Feng, Y. Y. Huang, I. Adesida, R. G. Nuzzo and J. A. Rogers, *Nature Materials*, **2006**, *5*, 33-38.

1.7 Electronic transport in Field effect transistors

TMDCs are being studied as promising materials for their use as semiconductors in FETs. One of the most important type of FETs is the metal-oxide-semiconductor FET (MOSFET) discovered by Ligenza and Spitzer,[57] in a silicon MOSFET, the gate contact is separated from the channel by an insulating silicon dioxide (SiO_2). The charge carriers of the conducting channel constitute an inversion charge, that is, electrons in the case of a p-type substrate (n-channel device) or holes in the case of an n-type substrate (p-channel device), induced in the semiconductor at the silicon-insulator interface by the voltage applied to the gate electrode.

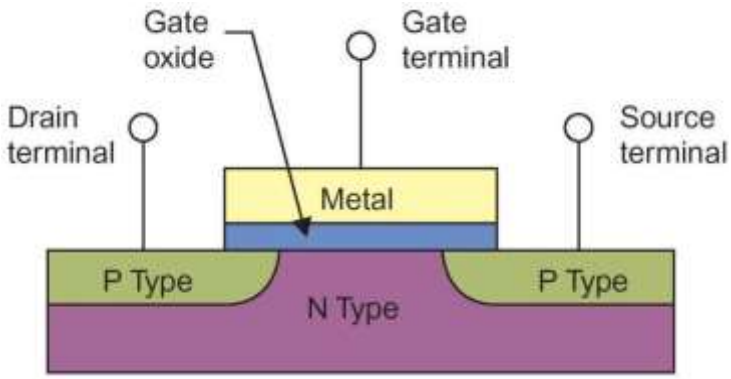

Figure 3.17. Drawing of a typical MOSFET structure.

In the common MOSFETs, the semiconducting channel is p-Si into which two n+-regions are formed (source and drain electrodes). The insulating layer is SiO_2 thermally grown for a high quality SiO_2-Si interface. The semiconductor surface can be inverted from p-type to n-type by applying positive or negative gate voltages, respectively. When we apply positive gate voltages the holes present beneath the oxide layer experience repulsive force and the holes are pushed downward with the substrate. Therefore, the gate voltage can be used to switch the device on/off. The gate voltage value for which the device switches from the on state to the off state is called *threshold voltage* and it depends on the work function of the channel material. There are two main ways to characterize a MOSFETs: the current-voltage characteristics (drain-source current as a function of drain-source voltage) and the transfer curve (drain-source current as a function of the gate voltage).

In general, the MOSFETs exhibit a current-voltage characteristics with three operating regions for a certain gate voltage (see Figure 3.18):

1. **Channel off**: In this zone the current $I_D = 0$ regardless of the V_{DS} value. This is given for values of $V_{GS} \leq V_T$, where threshold voltage (V_T) is defined as the minimum voltage that required to make the transistor ON.

2. **Linear Region**: it is given for V_{DS} value lower than saturation when $V_{DS} \leq V_{GS}-V_T$. In this zone the transistor behaves roughly as a resistor controlled by the gate voltage,

[57] J. Ligenza and W. Spitzer, *Journal of Physics and Chemistry of Solids*, **1960**, *14*, 131-136.

especially for small V_{DS}. When MOSFETs are made to operate in this region, they can be used as amplifiers.

3. **Saturation regions**: In saturation region, the I_{DS} constant inspite of an increase in $V_{DS.}$ Under this condition, the device will act like a closed switch through which a saturated value of I_{DS} flows.

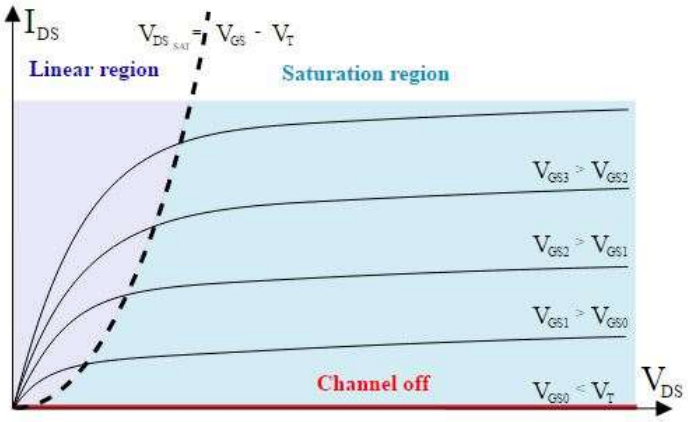

Figure 3.18. Current-voltage curved characteristics of a MOSFET for increasing gate voltage.

1.7.1 Carrier Mobility

Mobility describes the relation between drift velocity of electrons or holes and an applied electric field in a solid. In a semiconductor the mobility of electrons is different from that of holes. The reason is the band structure of the semiconductor and the different scattering mechanisms of these two carrier types. When one charge carrier is dominant, the conductivity of a semiconductor is directly proportional to the mobility of the dominant carrier. The mobility μ is usually deduced from the first-order one-dimensional model in the linear mode. At low drain voltages (V_{DS} = 10 − 50mV, where V_{DS} << V_{GS} − V_T), the effective mobility is related to the drain conductance where d*I*/dV_g is the slope of the transfer curve in the linear regime, *L* and *W* are the length and the width of the semiconducting channel, respectively, and C_{ox} is the insulator capacitance.

$$\mu = \frac{dI}{dV_g}\frac{L}{W}\frac{1}{V_{ds}\,C_{ox}}$$

1.8 FET characterization

The electrical characterization of the devices has been carried out with air-pressure homemade probe (see Figure 3.19). This probe station takes advantage of the reproducible geometry the devices fabricated on pre-patterned electrodes to make electrical contact by two fixed probes made of copper (or platinum) wires. A PCB board, consisting in three electrodes, two of approximately 7 mm x 5 mm and another one of approximately 15 mm x 10 mm, is used to make electrical contact between the probes and the electronics and between the substrate (used as gate) and the electronic equipment. The sample is placed in the biggest electrode (electrical contact with the substrate is done with silver conductive paint) while the two probes lie on the sample pads. The electronics consist of two source-meter source-measure units with voltage range from 20 mV to 200 V and current range from 10 nA (resolution of 500 fA) to 1 A (resolution of 50 µA).

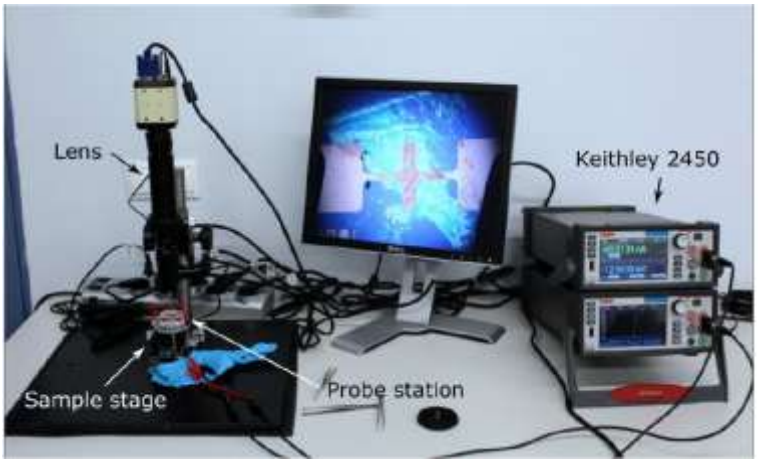

Figure 3.19. Picture of the whole setup for air-pressure device characterization.

1.8.1 Photoresponse in optoelectronic devices

Optoelectronics devices are electronic devices which can interact with light by either absorbing or emitting radiation from the ultraviolet (UV) to the near-infrared (NIR) region of the electromagnetic spectrum. Optoelectronics brings together optics and electronics within a single device, which allows for the manipulation of light, the manipulation of electrical current, and their interaction. In this way, devices can be designed to allow for the transformation of light into current and vice versa. Semiconductors are characterized by two types of mobile carriers, electrons in the conduction band and holes in the valence band. The concentration (n) of electrons in the conduction bands and the concentration (p) of holes in the valence band control the electrical conductivity ρ of semiconductors. The electron-hole separation mechanisms cover photoconduction and photovoltaic effect. In this chapter we are going to focus our attention about the physical effect (photoconduction and photovoltaic) that produce the photoresponse in optoelectronic devices.

1.8.2 Photoconductive effect

In this process when the energy of an incident photon, is greater than the energy gap E_g, free electron-hole pairs are produced in the crystal. These electrons and holes serves as the carriers of electrical current (see Figure 3.20). In semiconductor materials the electrons in the valence band are promoted to the conduction band by absorbtion of the incident photons. The electron-hole pairs generated by the incident light, in addition to those created thermally, increase the conductivity.

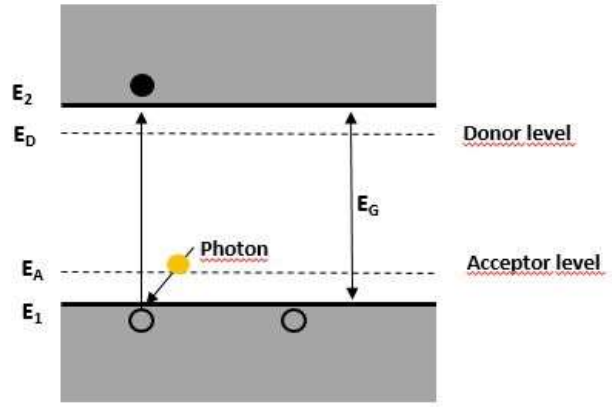

Figure 3.20. Schematic band structure of a photoconductive effect.

Photoconductive detectors are based on semiconducting materials that alter their characteristics when light energy impinges on them. In dark conditions a small current can flow through the semiconductor (dark current, I_{dark}) due to the thermal effect. When the photodetector is upon illumination with a light wavelength smaller than the cut off wavelength, the light absorption generates electron-hole pairs which are separated by a drain-source voltage. Thanks to the applied drain-source voltage, the electrons drift in one direction and the holes in the opposite one, resulting in a net current (I_{light}) that increases the material conductance. Photodetectors are characterized by certain key parameters as:

Responsivity (*R*): This is defined as the ratio between the photocurrent generated by light absorption and the power of incident light, giving an estimation of the sensitivity of the photodetector.

$$R = \frac{I_{ph}}{P_{eff}} = \frac{I_{ph}}{P_d\, A_{device}}$$

Where P_{eff} is defined as the power density of the incident light multiplied by the device area ($P_{eff} = P_d \cdot A_{device}$).This responsivity may be affected by photogating which is a particular case of the photoconductive effect. When there are charge traps in localized states of the band structure of the material, they can act as local gate modulating the conductance. These

localized trap states reside for long times and are usually located at defects or at the surface of the material.[58] This effect becomes particularly important at the nanoscale.

External quantum efficiency: The external quantum efficiency (*EQE*) is the ratio between the number of charge carriers responsible for the photocurrent (n_e) and the total number of incident photons. It can be related to the responsivity:

$$EQE = \frac{n_e}{n_{photon}^{total}} = R\frac{hc}{e\lambda}$$

Time response: is defined as the time needed for a photodetector to switch on (changing from dark current to illumination current) and off (changing from illumination current to dark current) when the incident light is switched on and off. From an experimental point of view, it is the time required for the photodetector to increase from 10% to 90% of the final output level. A good photodetector should have a small time response.

1.8.3 Photovoltaic effect

The photovoltaic effect was discovered in 1839 by Becquerel,[59] however, it was not until 1883 that Charles Fritts developed the first solar cell, based on selenium.[60] In 1954 Chaplin et al. from Bell Laboratories found that silicon doped with certain impurities was very sensitive to light.[61] The photovoltaic effect describes the generation of voltage when a device is exposed to light by the separation of photogenerated electron-hole pairs due to an internal electric field. The collection of light-generated carriers by the *p*-*n* junction diode or Schottky barriers causes a movement of electrons to the *n*-type side and holes to the *p*-type side of the junction.

Experimentally, the power generated by a device is calculated from its current versus voltage (I-V) curve, an example of which is shown in figure 3.21. The power generated is:

$$P_{out} = I_m V_m$$

Where P_{out} is the maximum power point and is given by the product of I_m and V_m (see Figure 3.21), alternatively, P_{out} can be expressed as:

$$P_{out} = V_{oc} I_{sc} FF$$

where I_{sc} is short circuit current and is defined as the current produced with zero bias voltage. V_{oc} is the open circuit voltage and is defined as the applied bias at which no current flows since

[58] M. Buscema, J. O. Island, D. J. Groenendijk, S. I. Blanter, G. A. Steele, H. S. van der Zant and A. Castellanos-Gomez, *Chemical Society Reviews*, **2015**, *44*, 3691-3718.
[59] A. E. Becquerel, Memoire sur les effects d'electriques produits sous l'influence des rayons solaires. Comptes Rendus de L'Academie des Sciences, **1839**, *9*, 561.
[60] C. E. Fritts, *Am. J. Sci.*, **1883**, *26*, 465-472.
[61] D. M. Chapin, S. C. Fuller and G. L. Pearson, *Journal of Applied Physics*, **1954**, *25*, 676-677.

the photogenerated current is equal to the dark current. Finally the fill factor (FF) describes how well the maximum power rectangle fills the area of the I-V curve.

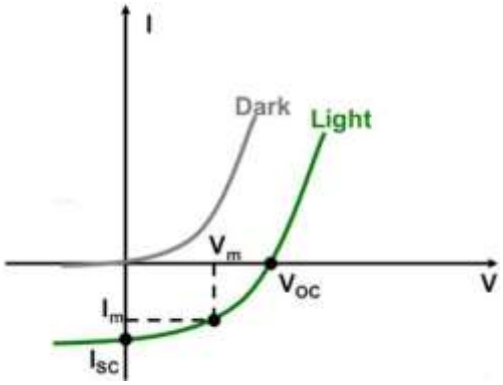

Figure 3.21. Current-voltage characteristic of the photovoltaic effect in a p-n junction. The internal electric field causes a zero voltage current (I_{sc}) and voltage at zero current (V_{oc}). I_m and V_m are current and voltage values for which the device reaches the maximum output power.

1.9 Optoelectronics characterization

The photoresponse of a device is characterized by the photogenerated current upon illumination, which can be evaluated by measuring current-voltage characteristics of the device in dark conditions and upon illumination. This characterization is performed in a similar way as for the field-effect devices using an air-pressure homemade probe station with commercial electronics. In addition to the probe station setup, optical fiber-coupled LED (or laser) beams are incorporated in the system to illuminate the devices with specific wavelength light in order to measure the photoresponse at different regions of the electromagnetic spectrum (see figure 3.22). The light source is provided by light emitting diodes with 8 different wavelengths (375 nm, 405 nm, 455 nm, 505 nm, 617 nm, 660 nm, 850 nm and 1050 nm). The light is coupled into a multimode optical fiber directly at the output of the LED source and directed into the probe station zoom lens. The beam spot size on the sample depends of the diameter of the fiber core used to guide the beam and ranges from 400 µm to 25 µm. The device is set at a gate voltage while it is illuminated with a light spot and the current-voltage characteristics are measured.

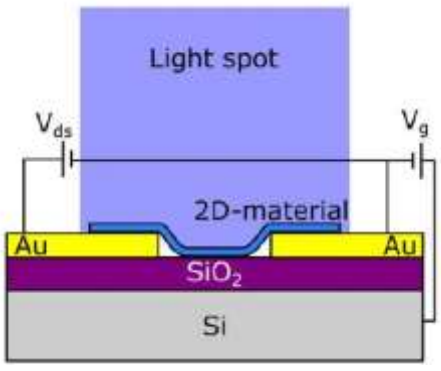

Figure 3.22. Schematic drawing of the photoresponse measurement

2. Objectives

The present chapter addresses one main objective: the modulation of the optoelectronic properties of TMDC-based through easy and reversible noncovalent functionalization. As part of the study of the properties of these new 2D material we will investigate:

i) FET characterization of the device in air and in dark condition before and after functionalization
ii) Optoelectronics measuresment to study the photoresponse and responsivity before and after functionalization.
iii) Reproducibility and reversibility of the functionalization/cleaning process with both molecules.

3. Engineering the optoelectronic properties of MoS_2photodetectors through reversible noncovalent functionalization.

3.1 Introduction

Among the novel two-dimensional (2D) materials,[62,63,64,65,66,67,68,69] transition metal dichalcogenides (TMDCs)[70,71,72] show particularly promising electronic and optoelectronic properties.[73] In particular, their intrinsic bandgap within the visible part of the spectrum, makes them highly interesting materials for optoelectronic applications.[74] In fact, the presence of a bandgap has allowed for the construction of a wealth of prototype electronic devices based on TMDCs.[75,76,77,78,79,80] In the last years, there has been a significant effort to modulate the optical properties of TMDCs in order to optimize the performance of the corresponding devices. Most of the strategies investigated so far rely on physical methods, such as strain-engineering,[81,82] field-effect doping,[83,84] or artificial stacking of different 2D materials.[85,86] In comparison, the chemical modification of TMDCs is still rather underexplored, despite the appealing combination of low-cost and high degree of control offered by synthetic chemistry.

---

[62] A. K. Geim and K. S. Novoselov, *Nat. Mater.,* **2007**, *6*, 183-191.
[63] P. Miro, M. Audiffred and T. Heine, *Chem. Soc. Rev.,* **2014**, *43*, 6537-6554.
[64] M. Xu, T. Liang, M. Shi and H. Chen, *Chem. Rev.,* **2013**, *113*, 3766-3798.
[65] Q. Tang and Z. Zhou, *Prog. Mater. Sci.,* **2013**, *58*, 1244-1315.
[66] R. Mas-Balleste, C. Gomez-Navarro, J. Gomez-Herrero and F. Zamora, *Nanoscale*, **2011**, *3*, 20-30.
[67] C. N. R. Rao, H. S. S. Ramakrishna Matte and U. Maitra, *Angew. Chem., Int. Ed*., **2013**, *52*, 13162-13185.
[68] G. Le Lay, E. Salomon, P. De Padova, J. M. Layet and T. Angot, *Aust. J. Chem*., **2014**, *67*, 1370-1372.
[69] S. Z. Butler, S. M. Hollen, L. Cao, Y. Cui, J. A. Gupta, H. R. Gutiérrez, F. Heinz, S. S. Hong, J. Huang, A. F. Ismach, E. Johnston-Halperin, M. Kuno, V. V. Plashnitsa, R. D. Robinson, R. S. Ruoff, S. Salahuddin, J. Shan, L. Shi, M. G. Spencer, M. Terrones, W. Windl and J. E. Goldberger, *ACS Nano*, **2013**, *7*, 2898-2926.
[70] R. Lv, H. Terrones, A. L. Elías, N. Perea-López, H. R. Gutiérrez, E. Cruz-Silva, L. P. Rajukumar, M. S. Dresselhaus and M. Terrones, *Nano Today*, **2015**, *10*, 559-592.
[71] M. Chhowalla, Z. Liu and H. Zhang, *Chem. Soc. Rev*., **2015**, *44*, 2584-2586.
[72] R. Lv, J. A. Robinson, R. E. Schaak, D. Sun, Y. Sun, T. E. Mallouk and M. Terrones, *Acc. Chem. Res*., **2015**, *48*, 56-64.
[73] F. H. L. Koppens, T. Mueller, P. Avouris, A. C. Ferrari, M. S. Vitiello and M. Polini, *Nat. Nanotechnol*., **2014**, *9*, 780-793.
[74] H. Zeng and X. Cui, *Chem. Soc. Rev*., **2015**, *44*, 2629-2642.
[75] D. Jariwala, V. K. Sangwan, L. J. Lauhon, T. J. Marks and M. C. Hersam, *ACS Nano*, **2014**, *8*, 1102-1120.
[76] K. Kang, S. Xie, L. Huang, Y. Han, P. Y. Huang, K. F. Mak, C.-J. Kim, D. Muller and J. Park, *Nature*, **2015**, *520*, 656-660.
[77] M. Chen, H. Nam, H. Rokni, S. Wi, J. S. Yoon, P. Chen, K. Kurabayashi, W. Lu and X. Liang, *ACS Nano*, 2015, *9*, 8773-8785.
[78] Y. Cui, R. Xin, Z. Yu, Y. Pan, Z. Y. Ong, X. Wei, J. Wang, H. Nan, Z. Ni, Y. Wu, T. Chen, Y. Shi, B. Wang, G. Zhang, Y. W. Zhang and X. Wang, *Adv. Mater*., **2015**, *27*, 5230-5234.
[79] Y. Ma, B. Liu, A. Zhang, L. Chen, M. Fathi, C. Shen, A. N. Abbas, M. Ge, M. Mecklenburg and C. Zhou, *ACS Nano*, **2015**, *9*, 7383–7391.
[80] C. C. Mayorga-Martinez, A. Ambrosi, A. Y. S. Eng, Z. Sofer and M. Pumera*, Adv. Funct. Mater*., **2015**, *25*, 5611-5616.
[81] H. J. Conley, B. Wang, J. I. Ziegler, R. F. Haglund, S. T. Pantelides and K. I. Bolotin, *Nano Lett*., **2013**, *13*, 3626-3630.
[82] A. Castellanos-Gomez, R. Roldán, E. Cappelluti, M. Buscema, F. Guinea, H. S. J. van der Zant and G. A. Steele, *Nano Lett*., **2013**,*13*, 5361-5366.
[83] Q. H. Wang, K. Kalantar-Zadeh, A. Kis, J. N. Coleman and M. S. Strano, *Nat. Nanotechnol.*, **2012**, *7*, 699–712.
[84] M. Buscema, D. J. Groenendijk, S. I. Blanter, G. A. Steele, H. S. J.van der Zant and A. Castellanos-Gomez, *Nano Lett*., **2014**, *14*, 3347-3352.
[85] C.-H. Lee, G.-H. Lee, A. M. van der Zande, W. Chen, Y. Li, M. Han,X. Cui, G. Arefe, C. Nuckolls, T. F. Heinz, J. Guo, J. Hone and P. Kim, Nat. Nanotechnol., **2014**, 9, 676-681.
[86] M. M. Furchi, A. Pospischil, F. Libisch, J. Burgdörfer and T. Mueller*, Nano Lett*., **2014**, *14*, 4785-4791.

Examples of doping of TMDCs through surface charge-transfer using metal atoms,[87] gases,[88] and a few organic molecules has already been demonstrated.[89,90] Responsivities of just a few $A \cdot W^{-1}$ have been reported for MoS_2 photodetectors functionalized with a rhodamine dye,[91] a rather modest value for MoS_2-based photodetectors. Among the readily available organic dyes, perylenediimides (PDIs) and porphyrins show remarkable optical properties, including large molar absorptivity —ca. 10^5 M^{-1} cm^{-1} for PDIs and 10^6 M^{-1} cm^{-1} for porphyrins—, and outstanding photostability under ambient conditions.

These intrinsic properties have made them two of the most popular families of organic dyes, particularly in the frame of photovoltaics.[92,93,94,95,96,97,98,99,100] However, their use for the modulation of the optoelectronic properties of TMDC-based devices has not been yet described. Considering this, we decided to investigate the effects of the noncovalent functionalization of MoS_2 photodetectors with the soluble PDI and tetraphenyl porphyrin (TPP) depicted in Chart 3.1.

3.2 Results and discussion

Here, we describe that the supramolecular functionalization of mechanically exfoliated MoS_2-based photodetectors with PDI and TPP leads to an enhancement of photocurrent generation of over four orders of magnitude, making our functionalized devices highly sensitive (responsivities up to 100 $A \cdot W^{-1}$). The process is technologically trivial, air-stable, reproducible and fully reversible. MoS_2 phototransistors are fabricated by deterministic transfer of mechanically exfoliated flakes onto pre-patterned drain and source electrodes fabricated by shadow mask evaporation of Ti/Au (5 nm / 50 nm) onto a SiO_2 (285 nm in thickness) substrate, thermally grown on a highly p-doped silicon chip.[101]

[87] H. Fang, M. Tosun, G. Seol, T. C. Chang, K. Takei, J. Guo and A. Javey, *Nano Lett*., **2013**, *13*, 1991-1995.
[88] H. Fang, S. Chuang, T. C. Chang, K. Takei, T. Takahashi and A. Javey, *Nano Lett*., **2012**, *12*, 3788-3792.
[89] D. Kiriya, M. Tosun, P. Zhao, J. S. Kang and A. Javey, *J. Am. Chem. Soc*., **2014**, *136*, 7853-7856.
[90] D. M. Sim, M. Kim, S. Yim, M. J. Choi, J. Choi, S. Yoo and Y. S. Jung, *ACS Nano*, **2015**, *9*, 12115-12123.
[91] S. H. Yu, Y. Lee, S. K. Jang, J. Kang, J. Jeon, C. Lee, J. Y. Lee, H. Kim, E. Hwang, S. Lee and J. H. Cho, *ACS Nano*, **2014**, *8*, 8285-8291.
[92] C. Huang, S. Barlow and S. R. Marder, *J. Org. Chem*., **2011**, *76*, 2386-2407.
[93] X. Zhan, A. Facchetti, S. Barlow, T. J. Marks, M. A. Ratner,M. R. Wasielewski and S. R. Marder, *Adv. Mater*., **2011**, *23*, 268-284.
[94] M. Urbani, M. Gratzel, M. K. Nazeeruddin and T. Torres, *Chem. Rev*., **2014**, *114*, 12330-12396.
[95] M. V. Martinez-Diaz, G. de la Torre and T. Torres, *Chem. Commun*.,**2010**, *46*, 7090-7108.
[96] T. Higashino and H. Imahori, *Dalton Trans*., **2015**, *44*, 448-463.
[97] L. L. Li and E. W. G. Diau, *Chem. Soc. Rev*., **2013**, *42*, 291-304.
[98] C. B. Nielsen, S. Holliday, H. Y. Chen, S. J. Cryer and I. McCulloch, *Acc. Chem. Res*., **2015**, *48*, 2803-2812.
[99] E. Kozma and M. Catellani, *Dyes Pigm*., **2013**, *98*, 160-179.
[100] C. Li and H. Wonneberger, *Adv. Mater*., **2012**, *24*, 613-636.
[101] A. Castellanos-Gomez, M. Buscema, R. Molenaar, V. Singh, L. Janssen, H. S. J. van der Zant and G. A. Steele, *2D Mater*., **2014**, *1*, 011002.

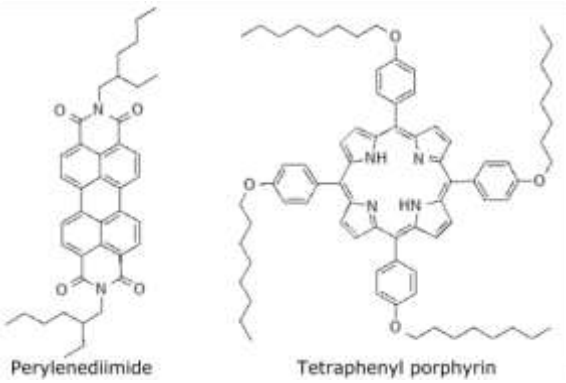

Chart 3.1. Chemical structure of the perylenediimide and tetraphenyl porphyrin investigated.

The heavily doped silicon is employed as a back gate electrode to tune the density of charge carriers by electric field- effect. Figure 3.23a-1 shows an artistic representation of a MoS_2-based field-effect transistor (FET) fabricated by transferring a MoS_2 flake bridging the drain and source electrodes. Figure 3.23b-1 shows an actual optical microscopy image of a fabricated device composed of a multilayer (~10 layers) MoS_2 flake. Right after the fabrication, we perform the FET characterization of the device in air and in dark conditions by sweeping the drain-source voltage and measuring the current passing through the MoS_2 flake. Figure 3.23c-1 shows a set of current vs. drain-source voltage curves (*IV*s hereafter) acquired at different applied gate voltages. The *IV*s show a typical n-type FET behaviour, i.e. the current increases with increasing back-gate voltage. The threshold voltage is ~ 0 V and the mobility ~ 2×10^{-3} $cm^2 \cdot V^{-1} \cdot s^{-1}$, although this value is lower bound since we are measuring with two terminals and a correction, which usually yields higher mobility values,[102,103,104,105,106] should be taken into account. Once the pristine device is electronically characterized, we functionalize the surface of the MoS_2 device by drop-casting a CH_2Cl_2 solution containing either PDI or TPP (see Figure 3.23a-2). The drop is placed on the device, covering both the MoS_2 flake and the electrodes, and it is kept in air until the solvent evaporates, resulting in a uniform coverage of the device with crystallites (see Figure 3.23b-2).

[102] N. R. Pradhan, D. Rhodes, Q. Zhang, S. Talapatra, M. Terrones, P. M. Ajayan and L. Balicas, *Appl. Phys. Lett.*, **2013**, *102*, 123105.
[103] A. Castellanos-Gomez, M. Barkelid, A. M. Goossens, V. E. Calado, H. S. J. van der Zant and G. A. Steele, *Nano Lett.*, **2012**, *12*, 3187–3192.
[104] H. Li, Z. Yin, Q. He, H. Li, X. Huang, G. Lu, D. W. H. Fam,A. I. Y. Tok, Q. Zhang and H. Zhang, *Small*, **2012**, *8*, 63–67.
[105] M. S. Fuhrer and J. Hone, *Nat. Nanotechnol.*, **2013**, *8*, 146–147.
[106] S. Ghatak, A. N. Pal and A. Ghosh, *ACS Nano*, **2011**, *5*, 7707–7712.

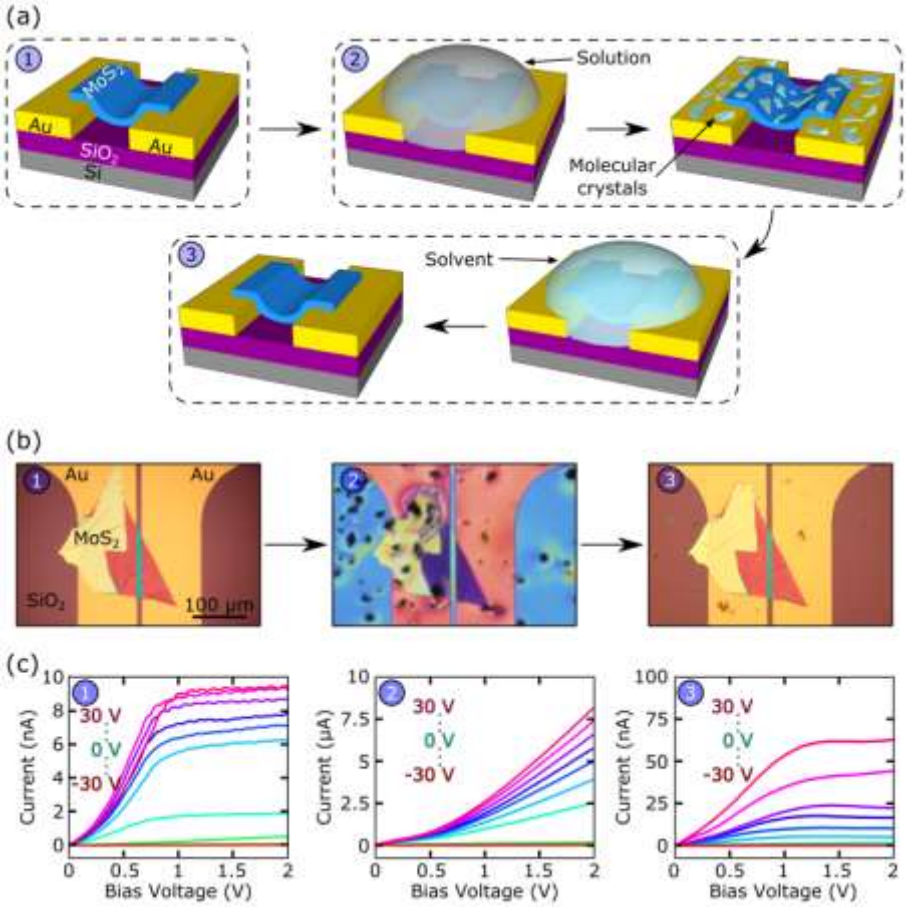

Figure 3.23. a) Artistic representation of the fabrication of a MoS_2 phototransistor device subjected to one functionalization-cleaning cycle. (1) The pristine device is fabricated: a few-layer MoS_2 flake is placed bridging two Au electrodes by deterministic transfer. (2) Molecular crystals are deposited on the device by drop-casting. (3) The device is washed with solvent to remove the deposited molecules, resulting in a clean device with similar performance as the pristine one. **b)** Optical microscopy images of the process described in (a): (1) Pristine device. (2) The same device covered with a layer of molecules (TPP in this case). (3) The same device after removing the molecules. **c)** *IV*s of the device shown in (b) for different back-gate voltages (from -30 V to 30 V) at the different steps of the process. Remarkably, after molecules deposition the current flowing through the device increases by three orders of magnitude.

After deposition of the dyes, the electronic characterization of the device is performed again in air and dark conditions. Figure 3.23c-2 shows the IVs acquired for different back-gate voltages with the molecule-coated device. As shown, the current is increased with respect to the pristine device by almost three orders of magnitude due to the doping created by the molecules that donate electrons to the MoS_2 flake. Despite the typically electron-acceptor character of PDI, both molecules behave as electron donors when faced with MoS_2. Similar behaviour has been observed even with positively charged (i.e. very strongly electron-accepting) organic molecules.[89] The result of this electron transfer process is an increase in the n-doping of the material, as can be depicted from the shift in the threshold voltage in the current-gate voltage traces (see Figure 3.24). We find that the mobility of the device is also increased from 3×10^{-3} $cm^2 \cdot V^{-1} \cdot s^{-1}$ in the pristine device up to ~ 1 $cm^2 \cdot V^{-1} \cdot s^{-1}$ both in the TPP and PDI functionalized devices. The current and mobility enhancement can be also due to the reduction of the Schottky barrier assisted by the molecular doping, as previously reported for MoS_2 FETs doped with Cl, an electron donor, particularly taking into account that we use a

chlorinated solvent.[107] However, the difference in results obtained with each molecule, and most convincingly, the fact that we can return to the initial state by washing with CH_2Cl_2 (vide infra) unambiguously support a molecule-specific doping mechanism. It is important to note that in the coated devices the molecules do not contribute significantly to the total current passing through the device.

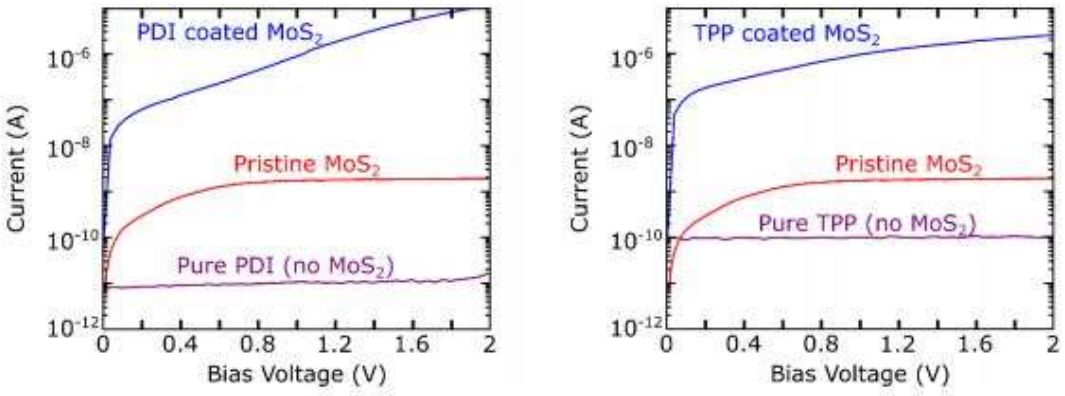

Figure 3.24. Comparison of the current-voltage curves measured in the pristine device, the coated device and the molecules without MoS_2 bridging the electrodes. It can be seen that the molecules are highly resistive when compared to the coated device.

Finally, the device is washed with CH_2Cl_2 in order to remove the molecules, as illustrated in Figure 3.23a-3. The device almost recovers the initial characteristics (see Figure 3.23b-3), although the current is still slightly enhanced (see Figure 3.23c-3), probably due to the presence of traces of molecules still adsorbed on the MoS_2 surface, or due to the solvent effect mentioned earlier.

We not only characterize the device in dark conditions, but also upon illumination. In Figure 3.25a we show a sketch of the optoelectronic measurement: the device is illuminated with a light beam guided through an optical fiber (the spot on the device has 200 μm in diameter, illuminating the whole device). The light is switched on and off while measuring the current. In Figure 3.25b and 3.25c we show the photocurrent (I_{ph}, the difference between the current upon illumination and in dark) as a function of time when the device is coated with PDI (Figure 3.25b, left) and with TPP (Figure 3.25c, left). The photocurrent is larger for the PDI coating than for the TPP coating due to the higher doping of the device by PDI and a better match of its absorption with the light source. In Figure 3.25b and 3.25c, right, we show the same measurements after cleaning the device with CH_2Cl_2 in order to remove the molecular coating.

[107] A. Castellanos-Gomez, M. Buscema, R. Molenaar, V. Singh, L. Janssen, H. S. J. van der Zant and G. A. Steele, *2D Mater.*, **2014**, *1*, 011002.

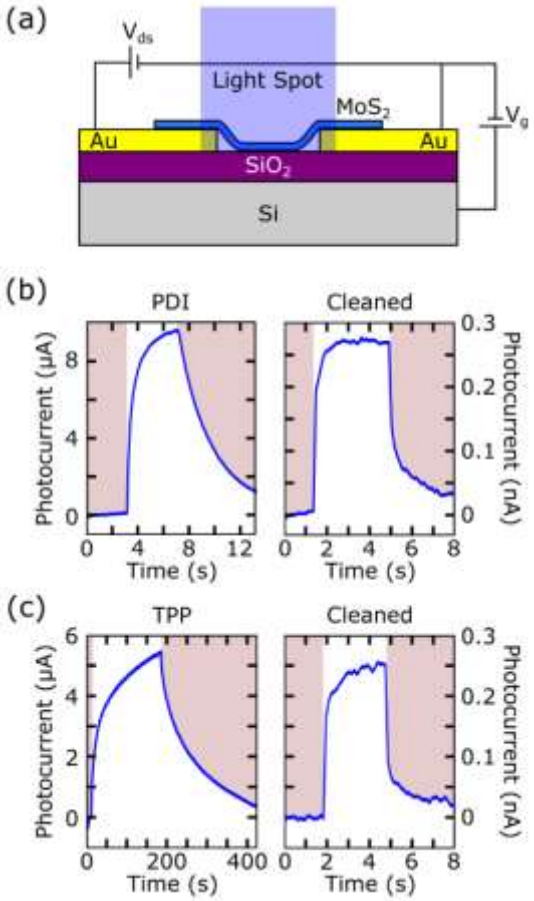

Figure 3.25 a) Schematic drawing of the measurement method: a light spot (typically a LED beam guided by an optical fiber) illuminates the whole flake while the current passing through the MoS_2 flake is measured. The light is switched on and off to measure the photocurrent. **b)** Photocurrent measured for the device shown in Figure 3.23b functionalized with PDI (left) and after cleaning the molecules (right) with light wavelength of 455 nm and power density of 72 mW/cm^2 (V_{ds} = 2 V, V_g = 30 V). The PDI functionalized device photoresponse is 3×10^4 times larger than that of the cleaned device. (c) Photocurrent measured for the device shown in Figure 1b covered by TPP (left) and after removing the molecules (right) with light wavelength of 455 nm and power density of 72 mW/cm^2 (V_{ds} = 2 V, V_g = 30 V). The functionalized device photoresponse is 2×10^4 times larger than after being cleaned.

The functionalized devices show a most remarkable enhancement of the photocurrent of 2×10^4 times for the TPP coating and 3×10^4 times for PDI. The scanning photocurrent (see Figure 3.26).

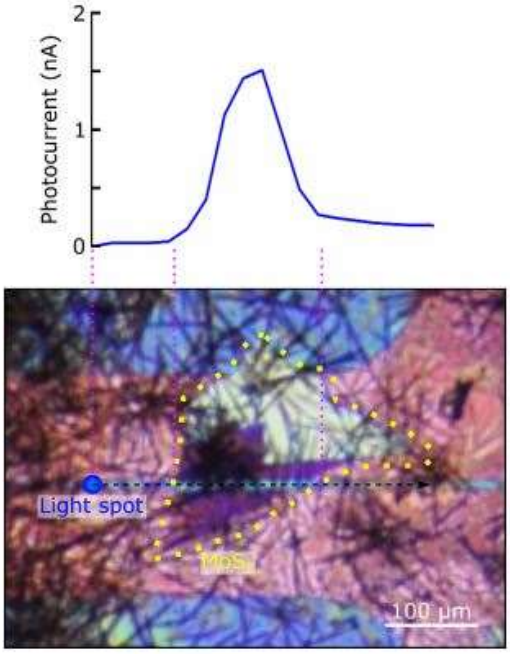

Figure 3.26. Scanning photocurrent of the PDI-coated device with light wavelength of 455 nm. The light spot (diameter of 25 µm) is displaced over the sample while the current between the source and drain electrodes is measured. As it can be seen, when the light spot is outside the MoS_2 flake there is not photocurrent generation.

Also the wavelength dependent photocurrent measurements (see Figure 3.27) show that the photocurrent is only generated when the MoS_2 is illuminated, and the MoS_2 absorption dominates over the molecules absorption. The device is responding to light for wavelengths shorter than 660 nm, where there is a photocurrent peak related to the MoS_2 exciton. The photocurrent is enhanced in the coated device about 3 orders of magnitude with respect to the pristine device, although in the TPP-coated device the spectrum seems to be on top of a background which could be due to a high absorption of the TPP at high energies.

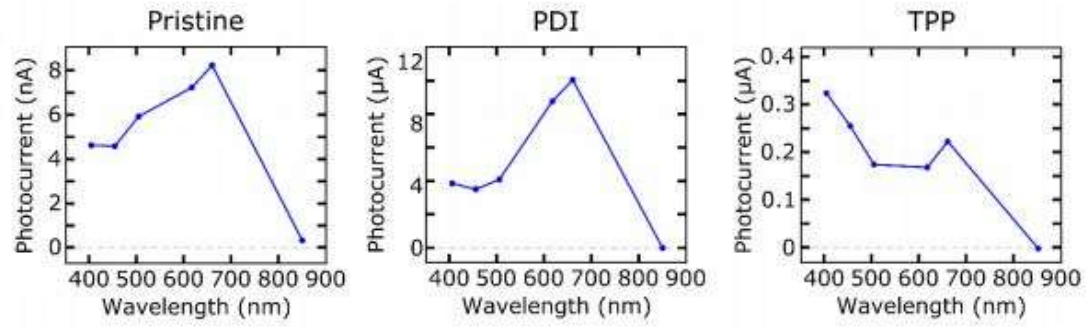

Figure 3.27. Photocurrent measured in the device shown in the main text as a function of the light wavelength for the pristine device, the TPP-coated device and the PDI-coated device. The LED power is 100 nW and the photocurrent is measured with Vds = 2 V and Vg = 30 V.

In order to study the reproducibility and reversibility of the functionalization/cleaning process, we repeat the characterization several times in the same device, not only coating with one molecule, but also changing the molecule. In Figure 3.28a we show a plot of the responsivity (*R*), a figure-of-merit for photodetectors that represents the input-output gain of the device for a given light power. The responsivity is defined as $R = I_{ph} / P_{eff}$, where P_{eff} is the effective light power reaching the device and is calculated as $P_{eff} = P \cdot A_{dev}/A_{spot}$, with *P* the light power reaching the substrate, A_{dev} the area of the flake between the two electrodes and A_{spot} the area of the spot on the device.

As it is shown in Figure 6a, the responsivity of the device is enhanced when it is functionalized with PDI (~ 10^2 $A \cdot W^{-1}$) three orders of magnitude with respect to the pristine device (~ 10^{-1} $A \cdot W^{-1}$). When the device is cleaned, we recover a similar situation as in the pristine device with a responsivity of ~ 10^{-2} $A \cdot W^{-1}$. The process is then repeated twice using the same device, obtaining a similar value for the responsivity with a PDI coating and in the cleaned device.

When the device is functionalized with TPP, the responsivity oscillates between 10^2 $A \cdot W^{-1}$ and 10^1 $A \cdot W^{-1}$, and after cleaning the responsivity drops to ~ 10^{-1} $A \cdot W^{-1}$. The dramatic enhancement of the responsivity originates from the combination of photogating effect and a high photoconductive gain. The photogating is due to the separation of photogenerated electron-hole pairs in the MoS_2 because of the trapping of holes in the molecular layer, thus quenching the recombination and enhancing the conductance of the device by the electric field-doping generated by the trapped charges. Apart from the photogating mechanism, hybrid MoS_2/molecular dye systems are expected to present a high photoconductive gain because of the short carrier transist time ($\tau_{transist}$), due to the high mobility of MoS_2, and the long trapping lifetime in the dye molecule ($\tau_{lifetime}$): the gain is $\tau_{lifetime} / \tau_{transist}$.[108,109]

We also investigate the rise/fall time of the device with and without coating, defined as the time measured between 10% and 90% of the maximum photocurrent in the rising or falling edge. Here we observe that the rise/fall time increases from ~ 1 s for the pristine and cleaned devices to ~ 10 seconds for the PDI-coated device and to ~ 300 seconds for the TPP-coated device (Figure 3.28b). This indicates that the trapping lifetime of the dye molecules is 1-2 orders of magnitude longer than those of intrinsic traps in pristine MoS_2 devices, in good agreement with a much higher photoconductive gain in the functionalized devices.

[108] M. Buscema, J. O. Island, D. J. Groenendijk, S. I. Blanter, G. A. Steele, H. S. van der Zant and A. Castellanos-Gomez, *Chem. Soc. Rev.*, **2015**, *44*, 3691-3718.
[109] D. Kufer, I. Nikitskiy, T. Lasanta, G. Navickaite, F. H. L. Koppens and G. Konstantatos, *Adv. Mater.*, **2015**, *27*, 176-180.

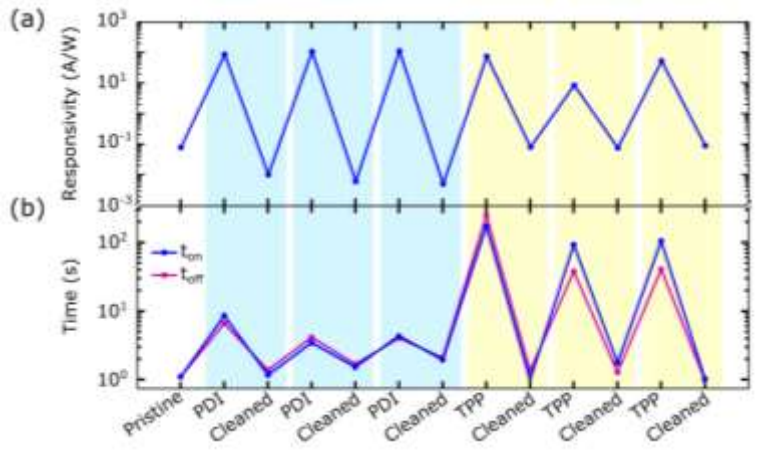

Figure 3.28. a) Responsivity for the different cycles of chromophore functionalization and solvent cleaning. The higher responsivity values are achieved when the device is covered with PDI. The LED wavelength is 455 nm, and the power density is 43 mW/cm^2. b) Time response for the different cycles. The fastest response is achieved with the pristine and cleaned devices, but the time response with PDI is just one order of magnitude larger than the pristine device.

3.3 Conclusions

In summary, we have effectively functionalized MoS_2-based photodetectors with PDIs and TPPs by a simple drop-casting method, resulting in a dramatic enhancement of the photoresponse and responsivity (three orders of magnitude higher) to visible light. The process is fully reversible and reproducible, demonstrating that molecular dyes are an easy and interesting way of improving the performance of photodetectors based on two-dimensional materials.

3.4 Experimental Section

3.4.1 Synthesis and characterization of perylenediimide (PDI) and tetraphenyl porphyrin (TPP)

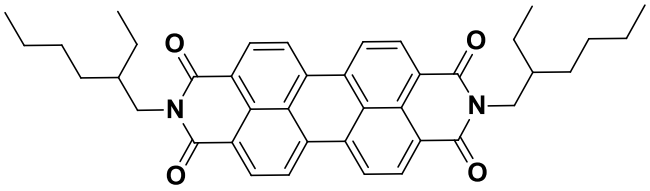

The **N,N′-bis(2-ethylhexan-1-amine)perylene-3,4,9,10-tetracarboxylic dianhydride** was synthesized and characterized as describe in *J. Org. Chem.,* **2015**, *80*, 3036-3049, and showed identical spectroscopic data to those reported therein.

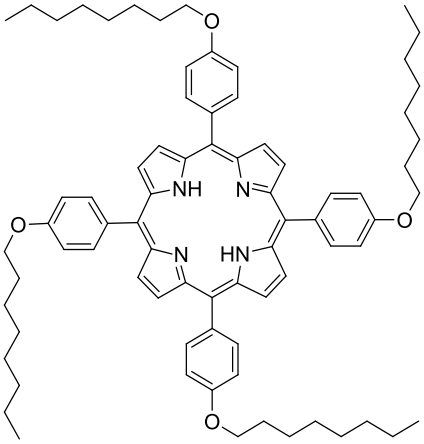

5,10,15,20-tetra-(4-octyloxyphenyl)porphyrin. 5,10,15,20-tetra-(4 hydroxyphenyl)porphyrin (500 mg, 0.74 mmol) was dissolved in dry DMF (100 mL) under argon and K_2CO_3 (2.65 g, 19.16 mmol) was added. 1-bromooctane (1.27 mL, 7.37 mmol) was added dropwise and the resulting mixture was stirred under reflux overnight. The mixture was poured onto cold HCl 1N and the solid was removed by filtration and dissolved in $CHCl_3$, then washed with water. The organic phase was dried over $MgSO_4$ and the solvent was removed under vacuum, obtaining the pure product. This compound (708 mg, 85% yield) was characterized by ^{1}H, ^{13}C-NMR and MALDI-TOF.

^{1}H *NMR* *(400 MHz, $CDCl_3$)* δ-2.68 (s, 2H), 0.97 (t, J = 6.9 Hz, 12H), 1.38 - 1.55 (m, 32H), 1.66 (q, J = 7.6 Hz, 8H), 2.01 (q, J = 6.8 Hz, 8H), 4.28 (t, J = 6.5 Hz, 8H), 7.30 (d, J = 8.8 Hz, 8H), 8.13 (d, J = 8.8 Hz, 8H), 8.89 (s, 8H). **^{13}C NMR** (101 MHz, $CDCl_3$) δ 14.2, 22.8, 26.3, 29.4, 29.5, 31.9, 68.3, 112.7, 119.9, 134.5, 135.6, 158.9. **MS** m/z: calculated for $C_{76}H_{94}N_4O_4$ 1127.6, found MALDI 1127.7.

3.4.2 Field-effect characteristics of the functionalized MoS_2-based devices

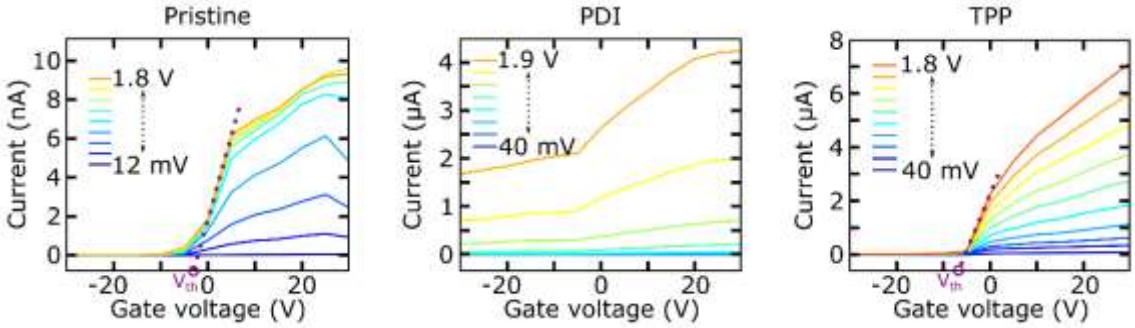

Figure 3.29. Current-gate voltage traces for different drain-source voltages of the device shown in the main text measured in the pristine device, the PDI-coated device and the TPP-coated device.

The current-gate voltage traces are measured in air and in dark conditions. The ON/OFF ratio in the pristine device is 400, with a mobility of 3.4×10^{-3} $cm^2/V \cdot s$ and a threshold voltage of ~ -3 V. When the device is coated with PDI, the ON/OFF ratio decreases approximately a factor of 100, the mobility increases a factor of 1000 and the threshold voltage shifts below -30 V, clearly showing a high n-doping due to the presence of the molecules. When the device is coated with TPP, the ON/OFF ratio remains the same, the mobility increases a factor of 1000 and the threshold voltage shifts to ~ -8 V, indicating a moderate n-type doping. Thus for TPP we attribute the current enhancement to be dominated by a reduction of the Schottky barrier height induced by the molecule/MoS_2 charge transfer rather than the direct n-type doping.

Field-effect characteristics of the MoS_2-based devices			
	Mobility ($cm^2/V \cdot s$)	V_{th} (V)	ON/OFF ratio
Pristine	$3.4 \cdot 10^{-3}$	-3	460
PDI	0.3	< - 30	10
Cleaned	$0.5 \cdot 10^{-3}$	0	30
PDI	1.11	< - 30	10
Cleaned	$0.3 \cdot 10^{-3}$	-2	20
PDI	-	-	-
Cleaned	-	-	-
TPP	-	-	-
Cleaned	$6.6 \cdot 10^{-3}$	0	1200
TPP	1.1	-8	400
Cleaned	-	-	-
TPP	0.6	-10	10
Cleaned	$7.4 \cdot 10^{-3}$	0	2200

Table 3.1. Field effect characteristics of the device shown in the main text at the different cycles of coating-cleaning-functionalization.

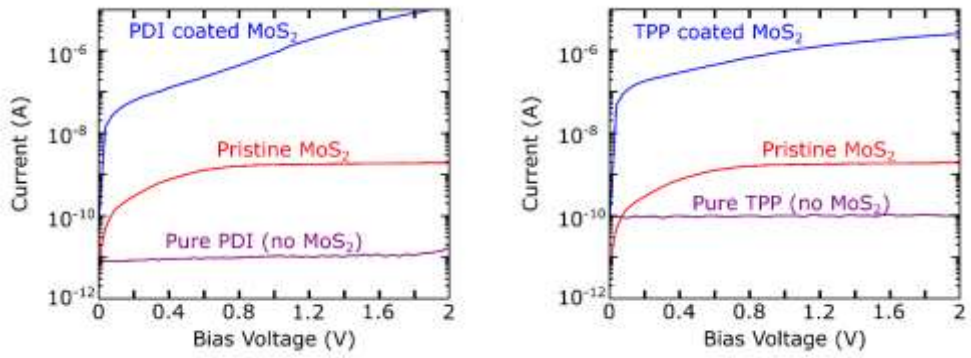

Figure 3.30. Comparison of the current-voltage curves measured in the pristine device, the coated device and the molecules without MoS_2 bridging the electrodes. It can be seen that the molecules are highly resistive when compared to the coated device.

3.4.3 UV-VIS spectra of PDI and TPP

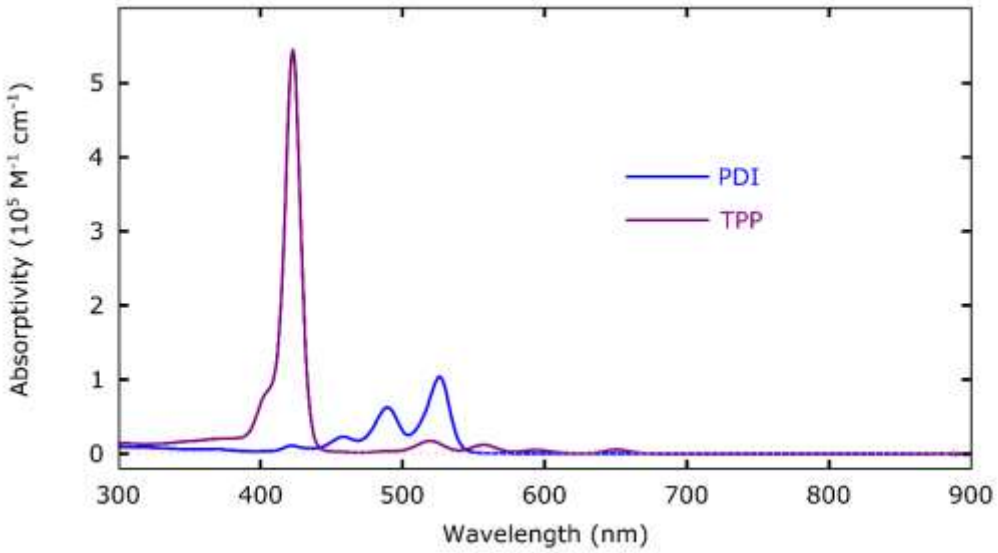

Figure 3.31. UV-VIS absorptivity spectra of PDI and TPP molecules in CH_2Cl_2 solution.

4. References

1. P. R. Wallace, *Phys. Rev*., **1947**, *71*, 622-634.
2. K. S. Novoselov, A. K. Geim, S. V. Morozov, D. Jiang, Y. Zhang, S. V. Dubonos, I. V. Grigorieva and A. A. Firsov, *Science* **2004,** *306*, 666-669.
3. K. F. Mak, C. Lee, J. Hone, J. Shan and T. F. Heinz, *Physical Review Letters*, **2010**, *105*, 136805.
4. B. Radisavljevic, A. Radenovic, J. Brivio, V. Giacometti and A. Kis, *Nat. Nanotechnol*., **2011**, *6*, 147-150
5. A. Splendiani, L. Sun, Y. Zhang, T. Li, J. Kim, C. Y. Chim, G. Galli and F. Wang, *Nano Lett*., **2010**, *10*, 1271-1275.
6. K. F. Mak, K. He, J. Shan and T. F. Heinz, *Nat. Nanotechnol*., **2012**, *7*, 494-498.
7. L. F. Mattheiss, *Physical Review B*, **1973**, *8*, 3719.
8. R. A. Bromley, *Physics Letters A*, **1970**, *33*, 242-243.
9. K. F. Mak, C. Lee, J. Hone, J. Shan and T. F. Heinz*, Phys. Rev. Lett*., **2010**, *105*, 136805.
10. J. A. Wilson and A. D. Yoffe, *Adv. Phys*., **1969**, *18*, 193.
11. T. Li. and G. Galli. Journal of Physical Chemistry C, **2007**, 44, 16192-16196.
12. S. Lebègue and O. Eriksson, *Physical Review B*, **2009**, *79*, 115409.
13. A. Splendiani, L. Sun, Y. Zhang, T. Li, J. Kim, C. Y. Chim, G. Galli and F. Wang, *Nano Lett*., **2010**, *10*, 1271-1275.
14. K. F. Mak, K. He, J. Shan and T. F. Heinz, *Nat. Nanotechnol*., **2012**, *7*, 494-498.
15. B. Radisavljevic, A. Radenovic, J. Brivio, V. Giacometti and A. Kis, *Nat. Nanotechnol*., **2011**, *6*, 147-150.
16. K. S. Novselov, D. Jiang, F. Schedin, V. V. Khotekevich, S. V. Morozov and A. K. Geim, *Proc. Natl. Acad. Sci. U. S. A*. **2005**, *102* 10451-10453.
17. A. Ayari, E. Cobas, O. Ogundadegbe and M. S. Fuhrer, *J. Appl. Phys.*, **2007,** *101*, 014507.
18. S. Bertolazzi, J. Brivio and A. Kis, *ACS Nano*, **2011**, *5*, 9703-9709.
19. Y. Yoon, K. Ganapathi and S. Salahuddin, *Nano Lett.,* **2011**, *11*, 3768-3773.
20. T. Cheiwchanchamnangij and W. R. Lambrecht, *Phys. Rev. B,* **2012**, *85*, 205302.
21. A. Ramasubramaniam, *Phys. Rev. B*, **2012**, *86*, 115409.
22. *M. Ye*, *D. Winslow, D. Zhang*, *R. Pandey and Y. K. Yap, Photonics*, **2015,** *2*, 288-307.
23. J. S. Ross, S. Wu, H. Yu, N. J. Ghimire, A. M. Jones, G. Aivazian, J. Yan, D. G. Mandrus, D. Xiao and W. Yao, *Nat. Commun*., **2013**, *4*, 1474.
24. Korn, S. Heydrich, M. Hirmer, J. Schmutzler and C. Schüller, *Appl. Phys. Lett*., **2011**, *99*, 102109.
25. K. F. Mak, C. Lee, J. Hone, J. Shan and T. Heinz, *Phys. Rev. Lett*., **2010**, *105*, 136805.
26. A. Splendiani, L. Sun., Y. Zhang, T. Li, J. Kim, C. Y. Chim, G. Galli and F. Wang, Nano Lett., **2010**, 10, 1271-1275.
27. H. J. Conley, B. Wang, J. I. Ziegler, R. F. Haglund, S. T. Pantelides and K. I. Bolotin, *Nano Lett.,* **2013,** *13*, 3626-3630.
28. A. Castellanos-Gomez, R. Roldán, E. Cappelluti, M. Buscema, F. Guinea, H. S. J. van der Zant and G. A. Steele, *Nano Lett*., **2013**, *13*, 5361-5366.
29. R. Das, B. Rakshit, S. Debnath and P. Mahadevan, *Physical Review B*, **2014**, 89, 115201.
30. Q. H. Wang, K. Kalantar-Zadeh, A. Kis, J. N. Coleman and M. S. Strano, *Nat. Nanotechnol*., **2012**, *7*, 699.
31. C. H. Lee, G. H. Lee, M. van der Zande, W. Chen, Y. Li, M. Han, X. Cui, G. Arefe, C. Nuckolls, T. F. Heinz, J. Guo, J. Hone and P. Kim, *Nat. Nanotechnol.*, **2014**, *9*, 676-681.
32. M. M. Furchi, A. Pospischil, F. Liebisch, J. Burgdörfer and T. Mueller, *Nano Lett*., **2014**, *14*, 4785-4791.
33. T. Mohiuddin, A. Lombardo, R. Nair, A. Bonetti, G. Savini, R. Jalil, N. Bonini, D. Basko, C. Galiotis, N. Marzari, K. Novoselov, A. Geim, A. Ferrari, *Phys. Rev. B*, **2009**, *79*, 1-8.
34. F. Xia, H. Wang, D. Xiao and M. Dubey, *Nat. Photon*., **2014**, *8*, 899-907.
35. S. Tongay, J. Zhou, C. Ataca, J. Liu, J. S. Kang, T. S. Matthews, L. You, J. Li, J.C. Grossman and J. Wu, *Nano Lett*., **2013**, *13*, 2831-2836.
36. B. Chakraborty, A. Bera, D. V. S. Muthu, S. Bhowmick, U.V. Waghmare and A. K. Sood, *Phys. Rev. B*, **2012**, 161403(R).
37. L. Britnell, R. V. Gorbachev, R. Jalil, B. D Belle, F. Schedin, A. Mishchenko, T. Georgiou, M. I. Katsnelson, L. Eaves, S. V. Morozov, N. M. R Peres, J. Leist, A. K Geim, K. S Novoselov and L. A. Ponomarenko, *Science*, **2012**, *335*, 947-950.

38. C. H. *Lee*, G. H. *Lee*, *A. M. van der Zande*, *W. Chen*, Y. Li, *M. Han*, *X. Cui*, *G. Arefe*, *C. Nuckolls*, *T. F. Heinz*, *J. Guo*, *J. Hone*, *P. Kim Nat. Nanotechnol*., **2014**, *9*, 676-681.
39. H. Fang, S. Chuang, T. C. Chang, K. Takei, T. Takahashi and A. Javey, *Nano Lett*., **2012**, *12*, 3788-3792.
40. H. Fang, M. Tosun, G. Seol, T. C. Chang, K. Takei, J. Guo and A. Javey, *Nano Lett.*, **2013**, *13*, 1991-1995.
41. D. Kiriya, M. Tosun, P. Zhao, J. S. Kang and A. Javey, *J. Am. Chem. Soc*., **2014**, *136*, 7853-7856.
42. S. H. Yu, Y. Lee ,S. K Jang, J. Kang, J. Jeon, C. Lee, J. Y. Lee, H. Kim, E. Hwang, S. Lee and J. H. Cho, *ACS Nano,* **2014**, *8*, 8285-8291.
43. Y. Huang, W. Zheng, Y. Qiu, and P. Hu, *ACS Appl. Mater. Interfaces*, **2016**, *8*, 23362-23370.
44. J. Pak, J. Jang, K. Cho, T. Y. Kim, J. K. Kim, Y. Song, W. K. Hong, M. Min, H. Lee and T. Lee, *Nanoscale,* **2015**, *7*, 18780-18788.
45. R. F. Frindt*, J. Appl. Phys*., **1966**, *37*, 1928.
46. J. Kim, S. Kwon, D. H. Cho, B. Kang, H. Kwon, Y. Kim, S. O. Park, G. Y. Jung, E. Shin, W. G. Kim, H. Lee, G. H. Ryu, M. Choi, T. H. Kim, J. Oh, S. Park, S. K. Kwak, S. W. Yoon, D. Byun, Z. Lee and C. Lee, *Nat. Commun.,* **2015**, *6*, 8294.
47. J. Kim, S. Kwon, D. H. Cho, B. Kang, H. Kwon, Y. Kim, S. O. Park, G. Y. Jung, E. Shin, W. G. Kim, H. Lee, G. H. Ryu, M. Choi, T. H. Kim, J. Oh, S. Park, S. K. Kwak, S. W. Yoon, D. Byun, Z. Lee and C. Lee, *Nat. Commun.,* **2015**, *6*, 8294.
48. P. Joensen, R. F. Frindt and S. R. Morrison, *Mater. Res. Bull***. 1986**, *21*, 457-461.
49. V. Nicolosi, M. Chhowalla, M. G. Kanatzidis, M. S. Stranoa and J. N. Coleman, *Science*, **2013**, *340*, 1226419-1226437.
50. Y. H. Lee, X. Q. Zhang, W. Zhang, M. T. Chang, C. T. Lin, K. D. Chang, Y. C. Yu, J. T. Wang, C. S. Chang, L. J. Li and T. W. Lin, *Adv Mater,* **2012**, *24*, 2320-2325.
51. G. F. Schneider, V. E. Calado, H. Zandbergen, L. M. K. Vandersypen and C. Dekker., *Nano Lett*., **2010**, *10*, 1912-1916.
52. C. R. Dean, A. F. Young, I. Meric, C. Lee, L. Wang, S. Sorgenfrei, K. Watanabe, T. Taniguchi, P. Kim, K. L. Shepard and J. Hone, *Nat. Nanotechnol*., **2010**, *5*, 722-726.
53. P. Zomer, S. Dash, N. Tombros, B. van Wees, Appl. Phys Lett., **2011**, *99*, 232104.
54. A. Castellanos-Gomez, M. Buscema, R. Molenaar, V. Singh, L. Janssen, H. S. J. van der Zant and G. A. Steele, *2D Materials*, **2014**, *1*, 011002.
55. C. Lee, H. Yan, L. E. Brus, T. F. Heinz, J. Hone and S. R. Yu, *ACS Nano*, **2010**, *4*, 2695-2700.
56. M. A. Meitl, Z. T. Zhu, V. Kumar, K. J. Lee, X. Feng, Y. Y. Huang, I. Adesida, R. G. Nuzzo and J. A. Rogers, *Nature Materials*, **2006**, *5*, 33-38.
57. J. Ligenza and W. Spitzer, *Journal of Physics and Chemistry of Solids*, **1960**, *14*, 131-136.
58. M. Buscema, J. O. Island, D. J. Groenendijk, S. I. Blanter, G. A. Steele, H. S. van der Zant and A. Castellanos-Gomez, *Chemical Society Reviews*, **2015**, *44*, 3691-3718.
59. A. E. Becquerel, Memoire sur les effects d'electriques produits sous l'influence des rayons solaires. Comptes Rendus de L'Academie des Sciences, **1839**, *9*, 561.
60. C. E. Fritts, *Am. J. Sci.*, **1883**, *26*, 465-472.
61. D. M. Chapin, S. C. Fuller and G. L. Pearson, *Journal of Applied Physics*, **1954**, *25*, 676-677.
62. A. K. Geim and K. S. Novoselov, *Nat. Mater.,* **2007**, *6*, 183-191.
63. P. Miro, M. Audiffred and T. Heine, *Chem. Soc. Rev.,* **2014**, *43*, 6537-6554.
64. M. Xu, T. Liang, M. Shi and H. Chen, *Chem. Rev.,* **2013**, *113*, 3766-3798.
65. Q. Tang and Z. Zhou, *Prog. Mater. Sci.,* **2013**, *58*, 1244-1315.
66. R. Mas-Balleste, C. Gomez-Navarro, J. Gomez-Herrero and F. Zamora, *Nanoscale*, **2011**, *3*, 20-30.
67. C. N. R. Rao, H. S. S. Ramakrishna Matte and U. Maitra, *Angew. Chem., Int. Ed*., **2013**, *52*, 13162-13185.
68. G. Le Lay, E. Salomon, P. De Padova, J. M. Layet and T. Angot, *Aust. J. Chem*., **2014**, *67*, 1370-1372.
69. S. Z. Butler, S. M. Hollen, L. Cao, Y. Cui, J. A. Gupta, H. R. Gutiérrez, F. Heinz, S. S. Hong, J. Huang, A. F. Ismach, E. Johnston-Halperin, M. Kuno, V. V. Plashnitsa, R. D. Robinson, R. S. Ruoff, S. Salahuddin, J. Shan, L. Shi, M. G. Spencer, M. Terrones, W. Windl and J. E. Goldberger, *ACS Nano*, **2013**, *7*, 2898-2926.
70. R. Lv, H. Terrones, A. L. Elías, N. Perea-López, H. R. Gutiérrez, E. Cruz-Silva, L. P. Rajukumar, M. S. Dresselhaus and M. Terrones, *Nano Today*, **2015**, *10*, 559-592.
71. M. Chhowalla, Z. Liu and H. Zhang, *Chem. Soc. Rev*., **2015**, *44*, 2584-2586.

72. R. Lv, J. A. Robinson, R. E. Schaak, D. Sun, Y. Sun, T. E. Mallouk and M. Terrones, *Acc. Chem. Res*., **2015**, *48*, 56-64.
73. F. H. L. Koppens, T. Mueller, P. Avouris, A. C. Ferrari, M. S. Vitiello and M. Polini, *Nat. Nanotechnol*., **2014**, *9*, 780-793.
74. H. Zeng and X. Cui, *Chem. Soc. Rev*., **2015**, *44*, 2629-2642.
75. D. Jariwala, V. K. Sangwan, L. J. Lauhon, T. J. Marks and M. C. Hersam, *ACS Nano*, **2014**, *8*, 1102-1120.
76. K. Kang, S. Xie, L. Huang, Y. Han, P. Y. Huang, K. F. Mak, C.-J. Kim, D. Muller and J. Park, *Nature*, **2015**, *520*, 656-660.
77. M. Chen, H. Nam, H. Rokni, S. Wi, J. S. Yoon, P. Chen, K. Kurabayashi, W. Lu and X. Liang, *ACS Nano*, 2015, *9*, 8773-8785.
78. Y. Cui, R. Xin, Z. Yu, Y. Pan, Z. Y. Ong, X. Wei, J. Wang, H. Nan, Z. Ni, Y. Wu, T. Chen, Y. Shi, B. Wang, G. Zhang, Y. W. Zhang and X. Wang, *Adv. Mater*., **2015**, *27*, 5230-5234.
80. C. C. Mayorga-Martinez, A. Ambrosi, A. Y. S. Eng, Z. Sofer and M. Pumera*, Adv. Funct. Mater*., **2015**, *25*, 5611-5616.
81. H. J. Conley, B. Wang, J. I. Ziegler, R. F. Haglund, S. T. Pantelides and K. I. Bolotin, *Nano Lett*., **2013**, *13*, 3626-3630.
82. A. Castellanos-Gomez, R. Roldán, E. Cappelluti, M. Buscema, F. Guinea, H. S. J. van der Zant and G. A. Steele, *Nano Lett*., **2013**,*13*, 5361-5366.
83. Q. H. Wang, K. Kalantar-Zadeh, A. Kis, J. N. Coleman and M. S. Strano, *Nat. Nanotechnol.*, **2012**, *7*, 699–712.
84. M. Buscema, D. J. Groenendijk, S. I. Blanter, G. A. Steele, H. S. J.van der Zant and A. Castellanos-Gomez, *Nano Lett*., **2014**, *14*, 3347-3352.
85. C.-H. Lee, G.-H. Lee, A. M. van der Zande, W. Chen, Y. Li, M. Han,X. Cui, G. Arefe, C. Nuckolls, T. F. Heinz, J. Guo, J. Hone and P. Kim, Nat. Nanotechnol., **2014**, 9, 676-681.
86. M. M. Furchi, A. Pospischil, F. Libisch, J. Burgdörfer and T. Mueller*, Nano Lett*., **2014**, *14*, 4785-4791.
87. H. Fang, M. Tosun, G. Seol, T. C. Chang, K. Takei, J. Guo and A. Javey, *Nano Lett*., **2013**, *13*, 1991-1995.
88. H. Fang, S. Chuang, T. C. Chang, K. Takei, T. Takahashi and A. Javey, *Nano Lett*., **2012**, *12*, 3788-3792.
89. D. Kiriya, M. Tosun, P. Zhao, J. S. Kang and A. Javey, *J. Am. Chem. Soc*., **2014**, *136*, 7853-7856.
90. D. M. Sim, M. Kim, S. Yim, M. J. Choi, J. Choi, S. Yoo and Y. S. Jung*, ACS Nano*, **2015**, *9*, 12115-12123.
91. S. H. Yu, Y. Lee, S. K. Jang, J. Kang, J. Jeon, C. Lee, J. Y. Lee, H. Kim, E. Hwang, S. Lee and J. H. Cho, *ACS Nano*, **2014**, *8*, 8285-8291.
92. C. Huang, S. Barlow and S. R. Marder, *J. Org. Chem*., **2011**, *76*, 2386-2407.
93. X. Zhan, A. Facchetti, S. Barlow, T. J. Marks, M. A. Ratner,M. R. Wasielewski and S. R. Marder, *Adv. Mater*., **2011**, *23*, 268-284.
94. M. Urbani, M. Gratzel, M. K. Nazeeruddin and T. Torres, *Chem. Rev*., **2014**, *114*, 12330-12396.
95. M. V. Martinez-Diaz, G. de la Torre and T. Torres, *Chem. Commun*.,**2010**, *46*, 7090-7108.
96. T. Higashino and H. Imahori, *Dalton Trans*., **2015**, *44*, 448-463.
97. L. L. Li and E. W. G. Diau, *Chem. Soc. Rev*., **2013**, *42*, 291-304.
98. C. B. Nielsen, S. Holliday, H. Y. Chen, S. J. Cryer and I. McCulloch, *Acc. Chem. Res*., **2015**, *48*, 2803-2812.
99. E. Kozma and M. Catellani, *Dyes Pigm*., **2013**, *98*, 160-179.
100. C. Li and H. Wonneberger, *Adv. Mater*., **2012**, *24*, 613-636.
101. A. Castellanos-Gomez, M. Buscema, R. Molenaar, V. Singh, L. Janssen, H. S. J. van der Zant and G. A. Steele, *2D Mater*., **2014**, *1*, 011002.
102. N. R. Pradhan, D. Rhodes, Q. Zhang, S. Talapatra, M. Terrones, P. M. Ajayan and L. Balicas, *Appl. Phys. Lett*., **2013**, *102*, 123105.
103. A. Castellanos-Gomez, M. Barkelid, A. M. Goossens, V. E. Calado, H. S. J. van der Zant and G. A. Steele, *Nano Lett*., **2012**, *12*, 3187–3192.
104. H. Li, Z. Yin, Q. He, H. Li, X. Huang, G. Lu, D. W. H. Fam,A. I. Y. Tok, Q. Zhang and H. Zhang, *Small*, **2012**, *8*, 63-67.
105. M. S. Fuhrer and J. Hone, *Nat. Nanotechnol*., **2013**, *8*, 146–147.
106. S. Ghatak, A. N. Pal and A. Ghosh, *ACS Nano*, **2011**, *5*, 7707–7712.

107. A. Castellanos-Gomez, M. Buscema, R. Molenaar, V. Singh, L. Janssen, H. S. J. van der Zant and G. A. Steele, *2D Mater.*, **2014**, *1*, 011002.
108. M. Buscema, J. O. Island, D. J. Groenendijk, S. I. Blanter,G. A. Steele, H. S. van der Zant and A. Castellanos-Gomez, *Chem. Soc. Rev.*, **2015**, *44*, 3691-3718.

CONCLUSION

i) We have described a novel method for the functionalization of SWNTs using NDI-based bisalkene U shape molecules as precursors.They can either ring-close around the SWNTs to form rotaxane-like MINTs or oligomerize through ADMP and then wrap the SWNTs. Varying the solvent system can control the final outcome of the reaction. In TCE, the NDI precursors show lower affinity for the SWNTs, and the non-templated metathesis reaction is very slow. In contrast, in DMF, the non-templated reaction is significantly faster, and the NDI precursors show much larger binding constants towards SWNTs, which results in the formation of a substantial amount of oligomer-wrapped SWNTs.

ii) We take advantage of the nanostructuration provided by a single monolayer of graphene grown on Ru(0001) to chemically functionalize the graphene overlayer with atomic-level selectivity and exquisite spatial periodicity. Acetonitrile is homolytically broken by electron bombardment producing cyanomethyl radicals that react with the nanostructured graphene in a spatially modulated fashion. These results offer the possibility for tuning the graphene properties through an adequate covalent functionalization of single layer graphene with long-range order on the order of hundreds of nanometers and a periodicity of almost 3 nm. Moreover, identical results were obtained for propionitrile, isobutyronitrile and 2-phenylacetonitrile, establishing a benchmark for the attachment of more complex molecular structures to specific atomic sites on graphene.

iii) We have described a method to functionalize MoS_2-based photodetectors with PDIs and TPPs by a simple drop-casting method, resulting in a dramatic enhancement of the photoresponse and responsivity (three orders of magnitude larger) to visible light. Furthermore, the process is fully reversible and reproducible, demonstrating that molecular dyes are an easy and interesting way of improving the performance of photodetectors based on two-dimensional materials.

CONCLUSIONES

i) Se ha descrito un nuevo método para la funcionalización de SWNTs que utilizan moléculas basadas en Naftalenos como precursores. Dichas moléculas pueden cerrar alrededor de los SWNTs dando lugar a MINTs de tipo rotaxano u oligomerizarse a través de ADMP envolviendo a los SWNTs. La variación del disolvente puede controlar el resultado final de la reacción. En TCE, los precursores de NDI muestran una menor afinidad por los SWNTs, y la reacción de metátesis se produce de manera lenta. Por el contrario, en DMF, la reacción es significativamente más rápida, y los precursores de NDI muestran mayores constantes de unión a los SWNTs, lo que da lugar a la formación de una mayor cantidad de SWNTs envueltos en oligómeros.

ii) Hemos aprovechado la nanoestructuración proporcionada por una monocapa de grafeno crecida sobre Ru (0001) para funcionalizar químicamente el grafeno con selectividad a nivel atómico y exquisita periodicidad espacial. El acetonitrilo se rompe homolíticamente mediante bombardeo de electrones produciendo radicales cianometilo que reaccionan con el grafeno de una manera perfectamente controlada. Estos resultados ofrecen la posibilidad de ajustar las propiedades del grafeno a través de una funcionalización covalente del grafeno con un orden de largo alcance del orden de cientos de nanómetros y una periodicidad de casi 3 nm. Además, se obtuvieron resultados idénticos para propionitrilo, isobutironitrilo y 2-fenilacetonitrilo, estableciendo un punto de referencia para la unión de estructuras moleculares más complejas a sitios atómicos específicos sobre grafeno.

iii) Hemos descrito un método simple para funcionalizar MoS_2 basado en tintes moleculares de PDIs y TPPs, observando un incremento de la fotorespuesta y responsividad a la luz visible (tres órdenes de magnitud mayor). Además, el proceso es totalmente reversible y reproducible, demostrando que PDIs y TPPs nos permiten mejorar el rendimiento de los fotodetectores basados en materiales bidimensionales de una manera fácil y sencilla.